POLITECNICO DI TORINO

Master's Degree in Aerospace Engineering





Master's Degree Thesis

Functional Analysis, Life Cycle Assessment and Life Cycle Cost for Active Debris Removal Missions: A Comparison of Different Architectures

Supervisors

Prof. Paolo Maggiore Dr. Giuseppe Governale

Prof. Frederico Afonso

Prof. Inês RIBEIRO

Candidate

Alessandro Melifiori

Acknowledgements

This work represents the culmination of a 5-years long journey made possible thanks to the help, advice, and encouragement of many people along the way.

First and foremost, I would like to express my sincere gratitude to professor Paolo Maggiore for agreeing to be my supervisor and providing institutional support throughout my thesis journey. I must thank professors Inês Ribeiro, Frederico Afonso and Giuseppe Governale for their invaluable support, reviewing my progresses constantly and guiding me through my thesis development.

I want to thank the whole "Aerospace Group" of Friday afternoons: the opinions and advices were very helpful and made the thesis' progresses more visible, even when it was difficult to notice.

I would also like to extend my thanks to the whole Instituto Superior Técnico and Politecnico di Torino, for the opportunity to spend a year in the fantastic city of Lisbon, and for financing my studies.

Beyond the institutions, the precious support of my family and friends was truly important during the entire journey.

To the Succanaut group, who managed to make me feel home even when I was hundreds of kilometres away. I will always remember the beautiful moments we spent together.

To the "last-row" friends from Politecnico, Antonino, Davide, Matteo and Matteo, for their support and for the laughs when the lessons were far too boring. To all other colleagues from PoliTO - you are too many to name individually, but thank you all for being there.

To my home-town friends, Marco, Mattia, Mattia, Alessandro, Federico, Chiara, and many others who accompany me from the very beginning. Thank you for the support, the laughs and the beers whenever necessary.

To my aunts and uncles, who are here and who are no longer with us, Mauro, Donata, Alda, Sandro, Irma, Gianpiero, Mariuccia and Giovanni. Thank you for always believing in me.

To my elder cousins, Sara, Francesca, Edoardo, Eleonora, Riccardo and Elena, who supported me during the entire journey and gave me useful advices.

To my grandparents, Costantino, Emilio, Nuccia and Rina, who always believed in me; thanks for all your love.

To my loyal companions, Zoe and Trilly, now happily running among the heavens.

To Marta. Thank you for your patience, your motivation, your support and, again, your patience: thank you for believing in me, you made the last three years special, and I can't wait to go on a thousand more adventures with you.

Finally, but the most importantly, to my mum and dad, for always believing in me, even when I didn't, even when it was difficult. Thank you for the love and the unconditioned support. You have a special place in my heart.

bosh no क्षु ग्रै।

("Forth Eorlingas!" - The Lord of the Rings - J.R.R. Tolkien)

Abstract

This thesis analyses possible Active Debris Removal (ADR) mission architectures by comparing them on multiple levels. The objective is to determine if the studied mission concepts, selected from the literature for their simplicity, are suitable for the removal of non-operational spacecraft and rocket second stages, considering environmental impact, cost, and mitigation strategies. A preliminary functional analysis is developed to determine the requirements and main functions that the ADR spacecraft shall accomplish. Due to the lack of publicly available information, the proposed architectures are sized, the obtained results are validated through both a benchmark and a sensitivity analysis, and the mass breakdown is analysed, being the starting point for the Life Cycle Assessment (LCA). Data for the Life Cycle Inventories are gathered from both previously developed LCAs and guidelines, while in some other cases, processes and materials are modelled by the author. Costs are then estimated, based on existing guidelines and the Advanced Mission Cost Model (AMCM) software. The environmental impact and the costs of the launch vehicle are included in the study, finding the most suitable option for each analysed spacecraft. Lastly, the compliance with the identified requirements is verified, proceeding with the final architecture comparison. Results show how single-target satellites are preferred to multiple-target spacecraft for the removal of critical debris because of their lower mass and consequently lower costs and environmental impact. In this study it was assessed also the possibility to integrate a deorbiting kit, spacecraft deorbiting devices that exploit the space environment to lower the target's altitude, on the analysed satellites. However, the results show that the uncontrolled re-entry performed by the deorbit kits exceeds the on-ground casualty risk imposed by the mitigation guidelines, being hence not suitable for the removal of the selected targets. The thesis contributes to the ADR research field by applying the functional analysis to ADR satellites and suggesting some requirements and functions for future operations. Moreover, the environmental performance of the architectures is evaluated through the LCA, whose results can be used for the selection of further ADR missions, combined with considerations regarding their cost effectiveness.

Contents

1	Intr	oduction 15				
	1.1	Objectives				
	1.2	Thesis Outline				
2	State Of the Art					
	2.1	Current and Future Perspectives of Space Debris				
		2.1.1 Current Space Debris Situation				
		2.1.2 Future Space Debris Perspectives				
		2.1.3 The Lunar Orbits Case				
	2.2	Mitigation Strategies and Sustainability in Near-Earth Space				
	2.3	Selecting Orbits and Debris to Remove				
	2.4	Operations Definition				
	2.5	High-Level Requirements				
		2.5.1 Mission-Driven Requirements				
		2.5.2 Mitigation Requirements				
3	Functional Analysis 39					
	3.1	Mission Statement and Objectives				
	3.2	Concept of Operations				
	3.3	High-Level Requirements				
	3.4	Functional Flow Block Diagrams				
	3.5	N2 Diagrams				
	3.6	Critical Functions				
4	Met	shodology 57				
	4.1	Assessment and Verification of Requirements				
	4.2	Subsystems Selection and Sizing Process				
		4.2.1 Δv Budget				
		4.2.2 Vital Subsystems				
		4.2.3 Mission Subsystems				
		4.2.4 Sizing Logic				
	4.3	Launcher Selection				
	4.4	Life Cycle Assessment (LCA) Implementation				
		4.4.1 Goal and Scope Definition				

		4.4.2 Life Cycle Inventory (LCI) Definition and Methods	78			
		4.4.3 LCI of the Selected Components				
		4.4.4 Use Phase LCI	85			
	4.5	Safe Disposal Assessment				
	4.6	Life Cycle Cost (LCC) Definition	88			
5	Sizi	ng, Life Cycle Assessment and Life Cycle Cost Results	91			
	5.1	Identifying Orbits and Debris to Remove				
	5.2	Sizing Results				
		5.2.1 Program Validation				
		5.2.2 Trade-Offs				
	5.3	Launch Solutions				
	5.4	LCA Results				
		5.4.1 End-of-Life and Disposal				
	5.5	LCC Results				
	5.6	Safe Disposal and Requirements Verification				
		5.6.1 Safe Disposal Verification				
		5.6.2 Requirements Verification				
	5.7	Discussion	116			
6	Cor	nclusions	119			
	6.1	Achievements	119			
	6.2	Future Works	120			
Bibliography 140						
\mathbf{A}	Det	ailed Sizing Process	141			
В	$\mathbf{1^{st}}$	Level Functions Sequence for the Selected ADR Architectures	155			
\mathbf{C}	Det	ailed N2 Diagrams	157			



Nomenclature

Greek symbols

- α Angular Acceleration
- δ Angular Deceleration
- ε Computational Variable
- η Efficiency
- γ Ratio of Specific Heats
- Λ Latitude
- λ Wavelength
- μ Earth's Gravitational Constant
- Ω Right Ascension of the Ascending Node
- ω Angular Velocity
- ω_p Anomaly of the Perigee
- Φ_b Debris Flux
- ρ Density
- ρ_b Bond Albedo
- ρ_s Semi-Amplitude of the Earth's Shadow Cone
- σ Tension Before Rupture
- σ_S Stephan-Boltzmann Constant
- σ_{zz} Normal Stress in z Direction
- au Shear Stress
- θ Angle

- ε Specific Mechanical Energy
- ε_r Radiator Emissivity
- φ Phase Angle
- ζ Impacts Number
- $\dot{\Omega}$ Time Variation of Ω

Roman symbols

- A Surface
- a Semimajor Axis
- a_h Horn Radius
- B Magnetic Field Vector
- B Bandwidth
- b Force's Arm
- C Specific Heat
- C_D Drag Coefficient
- $\frac{C}{N}$ Carrier to Noise Ratio
- c_v Specific Heat at Constant Volume
- D Drag
- d Directivity [lu]
- D_p Antenna's Diameter
- E Energy
- e Eccentricity
- \hat{e}_B Magnetic Field Unit Vector
- E_b Energy per bit
- EIRP Effective Isotropic Radiated Power
- E Electric Field Vector
- \hat{e}_r Radial Unit Vector
- E_r , E_t Electric Field Radial and Transversal Components

FForce Focal Distance fGGain [dBi] $Gain \ [lu]$ gGravity at Surface g_0 Altitude hHorn Height h_h Ι Inertia Moment iInclination Average Current I_{av} I_{ch} Characteristic Current I_p Polar Moment I_{sp} Specific Impulse Earth's J2 Perturbation J_2 KInteger Number LLosses lLength MMoment mMass \dot{m} Mass Flow Rate Electron's Mass m_e MORModule of Rupture M_t Torque NNormal Force Raised Cosine Coefficient n N_0 Background Noise

Electron Density

 N_e

p	Pressure			
q_e	Electron's Charge			
R	Data Rate			
R_e	External Radius			
r_E	Earth's Radius			
R_{He}	Helium Gas Constant			
R_i	Internal Radius			
R_r, R_t	Magnetic Field Radial and Transversal Components			
R_t	Tank's Radius			
s	Thickness			
T	Temperature			
t	Time Duration			
t_b	Burn Time			
T_{MAX}	Maximum Satellite Temperature			
T_{MIN}	Minimum Satellite Temperature			
T_{orb}	Orbital Period			
U	Internal Energy			
V	Volume			
v, \mathbf{v}	Velocity (Vector)			
V_{mag}	Apparent Magnitude			
w	Width			
x, y, z	Cartesian Components			
Subscripts				
α	Atmospheric			
ap	Apogee			
ex	Exhaust			

P

Power

- f Final Condition
- i Initial Condition
- ion Ionosphere
- j Counter
- k k-th Debris
- max Maximum
- min Minimum
- ntb Non-Tumbling
- opt Optimal
- p Propellant
- pe Perigee
- φ Azimuthal Component
- PL Payload
- $pm \qquad \text{Polarization Mismatch}$
- pr Pointing
- S Free-Space
- t Transmission Line
- tb Tumbling

Superscripts

- n Raised Cosine Coefficient
- x, y, z Cartesian Components

List of Acronyms

ADCS Attitude Determination and Control System

ADR Active Debris Removal

AKD Autonomous Kit De-orbit

AMCM Advanced Mission Cost Model

ARES Assessment of Risk Event Statistics

CFRP Carbon Fiber Reinforced Polymer

CMG Control Moment Gyroscope

COE Classical Orbital Elements

ComSys Telecommunication System

ConOps Concept of Operations

CROC Cross Section of Complex Bodies

CSSA Cislunar Space Situational Awareness

D4D Design For Demise

D4R Design For Removal

DHS Data Handling System

DockSys Docking System

DPS Debris Protection System

DRAMA Debris Risk Assessment and Mitigation Analysis

EPDM Ethylene-Propylene-Diene Monomer

EPS Electrical Power System

ESA European Space Agency

FFBD Functional Flow Block Diagrams

GEO Geostationary Orbit

GNC Guidance, Navigation & Control

GPS Global Positioning System

GSO Geosynchronous Orbit

GWP Global Warming Potential

HEO High Earth Orbit

IRI International Reference Ionosphere

ISS International Space Station

KRM Kit Returns to Mothership

LCA Life Cycle Assessment

LCC Life Cycle Cost

LCI Life Cycle Inventory

LEO Low Earth Orbit

MASTER Meteoroid and Space Debris Terrestrial Environment Reference

MEO Medium Earth Orbit

MIDAS MASTER (-based) Impact Flux and Damage Assessment Software

MITRI MIT Risk Index

MLI Multi-Layer Insulators

NASA National Aeronautics and Space Administration

OBC On-Board Computer

ODCS Orbit Determination and Control System

ODE Ordinary Differential Equation

OSCAR Orbital SpaceCraft Active Removal

OSR Optical Solar Reflector

PCB Printed Circuit Board

PMSynRM Permanent Magnet Synchronous Reluctance Motor

RAAN Right Ascension of the Ascending Node

RD Research and Development

SARA Re-entry Survival and Risk Analysis

SCMK Single Chaser Multiple Kits

SCMT Single Chaser Multiple Targets

SCST Single Chaser Single Target

SERAM Spacecraft Entry Risk Analysis Module

SESAM Spacecraft Entry Survival Analysis Module

SLS Space Launch System

TCS Thermal Control System

Chapter 1

Introduction

During the last century, the exponential growth of the space sector led to an increase in the number of launchers and satellites orbiting the Earth. The number of active satellites is only a small fraction of the total amount of objects sent by humanity in space, and non operative spacecraft represents a great concern for the safety of ongoing and future missions [1]. If no countermeasures are taken, in the next century the number of objects in Low Earth Orbit (LEO) is likely to triplicate [2], requiring immediate action to avoid their uncontrolled growth.

To alleviate the problem, many mitigation practices of varying degrees of strictness have been implemented to avoid the creation of new debris, but not at a level that ensures the sustainability of the space environment in the long run [3]. Besides mitigation strategies, another possible approach is Active Debris Removal (ADR) missions [4], which aim to remove objects directly from their location and dispose of them in the atmosphere or graveyard orbits, where they do not interfere with the operations of functioning satellites.

The fact that, during the last decades, space sustainability became a great concern is proven by the European Space Agency (ESA), which is currently implementing a policy to achieve "net zero pollution" within 2030 [5], which consists in the reliable removal of satellites from valuable orbits immediately after the end of their operative life; to prepare ADR, the satellites' architecture must also adapt to the new Design For Removal (D4R) mission concept [5]. By doing so, it is possible not only to prevent the generation of new debris in orbit, but also to remediate the root cause of the problem [6]. The impact of these different approaches has been compared, showing their high importance to prevent the growth of future debris population [7].

However, ADR missions may require some technological challenges to be solved [8], and the need for some reference scenarios to be developed becomes relevant [9]. Moreover, the environmental impact of the entire life-cycle of a space program emerged as a priority in the new space economy, as documented by the ESA guidelines regarding the Life Cycle Assessment (LCA) [10], which has become a useful instrument to estimate the emissions of a project.

The long-term sustainability of the space environment, intended as "the ability to maintain space activity indefinitely in time" [11], the safety of the ongoing space missions

and the environmental impact of space programs are concepts of crucial importance if mankind aims at achieving a safe and stable access to space. In this perspective, this work wants to propose some ADR mission concepts, comparing them under several aspects, ranging from the sizing to the costs, also considering the environmental impact these missions can generate during their entire lifecycle; a functional analysis is performed as well. The objective is to find the most suitable architecture for the removal of LEO debris.

Mission concepts and the functional analysis are part of a larger, comprehensive System Engineering approach, aiming at guiding engineers throughout the whole design of a project; the National Aeronautics and Space Administration (NASA) produced a Handbook to guide the development of a whole space mission [12]: the approach is valid not only for space-related projects, but also for those requiring different design phases before becoming operational. Since this thesis explores the feasibility of ADR missions, a preliminary pre-phase A analysis is performed, defining Concept of Operations (ConOps), requirements and functional analysis of ADR spacecraft.

To study the environmental impact of the analysed missions, LCA is used. The LCA is a structured and standardized method, useful to quantify the emissions and the environmental performance of a product or, in general, of a project [10]. Despite some limitations for space-related LCAs still exist, it has become a fundamental component in the early mission design phases, helping to define the most sustainable alternatives for potential products. The importance of this tool is highlighted by the development of a Handbook [10] and a specific space-related database [13] by ESA, which is more and more relying on LCA for environmental impact analyses. To have a comprehensive view on the sustainability of space missions, Life Cycle Cost (LCC) will be also considered in this work.

1.1 Objectives

Since previous works regarding ADR only give some insights about possible mission concepts and generic requirements, this thesis wants to first explore more in depth the mission objectives, defining more detailed and comprehensive requirements and concepts of operations. Moreover, a functional analysis is developed to help determine which subsystems are required by ADR satellites to successfully exploit their functions.

This work also wants to verify the feasibility of the selected missions through a complete sizing of the satellites. The obtained mass breakdown will then be used as the starting point for both LCA and LCC. The results of the previous analyses will be combined with the verification of the selected requirements in order to determine which mission architecture better suits the imposed constraints, being the most appropriate for the removal of the chosen debris.

Differently from previous studies on this topic, a multi-level analysis of different ADR mission concepts is performed, including requirements verification, environmental and economical sustainability, and launcher selection: the study will not only identify the most suitable architecture for the removal of the selected debris, but will also find the most convenient one in terms of environmental impact and costs.

1.2 Thesis Outline

Chapter 2 shows a State of the Art review about the topic. First, the current situation of space debris in the Near-Earth environment is analysed, giving some future perspectives about the possible evolution of the issue. Second, mitigation solutions are presented, followed by a literature analysis of some ADR mission concepts. Lastly, a review of the guidelines regarding mitigation requirements is conducted, focusing on the different aspects that can undermine the safety of space operations.

Chapter 3 presents the results of the functional analysis following the NASA System Engineering approach [12]. The mission statement and mission objectives for ADR programs are defined, followed by the identification of some suitable architectures through the ConOps. Design reference missions are then developed and requirements are selected. Lastly, a functional analysis is developed using Functional Flow Block Diagrams (FFBD), identifying the critical functions for ADR spacecraft, and N2 diagrams to define the interfaces of the system are drawn.

Chapter 4 shows the methodology adopted during the sizing process of the selected mission architectures, as well as the instructions about the development of both LCA and LCC. The logic of the sizing process is here explained, followed by some considerations regarding the selection of the most suitable launch vehicles for the chosen mission concepts.

In Chapter 5, the results of the sizing process, the LCA and the LCC are given, making a comparative analysis on the different satellites considered. The launch solutions are also determined, being part of the multi-level analysis conducted. Lastly, the compliance with the selected requirements is verified, and the results are then discussed.

Chapter 6 shows the conclusions of the work, determining which analysed mission concept better suits the defined requirements, considering emissions and costs as well. The achievements of the thesis are presented, followed by some considerations regarding possible future works, which may be developed in order to conduct more complete analyses on the topic.

Chapter 2

State Of the Art

This Chapter focuses on the current condition of space debris, giving some insights about future perspectives. Moreover, already developed models for Active Debris Removal programs are shown, followed by considerations regarding international guidelines and space missions' requirements.

2.1 Current and Future Perspectives of Space Debris

Before starting the ADR mission analysis it is important to characterize the current space debris environment, giving some insights about its expected evolution to fully understand the need of such a mission.

2.1.1 Current Space Debris Situation

Although the precise number of objects orbiting the Earth is still unknown, some estimations regarding the largest ones have been made; on November the 1st 2016, 34,000 bodies larger than 10 cm were identified, while 900,000 objects larger than 1 cm and more than 128 million larger than 1 mm were detected [3]. Currently, many different networks for tracking space debris and satellites are used, like the *U.S. Space Surveillance Network* (able to detect debris as small as 5 cm in LEO and 1 m in Geosynchronous Orbit (GSO)), as well as radar and optical measurements, capable of detecting even smaller objects [14]. However, some particles are too small to be detected even by the most advanced technologies, making the current number of microscopic objects orbiting the Earth a mere approximation [8].

Figure 2.1 shows the presumed distribution of objects orbiting the Earth, highlighting the great amount of small bodies.

LEO:Low Earth Orbit goes from the Earth's surface to 2000 kilometres of altitude and is the most overcrowded region [3], since passing through it is the only way to reach space, and most of the dead spacecrafts end up there due to disposal maneuvers and orbital perturbations [15]. The debris distribution varies depending on the altitude and the inclination of the orbit, as shown in Figure 2.2. The most crowded areas are the ones hosting the heaviest satellites as well [3].

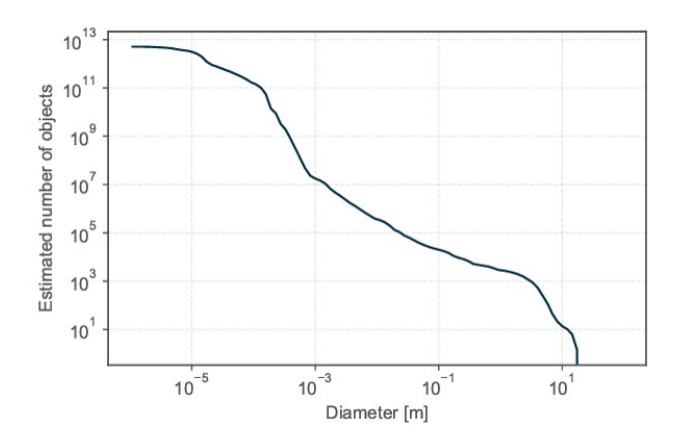


Figure 2.1: Estimated Number of Space Debris as a Function of their Size in Earth Orbit [3]

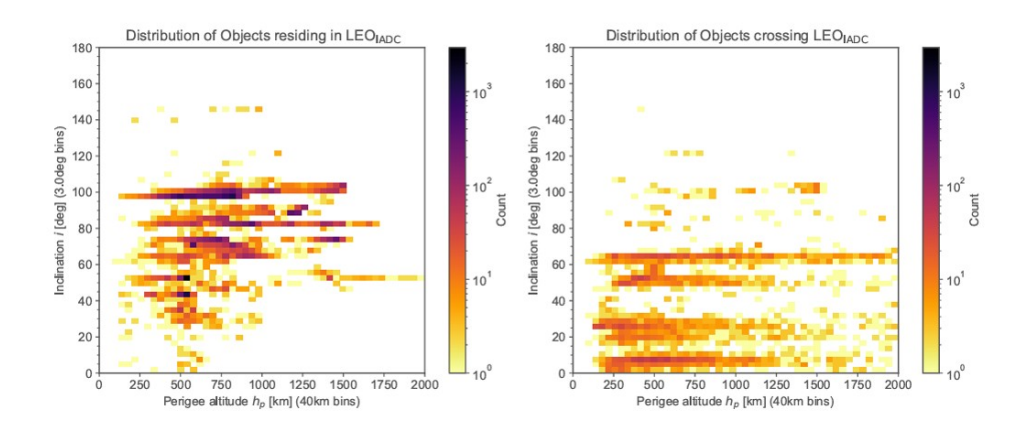


Figure 2.2: Estimated Number of Objects as a Function of Inclination and Perigee Altitude, Residing in LEO (left) and Crossing LEO (right) [3]

The high number of objects residing in LEO also causes a great amount of them to reenter the atmosphere every year: in 2022, more than 309 metric tons of material fell on Earth's surface, and most of them were aluminium debris, that can be a source of atmospheric pollution [2, 15, 16].

Although the majority of LEO objects resides in high inclination orbits (about 90 to 100 degrees, as depicted in Figure 2.2), the active LEO satellites are concentrated in orbits between 40 and 60 degrees of inclination and 500 to 600 kilometres altitude [3], meaning that the high inclination objects are mainly debris and dead spacecraft.

The high density of debris detected in LEO is also due to past impacts between satellites and intended break-ups in orbit: it is the case of the Chinese anti-missile test on the satellite Fengyun-1C in 2007, which resulted in an increase of 25% of the debris population, and the Iridium-33 and Cosmos-2251 (a defunct Russian satellite) impact in 2009,

which generated 2296 new catalogued debris and potentially thousands of smaller and undetected ones, creating an hazard for near by constellations [1].

LEO region is also the most critical regarding *conjunctions*, defined as geometric close approaches between two space objects (dead or operating), which trigger an analysis by the Ground Segment, but not necessarily a collision or an avoidance maneuver. The orbits where the most conjunctions happen are at about 500 km altitude and between 95 and 100 degrees of inclination, obviously resulting in the most crowded ones [3].

MEO: Medium Earth Orbit (MEO) ranges from 2000 to 35,786 kilometres altitude, and is generally not considered critical regarding space debris population, due to the small number of objects and the big volume it occupies. However, this region has a crucial role for global navigation and telecommunication constellations, and is regularly crossed by satellites heading to the upper Geostationary Orbit (GEO) and GSO regions [3]. Figure 2.3 shows the amount of active and inactive payloads in MEO.

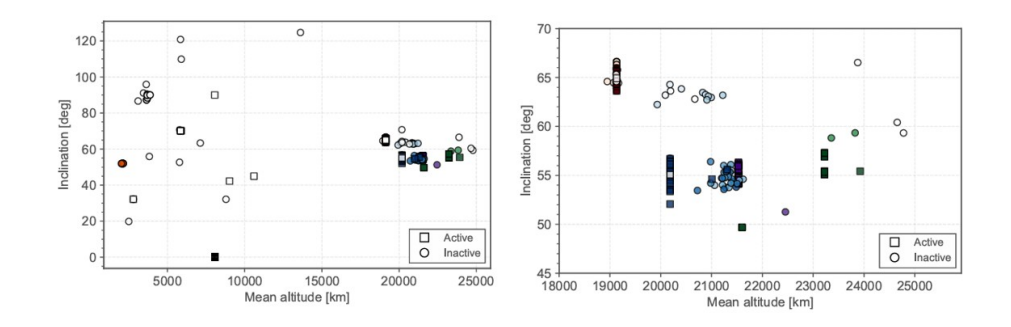


Figure 2.3: Distribution of Payloads in MEO in Mean Altitude and Inclination (Different Colours Mean Different Constellations) [3]

GEO: The Geostationary Orbit is located at 35,786 kilometres altitude and zero degrees inclination, and even if the number of satellites is smaller than in LEO region, it is considered a crowded orbit anyway. GEO region lacks of natural sink for the debris and dead spacecraft disposal (like aerodynamic drag in LEO), and the solar pressure makes it challenging to reliably predict the orbital path of spacecraft. Most of the satellites and rocket bodies reaching GEO region are large and heavy [3], resulting in an increase of the exposed area (which increments the risk of collision with other debris), as shown in Figure 2.4.

Lastly, since GEO and GSO orbits are very restricted and, due to their interesting physical properties, are ideal for telecommunication and many other uses [17], their accessibility must be preserved, limiting the interference of dead satellites and rocket bodies in those areas.

2.1.2 Future Space Debris Perspectives

Considering the current trend in sending satellites and objects into space, simulations about the future situation of space debris show a massive increase in the number of

objects orbiting the Earth [8], as represented in Figure 2.5.

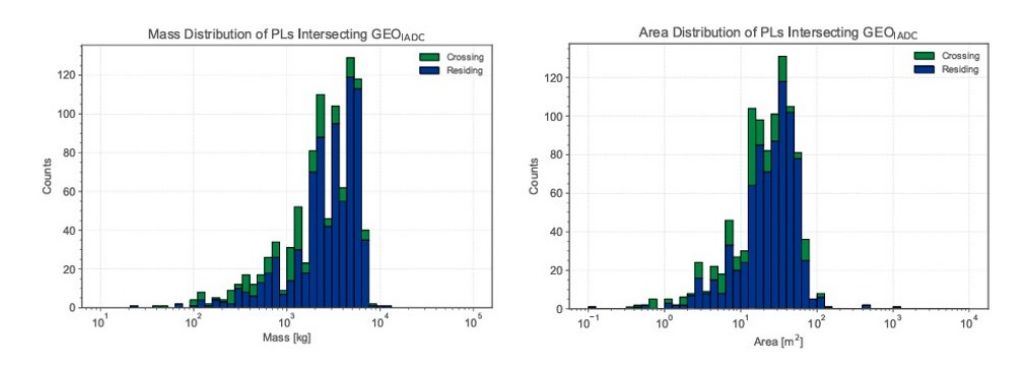


Figure 2.4: Mass (left) and Area (right) Distribution of Payloads in GEO [3]

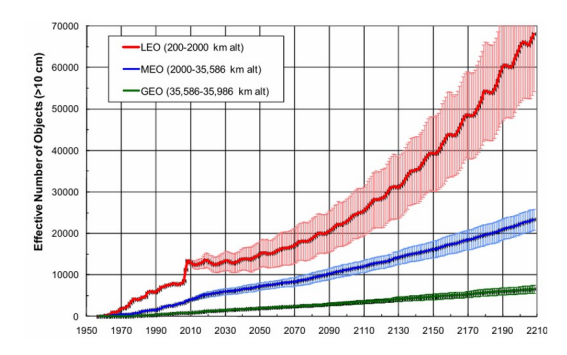


Figure 2.5: Simulated Future Debris Distribution in Different Orbits if No Countermeasures are Taken [8]

However, if some countermeasures are taken (for instance, rules about the maximum lifetime of satellites and the success rate of post-mission disposal maneuvers), it should be possible to avoid the uncontrolled debris growth [6, 8].

LEO:Since LEO is the region where most of the active satellites operate today, it will be the most crowded by dead spacecraft in the future [3]. Moreover, some commercial companies (SpaceX, Amazon, etc.) have shown great interest in launching large constellations there, raising the number of active payloads of several tens of thousands in the next decades [1]. The increase in the number of objects in LEO can also cause more conjunction events and collisions, representing a threat for active payloads and enhancing the number of debris created [18].

Using the ESA-Meteoroid and Space Debris Terrestrial Environment Reference (MASTER) software, it is possible to understand which LEO regions will be the most affected by the problem of space debris in the future. In Figure 2.6 can be noticed how in the immediate future the most affected orbits will be more or less the same, with a low but constant increase in the number of objects.

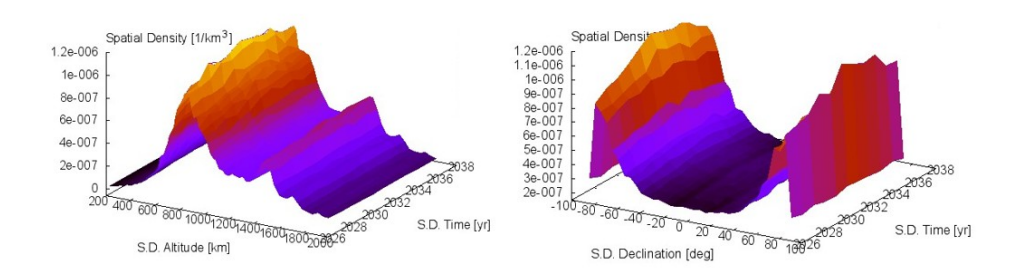


Figure 2.6: Simulated Future Debris Spatial Density in LEO Using the ESA-MASTER Software, by Altitude (left) and Declination (right); only Objects between 1 cm and 100 m Diameter are Considered

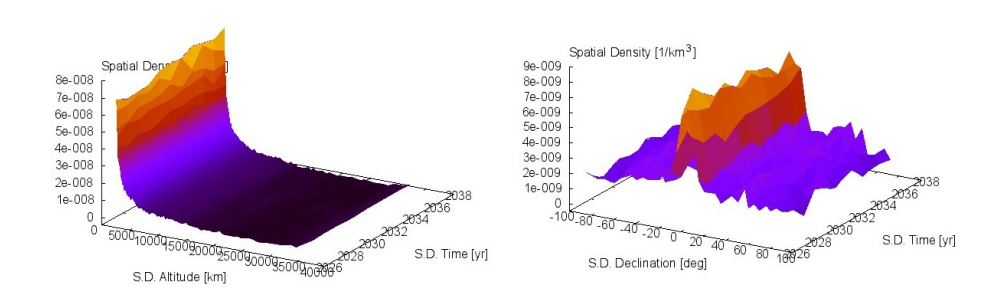


Figure 2.7: Simulated Future Debris Spatial Density in MEO Using the ESA-MASTER Software, by Altitude (left) and Declination (right); only Objects between 1 cm and 100 m Diameter are Considered

MEO: Since MEO is not a critical region, no environmental remediation is planned [8].

Simulations on ESA-MASTER in Figure 2.7 show how the spatial density of objects is higher in lower MEO, meaning that the largest amount of spacecraft and debris reside in the near LEO region. These graphs indicate a slow but constant growth in the number of objects for the next years.

GEO: Even if some authors agree that GEO regions do not need an urgent environmental remediation [8], the considerable number of active satellites and payloads makes it necessary to apply some disposal maneuvers at the end of life of the spacecraft, to fight for a certain time at least the effects of the perturbations acting in that area [3].

Simulations on ESA-MASTER in Figure 2.8 show the spatial density of the most massive objects is GEO. Clearly, the distribution of spacecrafts and debris for the next years will occupy the same altitude (about 35,800 km) and declination ($\pm 20 \text{ degrees}$), since it is the most profitable area for GEO and GSO applications.

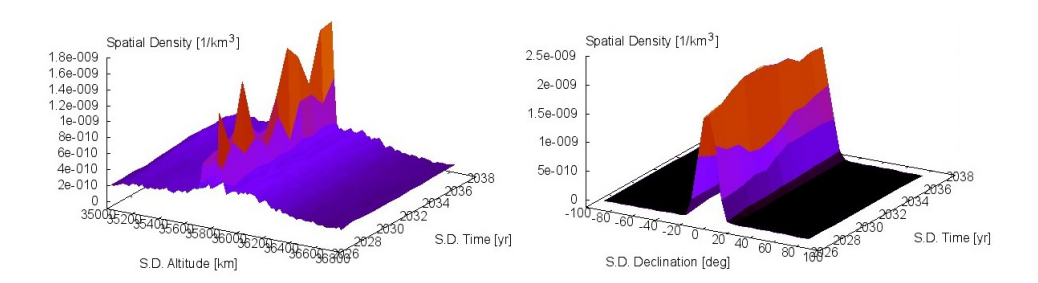


Figure 2.8: Simulated Future Debris Spatial Density in GEO Using the ESA-MASTER Software, by Altitude (left) and Declination (right); only Objects between 0.1 and 10,000 Kilograms are Considered

2.1.3 The Lunar Orbits Case

A wide region of Near Earth space is occupied by Lunar orbits; many different categories of Lunar orbits exist, depending on their shape and orbital elements. The simplest ones are conics around the Moon, but due to the proximity of the Earth, more complicated orbits have been studied, like three-body problem Earth-Moon-spacecraft orbits, Lagrange points [18], resonant orbits [19], halo orbits, Lyapunov orbits, distant retrograde and periodic orbits [20] and many more.



Figure 2.9: Examples of Lunar Orbits [20]

Nowadays, more and more satellites and payloads are heading into the cislunar space (between GEO and the Moon), and commercial companies seem interested in expanding their domain there, as well as the defence departments [21]. The main concern about this trend is the creation of a large number of space debris in that region, that can potentially lead to catastrophic consequences for the whole Near Earth area. Currently, some debris are already orbiting there, like the remains of the Apollo 13 oxygen tank (only explosion recorded in cislunar space) [22], but many more could be generated by further collisions. Many simulations were made in the last years about how space debris would develop in the cislunar region, showing how unpredictably the objects can spread in the whole Earth orbit. Simulations of explosions around the Lagrange points L1 and L2 [23, 24] and in lunar periodic orbits [22] indicate that the generated debris would likely be captured by the Earth, and some of them could even impact the Earth's surface, resulting in a great hazard for both the space and the terrestrial environment.

The apparently strange behaviour of these debris can be explained by the great amount

of different forces acting in that region; since the distance from the Earth is considerable, also the Sun and Jupiter's gravitational influences need to be considered, leading to an extremely dynamic environment [21, 23]. Moreover, some equilibrium points in the cislunar space are unstable (like the Lagrange points L1, L2 and L3), leading to further challenges in predicting orbits around them, while around stable points (like L4 and L5) large numbers of natural debris (the Kordylewski clouds) are thought to have been photographed at least once [25].

Since many future missions are heading to the cislunar space, and the interest of bringing humanity back on the Moon is rising [26], lunar orbits are being studied into detail to understand their distinctive dynamical behaviour. However, there is an increasing need to coordinate lunar and cislunar traffic, to prevent future impacts and collisions that can create a considerable population of new space debris [27]; the need for Cislunar Space Situational Awareness (CSSA) becomes then evident. A critical element for the future of the Near Earth space will be the full control of the lunar orbits, highlighting the need for space observations and orbital propagation for these highly unpredictable objects [21].

2.2 Mitigation Strategies and Sustainability in Near-Earth Space

The idea of applying mitigation strategies on new space missions first appeared in the second half of the 20th century, when some research papers were published regarding possible collision chain effects between debris in orbit, leading to the exponential growth of its population [28, 29, 30] (the so-called Kessler Syndrome). Due to the extremely high average impact speed (about 10 km/s [28]), the considerable masses of the objects involved and their dimensions, almost every collision between spacecraft can be considered catastrophic, leading to the fragmentation of both of them. The new debris generated during the impact can then be harmful for other orbiting objects [28]. This cascade effect occurs when a certain debris density is reached, and the sink effect that naturally removes the objects (aerodynamic drag for LEO) acts slower than the debris source [29, 31]: it has been estimated that the region between 900 and 1000 km altitude is permanently above the threshold density [29]. If the debris density increases even further, it can exceed the runaway threshold [30], meaning that the orbit tends to accumulate an infinite number of debris, and some of them (residing between 800 to 970 km) were measured to even exceed this limit during a survey in 1999 [30]. For higher orbits, where no aerodynamic drag is present, many debris can survive for potentially centuries if no further removal method is found [32].

Space debris can be considered both a long-term problem (potentially preventing future access to space) and a short-term problem (due to the mission-ending risk that it can generate), and the fact that even undetected sub-millimetres particles can be harmful for LEO missions [6] stresses the importance of mitigation strategies [28, 33] and retrieval techniques for dead satellites [28], as well as the development of new monitoring techniques for space objects [11]. The design of a new spacecraft shall consider these directives, and can be heavily influenced by these strategies [11, 28, 30].

The increase in number of satellites, as discussed before, can lead to safety issues, but can

also decrease the carrying capability of the orbits [1]. For this reason, protected regions have been created [5, 18, 34]: the "LEO Protected Region" is spherical and extends up to 2000 km altitude, while the "GEO Protected Region" is a segment of spherical shell at ± 200 km from GEO and with a declination of $\pm 15^{\circ}$, as represented in Figure 2.10.

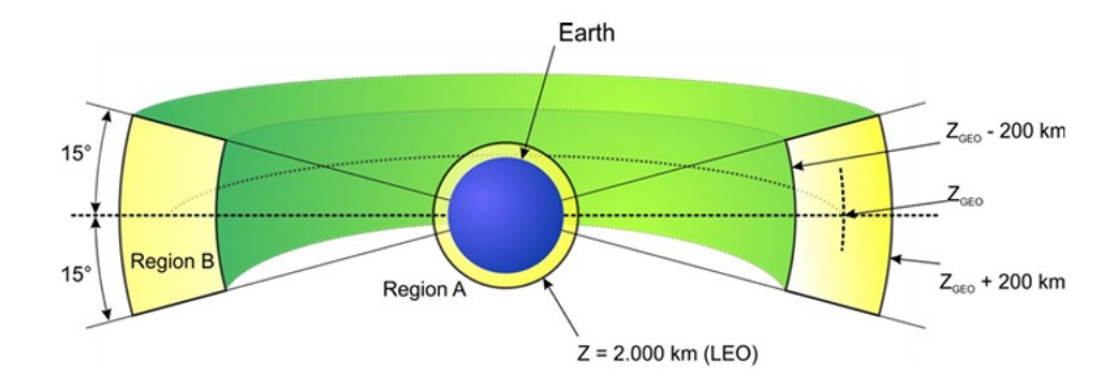


Figure 2.10: LEO and GEO Protected Regions [34]

For these regions, some important guidelines for the disposal operations are given, regarding the minimum time that a dead satellite must spend outside of these orbits and the success rate of the disposal maneuvers [5, 33, 34]. Guidelines for the lunar orbit case have been defined as well, determining both the success rate of end-of-life maneuvers and some of the preferred trajectories for disposal [18].

Lastly, atmospheric pollution is also a crucial factor to consider regarding the environmental sustainability of space: many disposal maneuvers aim at the ablation of the spacecraft structure in the atmosphere and, even though the environmental damage that this process can cause is still under investigation, some studies reveal a significant ozone depletion due to the products of the reactions happening during the re-entry [2, 15, 16]. Performing life cycle and atmospheric re-entry assessment becomes important to investigate the overall impact of a space mission [1, 35], assuring the environmental sustainability of the operations.

While the primary focus of the work remains the general sizing and LCA of ADR missions, this thesis also addresses the compliance of the operations with the mitigation strategies and requirements, following the international guidelines provided in Section 2.5.2. This aspect has received limited attention in already developed ADR studies, representing an interesting research gap which is explored in this document.

2.3 Selecting Orbits and Debris to Remove

To plan an ADR mission, the first step consists in defining the debris that are going to be removed. The results of the simulations contained in Section 2.1 show how LEO and GEO regions will be the most populated in the near future, and since more advanced simulations show that GEO will likely suffer only from a moderate debris population

growth, LEO should be the main target for ADR missions [4, 8].

Following the definition of the region, the focus must be the selection of the debris to remove; some previous studies suggest how preferred targets shall be debris with high $Mass \times Probability of Collision [4, 8]:$ the removal of these objects would not only mitigate the threat for operational spacecraft, but would also address the root cause of the problem, avoiding further collisions that can potentially end in the creation of many new debris [8]. So, ADR shall mainly be performed to control the debris population growth, rather than mitigating its effects [4]. Other methods to determine the most convenient objects to remove involve statistical approaches, targeting debris whose future dynamical behaviour can be critical [36]: using a Monte-Carlo model, researchers have been able to define an index, the MIT Risk Index (MITRI), that considers different types of data to give priority to some particular debris, considering aspects such as mass, background debris density, residual lifetime, probability of collision and others [36]. Further approaches can include the analysis of the catastrophic debris flux orbiting in specific regions, weighting it with its mass [37]; the fragility of the target, its attitude dynamics, and even political constraints must be considered while choosing the most suitable debris for ADR missions [37].

Lastly, the mission profile can significantly influence the choice of the objects; if a single target mission is selected, then the debris shall occupy one of the highest positions in the aforementioned priority lists, while if a multiple target mission is chosen (many orbital transfers performed during operations), the optimal debris list shall be created in such a way that the overall mission duration and the total required propellant mass are minimized, potentially leading to the selection of lower-ranked debris [9].

Since mass and probability of collision are key factors in the choice of the debris, almost every method described agrees on considering the bigger objects as the most critical ones. Large targets, though, are limited in number, and are mainly rocket bodies or large dead spacecraft [3, 38], with dimensions varying between 6 and 12 meters, and masses between 1.5 and 9 tons [8, 37].

The next aspect to take into account is the number of bodies to remove. Past researches and simulations show how the removal of five objects per year, chosen among the higher-rated ones, would be sufficient to stop the growth of the debris population in LEO and increase safety during space operations [4, 8].

In this document, the following approach is used [37]: the debris suitable for removal has been chosen among the most impactful ones, considering both the catastrophic flux in its orbit and its mass. Even though different mission architectures will be analysed, and in some cases multiple targets will be considered, the selected debris will remain the same. It would be possible to choose other debris to optimize the mission path, however it would no longer be among the higher-rated objects [9]. Five different bodies will be removed by each architecture in analysis, supposing that, replicating such missions in the future, it would allow to reach the stability of the debris population in LEO.

2.4 Operations Definition

To well-characterize an ADR mission, it is imperative to first define the operations that it shall perform. Literature shows different architectures for ADR and some reference models are here proposed [9, 38]:

- One Chaser for One Debris: each satellite deorbits one single object;
- One Chaser for Multiple Debris: each satellite deorbits many different objects. It requires additional maneuvering for orbit transfers [37];
- One Chaser for Multiple Deorbit Kits: each satellite deorbits many different objects, using some deorbit kits;
- Multiple Chasers for Multiple Deorbit Kits: multiple satellites deorbit many different objects, using some deorbit kits.

Basic mission profiles for the first three categories are represented in Figure 2.11.

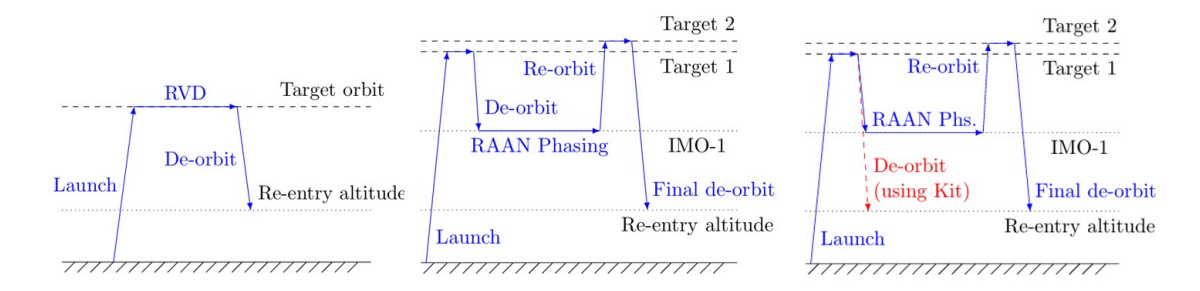


Figure 2.11: Basic Mission Profiles for One Chaser for One Debris (left), One Chaser for Multiple Debris (center) and One Chaser for Multiple Deorbit Kits (right) concepts [37]; RDV Refers to the Rendezvous Phase, while Right Ascension of the Ascending Node (RAAN) Phasing Refers to the Waiting Process for the RAAN Alignment in order to Save Propellant During the Transfer Maneuvers

Different concepts of deorbit kits can be defined as well:

- Non-Docking Deorbit Kits: released by the chaser satellite on the debris, they are not equipped with a own docking system (some examples in [39, 40]);
- Docking Deorbit Kits: after being released by the chaser satellite, they autonomously reach and dock with the debris (an example is shown in [41]).

It is worth noting that various mechanisms can be used to deorbit (or transfer) objects in space, some of which take advantage of the near-Earth space environment [42]:

• Electrodynamic Tethers: long, metallic tethers that exploit the gradient of the electron density in the ionosphere to generate an electric current when deployed toward Nadir [7, 43, 44, 45, 46, 47]; the current then interacts with the magnetic field of

the Earth, generating a Lorentz force that slows down the debris, allowing for a faster orbit decay [48]. The lightweight materials they can be made of (aluminium [48]) consent the deorbit of large debris using about 100 kg of instrumentation [7]. Electrodynamic tethers can be active (requiring power supply to help generating more current; more complex but more effective) or passive (only exploiting the relative motion with respect to the Earth's magnetic field; less complex, but also less effective) [38].

- Momentum Exchange Tethers: a vehicle in a higher orbit is connected to another vehicle in a lower orbit using a tether: since the orbital speed is proportional to the inverse square root of the distance to the center of the celestial body considered, the higher object is slower than the lower object, allowing for a decrease in the perigee of the lower object and an increase in the apogee of the higher one [38, 39]. Rotating tethered systems have been proposed as well [49]. However, it has been demonstrated that a 10 km long tether may be required to lower the perigee of the lower object of just 100 km, making this option unsuitable for ADR missions, due to the low effectiveness and the high-risk level [48].
- Inflatable Drag Augmentation Devices: they consist of inflatable structures that can rapidly increase their volume by combining two-component foams; their expanding ratio can range up to 1:1000 at standard atmospheric pressure; the gain in the area exposed to the residual atmosphere, as a consequence of the inflation, means an increase in the aerodynamic drag and a lower time required for the natural orbit decay of the object [39].
- Propulsion System: after docking, the propulsion system of the chaser satellite (or the kit) itself can be used to transfer the debris to a desired target orbit as shown in [38, 41], or even to de-tumble it [50]. Both chemical and electrical propulsion can be considered: while chemical propulsion is more suitable for precise proximity maneuvers and high thrust orbit changes [37, 38], electrical propulsion has higher specific impulse and lower thrust range [37], allowing for long-lasting, low thrust maneuvers [37, 38]. Many different solutions do exist, for instance bi-liquid propulsion systems, mono-propellant and hybrid propulsion [9], depending on the objectives to be accomplished.

Considering the basic mission profiles described in Figure 2.11, and the previously discussed solutions, it is possible to define the main operations that may occur during a typical ADR mission [39]: this breakdown will be further developed in the functional analysis presented in Chapter 3.

- 1. Launch and Separation from the Launcher: this event sets the beginning of the mission and it involves the launch and the deployment of either one or several chaser vehicles [38]. Some corrective maneuvers may be applied here [39];
- 2. Chasing the Debris: the first debris to be removed is targeted and approached [39]. It is worth noting that the debris order shall be optimized to require the least amount of propellant for the transfers, if a multiple target mission is chosen [36]. This phase may include the deorbit kit release if Docking Deorbit Kits are used [38];

- 3. Docking Phase: it includes capturing, coupling [39] and de-tumbling of the debris (if uncooperative) [9, 50]. This phase may involve the deorbit kit release if Non-Docking Deorbit Kits are used [38, 40]. Different mechanisms for docking can be applied, such as robotic arms [9, 48], capable of controlling all the degrees of freedom of the target and whose current technological level may be sufficient for ADR missions [7], or soft docking mechanisms, like harpoons, hooks or nets [9, 48].
- 4. Debris Deorbiting: by using one of the aforementioned deorbit mechanisms, the debris is removed from its initial orbit [38];
- 5. Targeting of the Next Debris: in case of a multiple target mission, the chaser vehicle may change its orbit multiple times; the transfers can be realised using in-plane or out-of-plane maneuvers [38], or exploiting the natural J2 perturbation of the Earth to shift the orbit's Right Ascension of the Ascending Node (RAAN), requiring less Δv for the maneuver, but more time to complete it [37, 38];
- 6. Self-Disposal: at the end of the mission, the satellite either re-enters the atmosphere or is moved to a graveyard orbit, in compliance with the mitigation requirements [38, 39] (see Section 2.5.2).

2.5 High-Level Requirements

Every space mission needs some requirements to be respected, in order to define its feasibility range. In general, requirements for most of the mission phases shall be determined, such as launch, propulsion, tracking, Guidance, Navigation & Control (GNC), stabilization, docking, deorbit and ground support; they are mainly given by the goal of the mission itself (*Mission-Driven Requirements*) and the safety of the space environment (*Mitigation Requirements*). While mission-driven requirements are very specific, mitigation requirements have been defined universally, and are collected in international guidelines [18, 51]. This Section focuses on the literature behind the requirements' selection, while the list of High-Level Requirements chosen for the analysed ADR missions is presented in Table 3.2.

2.5.1 Mission-Driven Requirements

Regarding ADR, High-Level Mission-Driven Requirements are mostly dictated by the objects that the satellite shall remove from their current orbits.

First, the *number* of debris to remove must be determined, as assessed by many studies [8, 9] and already discussed in Section 2.3.

Second, the *size* of the debris to remove shall be identified: while the removal of bodies sized between 1 and 5 cm could produce an instantaneous mitigation of the consequences of the debris issue, the deorbit of bigger objects, sized between 6 and 12 meters, offers a long-term solution to the problem [8, 9]. It is worth noting that ADR missions could also be extended to smaller debris, rather than considering only the larger ones; however, these missions may require different solutions to the ones proposed up to now, and due to the limited data available on this topic, this possibility will not be explored in the

document.

Third, the *stabilization* of the space environment shall be reached, reducing the risk of collisions to a level considered acceptable by operators and customers in the long run [9]; this requirement, however, can be seen as an effect of the previous ones, since it strongly depends on the success of the mission, or can also represent a way of selecting the debris to remove, by imposing the desired final risk level and choosing the objects as a consequence.

Lastly, the mission *duration* shall be determined, satisfying the imposed time constraints [38] and defining the most appropriate launch windows.

The aforementioned High-Level Mission-Driven Requirements can then be enriched with considerations regarding the high orbital range that ADR satellites shall endure, needing higher adaptability to different altitudes and solar local hours than typical LEO missions [38]; also, considerations regarding the possibility of docking, rendezvous and proximity operations can be included, imposing more stringent Lower-Level Requirements on the satellite's subsystems [38].

2.5.2 Mitigation Requirements

Since ADR missions aim at removing space debris and cleaning the space environment, mitigation requirements to avoid the release of further debris during operations, due to collisions or catastrophic failures of the spacecraft, are of crucial importance and shall be defined in an accurate way. Many High-Level Mitigation Requirements, concerning different aspects of the safety of the space environment, can be defined from guidelines [18, 51].

Space Debris Release Restriction: Satellites orbiting the Earth can release debris in many different ways, resulting in an increase in the probability of collision for other missions. Most satellites have deployable elements, such as antennae and solar panels, whose deployment can be triggered by pyrotechnic charges [52] that can potentially release a great amount of small objects in orbit. Another important source of debris during operations are solid or hybrid propellants [18]: these motors include up to 20% of aluminium powder to stabilize the combustion process and release aluminium oxides (Al₂O₃) that usually form high speed particles measuring less than 10 microns, but occasionally, due to instabilities in the combustion process, they can aggregate into larger particles called slags (up to 2 cm in size), whose low ejection speed allows for a longer orbital lifetime, generating dangerous impact fluxes [52]. Lastly, surfaces and Multi-Layer Insulators (MLI) can deteriorate in space due to the extreme environment, including ultraviolet radiation, atomic oxygen, thermal cycling, micro-particulates and micro-meteoroids: this phenomenon can shed big portions of material into space, aggravating the debris problem [52]. For these reasons, pyrotechnic devices, solid or hybrid motors and MLI or surfaces that deteriorate easily must be avoided, or alternatively can be used guaranteeing the non-release of debris larger than 1 mm [18], since they could damage in a critical way other spacecraft due to their speed.

Debris released in LEO protected region shall have an orbital lifetime shorter than 25 years, while debris released in GEO protected region shall not be perturbed for at least 100 years, leading to a change in their orbit and potential further collisions [51].

Avoid Break-Ups in Earth Orbit: One of the main contributors to the release of new debris are explosions of spacecraft and launchers' upper stages left on orbit: despite some explosions were intentional (as previously described in Section 2.1), the majority of them occurs accidentally, caused by onboard sources of energy not correctly managed. To avoid this problem, passivation shall be performed, depleting the dangerous fluids and deactivating electronics and moving parts at the end of the mission, when it no longer creates high risk to the payload [51]. This operation occurs before the end-of-life if no re-entry is expected, it is permanent and irreversible and 90% success rate shall be guaranteed (95% if performed in LEO or GEO protected regions) [18].

One of the major concerns regarding on-orbit break-ups are propellant tanks: the adverse environment, heating conditions and potential collisions can in fact trigger unexpected break-ups and explosions [52]. However, some design changes may be applied to avoid issues during the operations and the end-of-life phase; for instance, in bi-propellant systems, no common shaft valves between fuel and oxidizer shall be implemented, and a common tank separated by a bulk head shall be avoided, as well as single point failures common feed lines where fuel and oxidizer could mix and react unexpectedly; also, freezing-resistant vent lines could be implemented to clear the feed lines of the apogee engine after its shut-off, or alternatively a pressure relief mechanism can be applied [52]. The passivation of the propulsion system may be different for tanks with or without a membrane to separate the propellant from the pressurant: for tanks without membranes, the engine can be used to deplete both the propellant and the pressurant gas, achieving the safety pressure level required (far below the 5.5 bar limit, reaching less than 1 bar, through small thrusts of combined helium and hydrazine), while for tanks with membranes, the pressurant can moderately penetrate through the membrane itself due to its porosity, allowing for a partial emptying of the tank [53]. This last method, however, does not allow for a complete depletion, requiring higher safety margins [52]; alternatively, other passivation devices can be implemented, such as shape memory alloy valves and pyrovalves [53].

Another subsystem that shall be passivated at the end of a mission is the Electrical Power System (EPS), due to the high pressure contained in charged batteries, especially for NiH₂ devices [52], that can reach values up to 1000 psi [54]. The passivation of these items can include pressure relief valves or diaphragms, minding the potential decrease in reliability that could occur consequently [52]. Usually, the passivation sequence for batteries includes the shut-off of the charging lines (by cutting the wires between batteries and solar arrays [53]) and then the discharge (positive or natural) of the battery, decreasing considerably the risk of break-up; this method, however, should be combined with a correct design of the battery case to withstand the possible increase of the inner pressure during standard operations [52]. Special attention is required for Li-ions batteries, since they contain dangerous material inside, and a rupture due to overcharge can result in a leakage of reactive lithium metal; however, many Li-ions devices have safety relays to prevent this scenario, and if a complete disconnection of the feed line is performed at the end-of-life, risks related to a possible overcharge are eliminated [54].

A dangerous source of internal kinetic energy are momentum devices such as gyroscopes and reaction wheels, making them a potential threat for break-ups [51, 52]; however,

after the EPS has been shut-off, these instruments lose energy rapidly, being no longer a menace for the mission's safety [52].

Lastly, the telecommunication subsystem shall be deactivated in the end-of-life phase, preventing possible electromagnetic interferences with future missions using similar frequencies to communicate [54].

In conclusion, to avoid in-orbit break-ups, it is fundamental to de-energize the satellite's subsystems when the spacecraft will no longer be operative. Two different philosophies for passivation do exist: the *Hard Passivation* aims to completely deplete the satellite's stored energy (more conservative approach), while the *Soft Passivation* intends to partially deplete the subsystems' stored energy under a certain safety level, which is low enough to avoid accidental ruptures (less restrictive approach); studies regarding soft passivation have been made on pressurized gas vessels, showing, for instance, that an internal pressure equal to $\sim 15/25\%$ of the burst pressure can be enough to prevent catastrophic failures and explosions of the vessel [55], meaning no need for a complete depletion of the fluid. Both hard and soft passivation share the same objective of eliminating possible threats for in-orbit break-ups during the end-of-life phase of a space mission [51, 55]. Moreover, if any intentional explosion or break-up occurs, it shall not generate debris bigger than 1 mm with an orbital lifetime longer than 1 year [51].

Accidental Break-Ups by Collisions: The Near Earth space environment is populated by a large number of debris (as depicted in Section 2.1) that can potentially collide with other spacecraft, generating further dangerous bodies. Due to the high collision velocities, typically between 10 to 20 km/s, even an object much smaller than a satellite (millimetres to centimetres sized, weighting up to some grams) can produce a fragmentation event and a catastrophic collision; usually, debris with a diameter of 10 cm or larger are assumed to cause catastrophic collisions, resulting in a partial fragmentation of the impacted object [51, 52]. Impacts with smaller bodies can also produce further particulate, called ejecta, leaving the surface of the spacecraft, and even larger paint fragments called "spalls" (up to five times the diameter of the crater generated by the impact) can be released in space [52]. In addition to the external structural harm, debris or meteoroid impacts can cause punctures in propellant tanks and fuel leakages, as well as critical damage to attitude control sensors and electronics, resulting in higher risk of explosions and the eventual loss of control of the spacecraft [51].

It is possible to estimate the number of total impacts occurring during a certain amount of time by using:

$$\zeta = \Phi_b A t \tag{2.1}$$

where ζ is the impacts number, Φ_b the flux of fragments per square meter of surface per year (which is a function of the ratio between the masses of the satellite and the fragment), A the exposed area of the spacecraft and t the time span (in years) [14, 56]. During the design phase of the mission, impacts with debris and meteoroids larger than 1 mm diameter shall be assessed until the re-entry of the satellite, or at least for 100 years, including the possibility of shielding the sensible exposed area of the spacecraft [18]. Guidelines define thresholds regarding the acceptable probability of collision for each conjunction:

 \bullet < 10^{-6} for the cumulative probability of collision between the spacecraft and other

manned satellites, or between the spacecraft and its own deliverable payload, during the whole lifecycle [18];

- < 10⁻⁴ for the probability of collision per conjunction between the spacecraft and debris bigger than 1 cm diameter, during the operational lifetime [18];
- < 10⁻³ for the cumulative probability of collision between the spacecraft and debris bigger than 1 cm diameter, during the whole lifecycle and while performing proximity maneuvers, which may be crucial for ADR missions [18] (other guidelines [51] set this probability for debris bigger than 10 cm; a conservative approach considers the most restrictive value between the two given by the different documents);
- $< 10^{-2}$ for the cumulative probability of collision between spacecraft and debris capable of preventing compliance with the post-mission disposal operations, during the operational lifetime [51].

The term "whole lifecycle" refers to the time until re-entry, or alternatively 100 years are considered [18, 51]; for this time duration, the expected number of conjunctions, whose probability of collision fits between 10^{-6} and 10^{-4} , shall be evaluated [18]. When the probability of collision becomes higher than the accepted risk, it is necessary to perform an avoidance maneuver to change trajectory and guarantee a safety distance between the spacecraft and the debris [52]; these maneuvers are crucial and their number, required time and required Δv shall be considered in the design phase of the mission [18, 57]. Moreover, whenever an avoidance maneuver occurs, the probability of impact shall remain $< 10^{-4}$ for at least 4 days [18]. The guidelines show how crucial is the capability of performing maneuvers for LEO and GEO satellites, especially if they navigate across the protected regions [18]. It is worth noting, however, that only a small fraction of the debris has been tracked properly and is considered in the evaluation of the overall risk of collision [52] meaning that the real probability of impact could be higher than the predicted one.

Guidelines also assess the contact risk during proximity operations: the probability of unintentional contact shall be $< 10^{-4}$, considering possible perturbations, failures and multiple space objects involved during the maneuver. If the probability becomes higher than 10^{-4} , the threshold level shall be re-established at least for 7 days before proceeding with the next proximity operation attempt [18]. Also, recovery operations shall be considered in the design phase of the mission [18].

To guarantee its surveillance and tracking, the spacecraft must be wide enough to be passively detected by ground antennae: if the perigee of the orbit is contained in the LEO protected region, then the satellite shall have at least one dimension larger than 10 cm, otherwise it shall measure no less than 50 cm. The position accuracy achievable using ground antennae is 100 m for a satellite orbiting inside the LEO protected region, and 1000 m for a satellite in the GEO protected region [18]. Different antennae networks are used to track both satellites and debris, as already shown in Section 2.1.

In case of non-compliance with the prescribed cumulative probability of collision thresholds, mitigation options such as shielding shall be applied [18].

Disposal: At the end of the operational lifetime of a satellite, in order to avoid leaving the dead spacecraft in a protected orbit increasing the debris number and consequently the risk of further collisions, a disposal maneuver shall be performed. Different possibilities can be considered:

- Deorbit maneuver: it consists of a deceleration aiming at decreasing the perigee of the orbit, resulting in a direct atmospheric re-entry or a transfer into an orbit with a shorter residual lifetime [51, 52];
- Re-orbit maneuver: it consists of rising or lowering the spacecraft's orbit to an altitude where it no longer interferes with other operational spacecraft [51, 52];
- Retrieval: the satellite is retrieved and returns to the Earth [51];
- Earth Escape: only for missions allowing for this possibility [51].

Usually, the deorbit maneuver is performed by satellites orbiting inside the LEO protected region, or travelling across it (altitude < 2000 km), otherwise the required Δv would be too high [52], since it strictly depends on the altitude of the operative orbit [53]. Maneuvers during the end-of-life phase can be active, if the propulsion system of the spacecraft is involved (liquid mono- or bi-propellant systems, electrical propulsion, solid rocket motors), or passive, if the space environment is exploited to change the satellite's orbit (dynamic or electrodynamic tethers, drag augmentation systems, etc.) [52]. Moreover, for satellites orbiting inside the LEO protected region, natural re-entry shall take less than 25 years after the end of the mission, and retrieval (if applicable) shall take less than 5 years [51]; since MEO orbits are not critical regarding the debris issue (as already discussed in Section 2.1), disposal maneuvers are not required, although efforts could be necessary to avoid worsening the current debris condition in those orbits too [51].

Since the success of the disposal maneuver is of crucial importance to avoid catastrophic break-ups, explosions and collisions with other objects in orbit [51], it shall be measurable and the overall probability of success shall be > 0.9, considering possible failures [18, 51]. Also, new space debris shall not be generated during the disposal [57], stressing the necessity of assessing the collision probability in this phase of the mission. In case of a free-drift disposal in LEO, the deorbit shall last less than 5 years and the cumulative collision probability shall remain $< 10^{-3}$ during that time [18]. GEO targets shall be prepared for ADR missions both in cooperative and uncooperative ways [18]; for GEO missions capable of disposal maneuvers, the required propellant to exit the protected region is almost equivalent to the one used for 3 months of station-keeping operations [54], and the resulting economic impact of the reduction of the satellite's life can be considerable [52]. So, this operation is expensive in terms of propellant consumption, and it shall be performed safely at the end of the mission [52].

Spacecraft can either be removed cooperatively or not during ADR: if the target is cooperative, it shall support the removal operation and deliver its attitude data, while if it is uncooperative (inside the LEO protected region), it shall dump its angular rates and passively enable its attitude reconstruction [18]. In both cases, however, it shall passively support the navigation of the chaser satellite and give access to removal methods [18].

Requirements regarding the ground casualties during the re-entry phase are given by

guidelines as well: the spacecraft on-ground re-entry casualty risk shall be $< 10^{-4}$ for uncontrolled re-entries [18, 51], determined probabilistically with a 95% confidence level; if the threshold is not respected, the re-entry shall be controlled [18]. The probability is determined by evaluating the casualty area as follows:

Casualty Area =
$$\sum_{j} \left(0.6 + \sqrt{A_j}\right)^2$$
 (2.2)

where 0.6 is the diameter of the circular area occupied by a human body and A_j the physical area of each debris, whose kinetic energy is > 15 J (assuming this value as the minimum capable of causing potential human casualties [51]). To assess the 10^{-4} probability level, the casualty area shall measure 7.3 m² [51, 53]: a representation is shown in Figure 2.12.

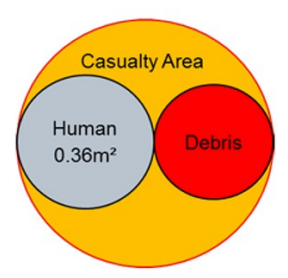


Figure 2.12: Estimation of the Casualty Area for an Atmospheric Re-entry [53]

It is evident how small satellites can assess this requirement more easily than larger ones. To avoid the survival of big portions of material, spacecraft shall be designed to almost completely burn during the re-entry phase, following the so-called Design For Demise (D4D) approach [51, 53]. This method consists in choosing materials for the satellite's components that are more likely to melt due to the extreme heat during the transit in the atmosphere: for instance, aluminium shall be used for low-pressure tanks instead of titanium, and also reaction wheels and gyroscopes shall be made of aluminium instead of steel, since it has a much lower melting point; furthermore, additive manufacturing can play a crucial role in the construction of complex shapes, allowing for a reduction of critical materials [53]. At a satellite level, subsystems can also be rearranged to expose the items that do not completely demise to the highest heat fluxes, or willingly breaking the spacecraft into different parts during re-entry, facilitating the demise of some critical elements [53].

If the on-ground re-entry casualty risk exceeds the 10^{-4} threshold, a controlled re-entry is then performed: it shall occur as soon as the mission ends, and a re-entry location shall be selected, possibly over a large uninhabited area of the ocean to minimize the risks for the ground population [51, 54]. This maneuver usually requires different low-altitude burns, needing powerful enough thrusters to guarantee a high control authority even when the aerodynamic drag becomes relevant [54]. For this re-entry option, the product between the probability of failure and the on-ground re-entry casualty risk shall remain $< 10^{-4}$

[51].

Dark and Quite Skies: To avoid interfering with astronomical observations, satellites shall appear faint enough not to be observed:

$$V_{mag} > 7.0 + 2.5 \log \left(\frac{h_{sat}}{550}\right)$$
 (2.3)

where V_{mag} is the visual magnitude of the spacecraft and h_{sat} the altitude of the spacecraft in km [18]. If $h_{sat} < 550$ km, the minimum allowed visual magnitude is set to be 7.0, and this threshold shall apply for all flight phases [18].

Lunar Orbits: Regarding the lunar orbits case, mitigation requirements are still under development. The main concerns are the avoidance of the creation of space debris in those areas and the overall probability of success of disposal maneuvers to be > 0.9 [18].

Special Operations: For some mission architectures requiring non-conventional operations, special mitigation requirements have been defined, being of crucial importance for ADR. For tethered systems, the generation of new debris due to the collision between the tether and other operational spacecraft shall be prevented, and the tether shall not remain deployed after the completion of its mission objective [51, 58]. Regarding rendezvous, proximity operations and satellite servicing, the mission design shall be oriented to avoid producing new debris, limiting the possibility of accidental collisions and explosions as a consequence of the operations [58]. Lastly, regarding ADR missions, the probability of accidental fragmentation of the debris structure, as well as the risk of unintentional collisions and explosions, shall be minimized [58].

As discussed in this Section, mitigation requirements are of crucial importance during the design phase of a mission, and statistical analyses are fundamental to assess the threats that a spacecraft can pose to both satellite population and people on ground. The informations here contained will be used in Section 3.3 to define the requirements of the analysed ADR mission architectures.

Chapter 3

Functional Analysis

This Chapter deals with the definition of the functions ADR satellites shall exploit. The NASA System Engineering approach [12] has been used, identifying the mission concepts, the requirements and the 1st and 2nd level functions which are necessary for the selected architectures. The analysis starts with the definition of a mission statement and mission objectives; some Concept of Operations adapted from the ones already discussed in Chapter 2 follow; requirements and functions are identified, and, lastly, N2 diagrams are developed. This procedure follows the steps' order presented by [12].

3.1 Mission Statement and Objectives

Before defining possible concepts of operations and requirements, it is necessary to choose an effective and straightforward mission statement to present the aim of the program to potential stakeholders; regarding ADR, a simple mission statement could be:

"The mission aims at removing non-operative satellites and rockets' second stages from Low Earth Orbit, to help reaching a sustainable and long-lasting access to space.,

Also, it is important to narrow down the mission's objectives in order to give more precise perspectives on the program to external parts and potential investors, explaining and motivating the main target. For the purpose of this document, the objectives shown in Table 3.1 have been chosen, following the considerations presented in Chapters 1 and 4.

Table 3.1: Selected Objectives for ADR Missions

N.	Objective		
1	The mission aims at removing non-operative satellites and rockets' second		
	stages from LEO, since smaller debris are more difficult to reach and detect,		
	and they are not considered to be the main responsible for catastrophic colli-		
	sions in orbit.		
2	The mission aims at guaranteeing a safe access to LEO and to space, prevent-		
	ing the Kessler cascade effect.		
3	The satellite will be disposed of at the end of its lifecycle, avoiding the release		
	and the potential creation of new debris in orbit.		

3.2 Concept of Operations

The ConOps is a crucial component for the success of a space mission, helping in both requirements definition and functional analysis development. ConOps typically includes a description of the main phases of the mission, the timeline, possible scenarios and critical events [12].

Different design reference missions and possible ConOps have been explored in Section 2.4, and a new categorisation is proposed here, based on which vehicle performs the rendezvous and proximity operations on the space debris; following this approach, it is also possible to define the amount of autonomous spacecraft maneuvering during the operations, giving a more realistic insight about the complexity of ADR missions.

Mothership Docking: In this scenario, the satellite itself docks with the debris. The mission starts with the satellite separation from the launcher and the approach to the first debris, proceeding with the proximity maneuvers and docking with it. After these first steps, depending on the mission architecture, the phases can vary significantly. Three main variations have been considered:

- Single Chaser Single Target (SCST): the satellite only docks with one debris. Immediately after the proximity operations and docking phase, the disposal takes place.
- Single Chaser Multiple Targets (SCMT): the satellite docks with the first debris. Then, it re-orbits the debris to a lower altitude, where the residual orbit lifetime is shorter. After the release of the first debris, the spacecraft approaches the next one, repeating the process until all the selected objects have been re-orbited.
- Single Chaser Multiple Kits (SCMK): the satellite docks with the first debris, then releases a deorbit kit to the target and separates from it. The spacecraft approaches the next debris, while the deorbit kit autonomously lowers the altitude of the previous one. In this mission architecture, the satellite carries more than one deorbit kit, and the aforementioned phases repeat until all the selected objects have been deorbited.

At the end of the mission, the disposal of the satellite takes place, considering both the possibilities of an atmospheric re-entry and the transfer into a graveyard orbit, waiting for further refurbishment. In SCST and SCMT, the satellite is disposed of together with the last debris docked.

Kit Docking: In this scenario, the deorbit kits are equipped to autonomously reach and dock with the selected debris. After the satellite separation from the launcher and the arrival to the desired orbit, the release of the deorbit kits takes place. Two different possibilities have been considered:

- Autonomous Kit De-orbit (AKD): the deorbit kit docks with the debris, and then deorbits it. The satellite meanwhile releases the other kits.
- **Kit Returns to Mothership (KRM)**: the kit docks with the debris, and then it brings it back to the mothership. The satellite meanwhile releases the other kits. In this mission architecture, the satellite keeps all the debris until the end of the mission, and the same kit can be used again to bring more targets to the spacecraft; it is worth noting that kits, in this case, are not properly deorbit kits, since they move the debris to the mothership and not to its disposal.

At the end of the mission, the disposal of the satellite takes place, considering both the possibilities of an atmospheric re-entry and the transfer into a graveyard orbit, waiting for further refurbishment. In KRM, the satellite is disposed of together with all the debris carried by the kits.

Figure 3.1 shows a comparison between the main phases for the analysed Mothership Docking architectures, while Figure 3.2 presents the main differences regarding the Kit Docking mission profiles.

Due to the intrinsic higher complexity of the Kit Docking mission architectures, involving many autonomous spacecraft operating at the same time, only Mothership Docking architectures will be considered and further analysed in this document. However, due to the higher flexibility that Kit Docking ConOps may offer, it could be worthwhile to further consider them in future analyses regarding ADR.

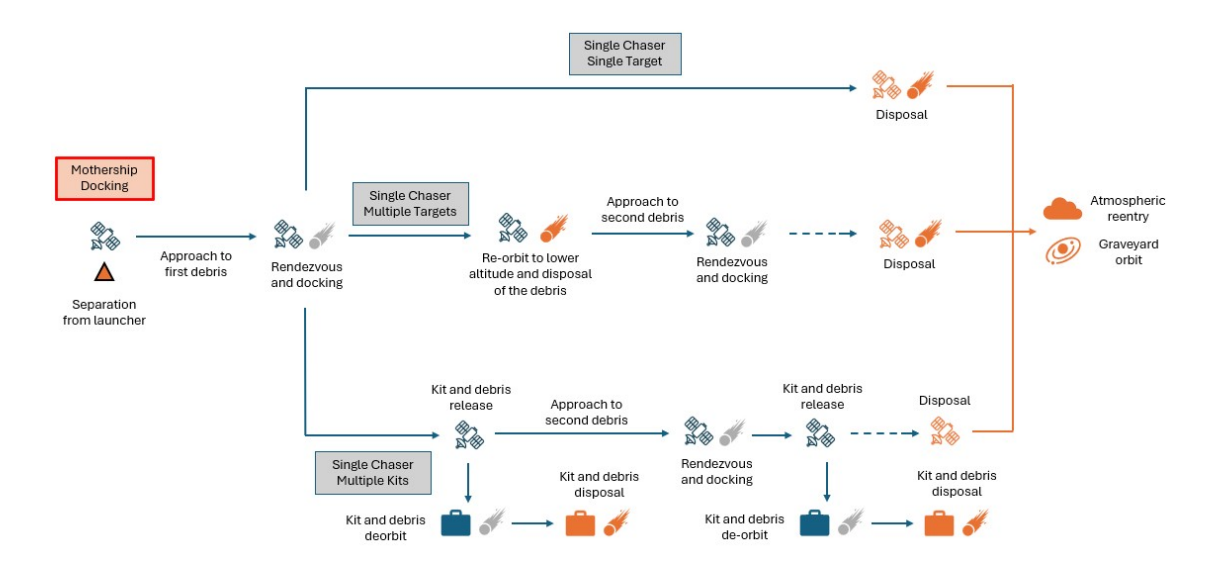


Figure 3.1: ConOps Comparison for the Different Mothership Docking Architectures Considered

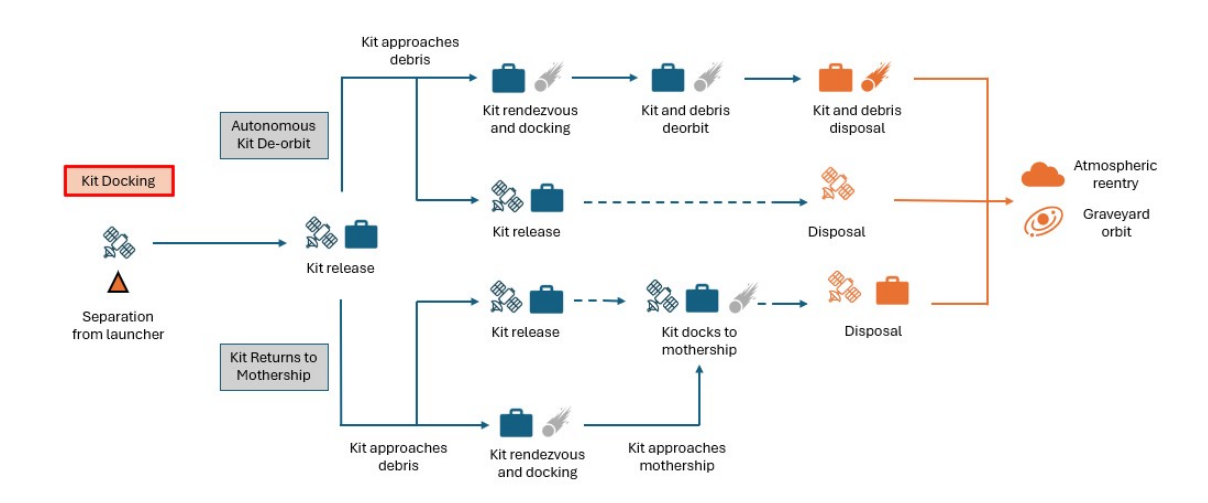


Figure 3.2: ConOps Comparison for the Different Kit Docking Architectures Considered

For the three selected ConOps, design reference missions are presented in Figure 3.3, 3.4 and 3.5, individually showing the sequence of the main mission phases for SCST, SCMT, and SCMK, respectively. The figures show the number of repeating phases, according to the number of targets to remove discussed in Section 2.3, and the main operations occurring from launch to disposal.

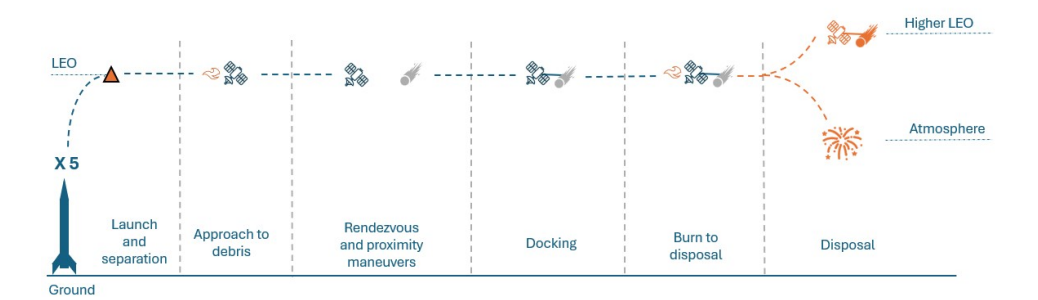


Figure 3.3: Design Reference Mission for SCST

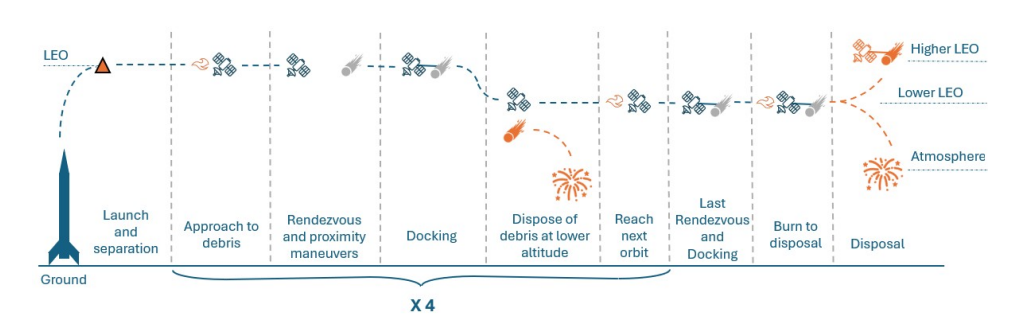


Figure 3.4: Design Reference Mission for SCMT

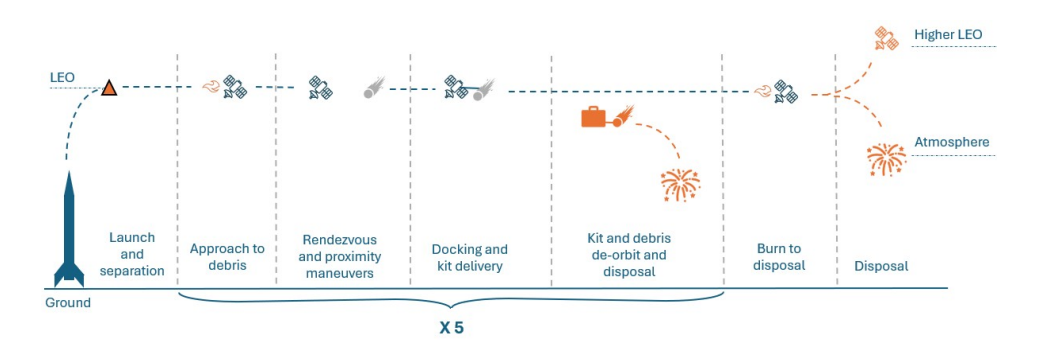


Figure 3.5: Design Reference Mission for SCMK

3.3 High-Level Requirements

Table 3.2 contains the selected requirements for all three ADR mission architectures analysed, while Table 3.3 completes the requirements definition with their rationale and verification methods. The category distinction of the requirements is given by [12].

Table 3.2: Requirements for the Selected ADR Mission Architectures

N.	Category	Requirement		
1	Operational	The mission shall remove 5 debris per year, with masses between		
		1.5 and 9 tons, and dimensions between 6 and 12 meters.		
2	Operational	The mission shall be operative in the orbits with altitude between		
		800 and 1000 km and inclination between 70 and 100 degrees.		
3	Functional	The satellite shall be able to perform proximity operations and		
		the docking system shall withstand the forces applied on it.		
4	Operational	The satellite shall have at least one side measuring > 10 cm.		
5	Safety	The satellite shall not release debris during operations. The proba-		
		bility of collision shall be $< 10^{-4}$ for each conjunction with debris		
		> 1 cm diameter. The cumulative probability of collision with		
		debris > 1 mm shall be $< 10^{-4}$ during the entire operative life-		
		time. The probability of contact during proximity operations shall		
		be $< 10^{-4}$. If the probability of collision exceeds the prescribed		
		values, shielding shall be applied on the sensible surfaces of the		
		spacecraft.		
6	Safety	The satellite and debris' disposal shall guarantee an on-ground casualty risk $< 10^{-4}$ if uncontrolled re-entry is performed; otherwise, a controlled re-entry shall be considered. The probability of		
		success of the disposal maneuver shall be > 0.9 . The satellite shall		
		be passivated at the end of its operative lifetime.		
7	Dark and	The satellite shall have an apparent magnitude > 7 during the		
	Quiet Skies	entire operative lifetime.		

Table 3.3: Rationale and Verification Methods for the Selected Requirements

N.	Rationale	Verification Methods
1	The debris to remove has been chosen following the considerations made in Section 2.3, and the list is presented in Section 5.1.	The selected ADR mission architectures have been sized to be able to deorbit the selected debris, as shown in Section 4.2.3.
2	The operative orbits have been chosen following the considerations made in Section 2.3, and their Classical Orbital Elements (COE) are presented in Section 5.1.	The selected ADR mission architectures have been sized to be able to operate in the selected orbits, as shown in Section 4.2.
3	In ADR missions, docking and rendezvous operations are of crucial importance, as explained in Section 2.4. The selected equipment must withstand the forces applied on it, without getting damaged.	The equipment for proximity operations has been selected in Section 4.2.3, while a method to verify its structural compliance is presented in Appendix A.
4	To allow the passive tracking of the spacecraft, the satellite shall be large enough to be detected by ground antennae, as reported in Section 2.5.2.	The dimensions of the satellites have been evaluated as shown in Section 4.2.
5	This is a necessary requirement to assess the compliance with the mitigation guidelines [18, 51] regarding the collision risk during operations, as discussed in Section 2.5.2.	ESA-Debris Risk Assessment and Mitigation Analysis (DRAMA) software [59] is used to assess the compliance of this requirement, with the methodology described in Section 4.1.
6	This is a necessary requirement to assess the compliance with the mitigation guidelines [18, 51] regarding re-entry casualty probability and in-orbit breakups risk, as discussed in Section 2.5.2.	ESA-DRAMA software [59] is used to assess the compliance of this requirement, with the methodology described in Section 4.1. Regarding passivation, some solutions are adopted as shown in Section 4.2.
7	Necessary requirement to assess the compliance with the mitigation guidelines [18, 51] regarding the interference with astronomical observations, as discussed in Section 2.5.2.	A simple methodology to assess the compliance with the requirement is presented in Section 4.1.

3.4 Functional Flow Block Diagrams

Following the NASA's approach described in [12], after the definition of the ConOps and the selection of the requirements, the following step in mission analysis is the logical decomposition of the system. Logical decomposition utilizes functional analysis as an instrument to decompose high-level requirements, allocating them to the desired project development level, helping identify the main functions that the system must achieve during its lifetime.

While performing a functional analysis, three key steps must be executed:

- 1. Translate top-level requirements into functions that the system must perform to be compliant with the selected requirements;
- 2. Decompose high-level functions and allocate them to lower levels;
- 3. From functions decomposition, identify and describe the needed subsystems and their interfaces.

This recursive and iterative process leads to the definition of the system architecture that accomplishes the chosen end product requirements. The detail level of the results depends on the mission design phase that is being studied (from Pre-Phase A, regarding a high-level feasibility study, to Phase E concerning the closeout after the end of the mission): since this document only concerns about feasibility studies of potential ADR missions (and not detailed subsystems' design), the level of the analysis performed will be a Pre-Phase A [12].

In this Section, the functional analysis of the architectures selected in Section 3.2 is performed by using FFBD: this technique allows to show the sequential relationship of low-level functions that the spacecraft must accomplish in order to obtain the fulfilment of the higher-level ones. A limit of this analysis is the absence of information regarding time duration (since only the sequence is shown, some functions may last seconds while some others days or even weeks): further studies may also consider this aspect of the missions more in depth, in order to give more detailed results about their feasibility.

FFBDs are developed from the top down, starting from high-level functions and decomposing them, level after level, up to the desired accuracy required by the design phase [12]. Starting from the main operations identified from literature in Section 2.4, it is possible to start defining the functions that ADR satellites shall perform: in the next paragraphs, a division between first-level and second-level functions will be provided [12]. The names of the developed phases are taken from Figure 3.1.

Separation from the Launcher: After reaching the desired orbit, the satellite detaches from the launcher's upper stage, starting its own operations; Figure 3.6 contains the 1st and 2nd level functions selected for this mission phase.

The functions here identified are common to all the three selected architectures, and are usually performed by most LEO satellites at the beginning of their operative life.

The first step consists in enabling the telecommunications with the Ground Segment, to prove the successful deployment from the launcher; to do so, energy must be provided,

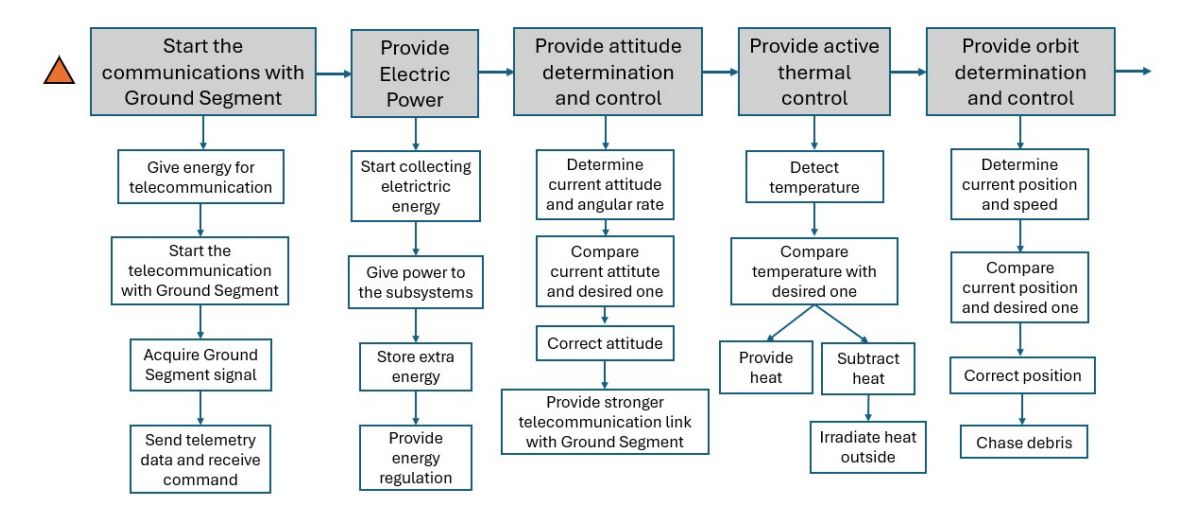


Figure 3.6: 1^{st} (Grey Boxes) and 2^{nd} (White Boxes) Level Functions regarding the Separation from the Launcher

and signals shall be sent to the ground station. Then, the transmissions from the station containing the first commands shall be acquired, and a consequent downlink communication containing vital data and telemetry shall be established. It is important to notice that the satellite, during this phase, is not yet capable of generating electrical power independently, and its attitude and position can only be estimated by ground tracking. The second step of this phase consists in gaining power self-sufficiency by start collecting electrical energy that can then be used to feed the subsystems, allowing the satellite to exploit its vital functions. The extra energy produced shall be stored to cope with unexpected peak power demands, and the power distribution shall be regulated and controlled to avoid malfunctions. These 2nd level functions usually occur before the attitude determination and control [60].

Once electrical power has been generated, it is possible to proceed with the attitude determination and control. A functioning attitude control is critical for space missions, and many successive 1st level functions depend on an accurate orientation of the spacecraft. First, the satellite shall be able to determine its current attitude and angular rates by collecting data; knowing the desired orientation, the system shall compare it with the detected one, understanding the required maneuvers to perform and proceeding with the corrections if necessary. Once the spacecraft has been oriented as desired, it is possible to provide a stronger and stable telecommunication link with the Ground Segment of the mission.

After the satellite has been correctly oriented in space, active thermal control can be provided. First, the temperature of the sensible components must be detected, allowing for a comparison with their operative temperature range. After that, two possibilities are considered: if the temperature of the component is too elevated, heat shall be subtracted and irradiated outside the spacecraft, while if the temperature is too low, heat shall be provided to warm up the item.

Lastly, once all the vital functions of the spacecraft have been provided, orbit determination and control becomes necessary [61]. The current position and velocity of the satellite shall be determined through data acquisition, and they shall be compared with the desired state vector. Once the maneuvers to perform have been determined, position and velocity vectors can be corrected and the chase of the first debris can begin.

Approach, Rendezvous and Docking: After the separation from the launcher and the exploiting of the vital functions, the ADR satellite can start chasing space debris, performing rendezvous and proximity operations. Figure 3.7 contains the 1st and 2nd level functions selected for this mission phase.

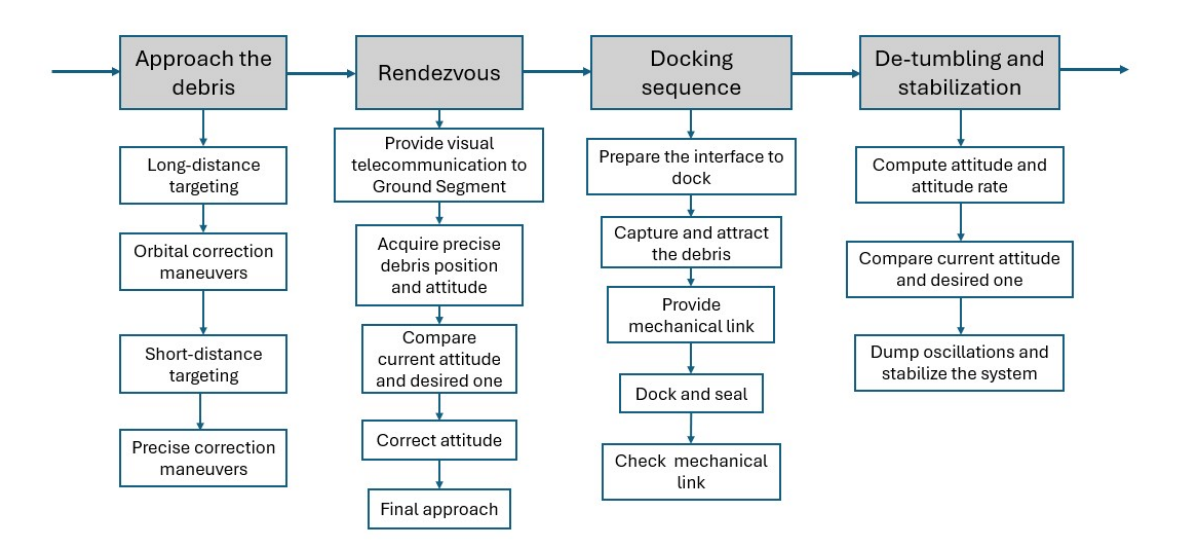


Figure 3.7: 1^{st} (Grey Boxes) and 2^{nd} (White Boxes) Level Functions regarding Approach, Rendezvous and Docking

Also in this case, the identified functions are common to all the three selected architectures; however, they are no longer ordinary for standard LEO spacecraft. The information contained in this paragraph is obtained from [39] and the process repeats whenever a debris is docked (in case of multiple-target missions such as SCMT and SCMK).

The approach to the debris is a process that can develop over different instants of time, and can be divided into long-distance targeting and short-distance targeting [9]. During long-distance targeting, the satellite is still far from the debris, and the object is detected from distance; once the maneuvers to apply to the satellite have been computed, orbital corrections are performed to get closer to the target. Then, short-distance targeting begins, allowing for a more accurate detection of the debris' position: new and more precise corrective maneuvers are computed and performed to get even closer to the object, allowing to proceed with rendezvous and proximity operations. Short-distance targeting may be difficult, since the debris might be uncooperative, showing a physical and optical status different from the expected one [9].

Rendezvous starts by providing visual telecommunication to the Ground Segment, allowing for more accurate proximity maneuvers that can be performed by ground personnel. After the link has been established, it is possible to start acquiring the debris relative position and attitude, determining where to perform docking; maneuvers for the final approach are then computed by comparing the current relative position and attitude of the spacecraft with the desired one, and the state vector of the satellite is then slowly corrected, allowing for the beginning of the docking sequence.

The docking sequence is the next 1st level function to occur, and during this phase the debris is captured by the chaser satellite. First, the docking interface shall be prepared for the operation in order to guarantee a smooth contact and to avoid the release of debris into space or damages to the target. The following capture and attraction of the debris (see Figure 3.7) is not mandatory, since it does not involve a stable mechanical link, but can be helpful in reaching an higher accuracy during the docking operations, facilitating the next 2nd level functions. The ADR satellite then provides a stable mechanical link to the target, proceeding with the docking and the sealing of the link, guaranteeing a stronger hold. Lastly, the mechanical link is checked in order to verify both the strength of the hold on the debris and the accuracy reached during the docking operations.

Since debris can be uncooperative, it may be necessary to de-tumble and stabilize the attitude after the docking process. Attitude and angular rates of the system (debris and spacecraft) must be detected or computed, comparing them with the desired ones. Corrective maneuvers shall be evaluated and performed, in order to dump the oscillations and stabilize the system. Caution must be applied during the whole docking sequence, since unintentional collisions and contacts can produce uncontrolled rotations of the system, exacerbating the de-tumbling and stabilization process.

Re-orbit to Lower Altitude and Disposal of the Debris: Regarding SCMT architecture, once the chaser docks with the debris, it re-orbits the target to a lower altitude, allowing for a shorter orbit residual lifetime. Figure 3.8 contains the 1st and 2nd level functions selected for this mission phase.

This phase begins with the correction of the attitude before the re-orbit maneuver, orienting the system (debris and spacecraft) towards the right direction for the orbit change. First, as explained in previous paragraphs, attitude and angular rates shall be detected and measured. Then, the sensed variables shall be compared with the desired ones in order to determine the maneuvers to apply to the spacecraft, correcting its orientation. After attitude determination and correction, the orbit shall be modified too, allowing for a decrease in the altitude of the system. The current state vector shall be measured and determined, proceeding with a comparison with the desired final state vector: from their difference, the maneuvers to perform are computed and executed, resulting in the re-orbit of the entire system to a lower orbit.

After the change of orbit, the satellite shall release the debris, preparing for the next approach phase. The release process consists of the same 2nd level functions of the docking sequence, but in inverse order. The first step is the check of the mechanical link, to assure no damage occurring during release. The mechanical link is then disconnected, weakening the hold to the debris, and retracted to allow the separation from the target.

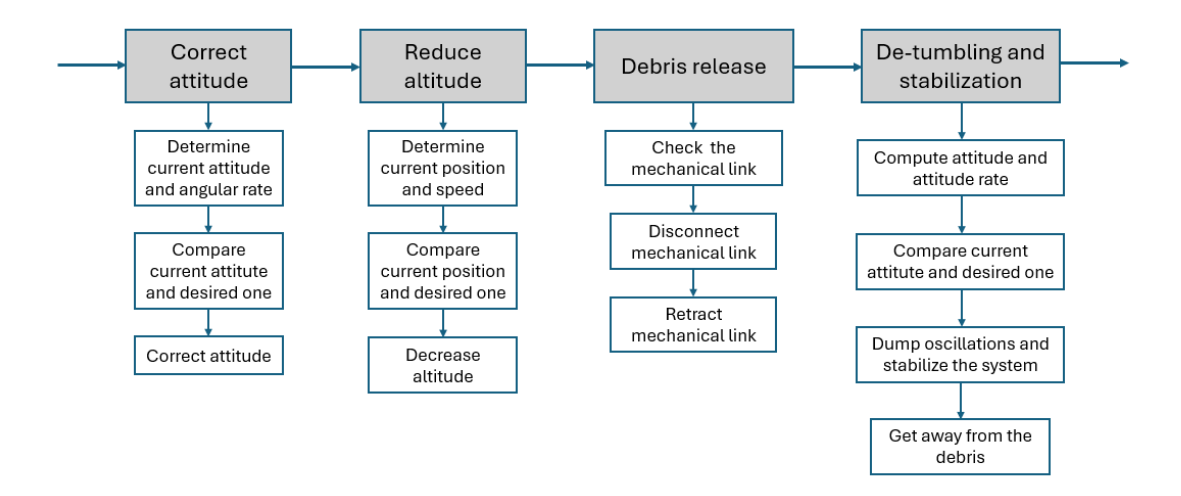


Figure 3.8: 1st (Grey Boxes) and 2nd (White Boxes) Level Functions regarding Re-orbit to Lower Altitude and Disposal of the Debris for SCMT Architecture

Since the system's mass and moment of inertia change during the target's release, transitioning from those of the combined spacecraft and debris to those of the spacecraft alone, undesired attitude rate and tumbling can affect the satellite. To correct the satellite's orientation, de-tumbling and stabilization shall be performed again, following the same steps discussed before: starting from computing attitude and attitude rate, the current orientation is compared to the desired one, evaluating the maneuvers to apply to dump the oscillations and stabilize the system. Lastly, the satellite is finally able to get away safely from the debris without any risk of accidental collisions, allowing a safety distance before the next targeting phase.

Kit and Debris Release: Regarding SCMK architecture, once the chaser docks with the debris, a deorbit kit is applied on the target's surface, allowing for the removal of the object. Figure 3.9 contains the 1st and 2nd level functions selected for this mission phase. The first step consists in sticking the kit on the debris' surface, assuring a strong hold to avoid unexpected detachments during operations. The health status of the kit shall first be monitored and checked before its delivery to the target, avoiding further deployment problems. The kit shall then be extracted from the satellite, and must be applied on the debris. Lastly, the mechanical link between the kit and the target shall be checked as well, to prevent the aforementioned detachment problems during its operative lifetime. The following three 1st level functions regarding attitude correction, debris release, detumbling and stabilization have already been discussed in the previous paragraphs. Finally, after the release of the debris, the deorbit kit can start removing the target from its orbit: a command shall be transmitted to deploy the kit, starting the object's removal. As explored in Section 2.4, the general working principle of a deorbit kit consists in reducing the debris' orbital speed, allowing for a decrease in its altitude. In the long run, this process leads to the atmospheric re-entry of the target, making its disposal possible.

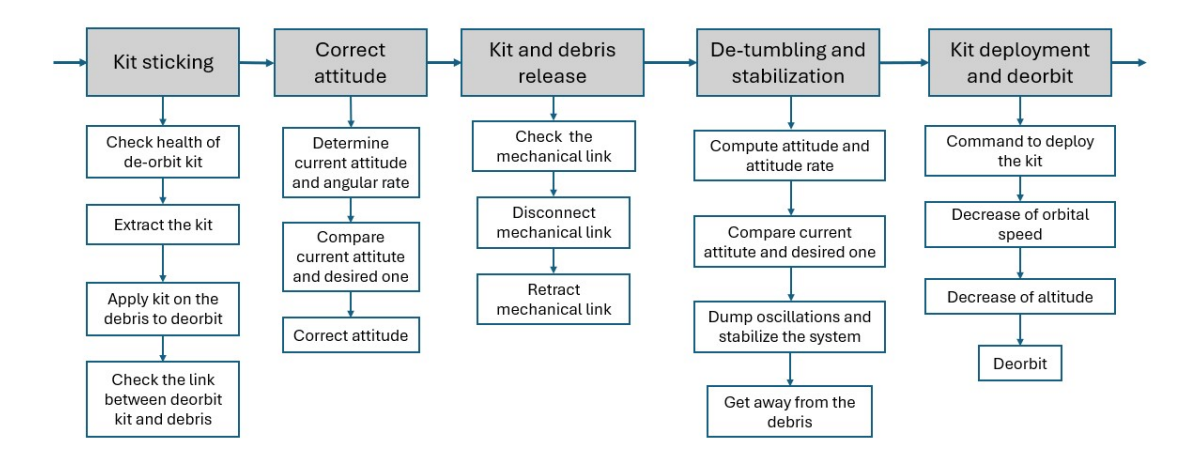


Figure 3.9: 1^{st} (Grey Boxes) and 2^{nd} (White Boxes) Level Functions regarding Kit and Debris Release for SCMK Architecture

Disposal: When the ADR satellite reaches its end of life phase, different disposal maneuvers can be applied, including atmospheric re-entry or re-orbit into a graveyard orbit. Passivation shall be applied as well, depleting the energy accumulated in the satellite. These phases shall be compliant with the mitigation guidelines described in Section 2.5 and the requirements defined in Section 3.3. Figure 3.10 contains the 1st and 2nd level functions selected for this mission phase.

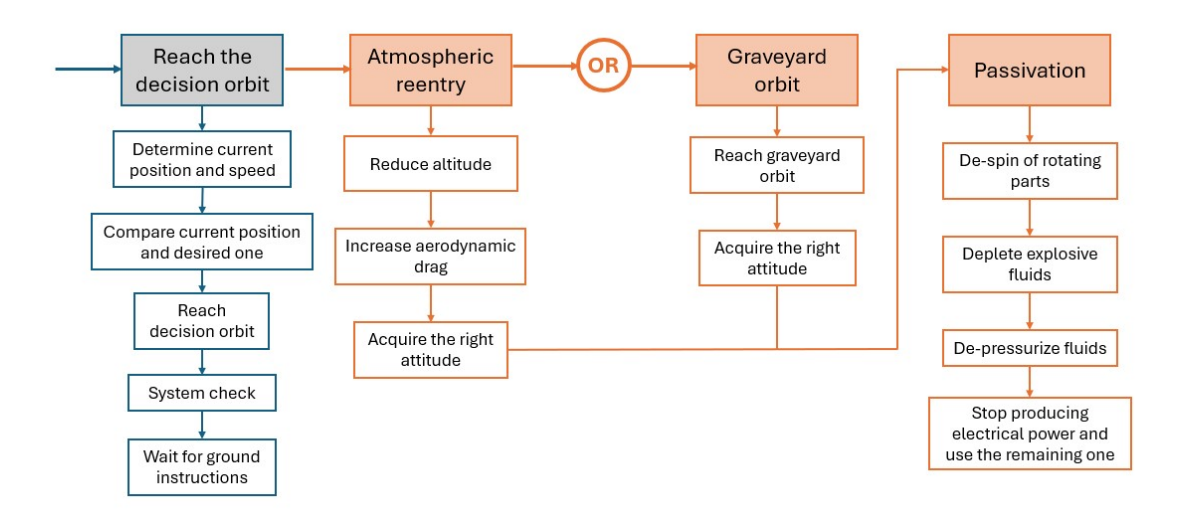


Figure 3.10: 1^{st} (Grey and Orange Boxes) and 2^{nd} (White Boxes) Level Functions regarding Disposal

The functions described in this paragraph are common to all three architectures considered in this analysis, and may be extended to any ordinary LEO mission approaching its

end of life phase.

Once the satellite docks with the last debris (for SCST or SCMT architectures) or releases the last kit (for SCMK architecture), a decision orbit to start the disposal maneuver may be reached: there, the satellite can wait until a disposal method is selected. To reach that orbit, the current state vector of the spacecraft shall be determined, comparing it to the desired one, computing and performing the necessary maneuvers. Before the disposal takes place, however, a system check may be necessary to verify the feasibility of the next operations and prevent the risk of an unsuccessful disposal sequence; a command from the Ground Segment shall then be sent to allow proceeding with the next phases.

If an atmospheric re-entry has been selected, the satellite starts reducing its altitude in time by lowering its orbital speed; the decrease in altitude results in an increase in the aerodynamic drag that lowers the orbital speed even further, producing a chain effect. It might also be possible to artificially increase the aerodynamic drag of the satellite [42]. The choice between controlled and uncontrolled re-entry is made depending on the onground casualty risk [62], which has already been discussed in Section 2.5. If the disposal into a graveyard orbit has been selected instead, the satellite shall change its state vector to reach the desired final position, as previously discussed. In both cases, the right attitude for the selected maneuver shall be acquired, following the aforementioned steps, allowing for a correct orientation during re-entry, or avoiding undesired perturbations in the graveyard orbit.

Before disposing of the spacecraft, passivation shall be performed whenever the selected disposal method allows for it [63, 64]: following the steps described in Section 2.5, rotating parts must be de-spun, potentially explosive fluids must be depleted and high-pressure fluids must be depressurized. Finally, electrical power sources shall be switched off, and the remaining electrical energy shall be depleted.

Appendix B contains the full sequence of the 1st level functions for all three selected architectures, showing the order of the main phases of the missions.

3.5 N2 Diagrams

Once all the subsystems and their components have been defined (following the methodology described in Chapter 4), the main concern is how do they communicate and exchange informations. To help figure out where data, energy and material flows are directed, as well as which components are in contact with each other, N2 diagrams are developed; these graphs show different entries, one for each subsystem or item, and when two lines meet, a symbol is added to represent the kind of interface occurring between the two components. N2 diagrams are useful to understand the mutual interaction between the subsystems of a satellite, while in more advanced mission design phases they may be fundamental to detect problems regarding interface compatibility [12].

Figure 3.11 contains the N2 diagram developed for the entire satellite, using all the subsystems as entries and showing their interactions. The figure also shows the deorbit subsystem, which has been analysed in Section 5.2.2 as a potential alternative to the burn to disposal, by equipping the satellite with an own electrodynamic tether.

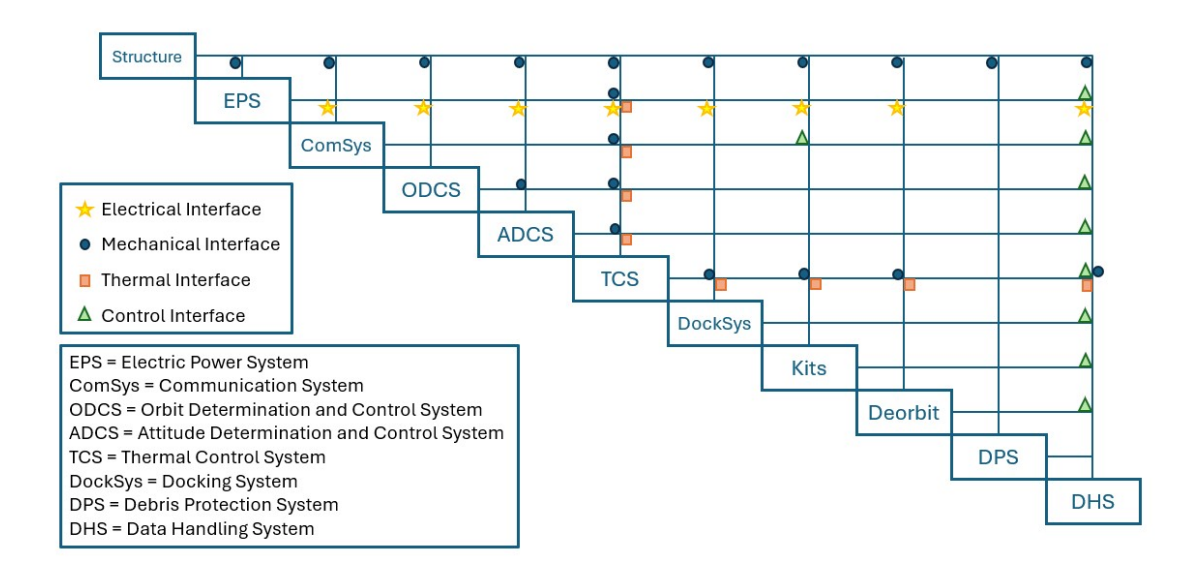


Figure 3.11: N2 Diagram of the Overall System

From the picture, it becomes evident that all the subsystems are mechanically connected to the structure, which is acting as a support frame for the other components; also, the Thermal Control System (TCS) results connected both thermally and mechanically to all the subsystems needing a thermal control device, such as cold plates, heaters or MLIs. Another subsystem heavily integrated with the others is the EPS, which is the responsible of delivering electric power to all the components requiring it to work; lastly, the Data Handling System (DHS) exchanges data and information with all the active subsystems, allowing for commands to be delivered and sensors to operate correctly. Some extra connections are worth of attention: the mechanical interface between Orbit Determination and Control System (ODCS) and Attitude Determination and Control System (ADCS) is justified by the use of the same tank for the propellant of both attitude and orbit control thrusters, while deorbit kits (in SCMK architecture) and Telecommunication System (ComSys) are connected since the electrodynamic tethers' deployment can be directly commanded by the telecommunication system of the satellite.

More detailed N2 diagrams for all the components of the subsystems are contained in Appendix C, showing the interactions between each item.

3.6 Critical Functions

Once the whole functional analysis has been developed, as well as the interactions among the subsystems, it is possible to point out which are the exclusive functions of an ADR mission, and which ones are critical for its success, representing potential failure points that could cause a catastrophic end of the operations.

To remove debris of noticeable dimensions through active methods, it is mandatory to dock with them, both to deorbit them or to deliver a deorbit kit. This phase of the

mission, and the related functions the ADR satellite shall exploit, become of critical importance for two reasons: first, the maneuvers and the approach shall occur safely, since every unintended impact (also at low speeds) can result in the release of debris and the fragmentation of the object or the satellite itself (which is against the statement of Requirement 5, Table 3.2), and second, a failure of the docking system (and its potential rupture) would inevitably compromise the success of the whole mission, meaning the spacecraft would not be able to dock with any other object (this time, Requirements 1, 2 and 3 from Table 3.2 would be violated). For these reasons, rendezvous, docking and proximity operations have already been recognized as critical functions for ADR missions [65, 66], underlining the importance of redundancies, backup and safety measures during this phase. These functions, however, are not exclusive of debris removal missions, since also on-orbit servicing and manned spacecraft usually perform docking sequences and proximity maneuvers: the difference lies in the fact that the body to dock with might be uncooperative, exponentially increasing the risks and the difficulty of the sequence (although some requirements regarding uncooperative debris can be defined as well, as discussed in Section 2.5.2).

After the docking sequence and the eventual deliver of the deorbit kit (for SCMK architecture only), the satellite shall perform a de-tumbling and stabilization maneuver of the entire system (debris and satellite) to correct its attitude. This phase of the mission can represent a critical failure point, since the whole safe disposal of the debris and the correct deployment of the kit (if delivered) depend on the control of the attitude and the angular rates the spacecraft provides to the object: Requirement 6 from Table 3.2 would not be respected as the on-ground casualty risk could exceed the 10^{-4} threshold. To guarantee an high control level during de-tumbling and stabilization phases, redundancies in ADCS equipment are fundamental, as well as selecting the right components to ensure maneuvers being applied safely and effectively. In more advanced mission design phases, where precise simulations regarding the disposal of the debris would be performed, these functions would gain an higher importance, allowing for different re-entry windows and safer locations on the Earth's surface, possibly implying different disposal methods being selected (controlled or uncontrolled re-entry). These functions, differently from rendezvous and docking, are almost exclusively part of ADR, since de-tumbling and stabilization necessity arises when an uncooperative target is approached and docked, minding its correct orientation while thinking about a possible disposal technique.

The last critical phase identified is the disposal of the spacecraft at the end of its operative life, and particularly its passivation. Despite this function may be part of every flown space mission, it assumes a fundamental role in ADR for safety reasons, especially regarding the architectures where a debris is deorbited while docked to the spacecraft (SCST and SCMT). If any explosions due to heated pressurized fluids, spinning devices or overcharged electrical components occur, not only the spacecraft would suffer from severe damage and potential fragmentation, but also the debris docked to it would likely be hit by a considerable number of smaller objects, damaging it and creating new debris instead of mitigating the issue (Requirement 5 from Table 3.2 would be violated). Moreover, the disposal of the satellite and the debris would be irreparably compromised, not assessing Requirement 6 from Table 3.2. For these reasons, the passivation of the

spacecraft is a function that is fundamental to perform in a correct and controlled way, allowing for a safe re-entry and avoiding ruptures and explosions during the last phases of the mission.

The functions analysed in this Section have been considered critical since a fail in performing them does not allow the mission to be compliant with the selected requirements, undermining the safety of the operations and the imposed objectives. It is worth noting, however, that every function a satellite shall perform is critical on its own, since the mission would be compromised anyway if a failure in complying one of them would occur; since the goal of this work are possible ADR solutions, only the functions strictly related to the topic have been analysed, despite many others can be defined critical as well.

Chapter 4

Methodology

4.1 Assessment and Verification of Requirements

Space mission requirements need to be verified, in order to assess the compliance of the designed solution with guidelines and mission objectives. In this Section, verification methods for the requirements displayed in Section 3.3 are provided.

Regarding mission-driven requirements, since the missions are designed to be capable of removing the debris chosen in Section 5.1, their assessment is already included in the sizing process of the ADR satellites; also, spacecraft are equipped with a docking system, allowing for proximity operations (see Section 4.2.3).

Regarding mitigation, Safety requirements (Table 3.2, Requirements 5 and 6) are verified by using the ESA-DRAMA software [59]. This program allows for a complete compliance analysis regarding different mitigation aspects, such as the collision risk with space debris, the evaluation of the necessary Δv for collision avoidance maneuvers and the assessment of a safe re-entry through the atmosphere.

ESA-DRAMA is composed of different independent modules, each of which designed to verify and quantify one precise aspect of the mitigation guidelines [59].

- Cross Section of Complex Bodies (CROC): it allows for the creation of a 3D model of the satellite from basic shapes, and computes its cross-section for a given aspect angle and rotation axis (tumbling is also possible).
- Orbital SpaceCraft Active Removal (OSCAR): if the duration of the disposal phase is unknown, this module evaluates the residual orbital lifetime of a satellite, requiring the COE of the initial orbit, the cross-section of the spacecraft evaluated by CROC and its mass. It is also possible to select among different disposal options, such as re-orbit, delayed deorbit and direct deorbit, using different technologies (chemical or electric propulsion, electrodynamic tethers or drag augmentation devices). Moreover, this module shows the evolution in time of the COE of the spacecraft, verifying the avoidance of prescribed target regions.
- Assessment of Risk Event Statistics (ARES): this module is used to evaluate the necessary Δv for collision avoidance maneuvers per year, given a target orbit and the radius of the circular cross section of the spacecraft (assuming it to be spherical).

It allows for the selection of a target debris population to avoid (choosing between a range of masses or diameters), and an accepted collision probability level.

- MASTER (-based) Impact Flux and Damage Assessment Software (MIDAS): given a target orbit and interval of time, this module evaluates the cumulative probability of collision with a selected debris population (choosing between a range of masses or diameters), assessing the risk of catastrophic impacts as well. Furthermore, the user can define a surface equipped with a customable shielding device from a pool of proposed ones: the program then evaluates the risk of penetration for that surface and performs a damage analysis.
- Re-entry Survival and Risk Analysis (SARA): this last module is composed of two separated tools; the first one, Spacecraft Entry Survival Analysis Module (SESAM), models the re-entry of a space system based on simplified aerothermal analysis, while the second one, Spacecraft Entry Risk Analysis Module (SERAM), assesses the risk of surviving components, evaluating the debris footprint and the casualty risk expectation (including different world population evolution models). To run this module, it is necessary to model the satellite with all its internal components using the materials from a built-in database, or adding new ones if required. Moreover, this module can be run in Monte-Carlo mode, allowing for more complete statistical results, including the evaluation of non-burning mass, casualty area and on-ground casualty risk.

Figure 4.1 shows the typical use routine of the ESA-DRAMA software (the sizing process and LCA are presented, respectively, in Sections 4.2 and 4.4).

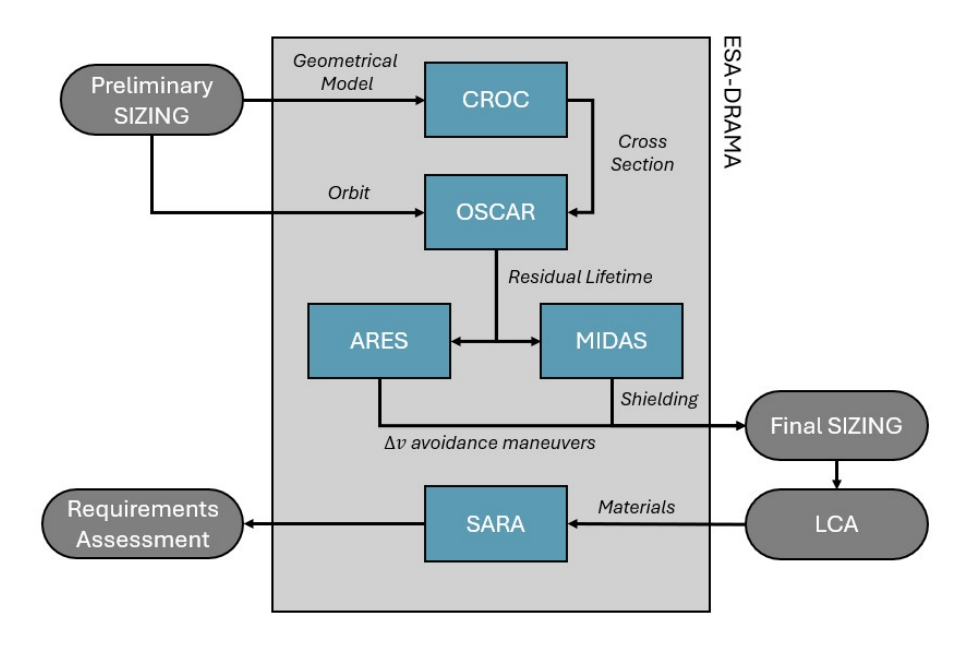


Figure 4.1: Sequence of a Typical ESA-DRAMA Use Routine

While Requirements 1, 2 and 3 from Table 3.2 are assessed during the sizing process, and

Requirement 4 is verified as a sizing result, Requirements 5 and 6 need ESA-DRAMA to be verified. Regarding Requirement 5, the collision avoidance with debris > 1 cm is assessed by evaluating the necessary Δv with ARES (1 cm is the lowest selectable limit for collision avoidance maneuvers) by setting the accepted risk level to 10^{-4} and considering instantaneous maneuvers, while impacts with debris sized between 1 mm and 1 cm are assessed with MIDAS; if the cumulative probability of collision exceeds the prescribed threshold, a shielding technique is implemented, sized on the biggest debris exceeding the allowable risk value. The lower limit for the impact analysis is justified, since collisions with debris sized 1 mm can produce mission-ending damages [6]. Requirement 6 is verified using SARA, defining which re-entry maneuver (controlled or uncontrolled) shall be performed. For both the probability of success of the disposal maneuver and the risk of accidental collisions during proximity operations, the success rates of the selected engines will be used, which are shown in Section 4.2.2.

Lastly, Requirement 7 of Table 3.2 is verified by using the following equation:

$$V_{mag} = -26.74 - 2.5 \log_{10} \left(\frac{2}{3\pi^2} A \rho_b \left[(\pi - \varphi) \cos \varphi + \sin \varphi \right] \right) + 5 \log_{10} h$$
 (4.1)

where V_{mag} is the apparent magnitude of the spacecraft, φ the solar phase angle (whose value is $[0 < \varphi < \pi]$), A the reflective cross-section area, ρ_b the bond albedo coefficient of the spacecraft (whose value is $[0 < \rho_b < 1]$) and h the altitude of the satellite (minimum spacecraft-observer distance) in km [67]. Due to the difficult estimation of ρ_b , a reference value of 0.175 has been considered [68], and since φ varies in time, the worst case scenario has been evaluated, by setting $\varphi = 0$ and maximizing the logarithm's argument. The simplified formula used to verify Requirement 7 is then (reflective satellite, worst case):

$$V_{mag} = -26.74 - 2.5 \log_{10} (0.037 \cdot A) + 5 \log_{10} h. \tag{4.2}$$

4.2 Subsystems Selection and Sizing Process

Once the requirements have been defined (see Section 3.3), and the functions that the spacecraft must perform have been developed (see Section 3.4), it is possible to proceed with the identification of the subsystems needed. This Section concerns the methodology behind the selection of the subsystems, their structure definition and the satellite sizing process. While only higher-level considerations are presented here, more detailed equations regarding the complete sizing are shown in Appendix A.

The necessary subsystems to successfully accomplish an ADR mission can be divided into two categories: *vital subsystems*, which are mandatory for almost every space mission and allow the satellite to exploit its vital functions, and *mission subsystems*, related to the fulfilment of the requirements and the achievement of the mission objectives for the selected ADR architecture.

Before sizing the components, however, the Δv budget of the mission shall be evaluated.

4.2.1 Δv Budget

The three architectures chosen in Section 3.2 perform different orbital maneuvers during their operative lifetime (attitude control maneuvers are considered in Section 4.2.2):

- SCST: it performs the approach maneuver to the selected target, collision avoidance maneuvers to avoid space debris and the disposal maneuver;
- SCMT: it performs the approach maneuver to all the five selected targets, four re-orbit maneuvers to lower the objects' perigees, collision avoidance maneuvers to avoid space debris and the disposal maneuver;
- SCMK: it performs the approach maneuver to all the five selected targets, collision avoidance maneuvers to avoid space debris and the disposal maneuver.

Supposing the satellites to be launched in the same orbit as the first target of the mission (whose feasibility is verified in Section 4.3), and since the required Δv for collision avoidance is evaluated using ESA-DRAMA (see Section 4.1), only the orbit transfers and disposal maneuvers have to be determined. Since a chemical propulsion system has been chosen (as defined in Section 4.2.2), the maneuvers are considered to be instantaneous as a first approximation.

Regarding orbit transfer and debris approach, a method that exploits the J2 perturbation of the Earth to shift the RAAN is chosen [69], which is described in more detail in Appendix A. The order of the debris to remove for multiple-target missions (SCMT and SCMK) has been chosen as the one that guarantees the minimum mass of propellant [48] (and not the minimum overall Δv , since a minimum Δv doesn't necessarily imply a minimum fuel consumption if the order of the maneuvers changes while the satellite is docked to different objects). Since the selected approach prioritizes an optimal maneuver (when J2 perfectly aligns the RAAN of the initial and final orbits), which can require a long waiting time, a limit of three years was selected for the overall mission duration before the disposal: if the ideal maneuver duration exceeds 3/4 of a year (since four transfers are necessary), a new one is selected instead, which guarantees the minimum Δv while lasting less than 3/4 of a year [69] (in order to achieve the lowest propellant consumption). It is worth noting that the duration of these maneuvers refers to the waiting time necessary for J2 to align the orbits, and not to the burning time of the engine. The SCST satellites are sized on the debris requiring the highest propellant mass to be deorbited.

Disposal maneuvers and re-orbits are evaluated as simple changes of eccentricity and semimajor axis at constant inclination, RAAN and anomaly of perigee [37, 70]. Maneuvers requiring a decrease in altitude are modelled as single-burns aiming at lowering the perigee of the initial orbit, allowing for higher aerodynamic drag and shorter residual orbital lifetime [36]. Graveyard orbit disposal maneuvers (whose feasibility is explored in Section 5.2.2) are modelled as double-burns aiming at increasing both the perigee and the apogee of the orbit outside the LEO protected region. More details about the equations describing these maneuvers are contained in Appendix A.

The propellant mass is evaluated by using Tsiolkovsky's rocket equation [37]:

$$\frac{m_i}{m_f} = e^{\frac{\Delta v}{I_{sp}g_0}} \tag{4.3}$$

where m_i and m_f are the masses before and after each maneuver, respectively, I_{sp} the engine's specific impulse and $g_0 = 9.81 \text{ m/s}^2$ the Earth's gravity on the surface. During orbital transfers, the satellite has been hypothesized to exactly reach the debris at the end of the maneuver; this is a simplified method that excludes eventual Lambert orbital corrections during the approach phase [48], requiring a precise evaluation of both position and true anomaly of spacecraft and debris, not available at this mission design stage. However, to consider these maneuvers during the sizing process, an extra propellant margin has been considered, allowing for more Δv if necessary (see Section 4.2.2).

4.2.2 Vital Subsystems

Telecommunication System

The ComSys is one of the most important subsystems for a satellite, allowing data and information exchange with other spacecraft or with the Ground Segment. The need for a communication subsystem becomes evident from the diagrams presented in Section 3.4, showing that a link shall be established for both telemetry and mission-related data. Since telemetry and command data are exchanged from the very beginning of the mission, when the attitude of the satellite has not been determined and controlled yet, a low-gain omnidirectional antenna becomes necessary in order to be able to transmit data in any direction; the selected one is a dipole antenna (2 dBi gain and 156° beamwidth) [71]. The following frequencies have been allocated for telemetry and command: 145 MHz for the downlink (50 MHz bandwidth) and 441 MHz for the uplink (10 MHz bandwidth) [72], extrapolated by knowing that the length of the dipole arms shall be equal to $\frac{\lambda}{4}$, where λ is the wavelength [73]. Omnidirectional antennas shall be already deployed, or shall be able to automatically do it after the separation from the launcher, like the selected one does [72].

To establish a stronger link, capable of transmitting mission-related data (for instance, visual communication during the docking phase), an high-gain antenna has been implemented. To determine its dimensions and gain, losses shall be estimated and the link budget must be evaluated by knowing the data rate of the communication. Since a visual communication link has been selected for the docking phase, this represents the highest data rate during the operations (telemetry only occupies 40-10,000 bit/s and commands 2-8 kbit/s), which has been evaluated as follows [74]:

$$data\ volume = bands \times \frac{bit}{pixel} \times resolution \longrightarrow data\ rate = data\ volume \times frame\ rate$$

$$(4.4)$$

Data for these equations has been gathered from [75]. Once the data rate has been determined, the compliance with the Shannon-Hartley theorem must be verified, determining an higher limit to the maximum possible data rate using a selected bandwidth B: supposing a FSK uncoded technology, and an allowable Bit Error Rate of 10^{-6} , the required $\frac{E_b}{N_0}$ is 13.5 dB [76]. The maximum allowable data rate is then:

$$\begin{cases}
R_{max} = B \log_2 \left(1 + \frac{C}{N} \right) \\
\frac{C}{N} = \frac{E_b}{N_0} + 10 \log_{10} \frac{R}{B}
\end{cases}$$
(4.5)

where $\frac{C}{N}$ is the carrier to noise ratio, E_b is the energy-per-bit, N_0 the background noise and R the data rate from Equation 4.4. If $R_{max} < R$, then the selected camera can

still be used by reducing the frames or the resolution up to the allowed level. To obtain an acceptable carrier to noise ratio, the bandwidth B shall be large enough to permit an high data rate: the frequency allocated for this transmission is 2245 MHz, which is reserved for space-to-Earth applications, and with a possible maximum bandwidth of 90 MHz centred in the carrier frequency [77, 78].

Once the maximum allowable data rate has been determined, the gain of the directional antenna can be evaluated using the link budget formula [71, 79, 80]:

$$\frac{E_b}{N_0} = EIRP + L + \frac{G}{T} + 228.6 - 10\log_{10}R \tag{4.6}$$

where L are the losses of the link [dB], $\frac{G}{T}$ the receiving ground antenna gain-to-noise ratio (17.50 dB/K is considered, which is typical for 11 m diameter antennas communicating at 2 GHz in S-band [81]), R the maximum allowable data rate and EIRP the Effective Isotropic Radiated Power in dBW. Also, $EIRP = P_t + G_t + L_t$, where P_t is the power of the transmitting antenna [dBW], G_t its gain [dBi] and L_t the related losses [dB].

The diameter of the parabolic reflector is calculated from [73]; regarding the feed, a conical horn antenna is selected, sized from [73], whose power supply is 5 W (allowing for reasonable dimensions of the reflector). A new lightweight and inflatable technology is chosen for the parabolic reflector [82], while the feed's structure is considered to be made of copper [83]. The feed supports are three glass fiber sticks, sized from [84] by knowing their length-to-width ratio, adapting it to the current case. To rotate the directive antenna, gimbals are used [85].

Other necessary components for the ComSys are a modem, filters, a transponder, a diplexer and coaxial cables [71]. The selected modem covers part of the bandwidth allocated for the communications, it ensures the desired FSK uncoded transmission and allows up to 25 Mbps data rate; its mass, volume and required power are taken from [86]. Filters are essential to delete the background noise; since they are usually small circuits, their mass and volume have been neglected, while the required power has been evaluated from [87]. The chosen transponder allows for the same coding method and operative frequencies of the modem, and its mass, volume and required power are contained in [88]. A diplexer is a fundamental component of the ComSys, allowing the same antenna to both transmit and receive signals: data for the selected diplexer has been gathered from [89]. Lastly, coaxial cables have been selected based on [90], assuming three 1-meter-long wires (one for each antenna, including redundancies). The mass is estimated by using the length-to-weight ratio provided by [90].

For safety reasons, redundancies are fundamental in the ComSys [91]; as a consequence, modem, transponder, diplexer and omnidirectional antenna have been doubled. More details regarding the sizing process are contained in Appendix A.

Attitude Determination and Control System

In this work, the Attitude Determination and Control System (ADCS) and the Orbit Determination and Control System (ODCS) are considered separately, since they are related to different 1st level functions (see Section 3.4), and due to the distinct methods implemented to compute the maneuvers in each case.

The components considered for the ADCS [61, 92] are star trackers, thrusters, pipelines and Control Moment Gyroscope (CMG) array. The choice of CMGs is motivated by their high authority and agility in attitude corrections [61], while thrusters have been selected for proximity maneuvers, where speed and precision are crucial; also, they can be useful for CMGs desaturation. Star trackers have been chosen since they guarantee the highest precision among the attitude determination sensors [92], which is fundamental during docking and rendezvous operations. No Inertial Measurement Unit has been considered, due to the lack of data.

The selected star tracker is taken from [93], where also its mass, volume and power are reported; normally, three of them are used simultaneously to determine the satellite's attitude, and some redundancies shall be included [91]: a final number of eight has been considered due to the criticality of the attitude determination for rendezvous and docking operations, and to fit inside the weight-window usually allocated for this component in flown spacecraft (about 2-5 kg [91]).

Regarding thrusters, four arrays of four engines each are implemented, following the example developed by [41]. Many catalogues have been checked for the thrusters' selection [94, 95, 96], and MONARCH-90HT was chosen for the final sizing [95], since it represents a good compromise between mass and generated thrust; it also burns hydrazine, which is the same fuel used by the orbit control engine (see Section 4.2.2), allowing for the same tank to store it. For the power budget evaluation, only eight engines have been considered to work simultaneously (three axes rotation at the same time).

Pipelines have been sized considering no friction losses as a first approximation, including the feeding lines of the ODCS as well. Pipes are chosen to withstand an internal pressure which is the maximum feed pressure among the attitude and orbit control engines' one: the tubes are made of stainless steel series 10S [97], whose diameter and thickness are taken from [98]. Eight 1-meter-long pipes have been considered (one for each attitude thrusters' array, two for the orbit control engine and two connecting the gas vessel with the propellant's tanks). Stainless steel is selected due to its compatibility with both hydrazine [99] and nitrogen tetroxide [100].

The selected CMGs are CMG8 [101]. An array of four CMGs is implemented, while only three of them are included in the power budget (the fourth one is redundant). The time required by the reaction wheels to rotate the spacecraft has been evaluated as reported in Appendix A, verifying the output torque to be strong enough to maneuver the satellite in an acceptable time slot.

Some sources reporting the propellant consumed by the ADCS have been consulted [102, 103]; however, the missions they are referred to did not perform any rendezvous and docking operation, making them not suitable for a comparison. To approximate the required hydrazine for attitude control, some maneuvers have been modelled as explained in Appendix A.

Orbit Determination and Control System

A functioning ODCS is mandatory for the success of the mission. Since a precise orbit determination is fundamental, ground tracking systems or Global Positioning System

(GPS) can be used to detect both position and velocity of the spacecraft [41, 61, 92]. The ODCS is composed of thrusters, propellant tanks, inert gas vessel and valves (pipelines have already been modelled in the ADCS). The overall selected architecture for combined ADCS and ODCS is shown in Figure 4.2.

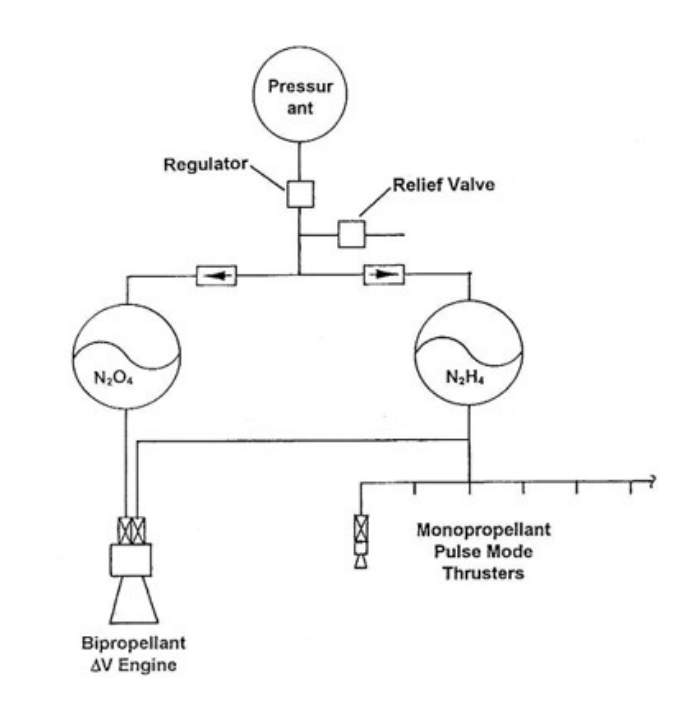


Figure 4.2: ADCS and ODCS Architecture [104]

Regarding the thruster selection, many catalogues have been consulted [94, 95, 96, 105, 106]. The selected engine is R-42DM by [106, 107], due to its low mass, high specific impulse and high thrust; the choice is also driven by the used propellant: it burns hydrazine and nitrogen tetroxide MON-3 (nominal mixture ratio of 1 [107]), allowing for the fuel to be consumed by ADCS thrusters as well, without the necessity of adding an extra tank. Only one engine has been considered for each analysed architecture; however, further studies could assess the possibility of adding more than one thruster to lower the time required by the maneuvers (see Section 6.2).

Tanks are considered to be spherical, made of Ti6Al4V [108, 109] due to their extended dimensions and high internal pressure. A method to size the tanks' thickness is presented in Appendix A.

The feed of the engine is regulated by a blowdown system requiring a pressurant gas: helium has been considered for this application [104]. The amount of gas required to pressurize the tanks is evaluated by considering an adiabatic emptying, meaning a fast propellant consumption: this assumption is justified by the evaluation of the required Δv considering instantaneous maneuvers rather than continuative burns (which are typical of electric propulsion instead); however, if long-lasting maneuvers are executed, an isothermal emptying of the vessel would be more correct, allowing for a smaller amount

of pressurant gas [104]. A simplified and conservative approach is taken, which considers the engines to deplete all the fluids at once, without the time to reach a thermodynamic equilibrium in the tanks after each maneuver (as a result, the amount of helium is slightly oversized). Some architectures require a large amount of propellant and, as a consequence, the gas vessel can reach considerable dimensions and weight: since the blowdown feeding method is the most reliable and the only one used in LEO applications, it has been implemented anyway during the sizing process; however, further studies could assess the possibility of other new feeding strategies (see Section 6.2). Regarding the evaluation of the fuel and oxidizer's mass, a 10% propellant margin has been added to cover extra Δv needs (same margin applied to ADCS' hydrazine) [91].

Valves have been modelled from [110], whose mass is given as a percentage of the ADCS and ODCS' dry mass. No data regarding off-the-shelf gimbals for chemical apogee engines has been found, so it has been considered to be part of the structural mass (see Section 4.2.2).

Data Handling System

Concerning the DHS, two main components have been sized: the On-Board Computer (OBC), which is necessary to elaborate the information, and the data bus to transmit it. Different models of light OBCs were compared [111, 112], both suitable for the data rate of the mission. The model from [111] has been selected due to its lower mass, and a redundancy of four is applied.

Regarding data buses, they have been modelled as a fraction of the overall DHS mass (30%, like the wiring mass percentage in the Electric Power System [113]), and their volume is sized consequently.

Thermal Control System

The TCS is of crucial importance for space missions, guaranteeing that each component remains in its operative temperature range. Different technologies are implemented, both passive (coatings, Multi-Layer Insulators (MLIs)) and active (pumps, heaters, radiators, etc.) [41].

MLIs are applied on the external surface of both tanks and gas vessel due to their low operative temperature range [108] (high temperatures can increase the pressure of the fluids, leading to potential explosions), avoiding excessive temperature changes during the operative lifetime of the satellite [114]. The selected MLI is taken from [115], allowing for a wider operative temperature range (-270°C to +150°C); the mass is evaluated from the surface density (140 g/m² [115]), and a volume of 0.01 m³/m² has been selected [114]. Coatings are used to cover the external surface of the satellite, and different kind of paints are usually applied, varying the reflectivity and absorptivity of the spacecraft [114]. The chosen technology is the ZinvisibleTM formula [116], composed by 56.4% of ZnO ($\rho = 5600 \text{ kg/m}^3$) and 43.6% of Kasil 2130 ($\rho = 1270 \text{ kg/m}^3$ [117]), whose thickness is 0.12446 mm [116].

Before sizing the active components of the TCS, the required heat to subtract or produce to keep each component within its operative temperature range shall be estimated. A conservative approach is adopted. First, reference values for the maximum and minimum temperatures of LEO satellites have been gathered from [118] (+77°C and -22°C): these temperatures are considered to be reached by all the components of the satellite when the spacecraft starts and finishes, respectively, its eclipse time in the shadow cone of the Earth. The maximum and minimum allowable temperatures of each component are then compared to these values and, if they exceed them, heat is either subtracted or added to the item. Lastly, the energy dissipated by each electrical component is defined by supposing an efficiency: this value is then added to the heat to subtract during the Sunexposure phase, and is subtracted to the heat to apply during eclipse time (the dissipated heat is used to warm up other components if necessary). More details regarding energy evaluation are contained in Appendix A.

Heaters are sized assuming an efficiency $\eta = 1$ (all the input power is converted into heat), and their mass is [114]:

$$m_{heaters} = 0.7 \times P_{warm} \text{ [kg]}$$
 (4.7)

where P_{warm} is the amount of power to add, in [kW]. Since redundancies are necessary for heaters [91], their mass has been multiplied by two.

To actively subtract heat from the subsystems, cold plates are used [114]:

$$P_{cool} < 5 \text{ kW}: \begin{cases} m_{plates} = 12 \times P_{cool} \text{ [kg]} \\ V_{plates} = 0.028 \times P_{cool} \text{ [m}^3 \text{]} \end{cases}$$

$$P_{cool} > 5 \text{ kW} : \begin{cases} m_{plates} = 17 + 0.25 \times P_{cool} \text{ [kg]} \\ V_{plates} = 0.016 + 0.0012 \times P_{cool} \text{ [m}^3] \end{cases}$$
 (4.8)

where P_{cool} is the amount of power to subtract, in [kW].

In active TCS, a pump is mandatory to move the coolant fluid inside the pipelines [114]:

$$\begin{cases}
m_{pump} = 4.8 \times P_{cool} \text{ [kg]} \\
P_{pump} = 23 \times P_{cool} \text{ [W]} \\
V_{pump} = 0.017 \times P_{cool} \text{ [m}^3]
\end{cases}$$
(4.9)

where P_{cool} is expressed in [kW]. Equation 4.9 refers to a pump and accumulator architecture, which is preferred to the heat pumps proposed by [114] due to its lower mass; these systems are common in single-phase active cooling, such as the selected one [119]. Due to its criticality, the pump has been redunded by a factor of two.

The active cooling system exploits water as coolant fluid [119], due to its high specific heat and the selection of a single-phase cooling system (the maximum considered LEO temperature is lower than water boiling temperature). Other possibilities have been explored, including a multi-phase active cooling exploiting ammonia or other fluids with different boiling temperatures [119, 120]; however, due to the lack of data regarding the sizing process for boilers, evaporators and sublimators, this option has been discarded. The mass of the coolant fluid has been considered to be 5% of the active TCS mass [114]. A radiator is mandatory to dissipate to the exterior of the spacecraft the heat affecting

the subsystems. Equation 4.10 shows the sizing approach applied (considering a fixed radiator instead of a deployable one, due to its lower mass):

$$\begin{cases}
m_{radiator} = 5.3 \times A_{radiator} & \text{[kg]} \\
V_{radiator} = 0.02 \times A_{radiator} & \text{[m}^3]
\end{cases}$$
(4.10)

where $A_{radiator}$ is the surface of the radiator [m²], whose sizing process is contained in Appendix A. The radiator is covered by louvers, allowing for a better control of the radiation emission; their mass and volume have been calculated as follows [114]:

$$\begin{cases}
m_{louvers} = 8 \times A_{radiator} \text{ [kg]} \\
V_{louvers} = 0.064 \times A_{radiator} \text{ [m}^3]
\end{cases}$$
(4.11)

where $A_{radiator}$ is the radiator's surface [m²].

To transfer the coolant fluid from the cold plates to the pump and the radiator, pipelines are implemented: usually, their mass is set to be 15% of the active TCS' one. However, new techniques under development aim at guaranteeing a better integration of the TCS pipelines in the structure of the satellites [121, 122]: for this reason, these components have been considered to be part of the mass margin allocated for the structure (see Section 4.2.2).

Lastly, sensors are necessary to detect the temperature of critical components and are assumed to be 5% of the active TCS mass [114].

Electrical Power System

The EPS produces and distributes the electrical power to all the subsystems that require it to perform their functions, making it the heart of the satellite. The components of the EPS are taken from [113].

Batteries are of crucial importance, as they allow for energy storage. Lithium-ion-manganese batteries have been selected, since they offer better performances with respect to other ones (for further information, see Section 5.2.2). The following specifics have been considered: a tension of 3.8 V [113], a charge time of one hour [113], a gravimetric density of 135 Wh/kg [113] and a volumetric density of 400 Wh/L [123]. Once the energy stored inside of the batteries has been identified (which is the necessary energy to feed all the subsystems during the eclipse phase of the orbit), their dimensions are determined. Since the performance of the battery decreases in time, and its depth-of-discharge lowers after multiple cycles, a redundancy of two is considered to avoid lack of energy issues. Moreover, batteries shall be already charged at launch, allowing the first telecommunications and maneuvers before the deployment of the solar arrays.

Since the planned missions would be operative in LEO, the Sun can be used as a source of energy; as a consequence, solar panels are necessary to collect the solar radiation, converting it into electrical power. A gallium-arsenide GaAs technology is chosen, allowing a 32% efficiency during energy conversion [113]. The surface A_{panel} of the solar panels can be determined by using Equation 4.12:

$$P_{output} = P_{Sun}\eta_{panel}A_{panel}\cos\theta \tag{4.12}$$

where $P_{Sun} = 1367 \text{ W/m}^2$ is the solar constant, η_{panel} is the efficiency, θ is the angle between the vertical to the panel and the Sun direction (since the panels can tilt, $\theta = 0^{\circ}$ is used), and P_{output} is the output power required. P_{output} is given by:

$$\begin{cases}
P_{output} = P_{sat} + \frac{P_{charge\ battery}}{\eta_{battery}} \\
P_{charge\ battery} = \frac{P_{sat\ bettiepse}}{t_{charge\ battery}}.
\end{cases}$$
(4.13)

Two different powers are involved in Equation 4.13, since solar panels need to both feed the subsystems and recharge the batteries while exposed to the Sun. P_{sat} is the power required by the satellite's subsystems, while $\eta_{battery} = 0.95$ represents the efficiency during the charge of the batteries (the efficiency during the subsystems' feeding is already considered in P_{sat} , due to the losses of the wiring). It becomes necessary to verify that $t_{light\ time} < t_{charge\ battery}$, allowing for the battery to be fully recharged during the solar exposure phase of the orbit. A simple method to evaluate $t_{eclipse}$ and $t_{light\ time}$ is contained in Appendix A. Like the batteries, solar panels suffer from degradation after a long exposure to the extreme space environment, decreasing their performance: to cope with this problem, the total surface of the arrays has been doubled, and their disposition is shown in Figure A.1; a thickness of 0.372 mm and a density of 5.32 g/cm³ are considered [124]. The described procedure represents an approximation of a real case scenario, since it does not consider some other variables such as the β angle between the orbital plane and the Sun direction, which varies throughout the year; further studies shall consider it during the EPS sizing (see Section 6.2).

To manage to rotate the solar arrays, both to protect them from overheating and to increase the θ angle [125], gimbals are necessary: the model from [126] has been implemented. As for CMGs and attitude control thrusters, the capability of the gimbals to rotate the panels in a short time has been tested, considering their inertia to be the same of a parallelepiped ($I = \frac{1}{12}m(l^2 + s^2)$), where m is the mass, l the length and s the thickness) and supposing a full 180° rotation about their axis. Once the angular acceleration and deceleration have been defined ($\alpha = M_t/I$, where M_t is the output torque of the gimbal), the time required for the rotation can be evaluated (see Equation A.21).

Since the passivation of the spacecraft has been identified as a crucial requirement for the missions (as presented in Section 3.3), switches to cut-off the subsystems from the feeding lines have been added, sized from [127]: eight switches are considered in the final architectures.

Lastly, distribution and regulation of the electrical power shall be implemented, guaranteeing an effective connection of the subsystems and increasing the safety by avoiding malfunctions. Wiring is assumed to be 30% of the total EPS mass and volume [113], while a Peak Power Tracking regulation technique is adopted (overall power > 100 W), consuming up to 7% of the EPS generated power [113].

Structure

Even though the structure is not strictly considered a subsystem, it is included in the sizing process as well since part of every satellite, providing support to the other components and being a frame to which they are attached. An average dry mass fraction

of 29.97% is considered for the structure [128]. The frame is considered to be made of 53.8% carbon resin material and 46.2% aluminium [10].

The overall volume of the satellite is considered to have a cylindrical shape, allowing for a good storage of the tanks and vessel and a lower surface area compared to other shapes (like cubes, see Section 5.2.2), decreasing the risk of debris impacts and allowing for a lighter Debris Protection System (DPS). The cylinder has a radius which is the biggest out of the aforementioned tanks and a length which is the sum of the diameters of the propellant tanks and gas vessel. The volume of tanks and vessel is then subtracted to the cylinder, obtaining the volume for the remaining subsystems:

$$V_{subsystems} = V_{sat} - V_{tanks} - V_{vessel} \tag{4.14}$$

This value is then compared to an empirical equation [91], aiming at verifying if the subsystems can fit inside the remaining space:

$$V_{subsystems, check} = 0.005 \times m_{subsystems} \text{ [m}^3\text{]}$$
 (4.15)

where $m_{subsystems}$ [kg] is the mass of the subsystems excluding tanks, vessel, propellant, helium, solar arrays (since external) and payload. If $V_{subsystems}$, $check > V_{subsystems}$, their difference is added to the final volume, and the cylinder increases its radius or its length depending on which change leads to a lower increase of the external surface.

Solar panels are considered to be attached in the middle of the external curved surface, symmetrically, by their shorter side (which measures half of the longer one), as represented in Figure A.1.

4.2.3 Mission Subsystems

Docking System

Since this document explores the feasibility of ADR missions, a functioning Docking System (DockSys) is fundamental to detect the debris and connect the spacecraft to the target. The components involved in this subsystem are selected from the functions that the satellite shall exploit during rendezvous and proximity operations, as described in Section 3.4.

First, a device capable of identifying the debris from medium distance (since the long-distance approach can be guided by ground stations tracking) and helping the ground operators to successfully perform the docking sequence is mandatory. Many possible solutions can be used, spacing from LIDARS [92, 129, 130], capable of reconstructing the debris' attitude from the distance, to simpler optical cameras [130, 131] able of guaranteeing a better control during proximity operations, and allowing for less than one degree uncertainty during the debris' attitude estimation process and 1% error while determining its relative position [131]. An optical camera has been selected for this role: data for the sizing process are taken from [75], while its data rate has been considered as the highest one of the overall mission for the ComSys sizing. Since the success of proximity operations rely on this component, one extra camera is considered for redundancy. Moreover, new technologies such as artificial intelligence can be integrated in this subsystem,

helping the reconstruction of the target's attitude in a more precise way [132].

To be physically able to link the spacecraft and the debris, an off-the-shelf telescopic arm has been selected [133], composed by six cylindrical, concentric and retractable sections; this solution offers a low mass and high mechanical properties thanks to its carbon fiber structure. However, since this component shall withstand the mechanical stresses applied on it during the maneuvers, according to the selected requirements (Section 3.3), a basic structural analysis is performed as described in Appendix A.

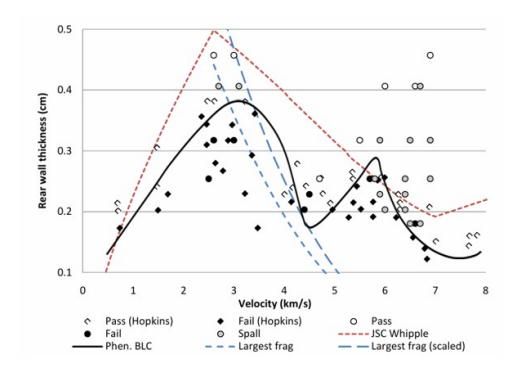
To unfold the robotic arm, an electric motor can be implemented, and the selected model is contained in [134]. Due to the importance of this component for the success of the mission, a redundancy of two is applied. The unfolding time of the robotic arm has been determined as well: starting from the required time and the power of the motor used in [133], the work has been evaluated, and the energy necessary to lift the end mass has been subtracted; then the energy to lift the new end mass has been added, and the result is divided by the power of the selected motor [134], obtaining the new unfolding time with different power and end mass. This value is then checked to fall inside of a feasibility range.

Robotic arms have been used in many missions and were considered during different ADR studies [66]: conventionally, they are equipped with grippers that can link the satellite to the target through already-prepared protrusions on the other spacecraft. However, space debris may not have been intended to be actively removed, and prepared protrusions to conventionally dock with them may not exist on their surface. Moreover, targets can also be uncooperative, risking to damage them if not approached cautiously enough. To cope with these problems, electrostatic pads are selected as a soft-docking mechanism that does not require a prepared surface on the target's body, being suitable for ADR missions [135, 136, 137, 138]. This device needs a high voltage energy source to work, to generate enough tension between its layers; however, since no data regarding the power source was found, it has been excluded from the power budget evaluation. Electrostatic pads can generate up to 300 lb/ft² force [139], and are made of one copper layer and two silicone layers [140], with an overall average thickness of 0.5 mm [141]. For sizing purposes, each layer has been considered to have the same thickness. The surface of the pads is calculated from Equation A.39, by considering $\sigma_{zz} = MOR$ (Module Of Rupture of the arm's material [142]), and solving for the maximum allowable force that can be applied on the arm before its rupture; this way, the pads assure a strong hold for every operative condition of the robotic arm. This technology also offers the advantage of being foldable [135], being easily storable and adhering to curved surfaces as well.

Debris Protection System

Since the planned missions aim at safely removing space debris, the selected requirements (Sections 2.5 and 3.3) show the importance of protection methods against potential impacts. For this purpose, Whipple shields have been implemented whenever necessary [143, 144]. Whipple shields consist of a rear wall and one or several layers of another material disposed all around, leaving a certain space between the satellite's surface and the shielding: when an object collides with the outer layers, it breaks into multiple fragments, or it even melts due to the high temperatures generated [144], and the remains

are blocked by the rear wall, avoiding damages penetrating the satellite's surface [14]. The thickness of the rear wall, given the shield thickness and the spacing, is determined through the so-called ballistic equations as a function of the diameter of the impacting debris and its relative speed [143, 144]: Figure 4.3 shows the thickness of the rear wall as a function of the object's velocity, reporting some experimental results.



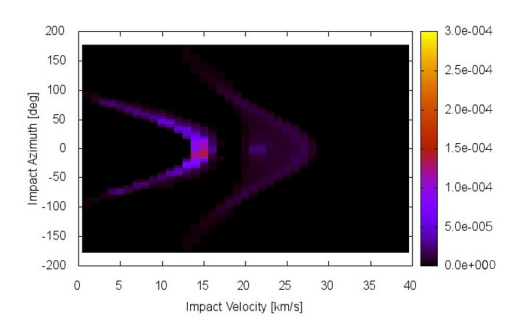


Figure 4.3: Rear Wall Thickness as a Function of the Debris' Relative Speed [144]

Figure 4.4: Impact Speed Distribution Varying the Azimuth Angle (by ESA-MASTER)

Figure 4.3 shows only a small range of possible impact velocities; the speed considered for the sizing has been estimated through the ESA-MASTER software: Figure 4.4 shows that impacts can usually occur at 15 km/s, falling in the hypervelocity impact region (Figure 4.4 only reports the velocity as a function of the Azimuth angle; however, simulations varying the elevation angle show the same impact speed). Regarding the selected debris' diameter, it has been individually evaluated for each mission concept, depending on the results obtained from ESA-DRAMA (see Section 4.1), and considering a spherical aluminium projectile. Two different Whipple shields have been implemented, choosing the lightest one during the sizing process: a single Whipple shield and a double Whipple shield [143]; detailed equations are contained in Appendix A. All the input quantities are taken from [143], using the same materials and measures from the COLUMBUS mission (the spacing between the layers is set to be 22.2 cm [145] instead of 6 cm, to reduce the shield's mass without compromising its resistance). Whenever necessary, the shielded area of the spacecraft has been considered to be the most exposed surface only, meaning the one facing the biggest debris flux in the direction of motion of the satellite. The selected solution uses aluminium for both rear wall and shields, according to some International Space Station (ISS) modules protection systems [145]; however, different materials can be used in different combinations, optimizing both the shield thicknesses and the distances between the layers, varying the volume of the subsystem and its mass.

Deorbit Kits

Lastly, for the SCMK mission profile only, deorbit kits are included in the sizing process and they can be considered the payload of that architecture. The selected kits exploit electrodynamic tethers to decrease the debris' altitude (see Section 2.4); this choice has

been guided by the high altitude of the selected targets (Section 5.1), not allowing for enough aerodynamic force if a drag augmentation system is employed, and its safety due to the absence of pressurized propellants inside the kits (which is necessary if a small propulsion system is applied).

To have a working kit, a long, aluminium [44, 146] tether is needed, allowing electric current to flow through it: a rectangular section, metallic tape is considered, whose width measures 3 cm and with a thickness of 0.05 mm [46]. Since electrons tend to accumulate when collected from the ionosphere, a Field Emitter Cathode is necessary to allow the current to flow without charge accumulation: a carbon nanotube cathode is implemented at one end of the tether [44], due to its simplicity and durability in a vacuum environment; the consumed power is contained in [147], while mass and volume are negligible [148]. The sizing equations for the tether itself, as well as the atmospheric and ionospheric models implemented to estimate the deorbit time of the debris, are contained in Appendix A. Since the tether is contained inside the kit's volume and needs to be deployed, a mechanism allowing for it is required: [149] shows a possible solution, where part of the kit structure is deployed together with the tether, and the initial impulse is given by compressed springs, impressing a force F on the eventual end mass or on the tether's tip; this mechanism is highly reliable, since it does not require any electrical power to work, and no electric components are present, reducing the probability of malfunctions. Four S-3079 stainless steel springs have been selected for this purpose [150].

To command the deployment from the distance, an omnidirectional antenna might be needed. The one selected for the ComSys is considered for this application [72].

If an end-mass is necessary (see Appendix A), it is assumed to be made of stainless steel due to its high density.

Since a power source is required by both the antenna and the electron emitter, solar panels are included in the kit, sized considering the highest power request modelled from Equation 4.13. Since panels are now fixed on the kit's surface, they are no longer capable of rotating, so the angle θ in Equation 4.12 is assumed to have an average value of 45°. The sizing process is the same one already described for the EPS; the eclipse time (Equation A.35) has been evaluated at the orbit's perigee. The produced energy is then stored inside of a battery, which is sized using the same data from EPS (lithium-ion-manganese). No active TCS is included in the kit's architecture; however, the battery is covered by MLIs all around its volume, considering it to be a cube. The MLI is the same one already discussed during the TCS sizing process.

The kit also includes an extra mass margin for structures and mechanisms, which is the same percentage of the satellite's structure (29.97% [128], end-mass excluded). Redundancies are applied to the battery, the solar array and the antenna, doubling these components.

To stick the kit on the debris' surface, electrostatic pads are applied, which cover one side of the kit's structure (considering it to be a cube), using the same data of the DockSys. Also, each kit is placed on the target by a dedicated robotic arm, equipped with an own electric motor, taken from the DockSys sizing process: no redundancies are here considered.

A similar deorbit kit (only considering the tether, the electron emitter and a deployment mechanism) has been analysed as an alternative disposal method for the spacecraft instead of a perigee-reducing burn (see Section 5.2.2).

4.2.4 Sizing Logic

Once all the subsystems and their sizing methods have been defined, they shall be combined together to obtain the final satellite's mass budget. The logic implemented is shown in Figure 4.5.

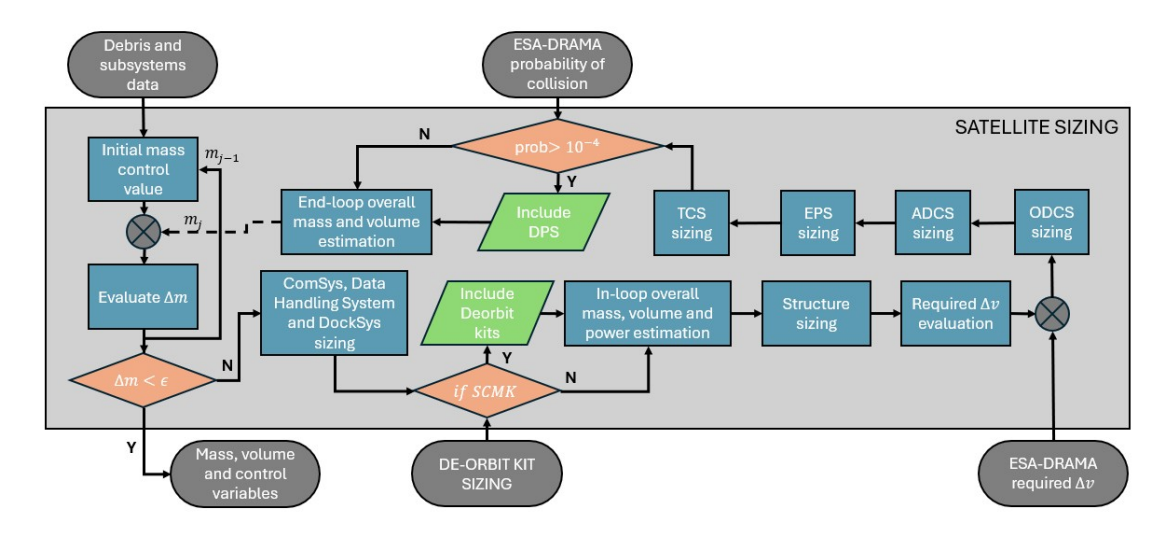


Figure 4.5: Logic Implemented for Satellites' Sizing

An iterative method is used. First, two initial control values for the mass are given, allowing for a high enough Δm to enter the code; then, all the subsystems whose mass is independent from others' masses and powers are sized (ComSys, DockSys and DHS), and a first in-loop mass approximation is done by considering also other fixed-mass components (such as the deorbit kits). After that, the Δv budget is defined, and the propellant mass is computed applying the Tsiolkovsky's equation (minding the mass the maneuver is applied to, considering the satellite docked with the debris whenever necessary and the sequential kits' release during the SCMK mission); the required propellant for debris avoidance maneuvers, whose Δv has been obtained from ESA-DRAMA, is evaluated at wet mass to be more conservative. The remaining ODCS is then sized, followed by ADCS, EPS and TCS. The last thing to evaluate is the necessity of a DPS: if the probability of impact given by ESA-DRAMA is higher than the prescribed value of 10^{-4} , then a shield is implemented, sized on the maximum projectile's diameter exceeding the allowable risk level. The overall mass of the satellite is then subtracted to the previous iteration's value, and if their difference is bigger than a prescribed control variable, ϵ , then the new mass overwrites the old one and the loop repeats, using the previous iteration's values as the new starting point. It is worth noting that ESA-DRAMA requires initial geometry and mass for both collision avoidance Δv and impact risk estimation: a first run of the program is made considering no collision avoidance maneuvers and no DPS; then, the debris risk assessment is performed and another run is made, this time considering the Δv for avoidance maneuvers and shielding.

Regarding the kits' sizing, another program has been implemented, following the logic shown in Figure 4.6.

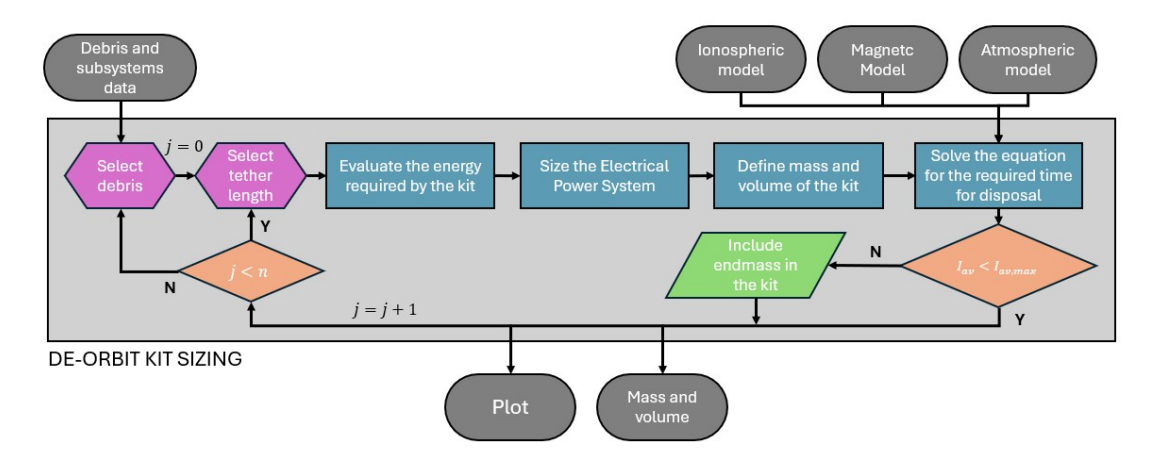


Figure 4.6: Logic Implemented for Deorbit Kits' Sizing

Here, the capability of deorbiting each selected debris has been analysed with different electrodynamic tethers (n is the number of different wire lengths considered). For each kit, the power budget is evaluated and the EPS is sized. Then, the masses of the other components are added and a first in-loop estimation of the mass is obtained. The models used to solve the disposal profile of the debris are then uploaded (see Appendix A), and the current flowing through the wire is evaluated. Lastly, if the current exceeds its maximum allowable value, an end-mass is added, leading to the final mass budget; the results are then printed and the program proceeds to the next evaluation.

4.3 Launcher Selection

Since the launch of a mission cannot be neglected in terms of costs and environmental impact, the selection of the launcher is of crucial importance during both LCA and LCC analyses. Different launchers have been investigated, spacing between various payload capabilities: Falcon 9 - Block 5, Falcon Heavy, Ariane 6 (4 and 2 boosters configurations), Vulcan Centaur (0, 2, 4 and 6 boosters configurations) and Space Launch System (SLS).

- Falcon 9 Block 5: heavy lift launcher, with a payload capability of 22,800 kg in LEO (full-expendable architecture, short fairing) [151, 152, 153] (structure and mass breakdown from [151, 152, 153, 154]).
- Falcon Heavy: super-heavy lift launcher, capable of inserting 63,800 kg payload in LEO (full-expendable architecture, short fairing) [155] (structure and mass breakdown from [155, 156]).

- Ariane 6: heavy lift launcher, able of launching more than 20,000 kg in LEO [157] (4 boosters version) (structure and mass breakdown from [157, 158, 159]).
- Vulcan Centaur heavy lift launcher, with a payload capability of 25,600 kg in LEO [160] (6 boosters version) (structure and mass breakdown from [161, 162, 163, 164, 165]).
- **SLS:** super-heavy launch vehicle, capable of injecting 95,000 kg in LEO [166] (structure and mass breakdown from [166, 167]).

For each mission analysed, the mass of the satellite has been compared to the maximum payload mass launched by the vehicles in the selected orbit (all five orbits for SCST mission architecture, and only the first target's orbit for SCMT and SCMK architectures); since the injectable mass varies with the inclination and the altitude of the final orbit, an online software has been used to estimate it [168], comparing a wide range of different launch vehicles while estimating the injectable mass, given the COE of the final orbit and the launch site. A final circular orbit has been hypothesized, and all vehicles are considered to be launched from Cape Canaveral (except for Ariane 6, whose launch site is located in Kourou, French Guyana). The program has been validated by inserting reference values and comparing the given results with the launcher's guidelines.

Regarding the SCST architecture, since each target is removed by a dedicated satellite, the debris would be replaced by the upper stage of the launcher if it is capable of injecting the spacecraft on the target's orbit. To avoid this problem, external ride-sharing programs are considered, aiming at more payloads to be released by a single launcher, giving a purpose to the debris left behind. This way, the emissions and the costs related to the launch can also be partitioned by the fraction of mass that the satellite occupies, with respect to the maximum possible payload evaluated by [168]. External ride-sharing programs are common in the modern space industry [169, 170], allowing for collaborations with other missions, and this concept can be extended to SCMT and SCMK as well.

Whenever possible, for SCST missions, the possibility of internal ride-shares has been analysed, exploring the feasibility of multiple ADR satellites launched by the same vehicle [171]. For each debris, the maximum injectable payload at its orbit is evaluated [168], and considering the data available for each vehicle analysed, the Δv of the upper stage at maximum payload is calculated (representing the Δv to get to the first target's orbit, which is not considered in the equations in Appendix A). Then, the payload is reduced to the sum of several SCST satellites (2 to 5), and the necessary propellant to perform the Δv transfers among the debris is evaluated (by using the same approach described in Appendix A, assuming a transfer time of 3 hours and applying the Tsiolkovsky's equation); the propellant mass is then subtracted to the initial mass, and if the remaining one is bigger than the structure and the residual payload, the program proceeds with the successive transfers.

After the payload capability and the fitting inside of the fairing, other characteristics of the launch vehicles have been compared: costs, emissions (evaluated through single score values on SimaPro, see Section 4.4.4, considering the launch only), the availability (launches per year), the potential reusability and the success rate (successful launches with respect to their total number); geopolitics and social issues regarding the launch site

have not been considered. Costs have been projected to their present value considering inflation, by using [172]. Among the aforementioned characteristics, availability has been prioritized since ADR missions evaluate their trajectories over free-flying objects, and orbit propagators cannot achieve a high precision in determining the evolution of their COE on the long run: for this reason, once the targets have been selected, the launch windows can be located in the very near future and can last for a short amount of time, requiring a highly available ready-to-fly launcher. Also, simulations reported in Section 2.1 show a potential growth in the debris number in the near future, requiring more launches to assess the mitigation strategies, which indirectly require highly available launch vehicles as well. It is worth noting, however, that the need for a high availability may imply the difficulty of external ride-share programs, since the missions would be injected in very specific orbits decided at the last moment, probably not arousing the interest of other programs.

Table 4.1 shows the values of the selected characteristics for the launch vehicles comparison.

Vehicle	Score [pt] ^a	$/\mathrm{kg}_{PL}$	$f Availability^{ m b}$	Reusable	Success Rate ^b
F9 - B5	63.7	3063.6 [151]	138/yy [151]	YES	99.5% [151]
FH	179	2456.5 [173]	2/yy [155]	YES	100% [155]
A6-4	541	5430.0 [174]	N.A.	NO	N.A.
A6-2	300	7426.4 [174]	~2/yy	NO	50%
VC-0	83.5	18,193.1 ^c	N.A.	NO	N.A.
VC-2	165	$11,579.5^{c}$	~2/yy	NO	100%
VC-4	246	10,130.3 [175]	N.A.	NO	N.A.
VC-6	328	9555.2^{c}	N.A.	NO	N.A.
SLS	1460	46,227.6 [176]	N.A.	NO	100%

Table 4.1: Characteristics of the Selected Launchers

4.4 LCA Implementation

In this document, a comparative LCA is developed, focusing on the different environmental impact produced by the selected mission architectures.

4.4.1 Goal and Scope Definition

The objective of this study is to evaluate the environmental impact and the emissions of the selected ADR mission architectures by performing a comparative LCA analysis,

^a Evaluated by using SimaPro as in Section 4.4.4; it refers to the overall environmental outcome over the different impact categories.

^b Whenever possible, the launches have been considered starting from 01/01/2024, date of 1st Ariane 6 launch, for comparison. Falcon Heavy considers the success rate of all launches instead, due to their low number

^c The considered payload is the mass to ISS; costs have been arranged as a fraction of the VC-4 costs, based on the mass variation (considering the different number of boosters involved).

in order to determine their feasibility under an environmental point of view. The obtained results will then be used to decide which mission concept better suits the imposed requirements and constraints, helping in possible further analyses. The target audience of this work are experts that might be in charge of deciding, in the future, which ADR mission would be convenient to develop, minding its impact and environmental sustainability. The analysis is performed using the SimaPro software, upgraded with the ESA database for space-specific LCAs [10]: the built-in method considers all the nineteen impact categories and shows the results obtained for each one of them (midpoint analysis), being more precise than a generic endpoint analysis, which only gives a global perspective instead. Despite the missions cover the ADR area, no impact category to consider the potential debris release in orbit has been implemented yet, even though some methods to assess it are under development [177, 178]: this represents a limitation of the current LCA analysis for the space sector [10].

The selected functional unit is [10]:

FUNCTIONAL UNIT: "One space mission in fulfilment of its requirements,"

The importance of choosing a good functional unit lies on defining a good scaling technique, allowing for comparable input and output data for the considered architectures. Different mission phases are considered: the production (without transportation), the transportation to the launch site, the launch event and the propellant consumption during the mission. Research and Development (RD) and testing phases are excluded from the analysis. The overall life cycle considered in the LCA is shown in Figure 4.7. The performed analysis is a *Cradle-to-Grave*, although the disposal phase has only been examined from a literature point of view (see Section 5.4.1), since no reliable data regarding its implementation has been found, representing another important space-specific LCA limitation.

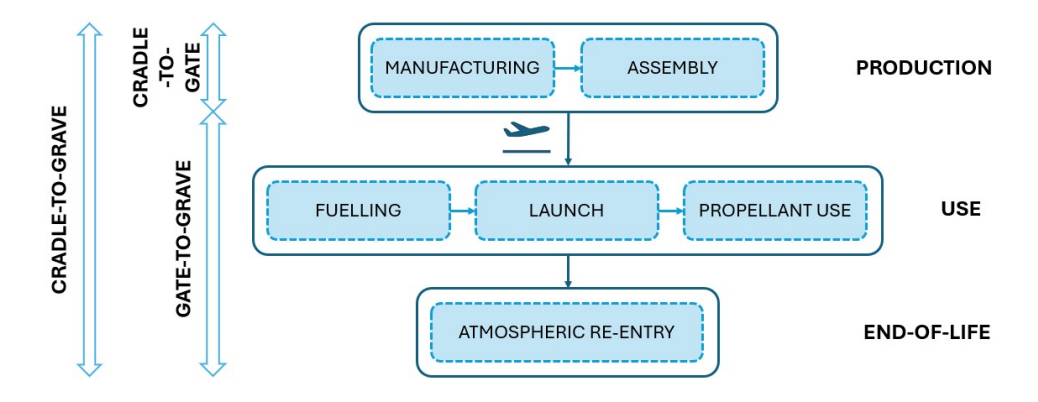


Figure 4.7: Life Cycle of the Analysed Missions

The *spatial coverage* of the production is Europe, while the launches take place in USA or French Guyana, depending on the selected vehicle. The propellant (of both launcher

and satellite) has been considered to be always produced in French Guyana, following the built-in processes in the ESA database: this represents a limitation of the analysis, since values for electricity consumption and raw materials can be slightly different if another production location is selected instead.

The temporal coverage of a single mission ranges from the initial investment to its launch date, supposing five years passing between the two events, and extends until the disposal; this topic is further developed in Section 4.6 regarding the mission's costs.

The technology coverage considers the best available technology for the items' production (following the processes from [10] whenever possible).

4.4.2 LCI Definition and Methods

After determining the boundaries and the limitations of the analysis, it is possible to start with the quantification of the inputs and outputs of the considered items throughout the whole life cycle of the missions [10]. Input data mainly regards energy consumption, raw materials used and other processed products, while output data is more focused on emissions (to air, water and soil), waste and co-products generated. Social and economic issues have not been considered in the analysis, since these are difficult to estimate at this mission design level.

Different categories of data do exist: *primary data*, which is directly collected from production sites, and *secondary data*, gathered from previous LCIs and from literature; during this work, only secondary data has been considered, minding that it can underestimate the real impacts of some processes [10].

Different strategies to create the LCIs of the items involved have been used:

- The main components of the satellite's subsystems, such as batteries, structure, solar arrays, etc. have been modelled by using the LCIs presented in [10], implementing them on SimaPro; in some cases, primary components (such as propellant tanks) are not contained in [10], but they have already been implemented on the ESA and Ecoinvent databases: these processes have been used as well;
- Regarding off-the-shelf products such as cameras, electric motors, etc. external LCIs have been used, slightly modifying them to make them suitable for the case in analysis;
- For minor components, such as pipelines and coatings, and for other items whose LCIs have not been found from literature, an own inventory has been developed, considering the raw materials, the production processes involved, the waste products and the generated emissions.

The satellites have been divided into subsystems and components, following the structure presented in Sections 4.2.2 and 4.2.3.

4.4.3 LCI of the Selected Components

Since the sizing results are expressed in kilograms, the components' LCIs primarily use **one kilogram** as fundamental functional unit, and it will then be multiplied by each

item's mass to obtain the final architecture to simulate; for mass-fixed components, whenever convenient, **one unit** is used instead.

Telecommunication System

The omnidirectional antenna has been modelled as explained in the ESA guidelines [10]. The directional antenna's gimbal is composed of an aluminium and titanium structure, and it contains two stepper motors [179, 180] rotatory actuators (Rotatory Type 3 Gimbal [85]). The two actuators' masses [180] are subtracted from the overall gimbal mass [85], and the remaining one is assumed to be equally divided between aluminium and titanium. A valid proxy for stepper motors is a Permanent Magnet Synchronous Reluctance Motor (PMSynRM) [181], which shows a similar behaviour and working principle, including the presence of permanent magnets (scaled to the 1 kg functional unit). The external surface is considered to be treated with anodizing and degreasing processes (by considering the cylindrical area containing the envelope of the mount [85]), as shown in [10]. The used PMSynRM contains some items not included in the databases, so they have been modelled as follows:

- Electrical Steel: it is made of 3.5% Si and 96.5% Fe in mass [182] and its production process is contained in [183] (considering non-oriented grains, since these are more versatile for motor applications).
- Forsterite (Mg₂SiO₄): it is used as insulant [183]. Since no data was found regarding the processes involved in its fabrication, only the elements consumption (magnesium, oxygen and silicon) to produce 1 kg of material is considered.
- Impregnation resin and painting: since not included in the database, epoxy resin and liquid epoxy resin have been used instead as a proxy.

Some of the component's processes are already included in the raw materials, while only copper drawing has been added separately.

The selected coaxial cables [90] have a silver plated inner conductor, a dielectric layer in solid PTFE, an outer copper tin soaked braid layer and an external FEP Blue jacket: a similar cable structure is used in jacketed single wire AWG 20 contained in the ESA database [10]. The connectors of the cables have been modelled from [90], considering two 7.32 mm long segments of wire as flanges for S-band communications. Only two connectors have been considered (since only a cable, the one for the directional antenna, operates at that frequency; regarding the frequencies at which the omnidirectional antennas operate, no data was found).

Processes and materials to fabricate the directional antenna's reflector are contained in [82]: the structure is made of CP-1 polymer and Kapton, covered by a 1200 Angstrom thick aluminium coating and surrounded by 80 Kapton tabs with a 1 cm diameter hole each; the thickness of reflector and tabs is assumed to be the same. Since CP-1 and Kapton precursors and processes [184, 185, 186] are not included in the databases on SimaPro, nylon 6-6 is used as a proxy, justified by its use for the same materials in built-in processes in the ESA database (nylon 6-6 is used as a proxy for Kapton, but it can be extended to CP-1 as well since they both are polyimides). The process involved

in the manufacturing of plastic materials in a desired shape is extrusion, modelled from the Ecoinvent database. Only the reflective side has been considered for the aluminium deposition, which is obtained through the sputtering process (by using [187] as a proxy, since the source involves metal sputtering of TiN instead of aluminium), proportioned by mass; anodizing and degreasing are applied on the metal surface [10].

The directional antenna's supports are made of glass fibers, whose protrusion process is already implemented on the ESA database.

The conical horn antenna to feed the parabolic reflector is considered to be a copper conical surface sealed through welding [83, 188]. To weld copper, Gas Tungsten Arc Welding (TIG) is used [188]: an existing process has been modified from the Ecoinvent database, adapting the aluminium TIG welding to the copper case as a proxy. The copper is assumed to be sheet-rolled to obtain the desired thickness.

The diplexer is modelled as a Low Integrated Circuit [10], due to the absence of an own processing unit, while MODEM (modulator) and transponder are modelled using the information contained in [10] (the transponder is assumed to be 50% transmitter and 50% receiver by mass).

Attitude Determination and Control System

The thrusters for ADCS have been modelled following the same procedure of the ODCS thruster, but since these engines burn hydrazine only, one valve is considered ((whose mass is taken from [110]).

Regarding the selected star trackers, they have been modelled following the camera model presented in the DockSys LCIs paragraph, with the only difference of using electronic memory units [10] instead of the standard electrical components (since star trackers are equipped with memory circuits, allowing for the implementation of a database of stars positions to compare the images taken during the mission [92]). The external aluminium surfaces are degreased and anodized [10], considering the envelope area calculated from [93]. Lastly, CMGs are modelled following the instructions from [10].

Orbit Determination and Control System

To model the ODCS thruster only the nozzle, the combustion chamber and the valves are considered [189]; satellite's engines are usually made of Inconel 718 [189], which is processed by additive manufacturing [190]. Inconel 718 is modelled as an iron-nickel-chromium alloy (according to ESA database's used proxies). The additive manufacturing processes are modelled from [191], including the subprocesses of atomization and selective laser melting; the volume produced by the selective laser melting of Inconel 718 reaches 15,000 mm³/h [192], or 0.12285 kg/h is terms of mass. Considering the latch valves presented in [110], the mass of two of them has been subtracted to the engine's mass, according to [107]. Each kg of Inconel 718 produced takes 8.1399 h to be manufactured, while 976.8 liters of gas argon [191] (1.7426 kg) per kg of Inconel 718 are required to create an inert atmosphere during the manufacturing. The necessary energy for the entire process is the sum of atomization (55.58 MJ/kg [191]) and selective laser melting (427.47 MJ/kg [191]) ones, being 483.05 MJ/kg.

The valves considered in the ADCS and ODCS are not pyrotechnical, to avoid the release of space debris during their activation (see Section 2.5.2). They are usually made of stainless steel 316L [193, 194] (which is compatible with both hydrazine and nitrogen tetroxide as already discussed), produced through selective laser melting [194]. Since no data regarding the internal components of valves has been found, only external structural components are considered in the LCA; atomization and selective laser melting processes are taken from [191]. Since not present in SimaPro databases, stainless steel 316L has been modelled by using stainless steel 304L as a proxy for the energy consumption, while considering SS316L's material composition [195]. Surface treatments for stainless steel are included on the valves' exposed area [10].

The selected tanks are made of Ti6Al4V [108], and the hydrazine tank is equipped with an Ethylene-Propylene-Diene Monomer (EPDM) hyperelastic diaphragm [108], which covers an internal hemispherical surface of the tank. Processes for the Ti6Al4V tanks (with Carbon Fiber Reinforced Polymer (CFRP) over-wrap in case of the helium vessel) are contained in the ESA database; regarding the diaphragm, the processes involved are synthesis, extrusion, vulcanisation (which are included in the production of the selected synthetic rubber) and molding (modelled as injection molding) [196].

Lastly, pipelines for both ADCS and ODCS are made of stainless steel 316L [98]; the processes involved in the production of the series 10S pipes are forming, welding, annealing and cold drawing [98]; welding is not considered here, since it can cause the embrittlement of the material. The external area is treated with superficial processes for stainless steel [10], scaled on data from [98].

Data Handling System

The OBC is modelled from [10]. The buses for the DHS are modelled as shielded jacketed single wires AWG 26, which are already implemented on the ESA database from [10]. This choice is due to the similarities in the processes involved for the production of standard data buses contained in [197]. Cable type AWG 26 has been selected instead of AWG 20, due to its similar mass-per-meter density [197].

Thermal Control System

As part of the TCS, MLIs are modelled as MLI blankets from [10]; this way, the inventory contains the same materials (PER and polyesters) used during the sizing process [115]. Coatings have been modelled using data from [116] for the ZinvisibleTM formulation, containing 43.6% Kasil 2130 and 56.4% ZinvisibleTM in mass; ZinvisibleTM consists of ZnO molecules, while Kasil 2130 is made of SiO₂ and K₂O [117] (2.10 mass ratio K₂O/SiO₂); since no data was found regarding the production processes of Kasil 2130, only the elements' consumption is considered (Si, O₂ and K). Regarding the coating's production, 0.792 kg water per kg of product are necessary [116]; the processes involved during the fabrication are milling in a ceramic mill (for 30 minutes [116], assuming 20 kW power required [198], meaning 10 kWh total energy consumed) and filtering (assuming the same time required by milling and a power consumption of 10 kW [199], meaning 5 kWh of total energy consumed). The overall energy consumption of 15 kWh is independent on

the mass produced, but is considered as an input per unit instead.

Cold plates are usually made of aluminium, which is manufactured through CNC machining processes, friction stir welding (or brazing) and stamping [200, 201, 202]. Considering 2 cm thick cold plates [202], one kilogram of aluminium consists of a parallelepiped with a square, ~ 13.58 cm long, face. The process used for cold plates is a modified version of "aluminium generic part with generic processes" from the ESA database, without considering turning and transports, adding friction stir welding on the plate's side and considering surface treatments for aluminium on the external surfaces [10]. Die forging is used instead of stamping, due to the lack of available data.

Patch-flexible heaters have been modelled for the LCA [114]; they are usually made of two insulating layers (made of polyimide [203, 204], Kapton, modelled as nylon 6-6 on SimaPro as previously discussed) with an inner conductive layer made of nichrome alloy [205] (assumed to be a continuous plate without holes). An overall thickness of 0.15 mm is assumed (0.05 mm each layer). Nichrome 80/20 has been modelled by implementing the production processes from [206, 207], using the mean values of the given ranges. The alloy is extruded, rolled [207] and then shaped through the etching process [208], requiring ferric chloride to corrode the metal [209]. The etching process is the same one implemented for the electrostatic pads in the DockSys LCIs paragraph, by using nichrome instead of copper; moreover, due to the different corrosive reactions occurring, the required quantity of ferric chloride changes: in facts, each Ni atom requires two FeCl₃ molecules and each Cr atom requires three of them (obtained by balancing the reactions). Considering a 80/20 composition, the total amount of FeCl₃ needed is 2.2 times the one required by the copper etching (one FeCl₃ per Cu atom) to corrode the same moles of material. The copper ions generated by the process have been substituted by chromium and nickel splitting them using the 80/20 mass ratio between Ni and Cr. The polyimide insulating layers undergo a plastic film extrusion process (also considering the wasted material), due to their reduced thickness.

Regarding the pump and accumulator system, an already existing LCI has been used [210, 211], considering the "Compressor, valves, and receiver" voice. From the mass breakdown, 1 kg of the system is composed by 0.1818 kg of compressor, 0.3636 kg of accumulator, 0.3636 kg of electronics and 0.0909 kg of valves [211]; electronics are low integrated circuits from the ESA database [10]. The accumulator is made of stainless steel 316L [108], and it is modelled by adapting the Ti6Al4V spherical tank to the stainless steel manufacturing (implementing a new TIG welding process as well). The compressor is modelled as shown in [210], without including the processes of degreasing and passivation due to the lack of data regarding the exposed surfaces. The radiator is modelled considering the mass distribution presented in [211] for a traditional radiator panel; for a kilogram of component, 0.07272 kg are Optical Solar Reflector (OSR)s, 0.2424 kg are aluminium face sheets, 0.2652 kg are aluminium honeycomb and the remaining 0.4242 kg are heat pipes [211]. OSRs are made of aluminium (which includes the sheet rolling process to obtain a thin foil) and PET (undergoing the extrusion process to obtain the plastic layer) [212]; the mass is assumed to be equally divided between aluminium and plastic material. The honeycomb core is taken from the structure processes contained in [10]. The two aluminium face sheets are modelled as the honeycomb core is, without considering the milling and turning processes since unusual for the machining of aluminium foils, and their total surface is treated by degreasing and anodizing [211]; the energy is evaluated by subtracting the power consumption of the excluded processes. Regarding the pipelines, they are obtained by extrusion and linked through welding [213]; the extrusion process is modelled as die forging, containing both hot and cold extrusion for aluminium. Considering one pipe every 15 cm [211], up to seven 1 m long pipes can fit in a square meter of radiator surface; assuming two welding lines per-pipe, allowing a double connection, a 14 m welding line is necessary, meaning 2.12 m per kg by proportion [211] (welding arc process is used).

Regarding the louvers, the mount is made of an aluminium case [214, 215] and aluminium blades, each one equipped with a bimetallic spring [91, 214, 215]. The processes to produce the aluminium components are mainly die forging and machining (drilling, turning, milling) [216]. From [215] a 1.29 kg mount is equipped with 20 bimetallic springs, 20 blades and 68 screws. Bimetallic springs are usually made of brass (70% Cu, 30% Zn [217]), and are modelled assuming a full material envelope(8300 kg/m³ density) and dimensions from [215, 217] (0.76 mm thickness and 12.7 mm radius), the mass of a bimetallic spring is 0.003196 kg. The processes that a spring undergoes are rolling (modelled from the copper sheet rolling from the databases) and annealing. The screws are the same one used for the DockSys camera. The mass of the aluminium parts is obtained by subtracting the springs and screws' one, and the overall exposed surface of the aluminium components (extrapolated from [215]) is anodized and degreased [10].

Sensors are modelled as low integrated electronic circuits from [10], since the included processes are typical for support instrumentation.

Electrical Power System

Many items of the EPS have been modelled from the ESA guidelines [10], such as batteries, solar arrays (using nylon 6-6 as a proxy for Kevlar) and switches, modelled as high integrated circuits from [127]).

The selected solar array gimbals [126] contain two Type 1 actuators [218]. The structure is obtained by subtracting the two actuators' masses, and it is considered to be made of aluminium and titanium in equal quantities. The Type 1 actuators are modelled as a scaled version of the Type 3 actuators from the ComSys LCIs paragraph. Considering the cylindrical envelope of the gimbal, anodizing and degreasing have been applied on the external surface. Lastly, wires are modelled as ESCC 3901 018 cables [122] by using AWG 26 single wires on SimaPro (lighter than AWG 20 type).

Structure

The structure is modelled by using the information contained in [10].

Docking System

One of the main components of the DockSys is the camera; external LCIs for cameras have been used to model it, containing representative materials [219] and processes [220]. To

model the lenses, ESA guidelines are used [10], while Printed Wiring Boards are chosen as a proxy for the FPCA; the Light Trap and the Retaining Collar Clip are modelled only accounting for the materials, since no data regarding the processes was found. All the masses are scaled to the model selected during the sizing process [75]. The surface containing the envelope of the camera [75] is anodized and degreased, according to [10]. The telescopic arm is a crucial component necessary to dock with the selected debris; since no data was found regarding robotic arms' LCI, processes and materials have been modelled on SimaPro by following the manufacturing steps involved during its production. The body is divided into six carbon resin tubes [133], and the pultrusion process is used to model them in the desired shape. Each section is connected to the adjacent ones by metallic rings (assumed to be made of aluminium) for a total of six, 1 cm thick, rings [133], sharing the same width of the carbon resin sections; the processes involved are casting (to obtain the initial aluminium discs), milling (to clear the interiors, giving the desired ring shapes), anodizing and degreasing [10]. The tubes are extracted by using an aluminium worm gear (extrapolated from [133]), assuming the grooves to occupy half of the volume between the inner and the outer radius; the processes involved are milling, anodizing and degreasing on the outer cylinder's surface. The arm contains 15 Vespel SP3 (polyimide [221, 222]) pins, which are modelled using nylon 6-6 as a proxy (as shown in the ESA database); they extend from the inner radius of the aluminium rings to the inner radius of the worm gear; since extrusion is not suitable for Vespel SP3 and no data about other processes was found, only the material's consumption is considered. Eighteen 4 cm long titanium latching pins are included in the arm's design [133], obtained by Electric Discharge Machining. Thirty 2 cm long and 1 cm wide compression springs are included as well to inter-guide the arm sections (extrapolated from [133]); regarding springs, K-81 model from [150] is selected and generic steel processes are used to model them. Lastly, the arm contains fifteen pins with a spherical tip, whose mass is extrapolated from [133] assuming aluminium; generic processes for aluminium are used to model these items. The robotic arm is deployed by using electrical energy: a DC brushed motor [134] has been selected. Since no data regarding DC brushed motors was found, a PMSynRM motor is used instead, adding the brushes as a first approximation: they are made of

treated with anodizing and degreasing [10].

Lastly, the processes involved in the electrostatic pads manufacturing are presented in [141]; the pads are made of two silicone upper and lower layers, and an intermediate copper layer. The conductive layer's pattern is created through etching by using ferric chloride, and it is considered to be full material (without holes); to model the middle layer, a built-in process from the Ecoinvent database is used (since it includes the operations shown in [225] for etching), and it has been adjusted by changing the corrosive medium, minding the different number of molecules necessary to isolate a Cu atom (FeCl₃ needs one molecule, while HCl needs two). Once the conductive layer has been completed and cleaned, a thin Mold Star silicone layer is spin coated and cured on the substrate: this process repeats other two times until the silicone layers are created [141]. A typical spin-coating machinery is shown in [226]; assuming 30 s duration for the process (typical for xylene and toluene spin coating), given the power consumption of the machine (5 kW),

graphite [223], undergoing machining processes (milling [224]). The motor's case is then

the overall energy consumption is 150 kJ: this value is then scaled to the silicone layers' mass of a 1 kg pad.

Debris Protection System

The Whipple shield is made of aluminium, and the processes used to create metal sheets are casting, die forging and sheet rolling. Once the dimensions of the shield have been defined, the anodizing and degreasing processes are applied on the surfaces (minding the number of layers of the structure) and the edges of the shield are separated through the laser cutting process.

Deorbit Kits

Many components belonging to the deorbit kits share their manufacturing processes with other subsystems' LCI; the telescopic arms to lift the kits, their motors and the electrostatic pads are described in the DockSys LCIs paragraph and the Switches to turn on each arm have already been explored in the EPS LCIs Section. Regarding the internal components of the kit itself, some items have been previously discussed as well, such as batteries, EPSs, solar arrays, antennas, electrostatic pads and structure.

Among the exclusives components of this subsystem, the deployment mechanism is modelled as four compression springs [150]. The electron emitter is a carbon fiber cathode [227]; assuming the dimensions of the smallest emitter available (1/4" [227]), the thickness of the cathode's carbon fiber and graphite layers are extrapolated from [227]. The masses of the layers can be evaluated through the density of carbon fibers and graphite (4.02 g and 31.8 g, respectively). Carbon fiber is modelled using the processes available in the ESA database and graphite from the Ecoinvent database. To link the two layers, a film of adhesive for metals is applied [228] (0.1 mm thickness, 1100 kg/m³ density [229]). The tether's end mass is made of stainless steel (due to its high density), assuming a cubic shape.

Lastly, the electrodynamic tether is modelled as an aluminium tape [46]. The metal is first sheet rolled to obtain the desired thickness, and is then cut to reach the final width; the selected cutting process is slitting (400 m/min [230], 20 kW power required [231]). The final surface of the tether is then anodized and degreased [10].

Table 4.2 resumes the main sources used to model the satellites' components.

4.4.4 Use Phase LCI

After the production process (described in Section 4.4.3), the use phase of the LCA shall be defined as well. Before launch, the satellites are transferred from the production plant to the launch site: since the assembly occurs in Europe (assuming Turin as production site, thanks to the available facilities), and the launches are expected to take place in the American continent (all the vehicles analysed in Table 4.3 can only be launched from USA or French Guyana), air transportation is assumed, considering Antonov AN-124 [233]. After the transportation to the launch site, the other operations considered during the use phase of the satellites are the launch event (where only the emissions generated by the

Table 4.2: LCI Sources

Subsystem	Components and Sources
	Omnidirectional Antenna [10, 13, 232], Directional Antenna Reflec-
ComSys	tor [10, 232], Directional Antenna Feed [232], Directional Antenna
Combys	Support [13], Gimbal [13, 232], MODEM [10, 13, 232], Transponder
	[10, 13, 232], Diplexer [10, 13], Coaxial Cables [13]
DHS	OBC [10, 13, 232], OBC Buses [10, 13]
DockSys	Camera [13, 232], Telescopic Arm [13, 232], Telescopic Arm Motor
DOCKBYS	[13, 232], Electrostatic Pads [232]
ODCS	Thruster [13, 232], Hydrazine Tank [13], NTO Tank [13], Helium
<u> </u>	Vessel [13], Pipelines [13, 232], Valves [13, 232]
ADCS	Thrusters [13, 232], Star Tracker [13, 232], CMGs [10, 13, 232]
EPS	Solar Arrays [10, 13, 232], Gimbals [13, 232], Battery [10, 13, 232],
	Switches [13], Wiring [13]
	MLIs [10, 13, 232], Coatings [232], Cold Plates [13, 232], Heaters [13,
TCS	232], Pump and Accumulator [13, 232], Radiator [13, 232], Coolant
	[232], Louvers [13, 232], Sensors [13]
Structure	Structure [10, 13, 232]
DPS	Whipple Shields [13, 232]
Deorbit Kits	Kits [13, 232]

rocket's propellant are examined) and the propellant consumption of the satellite during the entire mission; no afterburning is considered, meaning that the reactions occurring between the exhaust gases and the surrounding environment are neglected. The emissions generated by the Ground Segment during the whole mission duration are not considered, since it is out of the scope of the study.

Regarding the propellant use, the processes involved in its production for both satellites and launchers have been included in the analysis; however, the generated emissions are only considered if they are released at an altitude lower than 50-80 km [234]: as a consequence, the impact of the satellites and launchers' upper stages propellant only accounts for its production. The compartment on SimaPro where the emissions are allocated is "stratosphere + troposphere", since the lower stages start burning at ground level. To determine the emissions generated by the engines, the CEA software from NASA [235] is used, which estimates the mass of the products released during the combustion by using the Gibbs' free energy, requiring chamber pressure, expansion and mixture ratios of the thrusters.

Since Falcon Heavy burns the same propellant and mounts the same engines of Falcon 9, the same processes can be used. To model the boosters if included in the various analysed launch vehicles, the Ariane 6 ones have been used as a proxy due to their similar composition.

The allocated launch emissions only represent the percentage of the mass of the satellite with respect to the maximum payload to the injection orbit, which is evaluated by using

the methodology explained in Section 4.3. The output emissions do not represent, however, the whole particles released in the atmosphere, since many other minor species are produced, such as AlCl₂, AlOH, HO₂, etc.: these molecules are not implemented in the SimaPro's airborne emissions, representing a limit of the analysis. Despite the low mass fraction with respect to other major outputs, researchers are still trying to understand the real impact of these species on the atmosphere [236].

The method used for the analysis is the one implemented on the ESA database, which has been slightly modified by adding a Global Warming Potential (GWP) of 11.6 to the atmospheric hydrogen (instead of zero) [237] to better account for the launchers' emissions

Table 4.3 resumes the main sources used to model the satellites' use phase.

Item	Input	Output
ADCS and ODCS Use	Propellant Production [13]	Emissions [232, 235]
Antonov AN-124	Air Transportation [232]	_
Falcon 9 1 st Stage	Propellant Production [13]	Emissions [232, 235]
Falcon 9 2 nd Stage	Propellant Production [13]	_
Falcon Heavy 1 st Stage	see Falcon 9 1	st Stage
Falcon Heavy 2 nd Stage	see Falcon 9 2 ¹	nd Stage
Ariane 6 Boosters	Propellant Production [13]	Emissions [232, 235]
Ariane 6 Main Stage	Propellant Production [13]	Emissions [232, 235]
Ariane 6 2 nd Stage	Propellant Production [13]	_
Vulcan Centaur Boosters	see Ariane 6 I	Boosters
Vulcan Centaur 1 st Stage	Propellant Production [13]	Emissions [232, 235]
Vulcan Centaur 2 nd Stage	Propellant Production [13]	_
SLS Boosters	see Ariane 6 I	Boosters
SLS Main Stage	Propellant Production [13]	Emissions [232, 235]
SLS Upper Stage	Propellant Production [13]	_

Table 4.3: Use Phase LCI Sources

4.5 Safe Disposal Assessment

The study of the atmospheric re-entry of a satellite is fundamental to understand the risks posed to the population and the impact caused by burning components and released particles [2, 15, 16]. As described in Section 4.1, the safe disposal assessment is evaluated by using the ESA-DRAMA software. However, the SARA module needs some data which are available only after the definition of the LCIs of the items.

First, the satellites' components are modelled by using built-in shapes from the program: whenever the dimensions are unknown, the object is assumed to be a cube.

Second, part of the used metals and composites are already contained in the software's database; however, some components are made of materials which are not included, so they have been added separately: titanium [238], Kapton [239], glass fibers [240], Vespel

[221], silicone [140, 241], EPDM [242], PET [243], nichrome [207], PVC [244], brass [245], aluminium 6061T6 [246] and aluminium 2219T851 [247].

Third, all the components which are external to the structure are considered to be connected to it, while the internal items are released once the structure breaks up.

After the satellite has been implemented, the selected debris (see Section 5.1) shall be modelled as well. The ENVISAT uses data from [248] for the payload masses and dimensions, including information regarding wiring, CMGs and propellant tanks. The structure is modelled from [249, 250], while the other internal components are assumed to be proportional by mass to the ones evaluated for the SCMK satellite. The Zenit-2 is modelled from [251, 252, 253]: engines are assumed to be made of Inconel 718, including some steel components (proportionally to the one used during the sizing process), and approximative values for the mass percentages of the remaining subsystems are taken from [254]; the residual mass is considered to be aluminium structure. Once the program has been correctly set, simulations are run.

When simulating the deorbit of the debris and the satellite together, a controlled re-entry is selected, while uncontrolled re-entry is performed whenever the debris deorbits alone or it is equipped with a deorbit kit. The starting dates for the simulations are obtained through the sizing process. The program has been run in Monte-Carlo mode, allowing for statistically valid results by varying the initial true anomaly of the objects orbiting the Earth.

4.6 LCC Definition

The overall cost of a space mission considers different operations and aspects of the project, ranging from the manufacturing process of the spacecraft to the end-of-life phase, passing through the launch event. For the analysis concerning this document, production, transportation to the launch site, launch and operative costs have been included.

To estimate the production costs, the Advanced Mission Cost Model (AMCM) software is used [255]; to compile the program, the first satellites are assumed to be launched on Jan 1st 2030 (assuming 5 years for development and production) and represent a 1st generation spacecraft (if the mission is replicated in the future, the launch year changes as well as the block number). Due to the unusual functions the satellite must accomplish (such as multiple rendezvous and docking with uncooperative targets), the difficulty level of the mission on AMCM is set to be "High". The most suitable category to model the missions is chosen by comparing the mass budget of the spacecraft obtained through the sizing process with the one of flown satellites from [256]; since no "Active Debris Removal" category exists, SCST and SCMK are modelled as an average between High Earth Orbit (HEO) Earth Observation and Planetary spacecraft missions, while SCMT is modelled as a Planetary spacecraft due to the high amount of propellant required. The costs evaluated by AMCM are assumed to be an instantaneous initial investment.

Since AMCM only requires the dry mass of the spacecraft, the cost per kg of propellant and pressurant gas are added separately, following Table 4.4.

Table 4.4: Propellant Cost

Fluid	Cost (2025 \$) [257]
Hydrazine	$365.42 \ \text{\$/kg}$
Nitrogen Tetroxide MON-3	234.62 \$/kg
Helium, pressurant ^a	5802.17 \$/kg

^a Normal temperature and pressure assumed.

The launch costs are taken from the user guides of the analysed launchers; differently from Table 4.1, costs are not based on the kg of payload, but on the whole launch, since the orbit to inject the satellites into do not allow a full payload configuration. The costs of the launch are scaled proportionally to the mass of the spacecraft with respect to the allowable payload at the desired orbit (which is evaluated by using [168]). The costs related to the transportation to the launch site are 100,000 \$/h and the cruise speed to evaluate the flight time is 850 km/h [233].

Lastly, operative, ground segment and management costs are evaluated as 19.8% [258] of production, which is a specific value for servicing and rendezvous missions. Operative costs are allocated during the entire duration of the mission, from the launch to the beginning of the disposal maneuver, and the costs-per-year are the overall operative costs divided by the number of years the mission lasts (by applying inflation).

To correctly allocate the costs-per-year, inflation is considered: an inflation rate of 2.2% is assumed for Europe [259] (development, production, transportation and operations), while a rate of 2.3% is estimated for the USA [260] (launch). In the results, costs are expressed in Euros, considering a conversion of $1\$ = 0.88 \notin [261]$.

Figure 4.8 represents the costs allocated for a single ADR mission, supposing an initial investment in 2025.

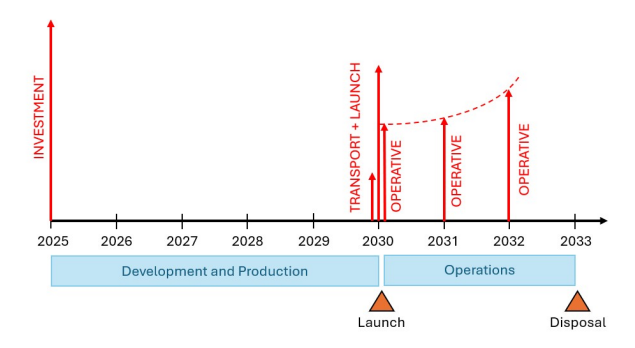


Figure 4.8: Example of Allocated Costs, considering the Initial Investment to occur in 2025 and a 5 years long Production Phase. Operations Costs are supposed to be Allocated at the Beginning of the Year they are applied to

Chapter 5

Sizing, Life Cycle Assessment and Life Cycle Cost Results

5.1 Identifying Orbits and Debris to Remove

Using the process described in Section 2.3, the following debris have been selected as the most significant to be removed [37]: their COE have been obtained from [262], at 02/03/2025 (no reliable orbit propagator was found to obtain the COE at the scheduled start time of the mission); the identification code associated to each debris is the NORAD Catalog Number.

	Table 5.1:	COE of t	he Selected	Debris for	ADR	Missions
--	------------	----------	-------------	------------	-----	----------

	a [km]	e	$i [\deg]$	$\Omega [\mathrm{deg}]$	$\omega_p \; [\mathrm{deg}]$
Envisat (27386)	7140	0.0001359	98.32	20.1382	86.7823
Zenit-2 (28353)	7222	0.0007490	71.00	294.7077	253.8799
Zenit-2 (31793)	7221	0.0002250	70.97	234.6513	255.5626
Zenit-2 (27006)	7373	0.0014042	99.72	216.5826	222.5612
Zenit-2 (26070)	7217	0.0015524	71.00	162.1003	22.4544

Table 5.1 contains the COE of the selected debris, where a is the semimajor axis, e the eccentricity, i the inclination, Ω the right ascension of the ascending node and ω_p the anomaly of the perigee. In Table 5.2 the mass and the cross-section areas of the debris are also reported. The values of the cross-section areas have been defined modelling the debris on the ESA-DRAMA software [59]; A_{ntb} is the area referred to the non-tumbling object (considering the axis along which the docking with the ADR satellite occurs), while A_{tb} is the area referred to the tumbling object. The data to model the Envisat on ESA-DRAMA was taken from [249, 250], while [263] contains the data to model the Zenit-2. Figure 5.1 shows the implemented models and their orbits.

Table 5.2: Mass and Cross Section of the Selected Debris for ADR Missions

	m [kg]	$A_{ntb} [\mathrm{m}^2]$	$A_{tb} [\mathrm{m}^2]$
Envisat (27386)	8111	72.6485	56.2409
Zenit-2 (28353)	9000	42.5155	38.1463
Zenit-2 (31793)	9000	42.5155	38.1463
Zenit-2 (27006)	9000	42.5155	38.1463
Zenit-2 (26070)	9000	42.5155	38.1463

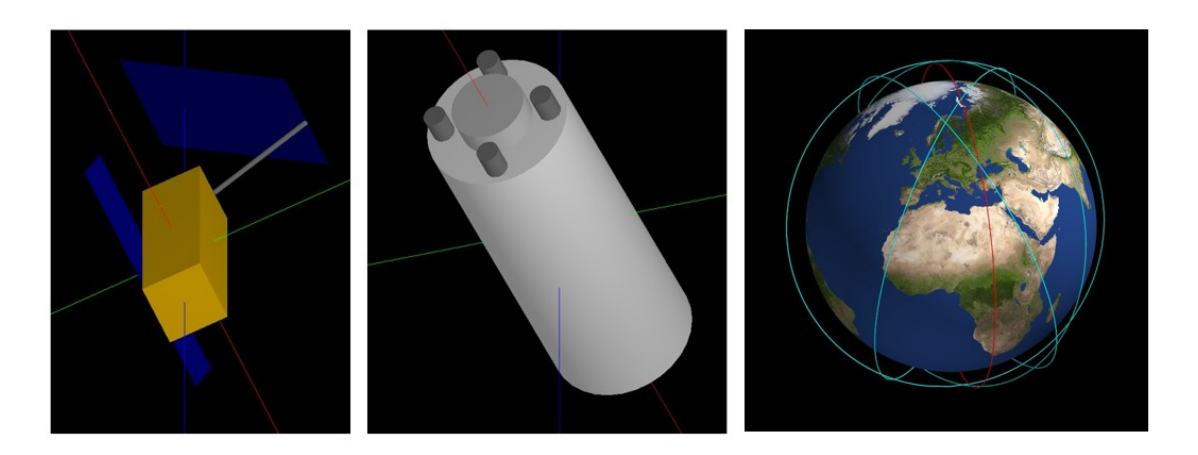


Figure 5.1: Envisat Model (left) and Zenit-2 Model (center) Implemented on ESA-DRAMA, and their Orbits (right, Envisat in Red and Zenit-2 in Cyan)

5.2 Sizing Results

By using the methods described in Section 4.2, Table 5.3 shows the mass breakdown of the three ADR architectures analysed. The table is divided minding the different subsystems involved in the simulations; the SCST column only refers to a single satellite.

Table 5.3: Mass Breakdown

Subsystem Component		SCST [kg]	\mathbf{SCMT} [kg]	SCMK [kg]
	Omnidirectional Antenna	0.230	0.230	0.230
	Directional Ant. Reflector	0.880	0.880	0.880
	Directional Ant. Feed	$6.333 \cdot 10^{-4}$	$6.333 \cdot 10^{-4}$	$6.333 \cdot 10^{-4}$
	Directional Ant. Support	0.219	0.219	0.219
ComSva	Gimbal	4.400	4.400	4.400
ComSys	MODEM	9.800	9.800	9.800
			α	.1

Continues in the next page

Filters	Subsystem	Component	SCST [kg]	SCMT [kg]	SCMK [kg]
Diplexer		Filters	0.0	0.0	0.0
DHS		Transponder	5.440	5.440	5.440
DHS OBC OBC Buses 0.129 0.129 0.129 0.129 Camera 4.800 4.800 4.800 4.800 4.800 2.900 2.900 2.900 2.900 2.900 2.900 2.900 2.200 3.20 3.30 1.30 3.30 1.30 3.30 1.30 3.30 1.30 4.31 4.44 1.04 4.81 1.88 2.48 2.48 2.48 2.48 2.48 2.48 2.48 2.48 2.48 2.48 2.48 2.48 2.48 2.48 2.48 2.48 2.50 2.50		Diplexer			
DockSys		Coaxial Cables	$4.409 \cdot 10^{-2}$	$4.409 \cdot 10^{-2}$	$4.409 \cdot 10^{-2}$
DockSys	DHG	OBC	0.300	0.300	0.300
DockSys Telescopic Arm Telescopic Arm Motor Electrostatic Pads 2.900 2.2494 2.494	DIIS	OBC Buses	0.129	0.129	0.129
Telescopic Arm Motor 2.200 2.200 2.200 Electrostatic Pads 2.494 2.944 2.494 2.494 2.944 2.494 2.944 2.494 2.944		Camera	4.800	4.800	4.800
Telescopic Arm Motor Electrostatic Pads 2.494	DockSys	Telescopic Arm		2.900	
ODCS Thruster Hydrazine Tank NTO Tank 10.29 453.6 136.5 136.5 136.5 136.5 NTO Tank 10.29 453.6 136.5 136.5 136.5 NTO Tank 10.29 453.6 136.5 136.5 NTO Tank 136.5 NTO Tank 10.29 453.6 134.7 94.11 14.14 103 433.5 14.14 103 433.5 14.14 103 433.5 14.14 103 433.5 14.14 103 433.5 14.14 103 433.5 14.14 103 433.5 14.14 103 14.14 103 14.15 11.14 10.14	DOCKDYS	Telescopic Arm Motor	2.200	2.200	2.200
$ \begin{array}{c ccccccccccccccccccccccccccccccccccc$		Electrostatic Pads	2.494	2.494	2.494
ODCS NTO Tank Helium Vessel Pipelines 6.962 32.43 314.7 1.444 · 10³ 94.11 433.5 Pipelines Valves 24.88 24.88 24.88 Valves 12.57 189.5 62.84 Thrusters 17.92 17.92 17.92 ADCS Star Tracker 1.880 1.880 1.880 CMGs 52.00 52.00 52.00 52.00 Propellant NTO 359.4 1.635 · 10⁴ 4920 Propellant NTO 359.4 1.624 · 10⁴ 4858 Helium 5.835 259.8 77.98 EPS Solar Arrays Gimbals 21.61 37.63 26.31 Gimbals 2.640 2.640 2.640 Battery 12.75 22.20 15.53 Switches 0.400 0.400 0.400 Wiring 16.03 26.95 19.23 Regulation 0.0 0.0 0.0 Cold Plates 8.600 11.48 9.447		Thruster	7.300	7.300	7.300
Helium Vessel		Hydrazine Tank	10.29	453.6	136.5
Helium Vessel 32.43 1.444 · 103 433.5 Pipelines 24.88 24.88 24.88 Valves 12.57 189.5 62.84 Thrusters 17.92 17.92 17.92 ADCS Star Tracker 1.880 1.880 1.880 CMGs 52.00 52.00 52.00 Hydrazine 370.9 1.635 · 104 4920 Propellant NTO 359.4 1.624 · 104 4858 Helium 5.835 259.8 77.98 Solar Arrays 21.61 37.63 26.31 Gimbals 2.640 2.640 2.640 Battery 12.75 22.20 15.53 Switches 0.400 0.400 0.400 Wiring 16.03 26.95 19.23 Regulation 0.0 0.0 0.0 MLIs 0.773 9.715 4.355 Coatings 5.300 44.16 19.82 Cold Plates 8.600 11.48 9.447 Heaters 0.375 1.725 0.758 TCS Pump and Accumulator 6.880 9.186 7.557 Radiator 20.62 26.73 22.42 Coolant (H ₂ O) 3.558 4.709 3.896 Louvers 31.13 40.34 33.85 Sensors 3.558 4.709 3.896 Structure Structure 148.6 1433 744.0 DPS Whipple Shields 12.91 566.9 254.6 Kits 0.0 0.0 0.0 427.8 Telescopic Arms 0.0 0.0 0.0	ODCS	NTO Tank	6.962		94.11
Valves	ODCS	Helium Vessel	32.43	$1.444 \cdot 10^3$	433.5
$ \begin{array}{c ccccccccccccccccccccccccccccccccccc$		Pipelines	24.88	24.88	24.88
$ \begin{array}{c ccccccccccccccccccccccccccccccccccc$		Valves	12.57	189.5	62.84
$ \begin{array}{c ccccccccccccccccccccccccccccccccccc$		Thrusters	17.92	17.92	17.92
Propellant Hydrazine 370.9 1.635 · 10 ⁴ 4920 Propellant NTO 359.4 1.624 · 10 ⁴ 4858 Helium 5.835 259.8 77.98 Solar Arrays 21.61 37.63 26.31 Gimbals 2.640 2.640 2.640 Battery 12.75 22.20 15.53 Switches 0.400 0.400 0.400 Wiring 16.03 26.95 19.23 Regulation 0.0 0.0 0.0 MLIs 0.773 9.715 4.355 Coatings 5.300 44.16 19.82 Cold Plates 8.600 11.48 9.447 Heaters 0.375 1.725 0.758 TCS Pump and Accumulator 6.880 9.186 7.557 Radiator 20.62 26.73 22.42 Coolant (H ₂ O) 3.558 4.709 3.896 Structure Structure 148.6 1433 74	ADCS	Star Tracker	1.880	1.880	1.880
Propellant NTO 359.4 1.624 · 10 ⁴ 4858 Helium 5.835 259.8 77.98 Solar Arrays 21.61 37.63 26.31 Gimbals 2.640 2.640 2.640 Battery 12.75 22.20 15.53 Switches 0.400 0.400 0.400 Wiring 16.03 26.95 19.23 Regulation 0.0 0.0 0.0 MLIs 0.773 9.715 4.355 Coatings 5.300 44.16 19.82 Cold Plates 8.600 11.48 9.447 Heaters 0.375 1.725 0.758 TCS Pump and Accumulator 6.880 9.186 7.557 Radiator 20.62 26.73 22.42 Coolant (H ₂ O) 3.558 4.709 3.896 Louvers 31.13 40.34 33.85 Sensors 3.558 4.709 3.896 Structure <t< td=""><td></td><td>CMGs</td><td>52.00</td><td>52.00</td><td>52.00</td></t<>		CMGs	52.00	52.00	52.00
$ \begin{array}{c ccccccccccccccccccccccccccccccccccc$		Hydrazine	370.9	$1.635 \cdot 10^4$	4920
$EPS \begin{array}{c ccccccccccccccccccccccccccccccccccc$	Propellant	NTO	359.4	$1.624 \cdot 10^4$	4858
EPS Gimbals 2.640 2.640 2.640 Battery 12.75 22.20 15.53 Switches 0.400 0.400 0.400 Wiring 16.03 26.95 19.23 Regulation 0.0 0.0 0.0 MLIs 0.773 9.715 4.355 Coatings 5.300 44.16 19.82 Cold Plates 8.600 11.48 9.447 Heaters 0.375 1.725 0.758 TCS Pump and Accumulator 6.880 9.186 7.557 Radiator 20.62 26.73 22.42 Coolant (H2O) 3.558 4.709 3.896 Louvers 31.13 40.34 33.85 Sensors 3.558 4.709 3.896 Structure Structure 148.6 1433 744.0 DPS Whipple Shields 12.91 566.9 254.6 Kits 0.0 0.0 427.8 Telescopic Arms 0.0 0.0 14.50		Helium	5.835	259.8	77.98
$\begin{array}{c ccccccccccccccccccccccccccccccccccc$		Solar Arrays	21.61	37.63	26.31
$ \begin{array}{c ccccccccccccccccccccccccccccccccccc$		Gimbals	2.640	2.640	2.640
$\begin{array}{c ccccccccccccccccccccccccccccccccccc$	FDC	Battery	12.75	22.20	15.53
$\begin{array}{c ccccccccccccccccccccccccccccccccccc$	121 5	Switches		0.400	0.400
$\begin{array}{c ccccccccccccccccccccccccccccccccccc$		Wiring	16.03	26.95	19.23
Coatings 5.300 44.16 19.82 Cold Plates 8.600 11.48 9.447 Heaters 0.375 1.725 0.758 Pump and Accumulator 6.880 9.186 7.557 Radiator 20.62 26.73 22.42 Coolant (H ₂ O) 3.558 4.709 3.896 Louvers 31.13 40.34 33.85 Sensors 3.558 4.709 3.896 Structure 148.6 1433 744.0 DPS Whipple Shields 12.91 566.9 254.6 Kits 0.0 0.0 427.8 Telescopic Arms 0.0 0.0 14.50		Regulation	0.0	0.0	0.0
$ \begin{array}{c ccccccccccccccccccccccccccccccccccc$		MLIs	0.773	9.715	4.355
$\begin{array}{c ccccccccccccccccccccccccccccccccccc$		Coatings	5.300	44.16	19.82
$\begin{array}{c ccccccccccccccccccccccccccccccccccc$					
$\begin{array}{c ccccccccccccccccccccccccccccccccccc$		Heaters	0.375	1.725	0.758
$ \begin{array}{c ccccccccccccccccccccccccccccccccccc$	TCS	Pump and Accumulator	6.880	9.186	7.557
Louvers 31.13 40.34 33.85 Sensors 3.558 4.709 3.896 Structure 148.6 1433 744.0 DPS Whipple Shields 12.91 566.9 254.6 Kits 0.0 0.0 427.8 Telescopic Arms 0.0 0.0 14.50		Radiator	20.62	26.73	22.42
Sensors 3.558 4.709 3.896 Structure 148.6 1433 744.0 DPS Whipple Shields 12.91 566.9 254.6 Kits 0.0 0.0 427.8 Telescopic Arms 0.0 0.0 14.50		Coolant (H_2O)	3.558	4.709	3.896
Structure Structure 148.6 1433 744.0 DPS Whipple Shields 12.91 566.9 254.6 Kits 0.0 0.0 427.8 Telescopic Arms 0.0 0.0 14.50		Louvers	31.13	40.34	33.85
DPS Whipple Shields 12.91 566.9 254.6 Kits 0.0 0.0 427.8 Telescopic Arms 0.0 0.0 14.50		Sensors	3.558	4.709	3.896
Kits 0.0 0.0 427.8 Telescopic Arms 0.0 0.0 14.50	Structure	Structure	148.6	1433	744.0
Telescopic Arms 0.0 0.0 14.50	DPS	Whipple Shields	12.91	566.9	254.6
		Kits	0.0	0.0	427.8
Deorbit Kits Electrostatic Pads 0.0 0.805		Telescopic Arms	0.0	0.0	14.50
	Deorbit Kits	Electrostatic Pads	0.0	0.0	0.805

Continues in the next page

Subsystem	Component	SCST [kg]	SCMT [kg]	SCMK [kg]
	Telescopic Arms Motors	0.0	0.0	5.500
	Switches	0.0	0.0	0.250
Dry Mass [kg]		495.9	4782	2482
Total Mass [kg]		1232	37,630	12,338
Orbital Maneuvers' Δv [km/s]		0.212	5.443	5.020
Lifet	ime before Disposal [dd]	0	721	866

The final dimensions of the satellites are contained in Table 5.4, while Table 5.5 shows the power consumption of the components included during the sizing process.

Table 5.4: Satellites' Dimensions

	SCST [m]	SCMT [m]	SCMK [m]
Satellite's Length	2.285	8.101	5.424
Satellite's Radius	0.627	1.572	1.053
Solar Array Short Side	1.652	2.179	1.823
Solar Array Long Side	3.304	4.358	3.646

Table 5.5: Power Consumption

Subsystem	Component	SCST [W]	SCMT [W]	SCMK [W]
	Omnidirectional Antenna	2.3	2.3	2.3
	Directional Antenna Feed	5.0	5.0	5.0
	Gimbal	10	10	10
ComSys	MODEM	90	90	90
	Filters	1.2	1.2	1.2
	Transponder	10	10	10
	Diplexer	2.0	2.0	2.0
DHS	OBC	2.0	2.0	2.0
DockSys	Camera	15	15	15
Docksys	Telescopic Arm Motor	10	10	10
ODCS	Thruster	45	45	45
ODCS	Valves	150	150	150
	Thrusters	576	576	576
ADCS	Star Tracker	4.0	4.0	4.0
	CMGs	90	90	90
EPS	Gimbals	10	10	10
EFS	Switches	0.8	0.8	0.8

Continues in the next page

Subsystem	Component	SCST [W]	SCMT [W]	SCMK [W]
TCS	Heaters	268.3	1232.3	541.3
105	Pump and Accumulator	16.5	22.0	18.1
Deorbit Kits	Telescopic Arms Motors	0.0	0.0	10
Deorbit Kits	Switches	0.0	0.0	0.1
	Losses	172.5	300.4	210.0
	Total	1480.6	2578.0	1802.8

To determine the Δv for collision avoidance maneuvers and the necessity of a DPS, ESA-DRAMA has been used, as described in Section 4.1. Some methodological differences have been applied during the study:

- SCST: only the deorbit phase has been considered, assuming the satellite to be launched to the desired final orbit and to be docked to the debris during the entire disposal phase; since five SCST spacecraft are launched, the worst case scenario has been considered (ENVISAT, since it has the highest cross section among the selected debris and its orbit shows the highest value of collision avoidance Δv).
- SCMT: two different phases have been analysed, whose required Δv are then summed. The first phase is coasting between the debris while maneuvering in space: to be conservative, the satellite is assumed to lie on the ENVISAT orbit, which represents the most critical one; the second phase is the deorbit, where the final orbit of the last debris targeted is considered while the SCMT spacecraft is still docked to the object.
- SCMK: like SCMT, two phases are considered. The first one is the coasting and maneuvering phase while the satellite is targeting each debris; the second phase is the deorbit, which in this case does not consider the spacecraft to be docked with the last debris. The first phase develops on the ENVISAT orbit as well, while the second one on the selected deorbit path.

In all three architectures, the models used on ESA-DRAMA are considered to have a fixed attitude if the spacecraft is either docked to the debris or it is alone. The starting date for the simulations is considered to be Jan 1st 2030, while other dates are obtained from the sizing process (Section 4.2). Regarding cross-section evaluations, the debris and the satellites are considered to be docked on the line connecting the centres of mass of the two objects, which also represents the direction of motion of the system, as shown in Figure A.2.

Table 5.6 shows the data collected from ESA-DRAMA regarding collision avoidance maneuvers and DPS analyses.

Table 5.6: ESA-DRAMA Results

	SCST	SCMT	SCMK
Disposal Time	103 dd	123 dd	179 dd
Δv Collision Avoidance	$1.164 \mathrm{m/s}$	1.875 m/s	$0.063 \mathrm{\ m/s}$
Whipple Shield Projectile Diameter	0.4 cm	$1.0~\mathrm{cm}$	1.0 cm
Probability of Penetration	$<7 \cdot 10^{-5}$	$< 9 \cdot 10^{-4}$	$< 1.8 \cdot 10^{-7}$
Probability of Catastrophic Collisions	0	0	0

Regarding SCMK, the mass and power breakdown of the selected deorbit kit is presented in Table 5.7; the overall volume measures $2.495 \cdot 10^{-2}$ m³, assumed to be a cube.

Table 5.7: Deorbit Kit Mass Breakdown

Component	Mass [kg]	Power [W]
Deployment	$1.92 \cdot 10^{-2}$	_
Electron Emitter	_	3.8
Battery	$5.28 \cdot 10^{-2}$	_
MLIs	$1.23 \cdot 10^{-4}$	_
Solar Arrays	0.166	_
Omnidirectional Antenna	0.230	2.3
Tether	40.50	_
Electrostatic Pads	0.128	_
Structure	17.59	_
End mass	26.88	_
Total	85.57	6.1

The time required by the kit to deorbit the debris is shown in Figure 5.2, comparing different tether lengths. Due to its lower mass and acceptable time to deorbit the selected targets, the 10 km long wire has been chosen. Despite the deorbit time of the fourth target exceeds the year, if such a mission in launched annually the number of debris removed per year on the long run would still be five.

Table 5.8 shows the order of the debris docked and removed by the SCMT and SCMK architectures, containing the approximated dates of the rendezvous events.

Table 5.8: Order and Dates of Rendezvous with Debris for Multiple Target Missions

N.	SCMT	SCMK
1	2030-01-01 (Zenit-2, 28353)	2030-01-01 (Zenit-2, 28353)
2	2030-06-13 (Zenit-2, 31793)	2030-10-01 (Zenit-2, 31793)
3	2030-12-25 (Zenit-2, 26070)	2031-07-02 (Zenit-2, 26070)
4	2031-03-23 (Zenit-2, 27006)	2031-08-17 (ENVISAT, 27386)
5	2031-12-22 (ENVISAT, 27386)	2032-05-17 (Zenit-2, 27006)

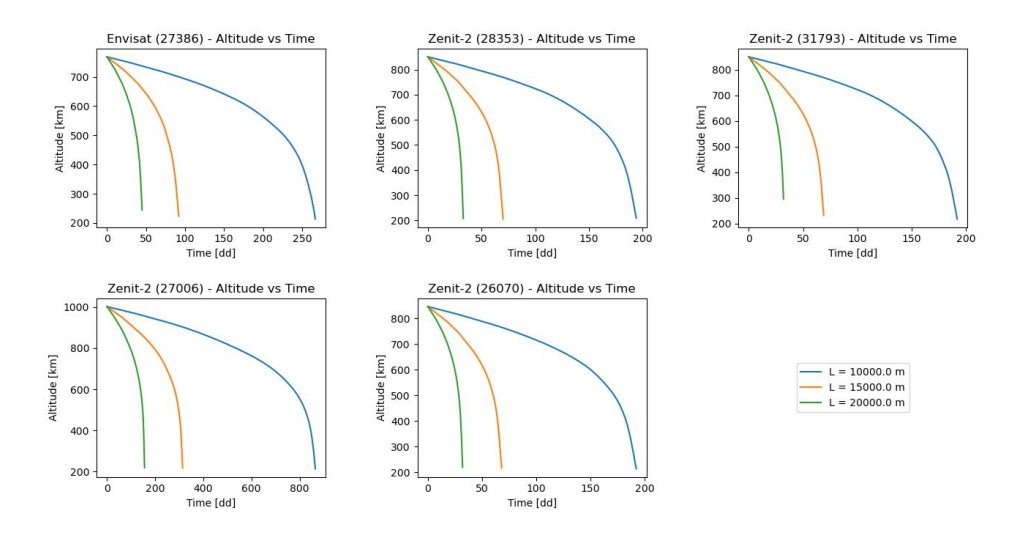


Figure 5.2: Deorbit Time required by different Tether's Lengths to Deorbit the Selected Debris

5.2.1 Program Validation

The results obtained from the sizing program, whose logic and development is shown in Section 4.2.4, have been validated through both benchmark analysis, by comparing them with flown spacecraft with similar architectures and mission objectives (taken from [256]), and sensitivity analysis, changing some input quantities and studying the final mass breakdown variation. Tables 5.9 and 5.10 show the comparison (in subsystems' mass and power percentage) of the sized SCMK architecture with some examples from [256, 264]; SCMK is compared since it is the only architecture to have a proper payload (the deorbit kits) allowing for a more accurate analysis.

Table 5.9: Benchmark Mass Analysis of the SCMK Architecture with Flown Spacecraft; all Percentages are referred to the Dry Mass of the Spacecraft. The "Other" Category [256] is Excluded

Subsystem	HEO	Planetary	Triana	Cassini	\mathbf{SCMK}
Payload [%]	32	15	18	27	18.58
EPS [%]	17	21	5	14	2.58
TCS [%]	4	6	2	3	4.27
DHS+ComSys [%]	4	7	3	11	0.87
Structure [%]	24	25	24	14	29.97 + 10.26 DPS
ODCS [%]	7	13	30	19	31.19
ADCS [%]	6	6	8	6	5.42
(Wet - Dry) [%]	72 ^a	110 ^a	419.1 ^b	259	397.01

^a No kick stage considered.

^b Kick stage included.

Table 5.10: Benchmark Power Analysis of the SCMK Architecture with Flown Spacecraft. The "Other" Category [256] is Excluded

Subsystem	HEO	Planetary	TDRS-7	NEAR	SCMK
Payload [%]	35	22	54	11	1.95
EPS [%]	7 ^a	10 ^a	1	1	$0.60 + 11.65^{a}$
TCS [%]	14	15	29	18	31.03
DHS+ComSys [%]	16	18	4	17	6.80
ADCS+ODCS [%]	18	23	13	53	47.98

^a Harness losses included.

Regarding the mass benchmark analysis, the satellite shares some important similarities with both HEO and planetary spacecraft categories, such as the payload mass, the TCS, the structure and the ADCS; some other categories are similar to flown spacecraft instead, such as the ODCS and the EPS (closer to Triana, which is a HEO Earth observation satellite). Other subsystems' percentages are also comparable with the Cassini mission, such as ODCS, ADCS and TCS. Lastly, the propellant mass fraction (reported as "wet - dry" to consider eventual kick stages) fits between both Triana and Cassini's values. The mass budget benchmark analysis shows that the sized SCMK architecture fits between both HEO and planetary mission categories: this fact can be justified by the high Δv required for orbital maneuvers. Moreover, some subsystems have a lower mass fraction than the analysed case (DHS, ComSys, EPS); this can be due to the proximity to the Earth and the absence of big data to handle and transmit to the Ground Segment, allowing for lighter OBCs and antennae, as well as the low power consumption required by the payload to be operative.

The power benchmark analysis shows again some similarities with both HEO and plane-tary spacecraft, like the EPS power which fits well between both cases, either considering or not the harness losses. Some other subsystems can be successfully compared to flown spacecraft as well, such as TCS, DHS and ComSys (closer to TDRS-7, a LEO communication satellite), while NEAR (a robotic space probe) shares some similarities in terms of ADCS and ODCS. The power required by the payload is not comparable with any of these categories, since the kits do not require direct power supply from the satellite, but they are just applied on the target and get their own energy instead. The power benchmark analysis shows that the SCMK architecture fits between the data of both HEO and planetary spacecraft.

The sensitivity analysis has been performed by changing three input quantities: the overall Δv of the mission, the mass of the payload (deorbit kits) and the power required by the payload (robotic arm); the mass and power budgets' variation of the system are then plotted.

Regarding Δv , Figure 5.3 shows the variation of mass (in both linear and logarithmic scales) and power breakdown among the subsystems.

The ODCS is the one increasing the most its mass (since it contains the propellant), by following a predicted exponential growth due to the Tsiolkovsky's equation implemented. Other subsystems increase their masses as well, such as the structure, the DPS, the TCS, the ADCS and the EPS: the ADCS, TCS and EPS masses increase is justified by the

valves, which are proportional to the dry mass of both ADCS and ODCS; as a consequence, the power required by the TCS increases as well.

Figure 5.4 shows the mass and power variation due to the increased payload.

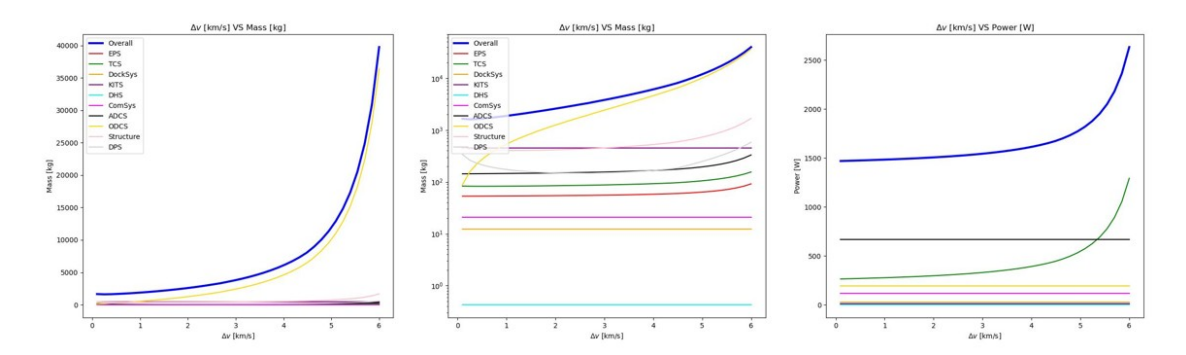


Figure 5.3: Plot of the Mass and Power Breakdown by Varying the Input Δv

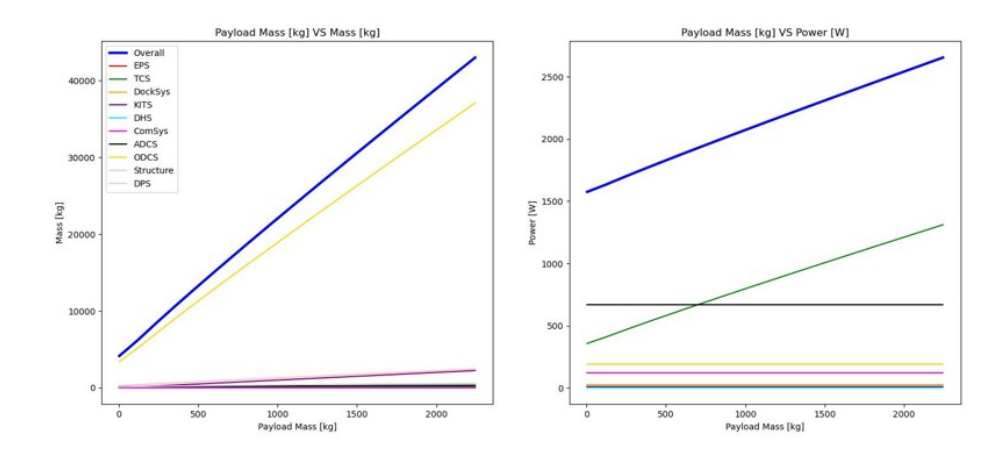


Figure 5.4: Plot of the Mass and Power Breakdown by Varying the Input Payload Mass

The overall mass increase follows an almost linear growth, which is coherent with the results proposed by [264] for LEO satellites. The TCS power shows the same trend, due to the valves' increase in the ADCS and ODCS mass budget.

In Figure 5.5 is reported the mass and power variation due to the increased power request by the payload. The increased power causes an increase in the EPS and in related subsystems' masses, rising the overall mass of the satellite. The power budget shows a curious decrease in the TCS: this phenomenon is due to the dissipations; the increase in the payload power causes more losses, that release heat which is used to warm up some components, decreasing the power required by the heaters (as explained in Appendix A). Lastly, the program simulating the deorbit of the debris using the kits has been validated as well: by neglecting the atmospheric drag (as in [46]), the plots showing the variation of the altitude in time (Figure 5.2) are similar and comparable to the ones presented in [46], validating the method used.

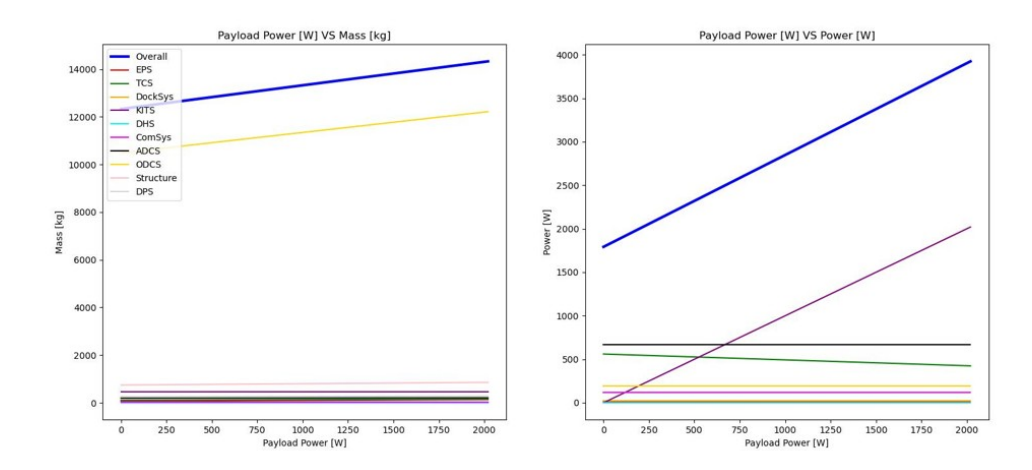


Figure 5.5: Plot of the Mass and Power Breakdown by Varying the Input Payload Power

5.2.2 Trade-Offs

During the subsystems' selection and data gathering phase, different options regarding possible design solutions have been analysed: in this Section, some results about those alternatives are presented, justifying the choices made during the sizing process.

Antenna Selection: The selected directional antenna is equipped with a parabolic reflector and a conical horn feed, resulting in an overall 1.1 kg mass, 5 W power consumption and 24.02 dBi gain. The same gain and power consumption can be obtained by an array of 6×6 patch antennas (7.5 dBi gain each) [73]: however, its thickness [265] and material [73] only allow for a 4.12 kg solution (excluding the dielectric mass). A single patch antenna is even worse, requiring up to 224 W and consequently increasing the EPS mass [73]. Another alternative are helix antennae: by considering an efficiency equal to one (assuming gain and directivity to share the same value), a single helix antenna would be 2.24 m long to achieve 24.02 dBi and 5 W power consumption [73, 266]. If nine helix antennae are implemented instead (3×3 array), the overall mass still exceeds the parabolic reflector's one (assuming an aluminium substrate to link the helixes together). Table 5.11 resumes the data regarding the directive antenna's selection.

	Power [W]	Gain [dBi]	$\mathbf{Mass}\;[\mathrm{kg}]$	Length [m]
Parabolic Antenna	5	24.02	1.1	_
Patch Antenna 6×6	5	24.02	4.115 + dielectric	_
Single Patch Antenna	224	7.5	Increase in EPS	_
Single Helix Antenna	5	24.02	_	2.24
Helix Antenna 3×3	5	24.02	1.27	0.25

Table 5.11: Trade-Off for the Directional Antenna Selection

Propulsion System: During the sizing process, electric propulsion has been considered as well: a 2.95 kg, 500 W electric thruster was tested in the program, ejecting xenon with a specific impulse of 1600 s [267]. Since no multi-phase thermal control system is implemented due to the lack of data, xenon is stored in a high-pressure gaseous form instead of a liquid one. The program, due to the considerable Δv required by the mission, does not converge, since the increase in the mass of the tank is not balanced by a reasonable amount of propellant to accelerate it (gaseous xenon's density is not high enough). Moreover, if electric propulsion is selected, the time required to perform the maneuvers would not be negligible, resulting in a much longer mission duration, which becomes impractical if the debris is tracked a little time before the mission's launch. Lastly, the approaching phase before the rendezvous and docking sequence would be difficult as well, since electric thrusters are not reactive enough to guarantee the success of corrective maneuvers performed in a short interval of time. For these reasons, a far more reactive chemical propulsion system has been chosen for the final satellites' architecture.

Electrical Power System: Regarding the EPS, trade-offs have been made on both the batteries and solar arrays selection. Among the possible batteries materials [113], lithium-ions-manganese batteries are selected, since they do not require maintenance, they have a low recharge time and low toxicity as well, making them suitable for an atmospheric re-entry. Table 5.12 resumes the main properties of different battery architectures.

Recharge Time Toxicity **Energy Density** Maintenance Li-ion-Mn 100-135 Wh/kg< 1 h No Low Li-ion-P 90-120 Wh/kg< 1 hNo Low Li-ion-Co 150-190 Wh/kg 1.5-3 h No Low Ni-metal hydride 60-120 Wh/kg 2-4 h Yes Low

Table 5.12: Trade-Off for the Battery Selection

Regarding the solar arrays' material, they are made of gallium arsenide (GaAs), since more efficient than traditional silicon panels.

Disposal Method: Since different disposal methods do exist, some of them have been analysed to determine which one is the most convenient to adopt. First, the alternative between the deorbit and the graveyard orbit is explored. By using the equations contained in Section 4.2.1, the required Δv for both cases is computed, and the satellites are then sized. The results are contained in Table 5.13.

Table 5.13: Trade-Off for the Disposal Method Selection

	Perigee	Apogee	SCST	SCMT	SCMK
Deorbit	200 km	_	1232 kg	37,630 kg	12,338 kg
Graveyard Orbit	2000 km	2100 km	1460 kg	54,337 kg	12,938 kg

It is evident how the graveyard orbit disposal is more expensive in terms of mass than the atmospheric re-entry in all three architectures; moreover, if a deorbit is not performed, the satellite would remain in space, becoming a debris and posing potential risks to future space missions.

Other than the disposal technique, also different technologies allowing for a deorbit have been compared for the SCMK architecture: the burn to disposal and the use of an own deorbit kit. Results for both cases are shown in Table 5.14.

Table 5.14: Trade-Off for the Deorbit Technology Selection

	Wet Mass	Dry Mass	Volume	Deorbit Time
Burn to Disposal	12,338 kg	2482.4 kg	18.91 m^3	179 dd
Own Deorbit Kit	11,502 kg	2468.6 kg	17.34 m^3	$\sim 250 \mathrm{dd}$

The own deorbit kit seems advantageous due to its lower mass, however some considerations are necessary. First, the greatest majority of the costs are allocated for the development and production of the satellite (see Section 5.5), which are referred to its dry mass, and whose difference is less than 15 kg; second, the electrodynamic tether doesn't allow for a controlled atmospheric re-entry if necessary, which can be guaranteed by using the propulsion system of the spacecraft instead (see Section 5.6). Lastly, the probability of success of the disposal maneuver would depend on the deployment of the tether, which is more difficult to estimate than the success rate of the selected engine. For these reasons, the disposal by using a deorbit kit has been discarded in the final SCMK architecture.

Satellite's Shape: The final shape of the satellite has also been investigated, to find a solution capable of the highest internal volume with the lowest exposed surface; the necessity of a compromise becomes evident while discussing the DPS, since a higher surface means a higher Whipple shield mass to be implemented. Two different shapes are analysed, the cube and the cylinder, and the overall mass comparison is reported in Table 5.15 for all three analysed architectures.

Table 5.15: Trade-Off for the Satellite's Shape Selection

	SCST	\mathbf{SCMT}	SCMK
Cylinder	1232.0 kg	37,630 kg	12,338 kg
Cube	1249.4 kg	106,927 kg	$36,\!306~\mathrm{kg}$

The cylindrical shape is modelled by following the methodology presented in Section 4.2.2, while the cubic shape is modelled by using as the main diagonal the sum of the

two bigger diameters among the tanks and vessel, adding an extra radius of the smallest one out of the three: this way, all three spherical tanks can fit inside the cubic shape in an efficient way. From the analysis it is evident how the cubic shape is worse than the cylindrical one, due to the higher external surface and, consequently, the higher DPS' mass.

5.3 Launch Solutions

By following the methodology presented in Section 4.3, Table 5.16 shows the possible launcher solutions found for the sized satellites: given their dimensions from Table 5.4, all of them fit inside the fairing of the selected launch vehicles.

	Launcher	Max PL at orbit [168]	$ m m_{sat}/m_{PL,max}$	Target ID				
	No Internal Ride-share							
SCST-1	Falcon 9	1427 kg	0.8633	27386				
SCST-2	Falcon 9	12,972 kg	0.0948	28353				
SCST-3	Falcon 9	12,990 kg	0.0948	31793				
SCST-4	Falcon 9	1633 kg	0.7544	27006				
SCST-5	Falcon 9	12,990 kg	0.0948	26070				
SCMT	Falcon H.	37,927 kg	0.9922	28353				
SCMK	Falcon 9	12,972 kg	0.9511	28353				
		SCST Internal Ride-s	share					
SCST-1	Falcon 9	1427 kg	0.8633	27386				
SCST-2	Falcon 9	12,972 kg	0.0948	28353				
SCST-3	Falcon H.	4440 kg ^a	0.5550^{a}	31793				
SCST-4	raicon II.	4440 Kg	0.0000	27006				
SCST-5	Falcon 9	12,990 kg	0.0948	26070				

Table 5.16: Launcher Solutions Table

It is worth noting that the selected solutions are not the only ones capable of launching the ADR satellites to the desired final orbit; also Ariane 6, Vulcan Centaur and SLS would be able of launching at least the SCST architecture at the desired final orbit, while Vulcan Centaur and SLS would even be capable of an internal ride-share program with two SCST satellites. However, Falcon 9 and Falcon Heavy have been selected instead due to their high availability (Table 4.1), which is prioritized over the other launchers' features, as previously discussed in Section 4.3. In all the analysed cases, no more than two targets could be reached by using one single launcher in an internal ride-share program. The SCMT and SCMK architectures are considered to be injected in the orbit of the first debris to dock with, as from Table 5.8.

Another consideration regarding Falcon 9 and Falcon Heavy can be done: these two

^a By using the approach described in Section 4.3.

launchers can in fact be reused, since retrievable. Injections by using recoverable launchers have been simulated as well, however they are discarded from the final solutions, since the retrievable version of Falcon 9 can only be applied to the lower inclination orbits (not reaching the two targets at the highest inclinations), and the launchers that can successfully bring the spacecraft to the desired position are affected by a strongly reduced maximum payload [168], meaning more emissions and costs to be allocated to the ADR satellites. Moreover, the costs published in the launcher's guidelines are only referred to their fully expendable versions, making it difficult to estimate the true cost effectiveness of the mission.

From the following section onwards, the term ride-share will refer to internal ride-share only if not specified, while no ride-share will exclude internal ride-shares but still consider external ones.

5.4 LCA Results

The impacts of the three mission architectures, also considering the different launch methods listed in Table 5.16, are now reported; this time, the SCST voices refer to the whole ADR program, considering all five satellites to be launched. Figure 5.6 shows the overall environmental footprint of the analysed missions. It is evident how the most impacting

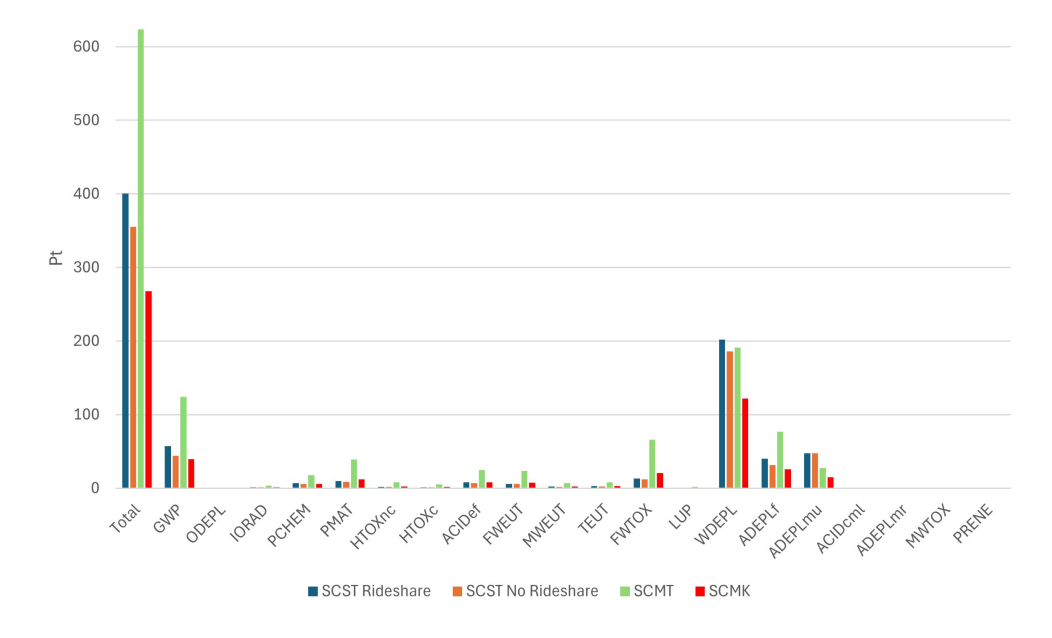


Figure 5.6: Overall Environmental Impact for the Analysed Architectures and Launch Combinations

architecture is SCMT, primarily due to its higher mass, while the SCMK architecture globally results the least impacting one. The categories with the highest scores are the

Global Warming Potential GWP, the water depletion (WDEPL), the fossil fuels consumption (ADEPLf) and the material (minerals and metals) use (ADEPLmu), meaning that the missions impact more on the natural resources consumption rather than on human health toxicity (which is defined by the categories HTOXnc for non-carcinogenic emissions and HTOXc for carcinogenic ones). The following analysis shows the environmental hotspots and the emission allocations per-phase, which are resumed in Figure 5.7.

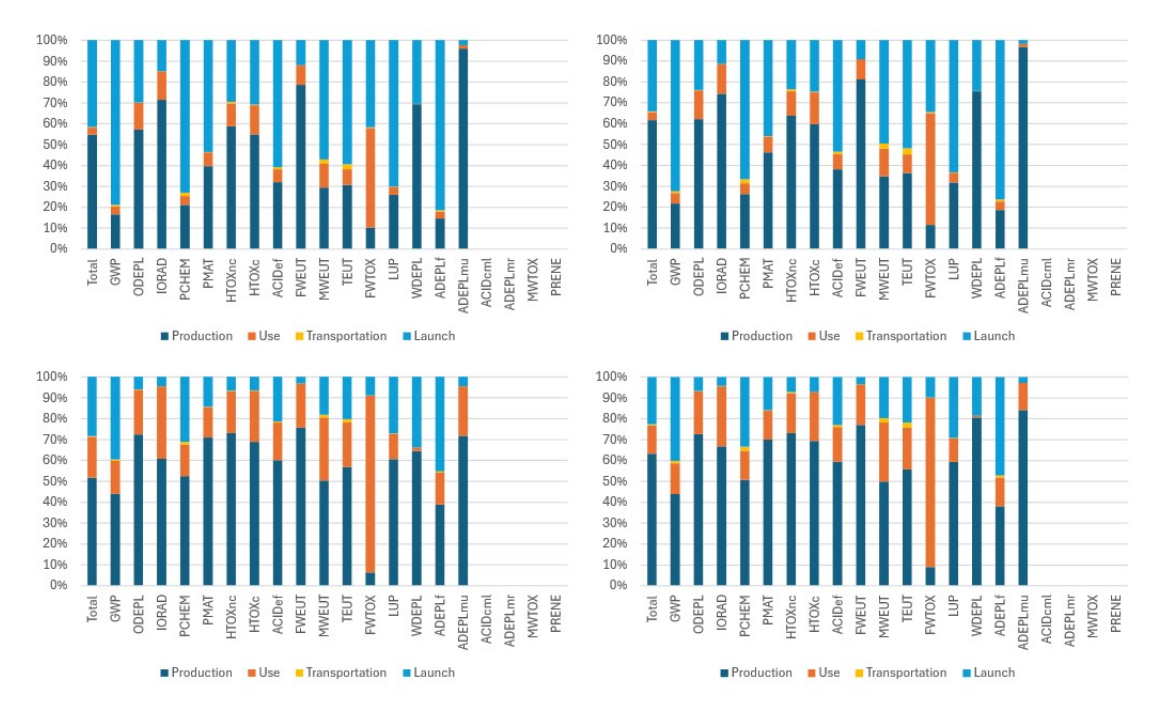


Figure 5.7: Emission Allocation Per-Phase for SCST with Rideshare (top left), SCST without Rideshare (top right), SCMT (bottom left) and SCMK (bottom right)

From Figure 5.8 it is possible to notice how the production of five SCST satellites impacts more than one single SCMK assembly due to its lower overall dry mass, while the SCMT architecture still results to be the one with the largest ecological footprint. However, the SCST satellites represent the solution with the highest overall resource consumption (water, minerals and metals), which is primarily due to the higher dry mass over wet mass ratio.

The comparison of the use phases of the satellites only is shown in Figure 5.9. This time, the most affected impact category is the freshwater ecotoxicity (FWTOX) caused by the propellant production (hydrazine and nitrogen tetroxide): the architecture with the highest amount of required propellant is the SCMT, followed by SCMK and, lastly, by the five SCST satellites, reflecting the previously discussed emissions' trend and Δv need.

Figure 5.10 shows the air transportation impacts. Since this process is scaled on the dry mass of the satellites, SCST and SCMK show a similar environmental footprint, due to the comparable value of the masses (considering all five SCST satellites and only one

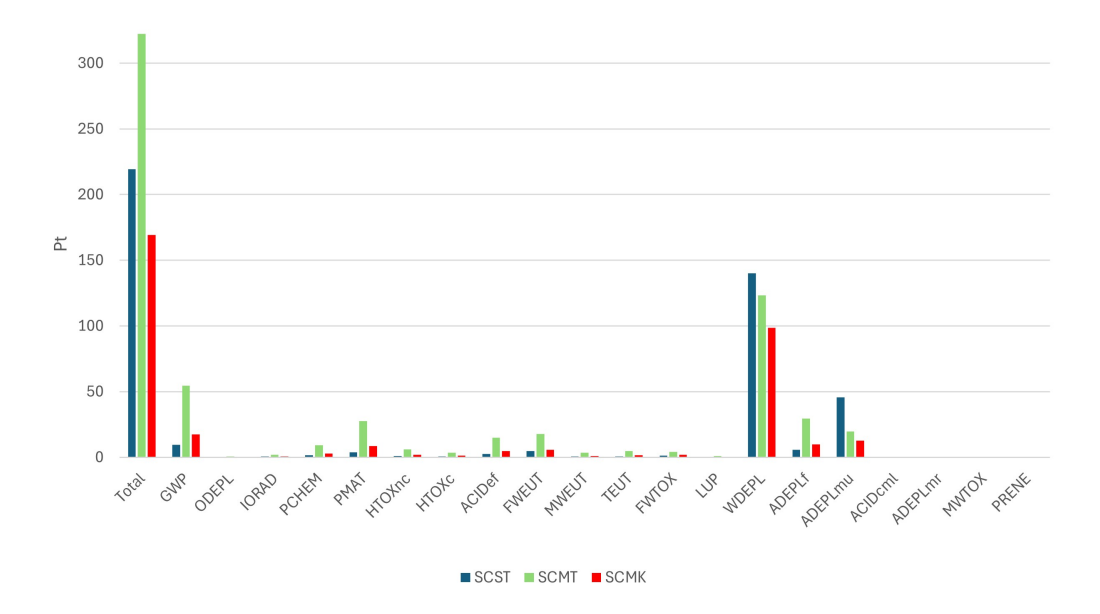


Figure 5.8: Production's Environmental Impact for the Analysed Architectures

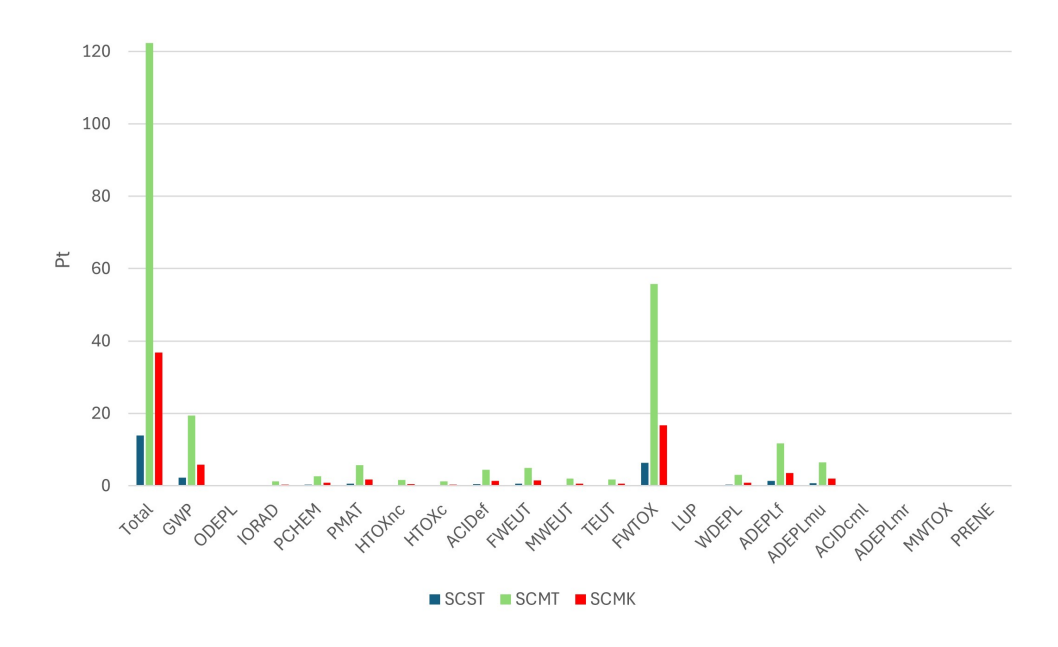


Figure 5.9: Satellites' Use Environmental Impact for the Analysed Architectures

SCMK). The most affected categories are GWP and fossil fuels consumption (ADEPLf), which are directly related to the plane's emissions.

The last comparison in Figure 5.11 reports the different environmental impact of the launch phase. From the solutions shown in Table 5.16 it becomes evident how the SCST

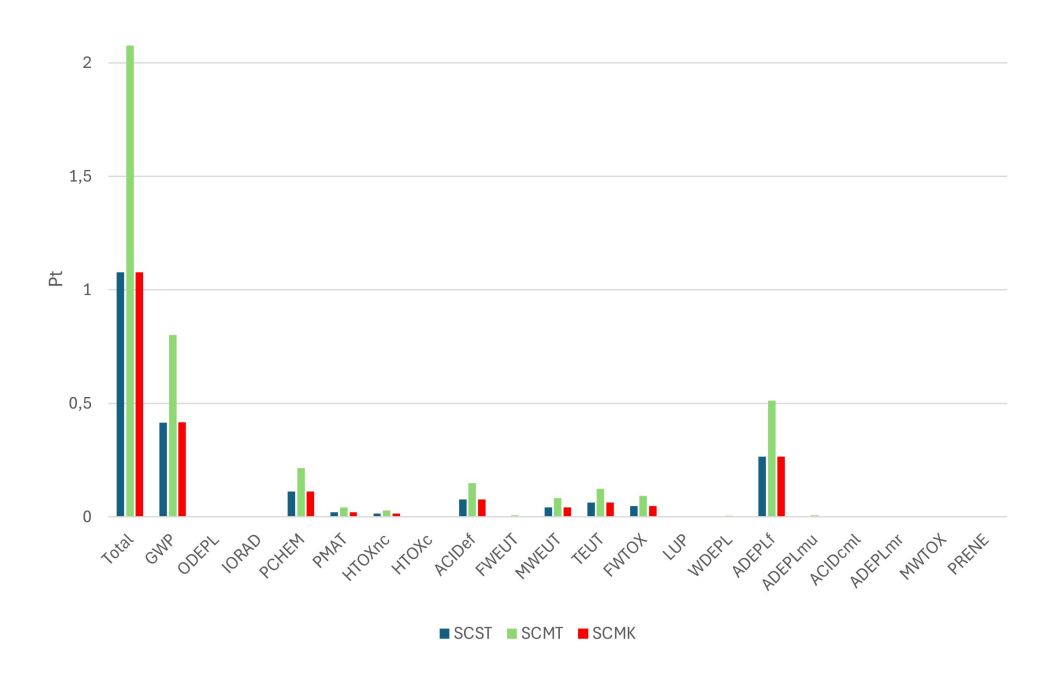


Figure 5.10: Transport Environmental Impact for the Analysed Architectures

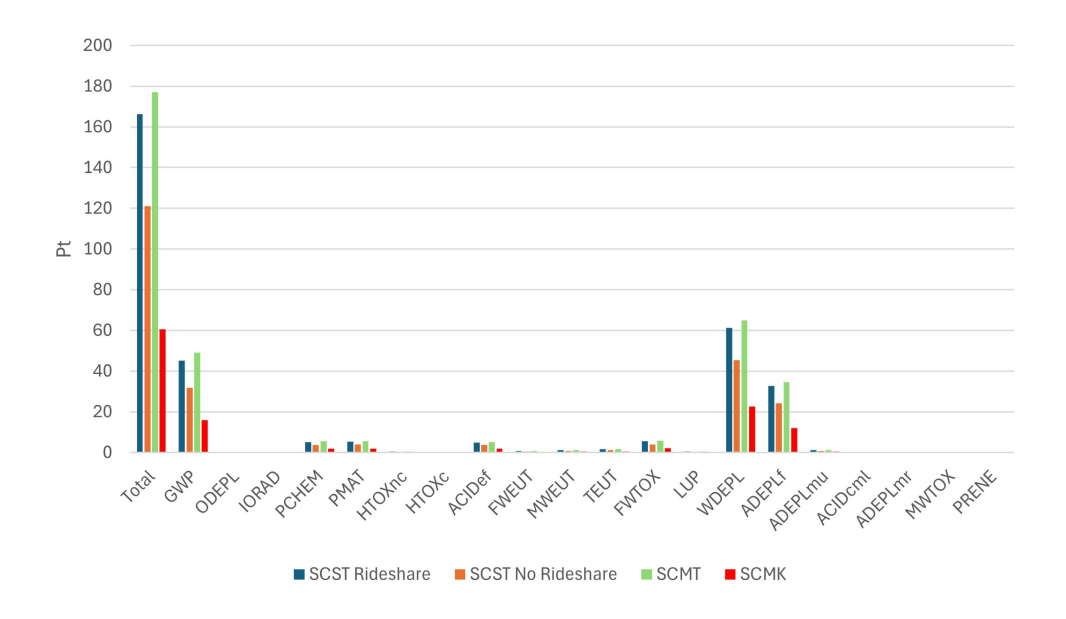


Figure 5.11: Launch Environmental Impact for the Analysed Architectures and Launch Combinations

ride-share option is far more impacting than the non-ride-share one, since only two satellites can be injected by a Falcon Heavy at once, being worse than two different Falcon

9. Also in this case, the SCMK mission architecture is the least impacting one, since it only requires one Falcon 9. It is worth noting that the launch event represents a major portion of the overall emissions (see Figure 5.6), meaning that its environmental impact cannot be neglected; consequently, finding ecologically valid launch alternatives becomes crucial if the mission aims at overall low emissions and materials consumption.

The most impacting mission phases with respect to the overall environmental footprint are production and launch, meaning that lighter solutions are preferred, as well as the ones occupying only a small fraction of the payload capability of the selected launch vehicle. The use phase of the satellite becomes negligible only if a small amount of propellant is involved (SCST case), while it shall be considered in the SCMT and SCMK architectures, due to the high Δv required by the orbital maneuvers. In all three cases, the transportation phase can be neglected due to its low score with respect to the overall value.

Regarding the satellite's production, Figures 5.12, 5.13 and 5.14 show the impact allocation upon the different subsystems included in the architectures. From Figure 5.12 it is

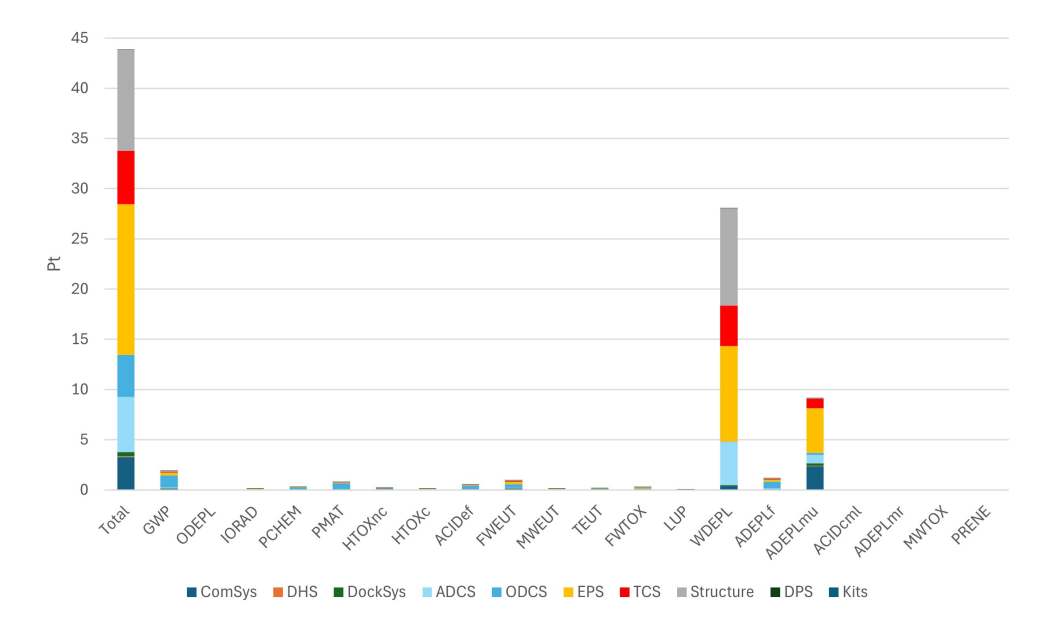


Figure 5.12: Production Environmental Impact for a SCST Satellite

evident how the EPS is the most impacting subsystem in low Δv applications, followed by the structure (whose mass is proportional to the dry mass of the satellite), the TCS and the attitude and orbit control systems. ComSys, DockSys and DHS have an overall lower impact, due to their lower masses. Water, metals and minerals depletion (WDEPL and ADEPLmu) are the most affected categories. On the other hand, Figure 5.13 shows how impacting the ODCS is in high Δv architectures: more than a half of the global single score is allocated to the orbit control system, which mainly impacts on global warming (GWP), particulate matter (PMAT), acidification (ACIDef), fresh water eutrophication (FWEUT) and fossil fuels consumption (ADEPLf). Lastly, from Figure 5.14 it is possible to measure the footprint of the deorbit kits, mainly acting on water depletion (WDEPL).

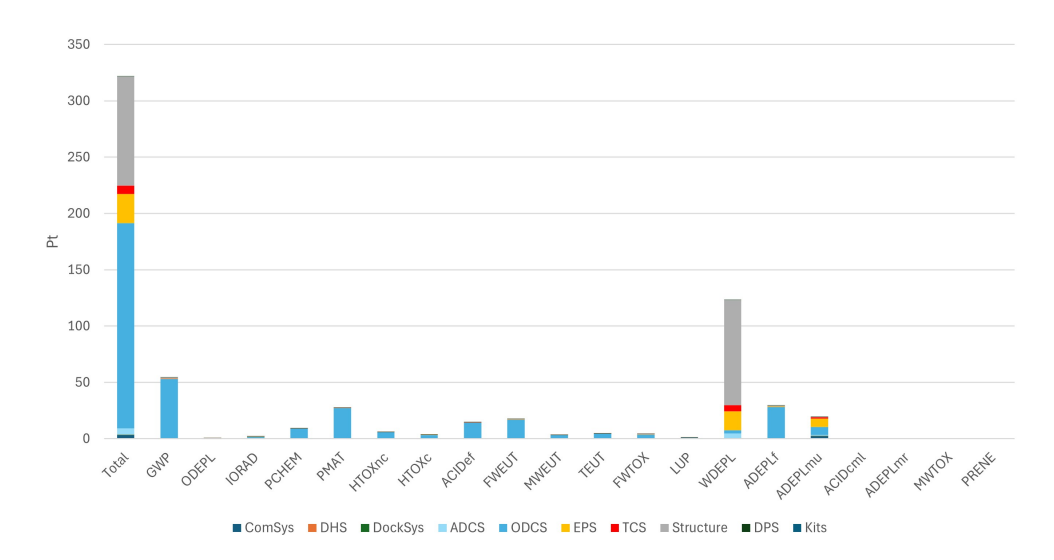


Figure 5.13: Production Environmental Impact for a SCMT Satellite

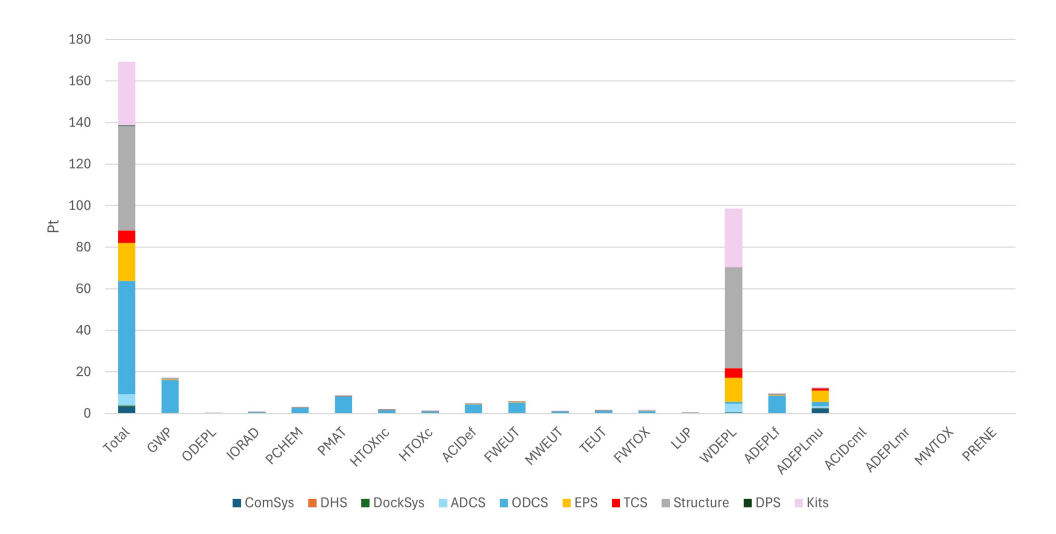


Figure 5.14: Production Environmental Impact for a SCMK Satellite

The comparison shows how the EPS and the TCS' impact is similar among the different ADR architectures, due to their close masses (see Table 5.3), while the structure maintains a similar percentage of the overall score. Also, the subsystem whose impact varies the most is the ODCS: its footprint strongly depends on the size of the tanks involved, meaning a higher impact the higher the required Δv is. In particular, it is possible to identify the tanks and the valves as the most impacting items inside the ODCS in high Δv architectures, since all the other components of the subsystem share the same masses among the three analysed concepts: the identified root cause of the high ecological footprint are the machining processes involved in the fabrication of the spherical tanks and vessel, due to the dimensions of the components to manufacture. Lastly, the ComSys,

DHS, DockSys and ADCS share the same score values among the different mission profiles since they are made of the same components. The impact of the DPS can be neglected in all three cases, despite its generally high mass.

Among the three analysed architectures, the EPS and the TCS occupy an important percentage of the overall emissions: the main contributors are the solar arrays for the EPS and the radiator for the TCS; in both the components, the high score value is due to the electrical energy required by the involved processes (directly modelled from [10] for solar arrays, while contained in the aluminium gathering process - "at plant" - for the radiator).

Figure 5.15 shows the impact distribution among the nineteen categories for the kits production (only one kit is here considered). It is possible to notice how the most critical

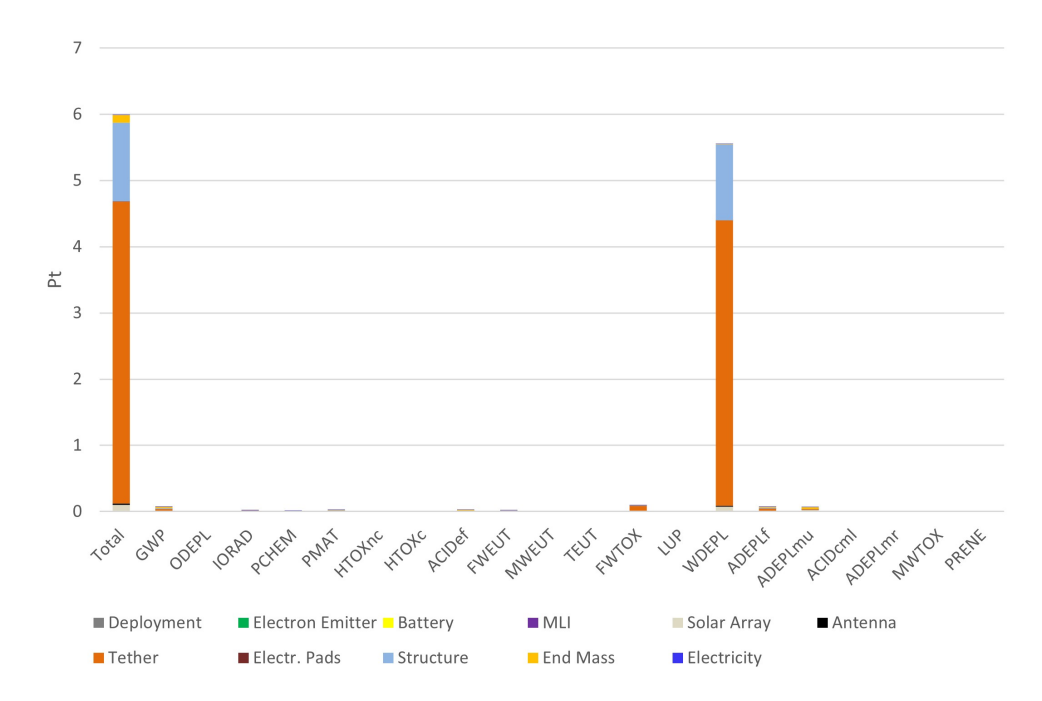


Figure 5.15: Production's Environmental Impact for the Analysed Deorbit Kits

items are the aluminium tether and the structure, meaning that the greater percentage of the single score values obtained for the kits in Figure 5.14 is due to these components. Moreover, the most affected impact category is the water depletion (WDEPL), and further investigations show that its high value is caused by the electrical energy employed in the fabrication of the tether itself, as a sub-process of the selected aluminium gathering procedure ("at plant"), showing how impacting is the aluminium production and collection in space industry.

As shown in Figure 5.15, the impact of the production of a single deorbit kit is only a fraction of the overall SCMK production (from Figure 5.14, the single score of a kit is about 4.3% of the global score of the other subsystems): however, since the mission where these devices are employed is a multiple-target one, five of them are needed and the value associated to them increases up to 17% of the final one, representing a substantial

portion of the total emissions.

5.4.1 End-of-Life and Disposal

When performing the LCA of a space mission, if a cradle-to-grave analysis is carried out, the disposal phase represents the last one to include. Different end-of-life scenarios can be studied, such as the re-orbit into a graveyard orbit or the atmospheric re-entry. However, the environmental impact of such operations is only partially known and represents a limit of the current space sector's LCA; it is indeed difficult to estimate the emissions occurring during the re-entry phase, since the chemistry involved is still largely unknown and only a small fraction of the material reaches the ground to be analysed. However, some studies [2, 15, 16] assess the impact of the chemical reactions involving aluminium and oxygen in extreme conditions, simulating the ablation process happening during the atmospheric re-entry: the results show that the aluminium oxides created can potentially act as an ozone depleting agent, making their environmental impact considerable.

If a graveyard orbit disposal is preferred, other mechanisms shall be considered, such as surfaces and coatings' degradation, that could potentially create new space debris; however, as discussed in Section 4.4.1, an impact category regarding the debris release has not been developed yet. Since no reliable data exists nowadays to correctly estimate and allocate the emissions of the end-of-life and disposal of the spacecraft, this phase has been excluded from the study, representing an important limitation of the LCA of space products.

5.5 LCC Results

By following the methodology presented in Section 4.6, the costs of the ADR missions are now reported. Figure 5.16 shows the overall costs of the different architectures.

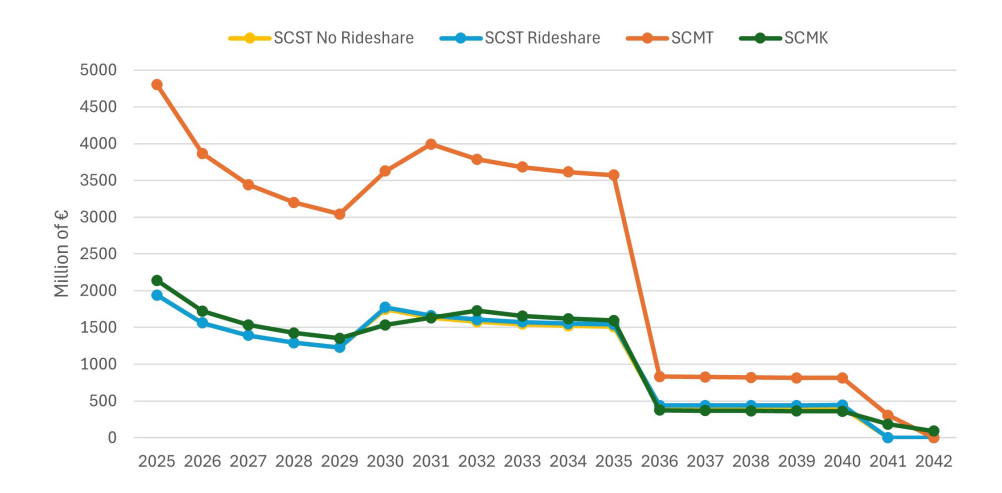


Figure 5.16: Overall Costs Comparison for the Different Architectures and Launch Combinations

The costs have been propagated for eleven satellite's generations, assuming launches from 2030 to 2040; the spacecraft's production costs are allocated from 2025 to 2035, while costs for transportation, propellant and launch events are distributed between 2030 and 2040. The operative costs are allocated between 2030 and 2042, assuming a duration of three and two years for each SCMK and SCMT mission, respectively. It is evident how the SCMT is the most expensive architecture among the selected ones, due to its higher mass (see Figure 5.17), while the different SCST and the SCMK architectures share similar cost profiles during the entire program duration.

In Figure 5.17 the costs related to the production, transportation and launch only are reported, while Figure 5.18 shows the operative expenses.

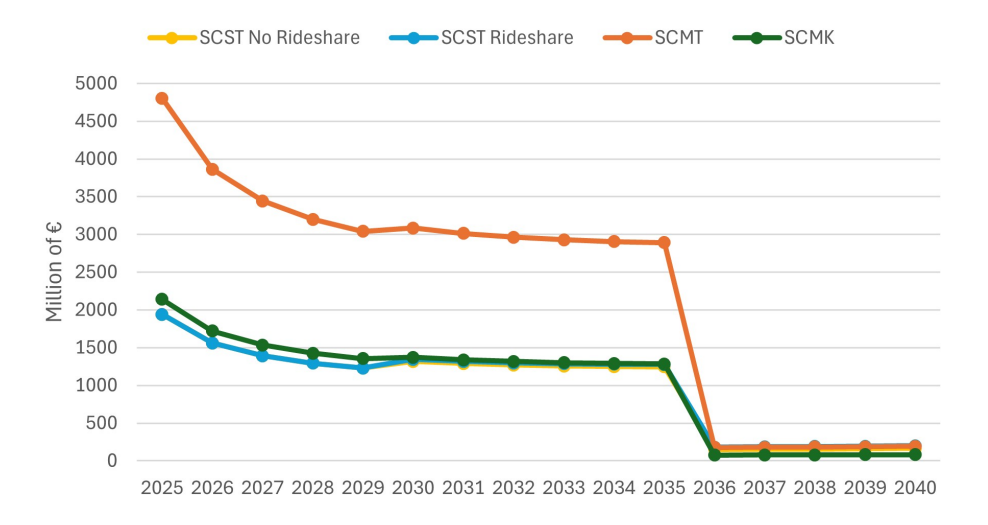


Figure 5.17: Production, Transport and Launch Costs Comparison for the Different Architectures and Launch Combinations

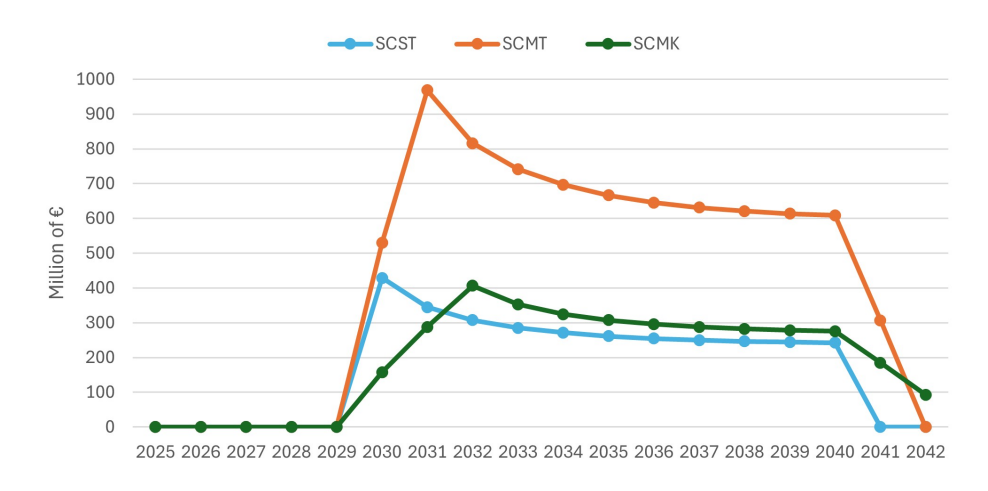


Figure 5.18: Operations Costs Comparison for the Different Architectures

It is worth noting that the production and operations costs decrease in time despite the inflation rate applied: this is caused by the increasing spacecraft generation ("block number") on the AMCM software, which evaluates the costs reduction in time due to the already existing designs developed in the previous years.

Table 5.17 contains the cumulative costs for each analysed mission architecture, dividing them into categories.

Costs in million of €						
	Production	Transport	Launch	Propellant	Operative	Total
SCST No	14,218.4	10.9	1618.7	15.5	3138.2	19,001.7
Rideshare						
SCST	14,218.4	10.9	1955.7	15.5	3138.2	19,338.7
Rideshare						
SCMT	35,163.9	10.9	1894.4	137.6	7846.5	45,053.3
SCMK	15,665.4	10.9	809.4	41.3	3534.2	20,061.2

Table 5.17: LCC Division of the ADR Architectures

Since no revenue is predicted in the short term, it is not appropriate to refer to the Net Present Value of the projects, since they would be all negative. To determine the most cost-effective architecture, the cumulative costs for the simulated ADR programs have been evaluated as in Table 5.17. It is possible to notice how the cheapest program is the SCST without internal ride-share, followed by the internal ride-share option and then by the SCMK, which is still close to the previous two alternatives. Also, from the given breakdown, the transport and propellant's costs are small with respect to production, launch and operations, meaning that they can be neglected without losing the validity of the results obtained.

5.6 Safe Disposal and Requirements Verification

In this Section, the safe disposal of both spacecraft and debris is explored, followed by an overview about the compliance of the requirements for all three selected ADR architectures.

5.6.1 Safe Disposal Verification

To verify the safe dispiosal of both satellites and debris, the SARA module of ESA-DRAMA is used (see Section 4.5). Table 5.18 shows the results of the analysis performed by using the Monte-Carlo method, reporting the mean on-ground casualty risk, the mean impact area, the mean surviving mass and the required re-entry method (C = Controlled, U = Uncontrolled).

Table 5.18: Safe Disposal Results Table

	On-ground risk	$\mathbf{A_{impact}} [\mathrm{m}^2]$	$\mathbf{m_{survive}}$ [kg]	Re-entry
SCST + ENVISAT	$7.929 \cdot 10^{-4}$	68.11	4945	С
(27386)				
SCST + Zenit-2	$3.414 \cdot 10^{-4}$	31.08	519.4	С
(28353)				
SCST + Zenit-2	$2.836 \cdot 10^{-4}$	31.08	520.4	C
(31793)				
SCST + Zenit-2	$1.780 \cdot 10^{-4}$	29.71	513.9	C
(27006)				
SCST + Zenit-2	$6.280 \cdot 10^{-4}$	31.08	520.0	C
(26070)				
Zenit-2 (28353)	$6.188 \cdot 10^{-5}$	5.927	269.4	U
Zenit-2 (31793)	$9.431 \cdot 10^{-5}$	5.927	269.7	U
Zenit-2 (26070)	$9.374 \cdot 10^{-5}$	5.927	269.4	U
Zenit-2 (27006)	$7.285 \cdot 10^{-5}$	5.927	248.9	U
SCMT + ENVISAT	$1.028 \cdot 10^{-3}$	95.85	8735	C
(27386)				
$\overline{\text{Zenit-2 } (28353) + \text{kit}^{\text{a}}}$	$4.878 \cdot 10^{-5}$	7.478	285.3	U
Zenit-2 $(31793) + kit^a$	$3.363 \cdot 10^{-5}$	7.478	285.4	U
Zenit-2 $(26070) + kit^a$	$2.452 \cdot 10^{-5}$	7.478	284.8	U
ENVISAT (27386) +	$3.656 \cdot 10^{-4}$	57.73	2429	C
kit ^a				
Zenit-2 $(27006) + kit^a$	$2.333 \cdot 10^{-5}$	6.046	207.0	U
SCMK	$7.833 \cdot 10^{-4}$	29.32	1567	С

^a Assuming the same trajectory of the controlled deorbit, since no starting orbital elements are available for this option.

From Table 5.18 it is evident how the most critical debris to dispose of is ENVISAT (27386), since the most of it survives the atmospheric re-entry phase, while the Zenit-2 upper stages almost completely burn during the deorbit trajectory, due to their high amount of aluminium (lower melting point).

The first block in Table 5.18 refers to the SCST deorbits; since all of them occur when the satellite is docked to the debris, all the re-entries are guaranteed to be controlled, since the spacecraft engines can be used to modify the trajectory in the last phases of the maneuver. The second block of Table 5.18 refers to the SCMT mission profile; since only one debris deorbits together with the spacecraft, it is the only one performing a controlled re-entry: from the simulations, the last target is ENVISAT (27386), allowing for the controlled disposal of the most critical debris; the other targets all deorbit following an uncontrolled disposal. The last block of Table 5.18 refers to the SCMK architecture; in this case, only the satellite deorbits in a controlled manner, while the targets perform an atmospheric uncontrolled re-entry with the deorbit kits only: however, ENVISAT (27386) (which is marked with the letter "C") would need a controlled re-entry, since the on-ground risk

level exceeds the 10^{-4} threshold.

It is worth noting how SCST and SCMT are the only two architectures allowing for a safe disposal of the debris, being compliant with Requirement 6 from Table 3.2.

A representation of a model implemented on ESA-DRAMA-SARA is shown in Figures 5.19 and 5.20.

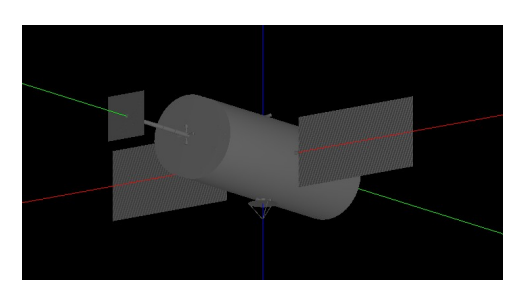


Figure 5.19: Exterior of the SCMK Model Implemented on ESA-DRAMA-SARA

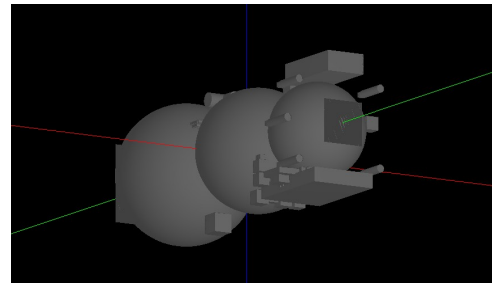


Figure 5.20: Interior of the SCMK Model Implemented on ESA-DRAMA-SARA

5.6.2 Requirements Verification

Once the satellite's structure and subsystems have been sized, it becomes necessary to verify if the solutions are compliant with the previously defined requirements (see Section 3.3). Table 5.19 shows the compliance of each analysed mission architecture with the selected requirements from Table 3.2 (Y = Yes, N = No).

	SCST	SCMT	SCMK
Requirement 1	Y	Y	Y
Requirement 2	Y	Y	Y
Requirement 3	Y	Y	Y
Requirement 4	Y	Y	Y
Requirement 5	Y	Y	Y
Requirement 6	Y	Y	N
Requirement 7	N	N	N

Table 5.19: Requirements Verification Table

Requirements 1, 2 and 3 are automatically verified through the sizing process, since the satellites are designed to be operative in the selected orbit, performing proximity operations and deorbiting the selected debris from Section 5.1. Moreover, the mechanical resistance of the robotic arm used during the docking sequence has already been tested, as explained in Section 4.2.3. Requirement 4 is verified as well, since the dimensions of the spacecraft largely exceed 10 cm, as shown in Table 5.4. Requirement 5 is divided in three sub-requirements; first, the probability of collision for each conjunction with debris

> 1 cm diameter is verified through ESA-DRAMA, finding the Δv for collision avoidance maneuvers which guarantees the imposed risk threshold (see Section 4.1). Second, the cumulative probability of collision with debris between 1 mm and 1 cm diameter is calculated with ESA-DRAMA, and a Whipple shield is implemented if the risk level exceeds 10^{-4} . The third sub-requirement is more difficult to verify, since it strongly depends on the reliability of the components used by the subsystems involved: assuming the success rate of the ODCS engine to be 100% [106], and supposing to extend that value to the ADCS thrusters as well, the probability of accidental collisions during proximity operations shall be minimized; however, more precise evaluations should be made in advanced mission design phases to verify Requirement 5.

Requirement 6 is divided into two parts. The first one concerns the safe disposal of the satellites and the debris, which is verified in Table 5.18: only the SCST and SCMT architectures allow for a safe re-entry of both the debris and the spacecraft, while the SCMK mission profile is compliant only regarding the chaser re-entry. The second part of Requirement 6 states that the probability of success of the disposal maneuver shall be > 0.9: as for Requirement 5, the success of the maneuvers involving the ODCS engine can be verified by using its success rate (which is 100%), while the successful deployment of the electrodynamic tether is more difficult to estimate at this mission design phase, assessing it in future research. Overall, SCST and SCMT are fully compliant with Requirement 6, while SCMK is not.

Table 5.20: Magnitude of the ADR Satellites at the Analysed Altitudes

	200 km	$1013~\mathrm{km}$
SCST	-14.5	-11.0
SCMT	-15.8	-12.3
SCMK	-15.1	-11.6

Lastly, Requirement 7 is verified by using Equation 4.2; two cases are considered, at the altitudes of 200 km (after the beginning of the disposal maneuver) and 1013 km (highest apogee during the entire mission) by considering the exposed surface to be the sum of the rectangular projection of the cylinder's side and the two solar arrays (from Table 5.4). Table 5.20 shows the magnitudes of the satellites in the analysed cases. It is clear how all three architectures are not compliant with Requirement 7 during their entire lifecycle; however, this represents the fully reflective worst case scenario [67], and further studies shall be made to find the reflectivity coefficient of the surfaces, allowing for better results.

5.7 Discussion

After the presentation of the results, it is finally possible to compare the different analysed ADR architectures in a comprehensive way, focusing on each aspect discussed in the document.

First, the different mission concepts have been compared under the environmental point of view: the results in Section 5.4 show how one single SCMK satellite impacts less than all five SCST spacecraft in both possible launch configurations. The SCMT architecture

results to be the most impacting one, with a score which doubles the SCMK's one.

Second, the costs of simulated mission programs have been compared, showing that the SCSTs are slightly more convenient, in both launch configurations, than the SCMK, while the costs of the SCMT are again more than twice the costs of the cheaper architectures. From the previous two analyses, the most appropriate launch configuration for the SCST satellites is the non-ride-share one, which is characterized by both lower costs and environmental impact than the ride-share option.

The last comparison concerns the requirements verification of the different architectures; excluding Requirement 7, only the SCST and SCMT mission architectures are compliant with the Requirements 1 to 6, while the SCMK mission profile does not allow for the safe disposal of all the selected debris (Requirement 6 is then not verified). Requirement 7 is not verified by any proposed mission concept: this is mainly due to the orbital ranges that the missions endure, including low orbits during the deorbit phase, which are unavoidable if the debris is disposed of into the atmosphere; for these reasons, Requirement 7 results to be way too restrictive for ADR missions, whose flight profiles would require less stringent apparent magnitudes values to be respected.

To determine the most appropriate mission architecture to successfully remove the selected debris from the LEO environment, it is necessary to give priority to certain aspects over others. While both SCST and SCMK are comparable in terms of costs and emissions, SCST and SCMT satisfy the same requirements. Supposing to prioritize requirements verification (so, having a reduced on-ground casualty risks and controlled re-entry) over low emissions, the SCST mission concept is the most appropriate one, since it is the cheapest, it is compliant with all the selected debris mitigation requirements and it is characterised by an acceptable emission score. The SCMT mission profile represents a valid alternative, since it complies the same requirements, however it is way more expensive and polluting than SCST. The SCMK architecture results to not be compliant with the safe disposal requirement, making it unsuitable to safely deorbit the selected targets; however, if different and more demisable debris in terms of surviving mass is chosen instead, this would represent a good alternative, due to the overall low cost and the lowest environmental impact among the analysed mission concepts.

One last consideration regarding the funding of the missions is necessary; since the ADR field does not produce a direct income at the moment (and it is difficult to imagine so in the near future, unless the savings for the reduced risk level produced by the lower collision potential are considered), it becomes necessary to understand how to raise enough capital to start a space program in this sector. Since every country capable of launching satellites is directly affected by space debris, a global economic fund for space debris removal could be defined and established to incentive the nations in the ADR field [7]: this method could allow the removal of five debris per-year (or five debris per-program, as for the SCMT and SCMK architectures, considering one launch each year), significantly reducing the risk of collisions in time, only requiring little expense from the involved nations.

Chapter 6

Conclusions

This thesis explored the feasibility of different Active Debris Removal (ADR) mission concepts: one designed to deorbit single targets (SCST), one capable of sequentially deorbiting multiple targets (SCMT) and one suitable for delivering multiple deorbit kits to the targets (SCMK). These concepts were compared in order to define the most suitable for large LEO debris removal, whose selection was made based on existing categorizations (see Section 2.3 and 5.1). A functional analysis has been performed to identify the functions that define ADR missions, and to determine which subsystems are necessary. The subsystems have been sized for all three architectures, and the satellites have been compared under both environmental and economical aspects; the Life Cycle Assessment (LCA) and Life Cycle Cost (LCC) have been performed in order to define the impact and costs of the three concepts, comparing them based on these criteria to determine which one is the least polluting and most cost-effective.

6.1 Achievements

The first achievement of this work was the development of a detailed functional analysis for the already existing concepts under comparison, which was not available in literature before. Some requirements were defined as well, regarding both the mission objectives and the debris mitigations strategies to adopt in the LEO environment.

One of the main goals of the thesis was to verify the feasibility of the studied ADR mission concepts. It has been achieved successfully, since both the compliance of the selected architectures with the chosen requirements and the feasibility of the launch through existing vehicles have been verified.

Moreover, the selected mission architectures have been successfully compared under the environmental and the economic point of view, to determine the cheapest and the least impacting one. The analysis did not include only the satellites' production, but also the launch event and the use phase, representing the first multi-level analysis performed on ADR missions known to the author.

Overall, the results show how single target satellites (SCST) are capable of deorbiting the previously selected debris, also guaranteeing the fulfilment of the debris mitigation requirements and allowing for lower costs and emissions compared to the other concepts considered. Multiple target satellites (SCMT) result in more expensive and environmentally impacting instead, but they are still compliant with the selected debris mitigation requirements. Also, an architecture delivering multiple deorbit kits (SCMK) has been analysed, representing a valid, cheap, and less impacting alternative to SCST; however, the selected debris size and materials do not allow safe disposal by using the sized deorbit kit, making the SCMK architecture suitable only if more demisable targets in terms of surviving mass during re-entry are chosen.

This thesis wanted to summarize different aspects of the design of ADR space missions, comparing different concepts of operations not only based on the mass budget, but also on more socially impacting areas, such as costs and environmental assessment. The results of the work show that different ADR mission concepts are possible, some of them more suitable than others under both the assessment of the selected debris mitigation requirements, and the environmental and economical impact; the study gives new perspectives on the selection of environmentally sustainable and cost effective mission concepts in the ADR field.

6.2 Future Works

This document analysed different aspects of ADR missions, from the definition of the requirements to LCA and LCC, passing through the sizing process and the launcher selection. However, many assumptions have been made, due to the high-level design phase of the missions (a feasibility study, also known as a Pre-Phase A [12]). Some suggestions about future works and recommendations follow, in order to be able to develop more precise analyses regarding the complex ADR field.

Debris Selection: All three mission architectures analysed consider the removal of the same five targets, as explained in Chapter 4; however, debris characterized by different size and lying on different orbits can be chosen instead, allowing for smaller satellites with far more optimized propellant consumption. Future work in this field can consider the selection of different and less critical targets, studying the retrieval of smaller debris.

Concept of Operations (ConOps): Different mission architectures can also be analysed and defined, starting from those discarded in Section 3.2; also, the reusability of satellites can be explored [50]. Moreover, regarding the architectures analysed in this work, more detailed mission timelines can be developed to better understand the sequence of functions that characterize the missions, helping to define in detail the mission phases and leading to more accurate power budgets.

Requirements: More detailed requirements can be developed for both satellites and deorbit kits (where considered). Also, more exhaustive (and, if possible, experimental) verification methods can be defined, aiming at a higher confidence level in the requirements' compliance: for instance, in-situ experiments aiming at verifying the effectiveness of the debris avoidance maneuvers can be performed.

 Δv **Budget:** Due to the high number and complexity of the maneuvers computed in the sizing process, they have been assumed to be instantaneous, and some margins have been assigned to perform eventual unplanned ones. More detailed maneuvers can be

studied, excluding the approximation of instantaneous burns, and modelling them more realistically.

Sizing: The sizing process can be improved as well. First, a multi-phase thermal control system can be developed, eventually allowing for electric propulsion to be implemented [41], and more detailed heat exchange mechanisms can be investigated to better size the components of the TCS. Second, the decrease in performance of the EPS in time shall be better explored, accounting for the effect of some variables, such as the β angle, which are not available at this mission design stage, and allowing for more precise estimations for both batteries and solar arrays. Third, different technologies for DockSys and deorbit kits can be studied, for instance soft docking mechanisms instead of robotic arms and drag augmentation devices rather than electrodynamic tethers; moreover, more accurate atmospheric and ionospheric models for the deorbit can be implemented [268], as well as for the Earth's magnetic field, including possible variations in time, solar maxima and minima. Lastly, the use of more ODCS engines can be explored, and even the use of turbopumps to feed them might be studied [41].

DPS: Different alternatives to the classical Whipple shields can be explored as well, by using different materials and geometries, optimizing the shield distances and thicknesses [145]. Furthermore, special shielding for pressurized tanks and vessels can be studied [269, 270], considering different angles of impact [143].

Launch: Since the high availability of the launcher has been prioritized over other features, some vehicles have been excluded from the analysis and may be considered in future examinations. Moreover, the geopolitical and social impacts of different launch sites' locations shall be considered in further studies.

Re-entry: In future re-entry analyses, both debris and satellites can be modelled more accurately in order to determine the possibility of a controlled or uncontrolled atmospheric re-entry. Moreover, research about more effective D4D techniques and materials can be done, allowing for a lower on-ground casualty risk; also, more complex dynamics (such as explosions, which can heavily affect re-entry dynamics and on-ground casualty risk) shall be included in the deorbit simulations. Lastly, different end-of-life maneuvers can be explored, allowing for faster or slower orbital decays.

LCA: The limitations of the current LCA shall be studied, and further works can be done in order to overcome and reduce them, allowing for more exhaustive analyses to be performed. Also, the ground segment impact and the orbital emissions shall be analysed. Lastly, RD and testing shall be investigated as well, allowing for a comprehensive impact assessment of the mission.

LCC: A more accurate cost model can be implemented to better estimate the economic impact of the missions' development. Also, costs related to different launch sites shall be defined if that possibility is explored.

Bibliography

- [1] L. Miraux. Environmental limits to the space sector's growth. *The Science of The Total Environment*, Oct 2021. doi: 10.1016/j.scitotenv.2021.150862.
- [2] J. P. Ferreira, K.-ichi Nomura, J. Wang and Z. Huang. Potential Ozone Depletion From Satellite Demise During Atmospheric Reentry in the Era of Mega Constellations. *Geophysical Research Letters*, 2024. doi: https://doi.org/10.1029/2024GL10 9280.
- [3] ESA Space Debris Office. ESA's Annual Space Environment Report. Technical report, European Space Agency, 2024. 8.0.
- [4] J.-C. Liou. The Top 10 Questions for Active Debris Removal. In *European Workshop on Active Debris Removal*, CNES HQ, Paris, France, Jun 2010.
- [5] F. Letizia, E. Stevenson, M. Papa, D. Bella, C. Turner, I. De Chiclana, S. Ventura and S. Lemmens. ESA's Space Debris Mitigation Requirements. In ESA-TECQI-HO-2024-002968, 2024.
- [6] Thales Alenia Space. Atmospheric Re-entry Assessment, ARA. In CleanSat Industrial Days, ESTEC, Oct 2017.
- [7] Scientific and Technical Subcommittee, Forty-ninth session. Active Debris Removal: an Essential Mechanism for Ensuring the Safety and Sustainability of Outer Space. Technical report, Committee on the Peaceful Uses of Outer Space, Feb 2012. V.12-50395 (E).
- [8] J.-C. Liou. Orbital Debris Modeling and the Future Orbital Debris Environment. Orbital Debris Lecture (ASEN 6519), Sep 2012. University of Colorad Boulder.
- [9] C. Bonnal, J.-M. Ruault and M.-C. Desjan. Active Debris Removal: Current Status of Activities in CNES. In 6th European Conference on Space Debris, Darmstadt, Germany, Apr 2013. ESA SP-723.
- [10] ESA LCA Working Group. Space system Life Cycle Assessment (LCA) guidelines, Oct 2016. European Space Agency. Available upon request.
- [11] Office for Outer Space Affairs. Guidelines for the Long-Term Sustainability of Outer Space Activities of the Committee on the Peaceful Uses of Outer Space, 2021. V. 21-02562.
- [12] National Aeronautics and Space Administration. NASA System Engineering Handbook. NASA Headquarters Washington, D.C. 20546, 2007. NASA/SP-2007-6105 Rev1.
- [13] European Space Agency. Life Cycle Inventory (LCI) Database, 2024. Available upon request.

- [14] National Aeronautics and Space Administration. Handbook for Limiting Orbital Debris, Jul 2008. NASA Handbook 8719.14.
- [15] J. P. Ferreira, K.-ichi Nomura and J. Wang. Space Debris Demise upon Re-entry as a Potential Atmospheric Pollutant. In 2024 IEEE Aerospace Conference, 2024. doi: 10.1109/AERO58975.2024.10521354.
- [16] J. P. Ferreira, K.-ichi Nomura and J. Wang. Preliminary Assessment of the Environmental Impact of Space Debris Demise during Atmospheric Reentry. In Advanced Maui Optical and Space Surveillance Technologies Conference (AMOS), 2023.
- [17] European Space Agency. Applications in Earth Orbit. https://www.esa.int/Enabling_Support/Space_Engineering_Technology/Automation_and_Robotics/Applications_in_Earth_Orbit. Accessed on: 04/04/2025.
- [18] ESA Space Debris Mitigation Working Group. ESA Space Debris Mitigation Requirements, Oct 2023.
- [19] M. Gupta. Navigating Chaos: Resonant Orbits for Sustaining Cislunar Operations. PhD thesis, Purdue University, 2024.
- [20] M. J. Holzinger, C. C. Chow and P. Garretson. A Primer on Cislunar Space, May 2021.
- [21] C. Frueh, K. Howell, K. J. DeMars and S. Bhadauria. Cislunar Space Situational Awareness. In 31st AAS/AIAA Space Flight Mechanics Meeting, Charlotte, North Carolina (virtual), Feb 2021.
- [22] A. P. Wilmer, N. R. Boone and R. A. Bettinger. Debris Propagation and Spacecraft Survaivability Assessment for Catastrophic Mishaps Occurring in Cislunar Periodic Orbits. *Journal of Space Safety Engineering*, 9:207–222, 2022. doi: https://doi.org/10.1016/j.jsse.2022.02.007.
- [23] N. Boone and R. Bettinger. Debris Propagation Following a Spacecraft Mishap at the Collinear Earth-Moon Lagrange Points, Mar 2021.
- [24] P. Bandyopadhyay, Ram K. Sharma and A. Tewari. Space Debris Hazards from Fragmentations in Collinear Earth-Moon Points. In ESA SP-672, 5th European Conference on Space Debris, Darmstadt, Germany, 30 Mar - 2 Apr 2009.
- [25] N. Boone and R. Bettinger. Sacceraft Survivability in the Neutral Debris Environment near the Stable Earth-Moon Lagrange Points. *Advances in Space Research*, 67:2319–2332, Feb 2021. doi: 10.1016/j.asr.2021.01.047.
- [26] National Aeronautics and Space Administration. Artemis 1 Map, Feb 2018. Accessed on: 31/01/2025.
- [27] B. F. Barakat and M. T. Kezirian. Establishing Requirements for Lunar and Cislunar Orbital Debris Tracking. In *Second Orbital Debris Conference*, 2023.
- [28] D. J. Kessler and B. G. Cour-Palais. Collision Frequency of Artificial Satellites: The Creation of a Debris Belt. *Journal of Geophysical Research: Space Physics*, 83 (A6):2637–2646, 1978. doi: https://doi.org/10.1029/JA083iA06p02637.
- [29] D. J. Kessler. Collisional Cascading: The Limits of Population Growth in Low Earth Orbit. *Advances in Space Research*, 11(12):63–66, 1991. doi: 10.1016/0273-1177(91)90543-S.
- [30] D. J. Kessler and P. D. Anz-Meador. Critical Number of Spacecraft in Low Earth Orbit: Using Satellite Fragmentation Data to Evaluate the Stability of the Orbital

- Debris Environment. In *Proceedings of the Third European Conference on Space Debris*, Darmstadt, Germany, Sep 2001.
- [31] Committee on Space Debris. Orbital Debris: A Technical Assessment. National Academy Press, 1995. doi: https://doi.org/10.17226/4765.
- [32] R. Walker, C. Martin, H. Stokes, J. Wilkinson, H. Sdunnus, S. Hauptmann, P. Beltrami and H. Klinkrad. Update of the ESA Space Debris Mitigation Handbook. Technical report, European Space Agency, 2002. ESA Contract 14471/00/D/HK, Ref:QINETIQ/KI/SPACE/CR021539.
- [33] Office for Outer Space Affairs. Space Debris Mitigation Guidelines of the Committee on the Peaceful Uses of Outer Space, 2010.
- [34] IADC Steering Group & Working Group 4. IADC Space Debris Mitigation Guidelines. Technical report, Inter-Agency Space Debris Coordination Committee, 2021. IADC-02-01 Rev.3.
- [35] J.-C. Liou. Orbital Debris Mitigation and Challenges to the Space Community. In Space Disposal and Debris Mitigation Conference, Mar 2021.
- [36] S. Servadio, T. St. Francis, N. Simha, D. Gusmini, D. Jand, A. D'Ambrosio and R. Linares. Optimal Target Selection for an Active Debris Removal Mission. In 33rd AAS/AIAA Space Flight Mechanics Meeting, Jan 2023.
- [37] V. Braun, E. Schulz and C. Wiedamann. Cost Estimation for the Active Debris Removal of Multiple Priority Targets. In 40th COSPAR Scientific Assembly, Moscow, Aug 2014.
- [38] Th. Martin, E. Pérot, M.Ch. Desjean and L. Bitetti. Active Debris Removal Mission Design in Low Earth Orbit. *Progress in Propulsion Physics*, 4:763–788, 2013. doi: 10.1051/eucass/201304763.
- [39] G. Guerra, A. C. Muresan, K. G. Nordqvist, A. Brissaud, N. Naciri and L. Luo. Active Space Debris Removal System. *INCAS BULLETIN*, 9(2):97–116, Jun 2017. doi: 10.13111/2066-8201.2017.9.2.8.
- [40] M. C. Wijayatunga, R. Armellin, H. Holt, L. Pirovano and A. A. Lidtke. Design and Guidance of a Multi-Active Debris Removal Mission. *Astrodynamics*, 7(4):383–399, 2023. doi: https://doi.org/10.1007/s42064-023-0159-3.
- [41] E. Carlson, S. Casali, D. Chambers, G. Geissler, A. Lalich, M. Leipold, R. Mach, J. Parry and F. Weems. Final Design of a Space Debris Removal System. NASA STI/Recon Technical Report N, 92:25382, Nov 1990.
- [42] National Aeronautics and Space Administration. 13.0 Deorbit Systems. https://www.nasa.gov/smallsat-institute/sst-soa/deorbit-systems/, . Accessed on: 06/02/2025.
- [43] Y. Egawa, K. Kamachi, D. Suzuki, L. Okajima, S. Kawamoto, Y. Ohkawa, T. Watanabe, T. Sato, T. Kuwahara, S. Fujita and Y. Sato. De-Orbit Demonstration Using Electrodynamic Tether System for Space Debris Removal. In 8th European Conference on Space Debris (virtual), Darmstadt, Germany, Apr 2021.
- [44] S. Kawamoto, Y. Ohkawa, S. Kitamura and S.-ichiro Nishida. Strategy for Active debris Removal Using Electrodynamic Tether. *JSASS Space Tech. Japan*, 7, 2009.
- [45] G. Sarego, L. Olivieri, A. Valmorbida, C. Bettanini, G. Colombatti, M. Pertile and E. C. Lorenzini. Deorbiting Performance of Electrodynamic Tethers to Mitigate

- Space Debris. International Journal of Aerospace and Mechanical Engineering, 15 (4), 2021.
- [46] C. Bombardelli, J. Herrera-Montojo, A. Iturri-Torrea and J. Peláez. Space Debris Removal with Bare Electrodynamic Tethers. Advances in the Astronautical Sciences. Jan 2010.
- [47] S. António da Rocha and B. de Aguiã Morant. Space Tether Systems. Master's thesis, Universidade de Beira Interior, 2014.
- [48] B. W. Barbee, S. Alfano, E. Piñon, K. Gold and D. Gaylor. Design of Spacecraft Missions to Remove Multiple Orbital Debris Objects. In 35th Annual AAS Guidance and Control Conference, Breckenridge, Colorado, Feb 2012. AAS 12-017.
- [49] V. Trushlyakov and V. Yudintsev. Method of Active Debris Removal Using Rotating Space Tether System. In *First International Orbital Debris Conference*, 2019.
- [50] J. Howlett, J. Forshaw and V. Valhondo. UK ADR: The UK Space Agency's Active Debris Removal Mission. In 2nd Orbital Debris Conference, 2023.
- [51] National Aeronautics and Space Administration. Process for Limiting Orbital Debris. Technical report, NASA, Nov 2021. NASA-STD-8719.14C.
- [52] International Academy of Astronautics (IAA). Position Paper on Space Debris Mitigation: Implementing Zero Debris Creation Zones, Oct 2005.
- [53] D. Briot. Impacts of the space debris mitigation rules on the spacecraft design in Airbus Defence and Space. In 7th European Conference on Space Debris, Darmstadt, Germany, Apr 2017.
- [54] S. M. Hull. End of Mission Considerations. https://ntrs.nasa.gov/citations/20130000278, Jan 2013. Accessed on: 01/02/2025.
- [55] W. P. Schonberg. Soft Passivation of Spacecraft Pressure VEssels. In *First International Orbital Debris Conference*, 2019.
- [56] D. J. Kessler, R. C. Reynolds and P. D. Anz-Meador. Orbital Debris Environment for Spacecraft Designed to Operate in Low Earth Orbit. Technical report, National Aeronautics and Space Administration, Apr 1989. NASA Technical Memorandum 100 471.
- [57] Office of Safety and Mission Assurance. Procedural Requirements for Limiting Orbital Debris and Evaluating the Meteoroid and Orbital Debris Environments. Technical report, National Aeronautics and Space Administration, Feb 2017. NPR 8715.6B.
- [58] U.S. Government. Orbital Debris Mitigation Standard Practices. Technical report, United States of America, Nov 2019. Updated.
- [59] S. Lemmens, V. Braun, R. Kanzler, A. Horstmann and Q. Funke. DRAMA 3.0.0: A One Stop Shop for the Verification of Space Debris Mitigation Requirements, Nov 2018. European Space Agency. Available upon request.
- [60] NOAASatellites. GOES-R Launch Sequence and Deployments. Published on Youtube, Oct 2016.
- [61] F. Stesina. Attitude and Orbit Control System (AOCS) / Part 1. University lecture, Sistemi Aerospaziali, 2024. Politecnico di Torino, Turin, Italy.
- [62] M. Wurdak, U. Gotzig and M. El Atrach. Equipment for Satellite End-Of-Life Management and Deorbit. In *Clean Space Industry Days*, Noordwijk, Oct 2023.

- [63] N. L. Johnson. The Disposal of Spacecraft and Launch Vehicle Stages in Low Earth Orbit. In 2nd International Association for the Advancement of Space Safety Conference, NASA Lyndon B. Johnson Space Center, May 2007.
- [64] Iridium Communications. Iridium Deorbit of Block 1 Constellation. Technical report, Iridium, Feb 2021.
- [65] Y. Shirasawa, Y. Komatsu, Y. Tsutsui, H. Katsumata, A. Wada, T. Iwata, K. Adachu and T. Fukushima. Concept Study of Spacecraft System for End-Of-Life Deorbit Service Using Low-Thrust Formation. In 8th European Conference on Space Debris (virtual), Darmstadt, Germany, Apr 2021. ESA Space Debris Office Ed. T. Flohrer, S. Lemmens & F. Schmitz.
- [66] Zhang W., Li F., Li J. and Cheng Q. Review of On-Orbit Robotic Arm Active Debris Capture Removal Methods. Aerospace, 10(13), 2023. doi: https://doi.org/ 10.3390/aerospace10010013.
- [67] M. D. Hejduk. Specular and Diffuse Components in Spherical Satellite Photometric Modeling. https://api.semanticscholar.org/CorpusID:15354379, Sep 2011.
- [68] K. J. Abercromby, P. Abell and E. Barker. Reflectance Spectra Comparison of Orbital Debris, Intact Spacecraft, and Intact Rocket Bodies in the GEO Regime. In 5th European Conference on Space Debris, Darmstadt, Germany, Apr 2009.
- [69] H.-X. Shen and L. Casalino. Simple ΔV Approximation of Debris-to-Debris Transfers. Journal of Spacecraft and Rockets, Dec 2020. doi: 10.2514/1.A34831.
- [70] H. Curtis. Orbital Mechanics for Engineering Students. Elsevier, 2005.
- [71] F. Stesina. Communication System. University lecture, Sistemi Aerospaziali, 2024. Politecnico di Torino, Turin, Italy.
- [72] ISISPACE. Antenna System for 6U/12U CubeSats. https://www.isispace.nl/product/antenna-system-for-6u-12u-cubesats/. Technical Datasheet, Accessed on: 02/03/2025.
- [73] C. A. Fernandes. Antennas Types. University lecture, Satellite Systems, 2024. Instituto Superior Técnico, Lisbon, Portugal.
- [74] F. Stesina. Payloads. University lecture, Sistemi Aerospaziali, 2024. Politecnico di Torino, Turin, Italy.
- [75] Malin Space Science Systems. Docking Camera (DCAM), Color/Monochrome Gigabit Ethernet CMOS Camera, Global Shutter, 2592x2048, 4.8μm pitch, 2024. Technical Datasheet.
- [76] F. Cercas and A. Rodrigues. Técnicas de Espalhamento de Espectro para Satélites. University lecture, Satellite Systems, 2024. Instituto Superior Técnico, Lisbon, Portugal.
- [77] Federal Communications Commission Office of Engineering and Technology Policy and Rules Division. FCC Online Tables of Frequency Allocations. Technical report, Federal Communications Commission, Jan 2025. 47 C.F.R. §2.106.
- [78] J. Walker. NASA Spectrum Usage. https://www.nasa.gov/directorates/somd/space-communications-navigation-program/nasa-spectrum-usage/, Sep 2023. Accessed on: 02/03/2025.
- [79] F. Cercas and A. Rodrigues. Análise e Projecto de uma Ligacao por Satélite. University lecture, Satellite Systems, 2024. Instituto Superior Técnico, Lisbon,

- Portugal.
- [80] F. Cercas and A. Rodrigues. Tecnologias de Comunicacoes Digitais. University lecture, Satellite Systems, 2024. Instituto Superior Técnico, Lisbon, Portugal.
- [81] S. L. Booth and M. A. Marsden. NASA/TM 2019-220203 Radio Frequency and Optical Communication Link Trade Studies Between Earth, Deep Space Gateway, and Lunar Surface. Technical report, National Aeronautics and Space Administration, Glenn Research Center, Cleveland, Ohio 44135, Dec 2019.
- [82] J. L. Gaspar, T. Sreekantamurthy, T. Mann, V. Behun, R. R. Romanofsky, K. Lambert and J. Pearson. Test and Analysis of an Inflatable Parabolic Dish Antenna. In 47th AIAA/ASME/ASCE/AHS/ASC Structure, Structural Dynamics, and Materials Conference, Newport, Rhode Island, May 2006.
- [83] Homo ludens electronicus. Designing and Building Conical Horn Antennas. https://ludens.cl/Electron/horn/horn.html. Accessed on: 02/03/2025.
- [84] A. Shelley. A 24ft/7.3m Parabolic Reflector Antenna Performance & Feed Design Analysis. Master's thesis, Morehead State University, 2010.
- [85] MOOG Inc. Space and Defence Group. Mechanisms, Type 33 Biaxial Gimbal, 2021. Technical Datasheet.
- [86] Comtech EF Data Corp. CDM-625A-ENI Advanced Satellite Modem, 2020. Technical Datasheet.
- [87] Texas Instruments Inc. TPS7A3501 High PSRR, Low-Noise, 1-A Power Filter, 2022. Technical Datasheet.
- [88] General Dynamics. Space Qualified Multi-Mode Standard Transponder (MST), 2019. Technical Datasheet.
- [89] Mini-Circuits. Surface Mount Diplexer LDP-1050-252+, . Technical Datasheet.
- [90] Mini-Circuits. Coaxial Cable 047-6SMP+, . Technical Datasheet.
- [91] W. J. Larson and J. R. Wertz. Space Mission Analysis and Design. Microcosm Press & Kluwer Academic Publishers, 3rd edition, 2005.
- [92] F. Stesina. Attitude and Orbit Control System (AOCS) / Part 2. University lecture, Sistemi Aerospaziali, 2024. Politecnico di Torino, Turin, Italy.
- [93] Sinclair Interplanetary by Rocket Lab. Second Generation Star Tracker (ST-16RT2), Jun 2021. Technical Datasheet.
- [94] Ariane Group. 1N, 20N, 400N and Heritage Thruster, . Technical Datasheet.
- [95] Moog Inc. Monopropellant Thrusters, 2024. Technical Datasheet.
- [96] Aerojet Rocketdyne An L3Harris Technologies Company. Monopropellant Rocket Engines, 2023. Technical Datasheet.
- [97] Worldwide Pipe and Supply. Barlow's Formula Calculator. https://www.worldwidepipe.com/barlows-formula.html#:~:text=The%20standard%20equation%20for%20hoop,the%20diameter%20of%20the%20pipe. Accessed on: 07/03/2025.
- [98] Atlas Steel. Stainless Steel Pipe, Fittings & Flanges, Oct 2016. Technical Datasheet.
- [99] Rocketdyne A Division of North American Aviation Inc. Mechanical System Design-Criteria Manual for Hydrazine. 6633 Canoga Avenue, Canoga Park, California, Sep 1961.
- [100] Rocketdyne A Division of North American Aviation Inc. *Nitrogen Tetroxide Handling Manual.* 6633 Canoga Avenue, Canoga Park, California, Sep 1961.

- [101] Blue Canyon Technologies. Control Moment Gyroscopes. Technical Datasheet.
- [102] NASA. GRACE-FO Quick Facts. https://gracefo.jpl.nasa.gov/overlay-quick-facts/. Accessed on: 02/03/2025.
- [103] F. Cossavella, J. Herman, L. Hoffmann, D. Fischer, H. Save, B. Schlepp and T. Usbeck. Attitude Control on GRACE Follow-On: Experiences from the First Years in Orbit. Space Operations, 2022. doi: https://doi.org/10.1007/978-3-030-94628-922.
- [104] D. Pastrone. Liquid Rocket Engines (LRE). University lecture, Endoreattori, 2024. Politecnico di Torino, Turin, Italy.
- [105] Ariane Group. 10N, 200N, 400N Chemical Bi-Propellant Thruster Family, . Technical Datasheet.
- [106] Aerojet Rocketdyne An L3Harris Technologies Company. Bipropellant Rocket Engines, 2023. Technical Datasheet.
- [107] Aerojet Rocketdyne. Bipropellant Propulsion: R-42DM 890N (200 lbf) Dual Mode High Performance Rocket Engine. Technical Datasheet.
- [108] MT Aerospace. Spacecraft Propellant Tanks. Technical Datasheet.
- [109] Moog Inc. Rolling Metal Diaphragm Propulsion Tanks, 2024. Technical Datasheet.
- [110] Rafael Advanced Defense Systems LTD. Rafael Space Propulsion Catalogue, 2024.
- [111] CAVU Aerospace UK. OBC1 Satellite OnBoard Computer (OBC), 2024. Technical Datasheet.
- [112] ISIS: Innovative Solutions In Space. *ISIS On Board Computer*, Aug 2023. Technical Datasheet.
- [113] S. Corpino. Electrical Power System (EPS). University lecture, Sistemi Aerospaziali, 2024. Politecnico di Torino, Turin, Italy.
- [114] S. Corpino. Thermal Control System (TCS). University lecture, Sistemi Aerospaziali, 2024. Politecnico di Torino, Turin, Italy.
- [115] Beyond Gravity. Thermal Insulation for Space and Launcher Applications. Technical Datasheet.
- [116] J. A. Johnson, A. I. Haines, L. A. Bedrossian and M. T. Kenny. Development of Improved Thermal Control Coatings for Space Assets. Technical report, Air Force Research Laboratory, Nov 2004.
- [117] PQ Corporation Industrial Chemical Division. *PQ®Potassium Silicates*, 2004. Technical Datasheet.
- [118] C. Versteeg and D. L. Cotten. Preliminary thermal analysis of small satellites. https://api.semanticscholar.org/CorpusID:236782747, 2018. Small Satellite Research Laboratory, The University of Georgia, Athens, Georgia, 30602.
- [119] H.J. van Gerner, R. C. Van Benthem, J. van Es, D. Schwaller and S. Lapensée. Fluid Selection for Space Thermal Control Systems. In 44th International Conference on Environmental Systems, Tucson, Arizona, Jul 2014.
- [120] Boeing. Active Thermal Control System (ATCS) Overview. Technical Report.
- [121] National Aeronautics and Space Administration. Small Spacecraft Active Thermal Control. www.nasa.gov, Apr 2016. Published on NASAfacts.
- [122] Arquimea. Heat Pipes for Space Applications. https://www.arquimea.com/products/heat-pipes-satellite-space-applications/. Accessed on: 30/04/2025.

- [123] A. K. Koech, G. Mwandila, F. Mulolani and P. Mwaanga. Lithium-ion battery fundamentals and exploration of cathode materials: A review. *South African Journal of Chemical Engineering*, Sep 2024. doi: DOI:10.1016/j.sajce.2024.09.008.
- [124] B. E. Anspaugh. GaAs Solar Cell Radiation Handbook. National Aeronautics and Space Administration, Jet Propulsion Laboratory, California Institute of Technology, Pasedana, California, Jul 1996.
- [125] Astro-Electronics Division Defense Electronic Products Radio Corporation of America. Application of Gallium-Arsenide Solar Cells to Solar Probe power Systems, Feb 1966. prepared for National Aeronautics and Space Administration, AMES Research Center, Moffett Field, California.
- [126] Moog Inc. Type 11 Biaxial Gimbal, 2022. Technical Datasheet.
- [127] CEDRAT Technologies and 38240 Meylan, France and G. Aigouy and S. Duc and M. Castruccio and A. Loubet and O. Sosnicki and F. Claeyssen. Cost Efficient Space Micro-Switches Based on Contactless Eddy Current Sensors. In *Proceedings of the 46th Aerospace Mechanisms Symposium*, May 2022. Virtual Session.
- [128] C. Cuerno-Rejado, J. López-Díez and A. Sanz-Andrés. Rapid Method for Spacecraft Sizing. Proceedings of the Institution of Mechanical Engineers, Part G: Journal of Aerospace Engineering, 209:165–169, 1995. doi: 10.1243/PIME_PROC_1995_209 __286_02.
- [129] J. A. Christian and S. Cryan. A Survey of LIDAR Technology and its Use in Space-craft Relative Navigation. In AIAA Guidance, Navigation, and Control (GNC) Conference, Boston, MA, Aug 2013. doi: https://doi.org/10.2514/6.2013-4641.
- [130] Hinkel, Heather and Zipay, John J. and Strube, Matthew and Cryan, Scott. Technology Development of Automated Rendezvous and Docking/Capture Sensors and Docking Mechanism for the Asteroid Redirect Crewed Mission. In 2016 IEEE Aerospace Conference, pages 1–8, 2016. doi: 10.1109/AERO.2016.7500637.
- [131] K. Kanani, A. Petit, E. Marchand, T. Chabot and B. Gerber. Vision Based Navigation for Debris Removal Missions. In 63rd International Astronautical Congress, Naples, Italy, 2012. hal-00750610.
- [132] K. Hovell and S. Ulrich. On Deep Reinforcement Learning for Spacecraft Guidance. In AIAA SciTech Forum, Orlando, FL, Jan 2020. doi: 10.2514/6.2020-1600.
- [133] L. Bourrec, L. Bernabé, V. Pires and S. Tremolieres. Telescopic Boom for Space Applications Engineering Model. In 14th European Space Mechanisms & Tribology Symposium ESMATS 2011, Constance, Germany, Sep 2011.
- [134] StepperOnline. Motoriduttore CC con cambio cilindrico 5:1 spazzolato 12V 10W 0,21Nm(29,74oz.in) 360RPM. https://www.omc-stepperonline.com/it. Accessed on: 17/03/2025.
- [135] C. Trentlage, P. Mindermann, M. Khalil Ben Larbi and E. Stoll. Development and Test of an Adaptable Docking Mechanism Based on Mushroom-Shaped Adhesive Microstructures. Sep 2016. doi: 10.2514/6.2016-5486.
- [136] I. Caracciolo. Developing Solutions for Active Debris Removal. Master's thesis, Università degli Studi di Padova, 2023.
- [137] B. Vishnuprakash and A. Radhakrishnan. Design And Development of a Robotic Arm for Space Debris Mitigation Using Electrostatic and Gecko-Inspired Gripping

- Technologies. Acceleron Aerospace Journal, 3(7):728–737, Dec 2024. doi: 10.61359/11.2106-2472. E-ISSN-2583-9942.
- [138] A. Bylard, R. MacPherson, B. Hockman, M. R. Cutkosky and M. Pavone. Robust Capture and Deorbit of Rocket Body Debris Using Controllable Dry Adhesion. In 2017 IEEE Aerospace Conference, pages 1–9, 2017. doi: 10.1109/AERO.2017.7943 844.
- [139] T. Bryan. Flexible Electrostatic Technologies for Capture and Handling, Phase 1, Jan 2015. Technical Report.
- [140] Smooth-On. Mold StarTM15, 16 and 30 Product Overview. Technical Datasheet.
- [141] D. Ruffatto III, J. Shah and M. Spenko. Optimization and Experimental Validation of Electrostatic Adhesive Geometry. In *IEEE Aerospace Conference Proceedings*, Mar 2013. doi: DOI:10.1109/AERO.2013.6496943.
- [142] Impact Materials. Carbon Fiber Density: Facts and Insights. https://ictfibers.com/carbon-fiber-density-facts-and-insights/, Jan 2024. Accessed on: 16/03/2025.
- [143] H.-G. Reimerdes, K.-H. Stecher and M. Lambert. Ballistic Limit Equations for the Columbus-Double Bumper Shield Concept. In First European Conference on Space Debris, Darmstadt, Germany, Apr 1993. ESA SD-01.
- [144] S. Ryan, M. Bjorkman and E. L. Christiansen. Characteristics of Whipple shield performance in the shatter regime. In 11th Hypervelocity Impact Symposium, 2009.
- [145] E. L. Christiasen. Meteoroid / Debris Shielding, Sep 2003. NASA Johnson Space Center, Houston, Texas.
- [146] J. R. Sanmartin, R. D. Estes and E. C. Lorenzini. Efficiency of Different Types of ED-Tether Thrusters. In Space Technology and Applications International Forum, 2001.
- [147] Y. Okawa, S. Kitamura, S. Kawamoto, Y. Iseki, K. Hashimoto and E. Noda. An Experimental Study of Carbon Nanotube Field Emission Cathodes for Electrodynamic Tethers. In 29th International Electric Propulsion Conference, Princeton University, 2005. Oct 31 - Nov 4.
- [148] X. Calderón-Colón, H. Geng, B. Gao, L. An, G. Cao and O. Zhou. A carbon Nanotube Field Emission Cathode with High Current Density and Long-Term Stability. Nanotechnology, Sep 2009. doi: DOI:10.1088/0957-4484/20/32/325707.
- [149] G. Sarego, L. Olivieri, A. Valmorbida, A. Brunello, E. C. Lorenzini, L. Tarabini Castellani, E. Urgoiti, A. Ortega, G. Borderes Motta and G. Sánchez Arriaga. Deployment Requirements for Deorbiting Electrodynamic Tether Technology. CEAS Space Journal, 13:567–581, 2021. doi: https://doi.org/10.1007/s12567-021-00349-5.
- [150] Century Spring. Compression Springs. www.centuryspring.com. Technical Datasheet.
- [151] SpaceX. Falcon 9. https://www.spacex.com/vehicles/falcon-9/, . Accessed on: 07/05/2025.
- [152] SpaceX. Falcon User's Guide, Sep 2021.
- [153] SpaceX. Falcon User's Guide Version 8, Mar 2025.
- [154] Wevolver. Falcon 9 v1.2 or Full Thrust Block 5. https://www.wevolver.com/specs/falcon-9-v12-or-full-thrust-block-5, . Accessed on: 08/05/2025.

- [155] SpaceX. Falcon Heavy. https://www.spacex.com/vehicles/falcon-heavy/, . Accessed on: 15/05/2025.
- [156] Wevolver. Falcon Heavy Block 5. https://www.wevolver.com/specs/falcon-heavy-block-5, . Accessed on: 09/05/2025.
- [157] ArianeSpace ArianeGroup. Ariane 6 User's Manual Issue 2 Revision 0, Feb 2021.
- [158] European Space Agency. All Engines for Ariane 6 Complete Qualification Tests. https://www.esa.int/Enabling_Support/Space_Transportation/Ariane/All_engines_for_Ariane_6_complete_qualification_tests?, Oct 2020. Accessed on: 12/05/2025.
- [159] European Space Agency. The Engines of Ariane 6. https://www.esa.int/Enabling_Support/Space_Transportation/Ariane/The_engines_of_Ariane_6?, Jun 2024. Accessed on: 12/05/2025.
- [160] United Launch Alliance. Vulcan Launch Systems User's Guide, Oct 2023.
- [161] Juno. ULA Vulcan Centaur Heavy. https://www.simplerockets.com/c/500wK2/ULA-Vulcan-Centaur-Heavy, Feb 2020. Accessed on: 13/05/2025.
- [162] S. Rosenstein. ULA ready for inaugural Vulcan flight. https://www.nasaspaceflight.com/2024/01/vulcan-flight-one-preps/, Jan 2024. NASASpaceFlight. Accessed on: 13/05/2025.
- [163] United Launch Alliance. Vulcan Centaur Data Sheet. https://www.ulalaunch.com/docs/default-source/rockets/vulcancentaur.pdf?sfvrsn=10d7f58f_10, 2022. Accessed on: 13/05/2025.
- [164] Eric Berger. Behind the Curtain: Ars goes inside Blue Origin's Secretive Rocket Factory. https://arstechnica.com/science/2016/03/behind-the-curtain-a rs-goes-inside-blue-origins-secretive-rocket-factory/, Mar 2016. Ars Technica. Accessed on: 13/05/2025.
- [165] Northrop Grumman. GEM 63 and GEM 63XL, 2020. Technical Datasheet.
- [166] National Aeronautics and Space Administration. NASA's Space launch System Reference Guide, Aug 2022. Version 2.
- [167] B. Donahue, S. Sigmon and D. Cooper. The NASA SLS Development and Mission Opportunities. In 2018 Joint Propulsion Conference, AIAA Propulsion and Energy Forum, Cincinnati, Ohio, Jul 2018.
- [168] Silverbird Astronautics. Launch Vehicle Performance Calculator. https://silverbirdastronautics.com/LVperform.html. Accessed on: 08/05/2025.
- [169] SpaceX. Rideshare Payload User's Guide Version 10, Sep 2024.
- [170] SpaceX. Cake Topper Payload User's Guide Version 2, Dec 2024.
- [171] P. J. S. Gil. Staging. University lecture, Space Launchers, 2022-2023. Instituto Superior Técnico, Lisbon, Portugal.
- [172] Calculator.net. Inflation Calculator. https://www.calculator.net/inflation-calculator.html. Accessed on: 15/05/2025.
- [173] Cierra Choucair. How Much Does It Cost to Launch a Rocket. https://spaceinsider.tech/2023/08/16/how-much-does-it-cost-to-launch-a-rocket/, Jan 2025. Space Insider. Accessed on: 16/05/2025.
- [174] Pascale Davies. Ariane 6 Launch: Why it Matters for Europe's Space Ambitions.

- https://www.euronews.com/next/2024/07/09/ariane-6-launch-how-to-wat ch-it-and-why-it-matters-for-europes-space-ambitions, Jul 2024. Euro News. Accessed on: 15/05/2025.
- [175] Eric Ralph. SpaceX Falcon 9 Crushes Next-Gen ULA Vulcan Rocket on Cost in First Competition. https://www.teslarati.com/spacex-falcon-9-beats-ula-vulcan-on-cost/, Mar 2021. Teslarati. Accessed on: 16/05/2025.
- [176] Sharmila Kuthunur. NASA's Mighty SLS Megarocket for Artemis Moonshots 'Unaffordable' for Sustained Exploration, Audit Finds. https://www.space.com/nasa-sls-rocket-artemis-moon-plans-unaffordable-gao-report, Sep 2023. Space.com. Accessed on: 23/05/2025.
- [177] T. Maury, P. Loubet, M. Trisolini, A. Gallice, G. Sonnemann and C. Colombo. Assessing the Impact of Space Debris on Orbital Resource in Life Cycle Assessment: a Proposed Method and Case Study. *Science of the Total Environment*, 667:780–791, 2019. doi: doi:10.1016/j.scitotenv.2019.02.438.
- [178] T. Maury-Micolier, A. Maury-Micolier, A. Helias, G. Sonnemann and P. Loubet. A New Impact Assessment Model to Integrate Space Debris within the Life Cycle Assessment-Based Environmental Footprint of Space Systems. Frontiers in Space Technologies, 2022. doi: 10.3389/frspt.2022.998064.
- [179] C. Monroe and P. Rossoni. Development of a Spacecraft Antenna pointing Gimbal. In 39th Aerospace Mechanisms Symposium, NASA Marshall Space Flight Center, May 2008.
- [180] MOOG. Type 3 Rotary Incremental Actuator, 2022. Technical Datasheet.
- [181] S. Orlova, A. Rassõlkin, A. Kallaste, T. Vaimann and A. Belahcen. Lifecycle Analysis of Different Motors from the Standpoint of Environmental Impact. Latvian Journal of Physics and Technical Sciences, Dec 2016.
- [182] K. de Naoum and R. Piccoli. All About Electrical Steel. https://www.xometry.com/resources/materials/electrical-steel/, Sep 2023. Xometry. Accessed on: 23/04/2025.
- [183] Posco Products. Electrical Steel Manufacturing Process. http://product.posco.com/homepage/product/eng/jsp/process/s91p2000720e.jsp. Accessed on: 23/04/2025.
- [184] DuPont. $DuPont^{TM}Kapton$, 2022. Technical Datasheet.
- [185] Z. Wang, X. Wang, S. Yuan, X. Ren, C. Yang, S. Han, Y. Qi, D. Li and J. Liu. Preparation and Characterization of Atomic Oxygen-Resistant, Optically Transparent and Dimensionally Stable Copolyimide Films from Fluorinated Monomers and POSS-Substituted Diamine. *Polymers*, Oct 2024. doi: 10.3390/polym16192845. Accessed on: 22/04/2025.
- [186] J. Kerszulis, A. Kannan, P. L. Poliak, L. Lopez, K. Hull, P. Homyak, G. Chachra, C. L. Mcgann, A. Zoombelt and K. Ishiwata. Process for Polyimide Synthesis and Polyimides Made Therefrom. https://patents.justia.com/patent/20240287 253?utm, Aug 2021. Patent, published on Justia, publication number 20240287253, application number 18/040,293, Accessed on: 22/04/2025.
- [187] M. Gassner, M. R. de Figueiredo, N. Schalk, R. Franz, C. Weiss, H. Rudigier, H. Holzschuh, W. Bürgin, M. Pohler, C. Czettl and C. Mitterer. Energy Consumption

- and Material Fluxes in Hard Coating Deposition Processes. Surface & Coatings Technology, 299:49–55, 2016.
- [188] Copper Development Association. The Welding Handbook, Welding Copper and Copper Alloys. American Welding Society, 1997.
- [189] J. M. Tizón and A. Román. A Mass Model for Liquid Propellant Rocket Engines. In American Institute of Aeronautics and Astronautics, Jul 2017. doi: 10.2514/6. 2017-5010.
- [190] V. V. Zafra. Material and Manufacturing Selection for Rocket Combustor Testing Prototype. Master's thesis, Aeronautical University in Queretaro, Oct 2021.
- [191] S. Kokare, J.P. Oliveira and R. Godina. Life Cycle Assessment of Additive Manufacturing Processes: A Review. *Journal of Manufacturing Systems*, 68:536–559, 2023. doi: https://doi.org/10.1016/j.jmsy.2023.05.007.
- [192] W. Zębala and A. Gaweł. Additive and Subtractive Manufacturing of Inconel 718 Components - Estimation of Time, Costs and Carbon Dioxide Emission - Case Study. Advances in Science and Technology Research Journal, 18:98–109, 2024. doi: https://doi.org/10.12913/22998624/176824.
- [193] Ariane Group. Pyrovalves, Fill, Drain and Vent Valves, Latch Valves, Flow Control Valve, Apr 2015. Technical Datasheet.
- [194] Y. Wang, T. Peng, Y. Zhu, Y. Yang and R. Tang. A Comparative Life Cycle Assessment of a Selective-Laser-Melting-Produced Hydraulic Valve Body Using Design for Property. *Procedia CIRP*, 90:220–225, 2020. doi: https://doi.org/10.1016/j.procir.2020.01.095.
- [195] ThyssenKrupp. Stainless Steel 316L 1.4404. https://www.thyssenkrupp-materials.co.uk/stainless-steel-316l-14404.html, 2023. Accessed on: 28/04/2025.
- [196] Global Risk Community. EPDM Rubber Manufacturing Process. https://global riskcommunity.com/profiles/blogs/epdm-rubber-manufacturing-process, Feb 2023. Accessed on: 28/04/2025.
- [197] Axon'. ESA Wires & Cables / AXALU®, Apr 2017. Technical Datasheet.
- [198] J. Lv, Z. Wang and S. Ma. Calculation Method and its Application for Energy Consumption of Ball Mills in Ceramic Industry Based on Power Feature Deployment. *Advances in Applied Ceramics*, 119:183–194, 2020. doi: https://doi.org/10.1080/17436753.2020.1732621.
- [199] Kintek. How much energy does a filter press use? Optimize Efficiency for Your Lab. https://kindle-tech.com/faqs/how-much-energy-does-a-filter-press-use?srsltid=AfmBOoqQwlnXRKm719xXwYVQGOEvzOWZYVZp2OAS-nO2hPKwFv4RBSGq, 2025. Accessed on: 02/05/2025.
- [200] Boyd. Liquid Cold Plates. https://www.boydcorp.com/thermal/liquid-cooling-systems/liquid-cold-plates.html, 2025. Accessed on: 04/05/2025.
- [201] Addman. Cold Plate Manufacturing. https://www.addmangroup.com/cold-plate-manufacturing/, 2025. Accessed on: 04/05/2025.
- [202] Compelma. Cold Plates The Ultimate Guide. Technical Datasheet.
- [203] Zoppas Industries. Flexible Heaters for Space Applications. In *Space Passive Component Days*, 1st International Symposium, Sep 2013.
- $[204] \ \ Zoppas \ Industries. \ \textit{Flexible Heater for Space Market (Satellite Vehicle Launcher)}$

- and Ground Segment). Technical Datasheet.
- [205] Editorial by Industrial Quick Search. Electric Heaters: Components, Types, Designs and Benefits. https://www.iqsdirectory.com/articles/electric-heater.html, 2025. Accessed on: 04/05/2025.
- [206] WilliamRowland. Nickel Chrome Alloys and Their Uses. https://www.william-rowland.com/news/item/nickel-chrome-and-their-uses#:~:text=Nichrome% 20alloys%20are%20typically%20crafted,to%20electrical%20flow%20and%20 heat., Oct 2016. Accessed on: 05/05/2025.
- [207] CES 2012 Edupack. Nickel-Chromium Alloy, Nichrome V, Annealed (Resistance Alloy). Technical Datasheet.
- [208] Jen Reyes. Patch Heaters: Custom Heating Solutions From Asphalt to Aerospace. https://www.powerblanket.com/blog/patch-heaters-custom-heating-solutions-from-asphalt-to-aerospace/, Jul 2024. PowerBlanket. Accessed on: 04/05/2025.
- [209] Fotofab. Nichrome Chemical Etching. https://fotofab.com/metals-we-etch/nichrome-chemical-etching/, 2025. Accessed on: 04/05/2025.
- [210] K. Autelitano, J. Famiglietti, T. Toppi and M. Motta. Empirical Power-Law Relationships for the Life Cycle Assessment of Heat Pump Units. *Cleaner Environmental Systems*, 10, Sep 2023. doi: 10.1016/j.cesys.2023.100135.
- [211] H.J. van Gerner, G. van Donk, A. Pauw and J. van Es. A Heat Pump for Space Applications. In 45th International Conference on Environmental Systems, Bellevue, Washington, Jul 2015.
- [212] Solar Brother. Adhesive Solar Reflector S.Reflect 500. https://www.solarbrother.com/en/buy/solar-reflector-adhesive-s-reflect-500/?srsltid=AfmBOooDTTA6Ed2giI5CdxO5jUp2_h2rOZIdVayrNQhx6UvezqJrpT-F, 2025. Accessed on: 05/05/2025.
- [213] Pascal Gigot. Manufacture of Aluminum Alloy Tubes. https://www.linkedin.com/pulse/manufacture-aluminum-alloy-tubes-pascal-gigot-p7vle, Jan 2024. LinkedIn. Accessed on: 05/05/2025.
- [214] D. T. Cowan. Actively Controlled Louver for Human Spacecraft Radiator Ultraviolet (UV), Dust, and Freeze Protection. In 52nd International Conference on Environmental Systems, Calgary, Canada, Jul 2023.
- [215] Sierra Space Spaceflight Hardware Catalog. *Passive Thermal Louvers*, 2023. Technical Datasheet.
- [216] XinJin. The Production Process for Aluminum Louver Pergolas. https://www.china-ceiling.com/news/the-production-process-for-aluminum-louver-pergolas, Feb 2024. Accessed on: 06/05/2025.
- [217] Engineered Materials Solutions Wickeder Group. Thermostatic Bimetal Designer's Guide. Technical Datasheet.
- [218] MOOG. Model Type 1 Rotary Incremental Actuator, 2019. Technical Datasheet.
- [219] A. Wazeem. Life Cycle Assessment of a Camera System a Case Study at Veoneer. Master's thesis, KTH Royal Institute of Technology, Nov 2022.
- [220] S. Dossanovaa and T. Mirabdolbaghi. Life Cycle Assessment of a Camera System for Automobiles. Master's thesis, Chalmers University of Technology, 2024.

- [221] Schmidt + Bartl. Vespel®SP3 Material Data Sheet. Auf Herdenen 30 78052 VS Villingen.
- [222] Plastic Machining Inc. Vespel SP-3 (Moly) Data Sheet. https://www.plasticmachininginc.com/vespel-sp-3-data-sheet/, 2023. Accessed on: 25/04/2025.
- [223] Mersen. Carbon Brushes for Motors and Generators. Technical Manual.
- [224] Editorial by Industrial Quick Search. Graphite Machining: Uses, Grades and Benefits. https://www.iqsdirectory.com/articles/graphite-machining.html#: ~:text=The%20process%20of%20machining%20graphite,technique%20similar %20to%20plowing%20snow. Accessed on: 25/04/2025.
- [225] Precision Micro. Chemical Etching Process Step-by-Step. https://www.precisionmicro.com/chemical-etching-a-step-by-step-guide/, 2025. Accessed on: 27/04/2025.
- [226] TMAX Battery Equipments. Standing Cabinet Type Spin Coater with Vacuum Oilless Pump. https://www.tmaxcn.com/standing-cabinet-type-spin-coate r-with-vacuum-oilless-pump_p2838.html. Accessed on: 27/04/2025.
- [227] Kulr. Cathodes. https://kulr.ai/products/thermal-solutions/cathodes/. Accessed on: 07/05/2025.
- [228] J. Li, L. Liang, X. Liu, H. Ma, J. Song and Y. Wei. Experimental Studies on Strengthening and Failure Mechanism for the Metal/Silicone Rubber/ Metal Bonding System. *International Journal of Applied Mechanics*, Apr 2018. doi: 10.1142/S1758825118500291.
- [229] Sika. SikaPower®- 1277. Sika Italia S.p.A., Via Luigi Einaudi 6, 20068 Peschiera Borromeo (MI), Italy, 2019.
- [230] Fagor Arrasate. Slitting Lines. https://fagorarrasate.com/solution/slitting-lines/, 2025. Accessed on: 27/06/2025.
- [231] Kesheng Machinery. Automatic Aluminum Foil Laminated Plastic Film Slitting Machine. https://www.ksslitter.com/slitting-machine/aluminium-foil-slitting-machine/automatic-aluminum-foil-laminated-plastic.html. Accessed on: 27/06/2025.
- [232] Ecoinvent Association. Ecoinvent Database, Version 3.9. https://www.ecoinvent.org, 2022.
- [233] Safe Fly Aviation. The Antonov An-124: The Ultimate Guide to the World's Heavy-Lift Aircraft. https://safefly.aero/the-antonov-an-124-the-ultimate-guide-to-the-worlds-heavy-lift-aircraft/, Apr 2025. Accessed on: 24/05/2025.
- [234] T, F. M. Brown, M. T. Bannister, L. E. Revell, T. Sukhodolov and E. Rozanov. Worldwide Rocket Launch Emissions 2019: An Inventory for Use in Global Models. *Earth and Space Science*, 2019. doi: https://doi.org/10.1029/2024EA003668.
- [235] National Aeronautics and Space Administration. CEARUN. https://cearun.grc.nasa.gov/, . Accessed on: 13/05/2025.
- [236] R. G. Ryan, E. A. Marais, C. J. Balhatchet and S. D. Eastham. Impact of Rocket Launch and Space Debris Air Pollutant Emissions on Stratospheric Ozone and Global Climate. *Earth's Future*, 10, 2022. doi: https://doi.org/10.1029/2021EF00 2612
- [237] M. Sand, R. B. Skeie, H. Bryant, R. Derwent, M. Sandstad, S. Krishnan, G. Myhre,

- D. Hauglustaine, F. Paulot, M. Prather and D. Stevenson. A Multi-Model Assessment of the Global Warming Potential of Hydrogen. *Communications, Earth & Environment*, 4:203, 2023. doi: https://doi.org/10.1038/s43247-023-00857-8.
- [238] Aerospace Specification Metals Inc. Titanium Grade 1. https://www.aerospacemetals.com/wp-content/uploads/2023/07/Titanium-Grade-1.pdf, . Accessed on: 17/05/2025.
- [239] DuPont. DuPontTMKapton®500VN Polyimide Film, 125 Micron Thickness. https://www.matweb.com/search/datasheet_print.aspx?matguid=338573ad1bdf4586aa17fab95f3a57d7. Accessed on: 02/03/2025.
- [240] MatWeb. E-Glass Fiber, Generic. https://www.matweb.com/search/datashee t.aspx?MatGUID=d9c18047c49147a2a7c0b0bb1743e812&ckck=1. Accessed on: 17/05/2025.
- [241] AZO Materials. Silicone Rubber. https://www.azom.com/properties.aspx?ArticleID=920. Accessed on: 17/05/2025.
- [242] Netzsch Polymers. EPDM: Ethylene-Propylene-Diene Rubber. https://polymers.netzsch.com/Materials/Details/55. Accessed on: 16/05/2025.
- [243] Wilhelm Herm. Müller. *Material Data Sheet PET White*. Heinrich-Nordhoff-Ring 14 30826 Garbsen Postfach 141230 30812 Garbsen.
- [244] Laminated Plastics. Technical Data Sheet PVC.
- [245] Luvata. Brass Alloy SM 1065. Luvata Sweden AB SE-721 10 Västerås Sweden.
- [246] Al6061t6. Aluminum 6061-T6 6061-T651.
- [247] Aerospace Specification Metals Inc. Aluminum 2219-T851, .
- [248] P.A. Dubock, F. Spoto, J. Simpson, D. Spencer, E. Schutte and H. Sontag. The Envisat Satellite and Its Integration. ESA bulleetin, Bulletin ASE, European Space Agency, June 2001.
- [249] R. Opromolla, G. Fasano, G. Rufino and M. Grassi. A Model-Based 3D Template Matching Technique for Pose Acquisition of an Uncooperative Space Object. Sensors, Mar 2015. doi: 10.3390/s150306360.
- [250] National Aeronautics and Space Administration NASA Space Science Data Coordinated Archive. Envisat 1. https://nssdc.gsfc.nasa.gov/nmc/spacecraft/display.action?id=2002-009A. Accessed on: 28/03/2025.
- [251] RussianSpaceWeb. Stage II of the Zenit Rocket. https://www.russianspaceweb.com/zenit_stage2.html, Jan 2013. Accessed on: 12/03/2025.
- [252] Astronautix. RD-8. http://www.astronautix.com/r/rd-8.html, . Accessed on: 20/05/2025.
- [253] Astronautix. RD-120. http://www.astronautix.com/r/rd-120.html, . Accessed on: 20/05/2025.
- [254] D. L. Akin. Mass Estimating Relations. University lecture, Launch and Entry Vehicle Design, 2016. University of Maryland.
- [255] GlobalSecurity.org. Advanced Mission Cost Model. https://www.globalsecurity.org/military/intro/reference/calc/AMCM.htm#Definitions, Apr 2005. Accessed on: 28/05/2025.
- [256] J. R. Wertz, D. F. Everett and J. J. Puschell. Space Mission Engineering: The New SMAD. Microcosm Press, 2011.

- [257] Defense Logistic Agency. Standard Prices for Aerospace Energy Category Items. 8725 John J. Kingman road, Fort Belvoir, Virginia, 2024.
- [258] N. Davinic, A. Arkus, S. Chappie and J. Greenberg. Cost-Benefit Analysis of On-Orbit Satellite Servicing. *Journal of Reducing Space Mission Cost*, 1:27–52, 1998.
- [259] Trading Economics. Euro Area Inflation Rate. https://tradingeconomics.com/euro-area/inflation-cpi, 2025. Accessed on: 01/06/2025.
- [260] Trading Economics. United States Inflation Rate. https://tradingeconomics.com/united-states/inflation-cpi, 2025. Accessed on: 01/06/2025.
- [261] Xe Currency Converter. 1 USD to EUR Convert US Dollars to Euros. https://www.xe.com/currencyconverter/convert/?Amount=1&From=USD&To=EUR. Accessed on: 01/06/2025.
- [262] N2YO. https://www.n2yo.com/satellite/?s=27386#results. Accessed on: 02/03/2025.
- [263] C. M. Barnes and E. M. Botta. A Quality Index for Net-Based Capture of Space Debris. *Acta Astronautica*, Jun 2020. doi: 10.1016/j.actaastro.2020.06.044.
- [264] M. Ehresmann, G. Herdrich and S. Fasoulas. An Automated System Analysis and Design Tool for Spacecrafts. CEAS Space Journal, Aug 2021. doi: 10.1007/s12567 -021-00383-3.
- [265] nVent. Copper Ground Plate. https://www.nvent.com/en-us/erico/products/copper-ground-plate-0. Accessed on: 03/04/2025.
- [266] Amazon. QWORK®Fio de cobre puro Ø2 mm comprimento 10 m fio 99 DIY. https://www.amazon.es/dp/B0CCKZVJQD/ref=asc_df_B0CCKZVJQD?language=pt_PT&mcid=f3c51872e2573c489157e3c3a2b4d27c&tag=ptgogshpadde-21&linkCode=df0&hvadid=718197195487&hvpos=&hvnetw=g&hvrand=12813241601491038567&hvpone=&hvptwo=&hvqmt=&hvdev=c&hvdvcmdl=&hvlocint=&hvlocphy=1011742&hvtargid=pla-2242287553438&gad_source=1&th=1. Accessed on: 03/04/2025.
- [267] N. J. Meckel, R. J. Kay, C. S. Engelbrecht, J. C. Dickens, A. D. Gallimore and M. J. Patterson. High Performance, Low Power Ion Propulsion System Design Concept. Proceedings of the Electric Rocket Propulsion Society, 2001.
- [268] Marshall Space Flight Center, National Aeronautics and Space Administration. Solar Cycle Progression and Forecast. https://www.nasa.gov/solar-cycle-progression-and-forecast/. Accessed on: 03/02/2025.
- [269] I. Ye. Telitchev and A. G. Prokhorov. Damage Parameters Analysis of Shielded Pressure Vessels Under Space Debris Impact. In Second European Conference of Space Debris, ESOC, Darmstadt, Germany, Mar 1997. ESA SP-393.
- [270] I. Telichev. Orbital Debris: Effect on Spacecraft Pressurized Structures. University of Manitoba.
- [271] F. Drouhin and S. Bindel. Routing and Data Diffusion in Vehicular Ad Hoc Networks: Path Loss. In *Building Wireless Sensor Networks*. Elsevier, 2017.
- [272] J. M. Felício. Radiopropagation: Atmospheric Effects. University lecture, Satellite Systems, 2024. Instituto Superior Técnico, Lisbon, Portugal.
- [273] J. M. Felício. Antenna Radiation. University lecture, Satellite Systems, 2024. Instituto Superior Técnico, Lisbon, Portugal.

- [274] European Space Agency and B. Bastida Virgili and S. Lemmens and H. Krag. Investigation on Envisat Attitude Motion, May 2014. Deorbit Workshop.
- [275] I. Korhonen and J. Ahola. Estimating the Specific Heat Capacity and Heating of Electronic Sensors and Devices. *IEEE Instrumentation & Measurement Magazine*, Feb 2018.
- [276] TCS Micropumps. Centrifugal Impeller Pumps (M-Series). https://micropumps.co.uk/centrifugal-impeller-pumps-m-series/. Accessed on: 27/03/2025.
- [277] J. Evans. Pumps & systems: Pump efficiency: What is efficiency? https://www.pumpsandsystems.com/pump-efficiency-what-efficiency#:~:text=Many%20 medium%20and%20larger%20centrifugal,break%20the%2090%20percent%20bar rier., Jan 2020. Accessed on: 17/03/2025.
- [278] Battery Design from Chemistry to Pack. Specific Heat Capacity of Lithium Ion Cells. https://www.batterydesign.net/specific-heat-capacity-of-lithium-ion-cells/, Jan 2022. Accessed on: 10/03/2025.
- [279] E. Redondo-Iglesias and S. Pelissier. On the Efficiency of LFP Lithium-ion Batteries. In Second International Conference on Sustainable Mobility Applications, Renewables and Technology (SMART), IEEE, Cassino, Italy, Nov 2022. doi: 10.1109/SMART55236.2022.9990093.
- [280] Quantum Controls. How do I classify the temperature limits of an Electric Motor? https://www.quantum-controls.co.uk/insights/faqs/how-do-i-classify-the-temperature-limits-of-an-electric-motor/. Accessed on: 19/03/2025.
- [281] J. Yu and J. Qian. Testing Methods for Electric Motors: Motor Losses and Efficiency Expression. In *Electrical Motor Products*. Elsevier, 2011.
- [282] X. Kong, H. Sun, S. Liang, Z. Yi, N. Gu and Y. Yi. Intelligent Space Thermal Control Radiator Based on Phase Change Material with Partial Visible Transparency. Coatings, 2024. doi: https://doi.org/10.3390/coatings14050535.
- [283] A. Pagani and M. Filippi. Esercitaioni dal corso di Fondamenti di Meccanica Strutturale. University lecture, 2022. Politecnico di Torino, Turin, Italy.
- [284] S. Brischetto. Modello della Trave a Semiguscio Ideale. University lecture, Costruzioni Aeronautiche, 2022-2023. Politecnico di Torino, Turin, Italy.
- [285] V. O. Gonçalves, L. C. Pardini, K. Garcia, A. C. Ancelotti Jr and E. M. Bezerra. Resistência ao cisalhamento losipescu em compósitos de fibras de carbonio e de vidro com resina epóxi. *Journal of Aerospace Technology and Management*, 1, Jun 2009.
- [286] S. Brischetto. Analisi della Stabilitá Elastica delle Strutture Aeronautiche. University lecture, Costruzioni Aeronautiche, 2022-2023. Politecnico di Torino, Turin, Italy.
- [287] L. Juusola and R. Hynönen. Chapter 3: The Earth's Dipole Field. Lecture, Geomagnetism, 2015. Ilmatieteen Laitos, Helsinki, Finland.
- [288] X. Wang, T. Ren, R. Wang, B. Luo, E. Aa, L. Cai, M. Li, J. Miao, S. Liu and J. Gong. Estimates of Spherical Satellite Drag Coefficients in the Upper Thermosphere During Different Geomagnetic Conditions. *Space Weather*, 22, Oct 2024. doi: https://doi.org/10.1029/2024SW003974.
- [289] M. C. N. Fiolhais, L. Gonzalez-Urbina, T. Milewski, C. Chaparro and A. Ferroglia.

- Orbital Decay in the Classroom, 2023. published by the City University of New York (CUNY).
- [290] Ulrich W. Astronautics: The Physics of Space Flight. Springer, 3rd edition, 2018.
- [291] National Aeronautics and Space Administration. CMCC Instant Run System, IRI. https://kauai.ccmc.gsfc.nasa.gov/instantrun/iri/, . Accessed on: 13/03/2025.
- [292] Fleron, R. A. W. and Blanke, M. Electron Emitter for small-size Electrodynamic Space Tether using MEMS Technology. In *Proceedings of the ESA Symposium on Small Spacecraft Systems*, pages 227–232, 2004.
- [293] M. Romano. Gravity Gradient Force and Torque. University lecture, Orbital Robotics and Distributed Space Systems, 2024. Politecnico di Torino, Turin, Italy.

Appendix A

Detailed Sizing Process

Δv Budget

Regarding orbit transfers, the approach described in Section 4.2.1 is here explained [69]. The time variation of the RAAN caused by J2 is given by:

$$\frac{\mathrm{d}\Omega}{\mathrm{d}t} = -\frac{3}{2}\sqrt{\frac{\mu}{a^3}} \frac{J_2 \cos i}{(1-e^2)} \left(\frac{r_E}{a}\right)^2 \tag{A.1}$$

where Ω is the RAAN, μ the Earth's gravitational constant, a the orbit's semimajor axis, i the orbit's inclination, e the orbit's eccentricity and r_E the Earth's radius. The time required for the optimal transfer (minimum Δv) is then:

$$t_{opt} = \frac{\Omega_k(t=0) - \Omega_{k+1}(t=0) + 2K\pi}{\dot{\Omega}_{k+1} - \dot{\Omega}_k}$$
 (A.2)

where the subscripts k and k+1 identify the parameters of the initial and final orbits respectively, K is the smallest integer (in module) allowing for $t_{opt} > 0$ and $\dot{\Omega}$ is the time rate of the RAAN, evaluated by using Equation A.1. After defining the optimal transfer time, the Δv consumption is evaluated as follows:

$$\frac{\Delta v}{v} = \sqrt{\left(\frac{0.5\Delta a}{a}\right)^2 + \Delta i^2 + (0.5\Delta e)^2} \tag{A.3}$$

where a is the average value of the semimajor axis of the two orbits, v the corresponding speed associated to the circular orbit with radius equal to a and Δ represents the differences between the COE of final and initial orbits.

If t_{opt} is too high and the time for the transfer is given beforehand, the Δv consumption is evaluated as follows [69]:

$$\Delta v = \sqrt{\Delta v_a^2 + (0.5\Delta v_e)^2} + \sqrt{\Delta v_b^2 + (0.5\Delta v_e)^2}$$
(A.4)

where:

$$\begin{cases}
\Delta v_a = \sqrt{(s_x x)^2 + (s_y y)^2 + (s_z z)^2} \\
\Delta v_b = \sqrt{(x - s_x x - \Delta x)^2 + (y - s_y y)^2 + (z - s_z z)^2} \\
\Delta v_e = \frac{1}{2} v_0 \sqrt{\Delta e_y^2 + \Delta e_x^2}.
\end{cases}$$
(A.5)

The parameters for Equation A.5 are obtained from [69].

The re-orbit and deorbit maneuvers are modelled as single-burns aiming at lowering the perigee of the starting orbit, and are performed at the apogee to be most effective [70]. Starting by evaluating the specific energy associated to the starting orbit at its apogee:

$$\varepsilon_i = -\frac{\mu}{2a_i} = \frac{v_{ap,i}^2}{2} - \frac{\mu}{r_{ap,i}} \tag{A.6}$$

where a_i is the semimajor axis, $v_{ap,i}$ the velocity at apogee and $r_{ap,i}$ the apogee altitude (from Earth's center), and introducing $r_{ap,i} = a_i(1 + e_i)$, it is possible to obtain the starting apogee speed:

$$v_{ap,i} = \sqrt{\frac{\mu}{a_i} \left(\frac{1 - e_i}{1 + e_i}\right)} \tag{A.7}$$

Since only the perigee changes while the apogee remains constant, the final semimajor axis is given by $a_f = (r_{pe,f} + r_{ap,i})/2$, where $r_{pe,f}$ is the new perigee. It is then possible to evaluate the new apogee speed:

$$v_{ap,f} = \sqrt{2\mu \left(\frac{1}{r_{ap,i}} - \frac{1}{2a_f}\right)} \tag{A.8}$$

The cost of the maneuver is $\Delta v = |v_{ap,f} - v_{ap,i}|$, where the module has been considered since both an increase and a decrease in the perigee are possible using this method. For re-orbit maneuvers varying the apogee, the procedure is the same: once the energy of the orbit has been defined at its perigee, the initial and final speeds in that position are evaluated as $v_{pe,i}$ and $v_{pe,f}$ respectively:

$$v_{pe,i} = \sqrt{\frac{\mu}{a_i} \left(\frac{1+e_i}{1-e_i}\right)}$$
 $v_{pe,f} = \sqrt{2\mu \left(\frac{1}{r_{pe,i}} - \frac{1}{2a_f}\right)}$ (A.9)

where $a_f = r_{pe,i} + r_{ap,f}$. The cost of the maneuver is then $\Delta v = |v_{pe,f} - v_{ap_i}|$.

Telecommunication System

The link budget formula (Equation 4.6) can be expanded as follows [71, 79, 80]:

$$\frac{E_b}{N_0} = P_t + G_t + L_t + L_{pr} + L_\alpha + L_S + \frac{G}{T} + 228.6 - 10\log_{10}R$$
 (A.10)

 L_t are the losses related to the transmitting antenna's line, and a typical value of 1 dB has been considered [271]. L_{pr} are the antenna pointing losses, assumed to be 0 dB. L_S are the free space losses:

$$\begin{cases} L_S = -22 + 20 \log_{10} \frac{\lambda}{S} \\ S = \sqrt{(r_E + h)^2 - r_E^2} \end{cases}$$
 (A.11)

where λ is the wavelength, h the satellite's altitude and r_E the Earth's radius [71]. To correctly evaluate L_S , the highest value of h during the mission shall be considered (worst case scenario) [79]. L_{α} are the atmospheric losses:

$$L_{\alpha} = L_{pm} + L_{qas} + L_{rain} + L_{clouds} + L_{ion} \tag{A.12}$$

where L_{pm} are the polarization mismatch losses (assumed to be 0.3 dB [71]), L_{gas} the atmospheric gas losses, L_{rain} the rain-induced losses, L_{clouds} the clouds-induced losses and L_{ion} the ionosphere losses [71]; each one of these losses can be evaluated from tables, given the frequency [272]: for the losses requiring a location, Lisbon has been selected, supposing the operative center to be located there. Ionospheric diffraction is neglected in Equation A.10, due to the high frequency of the communications [272].

The directional antenna's size has been evaluated as follows [73]; by obtaining the gain G_t from Equation A.10 in [dBi], after converting it to linear units, Equation A.13 can be applied:

$$g_t = \left(\frac{\pi D_p}{\lambda}\right)^2 \eta_{ap} \tag{A.13}$$

where g_t is the gain in linear units, D_p the antenna's diameter and η_{ap} the aperture efficiency. By considering the highest possible efficiency $\eta_{ap} = 0.81$, D_p can be evaluated. From graphs contained in [73], given η_{ap} and the selected feed system (conical horn), it is possible to determine f/D_p , where f is the focal distance (between reflector and feed), using a raised cosine coefficient of n = 2 [73]. By knowing the reflector's diameter, its density (Kapton [82], 1.42 g/cm³ [239]) and its thickness [82], the mass can be determined. Once the reflector's dimensions have been evaluated, it is possible to find the feed's directivity:

$$\begin{cases} d(\theta) = d_0 \cos^n(\theta) \\ d_0 = 2(n+1) \end{cases}$$
 (A.14)

where θ is the beamwidth angle $[0 < \theta < \theta_0]$, θ_0 the angular aperture of the antenna and d_0 the directivity (in linear units) at $\theta = 0^{\circ}$. A perfect coverage of the reflector has been hypothesized (no spillover or taper effects [73]). The radius of the horn antenna has been determined as follows:

$$d_0 = \left(\frac{2\pi a_h}{\lambda}\right)^2 \tag{A.15}$$

where a_h is the unknown value. After defining the half-power beamwidth of the cone [273]

$$\theta = \sqrt{\frac{4\pi}{d_0}} \tag{A.16}$$

its height can be determined:

$$h_h = \frac{a_h}{\tan \theta}.\tag{A.17}$$

A 0.1 mm thick copper foil has been considered for the conical horn feed structure [83]. The length of the support sticks has been evaluated as $l = \sqrt{(D_p/2)^2 + f^2}$, where D_p is the reflector diameter and F the focal distance.

The capacity of the gimbal [85] to rotate the antenna has been proven as well. The

parabolic reflector has been considered to be a disc, whose inertia moment is $I = \frac{1}{4}m\left(\frac{D_p}{2}\right)^2$ for a rotation about its diameter (since the thickness is small compared to the radius, the $\frac{1}{12}ms^2$ contribute has been neglected). Supposing the antenna pointing at Nadir while the satellite is at its perigee (most demanding movement in terms of angular velocity), the time required to move the antenna has been estimated as follows. First, perigee's orbital speed and altitude have been evaluated [70]:

$$\begin{cases} v_{pe} = \sqrt{\frac{\mu}{a} \frac{1+e}{1-e}} \\ r_{pe} = a(1-e) \end{cases}$$
 (A.18)

where μ is the Earth's gravitational constant, a the semimajor axis of the orbit and e the eccentricity of the orbit; the instantaneous angular velocity at which the Nadir moves is then:

$$\omega = \frac{v_{pe}}{r_{pe} - r_E} \tag{A.19}$$

where r_E is the Earth's radius. By knowing the torque M_t the gimbal can apply [85], the time t required for the rotation is calculated:

$$M_t = I\alpha = \frac{I\omega}{t} \tag{A.20}$$

The value of t is then checked to be low enough (< 1 s) for a successful tracking of the ground station.

Attitude Determination and Control System

To evaluate the time required by CMGs to rotate the system (spacecraft only or spacecraft and debris) of 180°, the inertia of the satellite shall be evaluated first. The spacecraft is considered to be a cylinder (see Section 4.2.2): Figure A.1 shows the selected reference frame, while Figure A.2 shows the same frame applied to the system considering both satellite and debris.

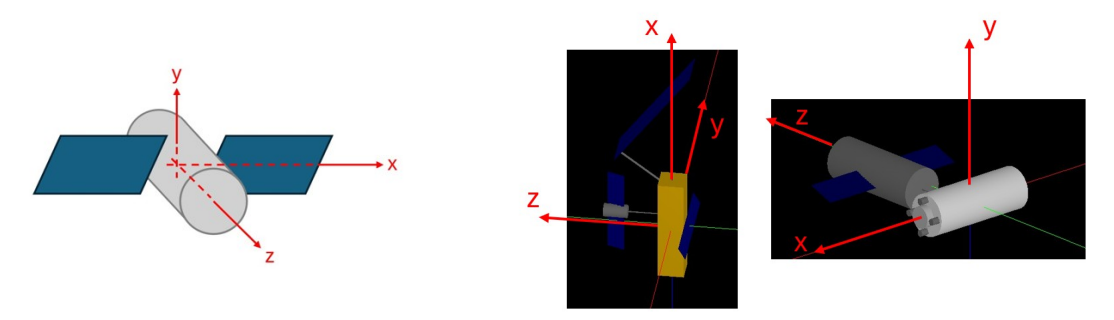


Figure A.1: Satellite Reference Frame

Figure A.2: Satellite Reference Frame Applied to EN-VISAT (SCST, left) and Zenit-2 (SCMT, right)

In both cases, the origin of the reference frame coincides with the center of mass of the

system, and the robotic arm for docking lies on the line connecting the centers of mass of the satellite and the debris. Once the mass and the dimensions of the satellite are known, it is possible to evaluate its moments of inertia for rotations about the axes x, y and z. The moments of inertia of the solar panels have been calculated separately, considering two rectangles whose long sides are twice the length of the short sides. Lastly, the inertia of the debris is added: data for ENVISAT and Zenit-2 are taken from [274] and [250] respectively. No coupling between rotations is considered $(I_{xy}, I_{xz}, I_{yz} \ll I_{xx}, I_{yy}, I_{zz})$. Once the moments of inertia of the system have been evaluated, the angular acceleration α is obtained by dividing the output torque M_t of the CMGs (only one per axis considered) by the moment of inertia I. The time required for the full 180° maneuver is then:

$$t = \sqrt{\frac{2\theta}{\frac{1}{\alpha} + \frac{1}{\delta}}} \left(\frac{1}{\alpha} + \frac{1}{\delta} \right) \tag{A.21}$$

where $\delta = \alpha$ is the angular deceleration, to guarantee the rotation to stop at exactly 180°, and $\theta = 180$ °.

To model the amount of propellant required by attitude control thrusters, a fixed burn time has been considered: 1 s when the satellite is not docked to the debris and 10 s when the satellite and the debris are linked (since the inertia is much larger, a longer time interval has been considered to speed up the maneuver). The number of the considered maneuvers changes depending on the mission architecture: whenever the spacecraft docks or separates from a debris, two full rotations of 180° about each axis (x, y and z) are considered as a first conservative approximation (one rotation without debris, and the other one considering docking with the target). To determine the consumed hydrazine for each burn, the mass flow rate of the engines has been calculated from $\dot{m} = \frac{F}{v_{ex}}$, where F is the thrust, $v_{ex} = I_{sp}g_0$ is the exhaust speed and I_{sp} is the engine's specific impulse; the fuel consumption for each engine is then $m_p = \dot{m}t_b$, where t_b is the burn time. The disposition of the attitude control thrusters is shown in Figure A.3. For each maneuver,

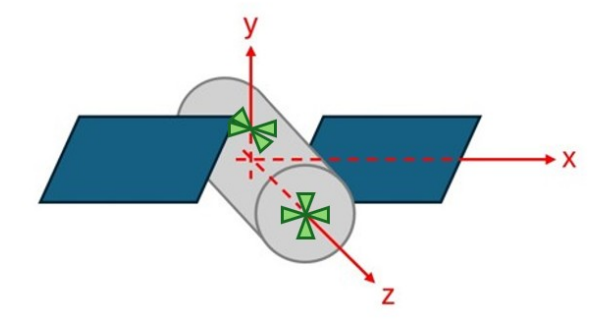


Figure A.3: ADCS Thrusters Disposition (only Visible Ones are Included, the remaining Two Arrays are Symmetrical with respect to the Center of Mass of the Satellite)

only the engines generating a moment about the selected axis are considered to be active. The overall torque applied by the engines on the system is $M_t = \sum_j F_j b_j$, where F is the thrust and b the distance between the application point of F and the rotation axis. The angular acceleration of the system is $\alpha = \frac{M_t}{I}$ where I is the moment of inertia for

a rotation about the chosen axis, and by knowing the burning time t_b , the final angular velocity is $\omega = \alpha t_b$. Once the rotation angles of the system during acceleration (θ_a) and deceleration (θ_d) have been determined through the kinematic equations, the overall time required by the maneuver is $t = 2t_b + \frac{\pi - \theta_a - \theta_d}{\omega}$.

Orbit Determination and Control System

Tanks and vessel's wall thicknesses have been evaluated by using Equation A.22:

$$2\pi R_t s\sigma = 1.2\pi R_t^2 p_0 \tag{A.22}$$

where R_t is the tank's radius, s is the unknown wall thickness, p_0 is the internal pressure, σ is the maximum tension before rupture and 1.2 is a safety factor [104]. The internal pressures considered for the tanks are: the highest of the maximum inlet pressures of ADCS and ODCS thrusters for the hydrazine tank, the maximum inlet pressure of the ODCS thruster for the nitrogen tetroxide tank and 310 bar for the helium vessel [108]. Values for σ and ρ (density) of Ti6Al4V are taken from [104]. No friction losses are considered in the pipelines connecting tanks and engines.

The amount of helium needed to successfully pressurize both fuel and oxidizer's tanks considering an adiabatic emptying is determined as follows; first, the 1st thermodynamic principle shall be applied before and after the transformation:

$$\begin{cases}
pV_p = U_i - U_f \\
U_i = c_v m_0 T_0 \\
U_f = c_v m_g T_g + c_v mT
\end{cases} \longrightarrow pV_p(\gamma - 1) = p_0 V_0 - p_g V_0 - pV_p \tag{A.23}$$

where V_p is the volume of the consumed propellant, p the final pressure inside the tanks (which is equal to the final pressure inside the vessel), p_0 the initial pressure inside the vessel, V_0 the vessel's volume, p_g the final pressure inside the vessel and γ the ratio of the specific heats: the only unknown quantity is V_0 . Then, the mass of the pressurant gas can be evaluated by using Equation A.24 [104]:

$$m_0 = \frac{\gamma p V_p}{1 - p_0/p_0} \frac{1}{R_{He} T_0} \tag{A.24}$$

where R_{He} is the helium gas constant.

Thermal Control System

Table A.1 contains data regarding components requiring an active TCS to work properly: C is the specific heat, T_{max} and T_{min} the maximum and minimum operative temperatures and η the efficiency.

Table A.1: Data for Components Requiring an Active TCS

	C [J/kgK]	T_{max} [K]	T_{min} [K]	η
Omni. Antenna (ComSys)	690 [275]	353 [72]	253 [72]	$0.95^{\rm b}$
Dir. Antenna (ComSys)	690 [275]	353 [72]	253 [72]	$0.95^{\rm b}$
Modem (ComSys)	690 [275]	323 [86]	273 [86]	$0.95^{\rm b}$
Transponder (ComSys)	690 [275]	344 [88]	239 [88]	$0.95^{\rm b}$
Diplexer (ComSys)	690 [275]	353 [89]	233 [89]	$0.95^{\rm b}$
Gimbal (ComSys)	$604.56^{\rm e}$	353 [85]	233 [85]	$0.95^{\rm b}$
Coaxial Cables (ComSys)	690 [275]	358 [90]	228 [90]	$0.95^{\rm b}$
CMG (ADCS)	604.56^{c}	313 [101]	263 [101]	$0.95^{\rm b}$
Star Tracker (ADCS)	690 [275]	368 [93]	233 [93]	$0.95^{\rm b}$
Valves (ADCS and ODCS)	$466^{\rm d}$	353 [110]	278 [110]	$0.95^{\rm b}$
OBC (DHS)	690 [275]	358 [111]	233 [111]	$0.95^{\rm b}$
Pump (TCS)	$466^{\rm d}$	353 [276]	273 [276]	0.70 [277]
Battery (EPS)	1040 [278]	318 [113]	253 [113]	0.95 [279]
Solar Arrays (EPS)	$330^{\rm a}$	383^{a}	123 ^a	0.32 [113]
Gimbal (EPS)	$604.56^{\rm e}$	353 [126]	233 [126]	$0.95^{\rm b}$
Wiring (EPS)	690 [275]	473 [197]	73 [197]	0.95 [91]
Switches (EPS)	690 [275]	363 [127]	223 [127]	0.95 [91]
Regulation (EPS)	_	_	_	0.80 [91]
Camera (DockSys)	690 [275]	313 [75]	243 [75]	$0.95^{\rm b}$
Electric Motor (DockSys)	690 [275]	313 [280]	253 [280]	0.89 [281]
Electric Motor (Kits)	690 [275]	313 [280]	253 [280]	0.89 [281]
Switches (Kits)	690 [275]	363 [127]	223 [127]	0.95 [91]

^a Typical value for GaAs.

Considering the satellite to reach the maximum LEO temperature T_{MAX} (+77°C) at the end of its exposure to sunlight and assuming a linear increase of the temperature during that time, the total energy to subtract is:

$$E_{cool} = \sum_{j} C_j m_j (T_{MAX} - T_{max,j})$$
(A.25)

where m_j is the mass of the j-th component, C_j its specific heat and $T_{max,j}$ its maximum operative temperature. Meanwhile, the subsystems of the satellite are active and they dissipate energy as well; the power dissipation is given by:

$$P_{diss} = \sum_{j} P_j (1 - \eta_j) \tag{A.26}$$

^b Assumed value for η .

 $^{^{\}rm c}$ Assuming 1/3 aluminium and 2/3 steel [10].

^d Assuming steel [193].

 $^{^{\}rm e}$ Assuming same C of CMGs, due to their similar composition.

where P_j is the electrical power flowing through the j-th component and η_j its efficiency. The overall power to subtract to the satellite by active cooling is then:

$$P_{cool} = P_{diss} + \frac{E_{cool}}{t_{Sun}} \tag{A.27}$$

where t_{Sun} is the exposure time at sunlight, evaluated in Appendix A. Since solar panels are external to the spacecraft, they are excluded from this process and are cooled down by tilting them instead (see Section 4.2.2).

When the satellite crosses the Earth's shadow cone, its temperature is assumed to decrease linearly until it reaches the minimum LEO temperature T_{MIN} (-22°C) at the end of the eclipse time. The energy to add to the subsystems to warm them up is:

$$E_{warm} = \sum_{j} C_{j} m_{j} (T_{min,j} - T_{MIN}) \tag{A.28}$$

where $T_{min,j}$ is the minimum operative temperature of the j-th component. Also in this case, power dissipation is considered and the heat produced can be exploited to warm up the spacecraft. The total power required to warm up the spacecraft is then:

$$P_{warm} = \frac{E_{warm}}{t_{eclipse}} - P_{diss} \tag{A.29}$$

where $t_{eclipse}$ is the eclipse time. Since solar arrays are external to the satellite, they have been excluded from the evaluation of P_{diss} . P_{warm} also considers the power to avoid the coolant fluid to freeze during the eclipse phase (since water is used).

Once P_{cool} has been determined, supposing no losses between the cold plates and the radiator, the heat shall be irradiated outside the spacecraft. The surface A of the radiator is sized by using the Stephan-Boltzmann law:

$$P_{cool} = \varepsilon_r \sigma_S A (T_{fluid}^4 - T_{space}^4)$$
 (A.30)

where ε_r is the emissivity of the radiator (assuming a value of 0.51 [282]), σ_S the Stephan-Boltzmann constant, T_{space} the outer temperature (supposed to be equal to $T_{MIN} = -22^{\circ}\text{C}$), and T_{fluid} the temperature of the coolant fluid entering the radiator. T_{fluid} has been estimated as follows; first, the power subtracted by the j-th cold plate (associated to the j-th component) has been transformed in an increase in the temperature of the mass-flow rate of coolant:

$$P_{cool,j} = \dot{m}_{coolant,j} C_{coolant} (T_{max,j} - T_{min})$$
(A.31)

where $T_{max,j}$ is the maximum operative temperature of the j-th component and T_{min} the initial temperature of the coolant entering the cold plate; Equation A.31 is then solved for $\dot{m}_{coolant}$, allowing for the evaluation of the mass flow rate passing through the j-th cold plate. The overall thermal power associated to the mass flow rate entering the radiator is given by:

$$P_{rad} = \sum_{j} \dot{m}_{coolant,j} C_{coolant} T_{max,j} = \left(\sum_{j} \dot{m}_{coolant,j}\right) C_{coolant} T_{fluid}. \tag{A.32}$$

 T_{fluid} can then be evaluated:

$$T_{fluid} = \frac{\sum_{j} \dot{m}_{coolant,j} C_{coolant} T_{max,j}}{(\sum_{j} \dot{m}_{coolant,j}) C_{coolant}} = \frac{\sum_{j} \dot{m}_{coolant,j} T_{max,j}}{\sum_{i} \dot{m}_{coolant,j}}$$
(A.33)

During the whole estimation process, losses are neglected, and pipelines have been considered not to interfere during thermal exchanges.

Electrical Power System

A simple procedure to evaluate the eclipse time of an orbit is here presented [113], which might be useful not only during EPS sizing, but also to determine the solar exposure for the TCS. First, considering a circular orbit, it is possible to define the semi-amplitude of the shadow cone of the Earth, ρ_s , as follows:

$$\rho_s = \arcsin\left(\frac{r_E}{r_E + h}\right) \tag{A.34}$$

where r_E is the Earth's radius and h is the orbit's altitude. Then, by proportion, the eclipse time of the orbit is given by:

$$\begin{cases} t_{eclipse} = \frac{2\rho_s}{2\pi} T_{orb} = \frac{\rho_s}{\pi} T_{orb} \\ T_{orb} = 2\pi \sqrt{\frac{(r_E + h)^3}{\mu}} \end{cases} \longrightarrow t_{light\ time} = T_{orb} - t_{eclipse}$$
 (A.35)

where μ is the Earth's gravity constant and T_{orb} the orbital period at altitude h.

DockSys

A basic approach to verify the structural requirements for the robotic arm is reported. First, knowing the geometry and the mass of the robotic arm, we can define the thickness of the tubes that compose it. The volume V of the carbon fiber material of the arm is given by its mass divided by the density [142]. Knowing the external radius R_e of the outer section, the internal radius of the inner tube can be defined:

$$R_i = \sqrt{R_e^2 - \frac{V}{l\pi}} \tag{A.36}$$

where l is the length of each section (or the overall length of the retracted arm). The thickness of each tube is then:

$$s = \frac{R_e - R_i}{6}.\tag{A.37}$$

Three different analyses are performed on the arm's structure: bending during attitude control maneuvers, torsion during attitude control maneuvers and buckling during accelerations (since the arm extends between the centers of mass of spacecraft and debris, and an acceleration of the system leads to its compression).

• **Bending:** During attitude control maneuvers about axes x and y (Figure A.1), the robotic arm connecting the satellite and the debris shall withstand the applied

bending. First, the inertia moment of each section of the arm shall be evaluated [283]:

$$I_x = I_y = \frac{\pi}{4} (R_e^4 - R_i^4) \tag{A.38}$$

Equation A.38 applies on ring sections, such as the ones of the telescopic arm. A beam with fixed-free edges represents the worst case configuration for the structural analysis, allowing for the maximum value of the moment to be applied at the fixed end [283]. Then, using the Navier formula (Equation A.39), the maximum value of σ_{zz} has been calculated:

$$\begin{cases}
\sigma_{zz,x} = \frac{N}{A} + \frac{M_x}{I_x} y + \frac{M_y}{I_y} x = \frac{M_x}{I_x} y \\
\sigma_{zz,y} = \frac{N}{A} + \frac{M_x}{I_x} y + \frac{M_y}{I_y} x = \frac{M_y}{I_y} x
\end{cases}$$
(A.39)

where N is the normal stress, A the section's area, M_x and M_y the moments generated by the maneuvers about the x and y axes respectively, and x and y the coordinates along the x and y axes. To be conservative, the maximum value of $\frac{R_e}{I}$ has been considered for $\frac{y}{I_x}$ and $\frac{x}{I_y}$. The obtained values of σ_{zz} are then compared to the module of rupture of the arm's material [142]. No torsion is applied to the arm during these maneuvers, since its section is bi-symmetrical.

• Torsion: During attitude control maneuvers about the z axis (Figure A.1), the robotic arm connecting the satellite and the debris shall withstand the applied torsion. The De-Saint-Venant beam theory is applied (Equation A.40) [284]:

$$\tau_{max} = \frac{M_z}{I_p} s \tag{A.40}$$

where M_z is the torque, $I_p = I_x + I_y$ the polar moment of inertia of the section and s the section's thickness. To be conservative, the minimum I_p has been considered for the sizing process (since s is assumed to be constant among the arm's sections). τ_{max} is then checked to be smaller than the maximum allowable shear stress [285]. During the process, the arm is supposed to be perfectly aligned with the center of mass of satellite and debris (pure torsion case).

• Buckling: During orbital control maneuvers, the robotic arm connecting the satellite and the debris shall withstand the applied compression force. Supposing the engine to be perfectly aligned with the robotic arm (so, a pure compression is generated), buckling shall be avoided. The critical load for a compressed rod is obtained from Equation A.41 [286]:

$$F_{cr} = \kappa \frac{\pi^2 EI}{l^2} \tag{A.41}$$

where κ is a factor depending on the external constraints, $EI = 7000 \text{ Nm}^2$ [133], and l is the length of the arm. The worst case scenario (smallest F_{cr}) consists of a fixed-free rod ($\kappa = 0.25$). F_{cr} is then compared to the thrust generated by the engine, verifying the buckling resistance of the structure.

Debris Protection System

The sizing process of the Whipple shields is taken from [143]. To determine the thickness of the rear wall for a single Whipple shield, Equation A.42 is applied:

$$s_{wall} = 0.167 F_2^* \rho_s^{1/6} m_p^{1/2} v \sqrt{\frac{482}{S\sigma_y}}$$
 (A.42)

$$F_2^* = \begin{cases} 1 & if & \frac{t_s}{d} > 0.2\\ 5 - 40\left(\frac{t_s}{d}\right) + 100\left(\frac{t_s}{d}\right)^2 & if & \frac{t_s}{d} < 0.2 \end{cases}$$
(A.43)

where ρ_s is the shield's density [g/cm³], t_s the shield's thickness [cm], m_p the projectile's mass [g], σ_y the yielding tension of the rear wall [ksi], v the projectile's relative speed [km/s], d the projectile's diameter [cm] and S the distance between shield and wall [cm]. For a double Whipple shield, Equation A.44 is used:

$$s_{wall} = 0.167 F_3^* K_3 \rho_{s,1}^{1/6} m_p^{1/2} v \sqrt{\frac{482}{S_{tot} \sigma_y}}$$
(A.44)

$$K_3 = 0.395 \left(\frac{d - d_B}{d_B}\right)^{0.25} \tag{A.45}$$

$$d_B = \left(\frac{8.29t_{s,2}}{F_2^* \rho_{s,1}^{1/6} \rho_p^{1/2} v} \sqrt{\frac{S_1 \sigma_y}{482}}\right)^{2/3}$$
(A.46)

$$F_3^* = \begin{cases} 1 & if \quad \frac{t_{s,1}}{d} > 0.15\\ 5 - 53.33 \left(\frac{t_{s,1}}{d}\right) + 177.78 \left(\frac{t_{s,1}}{d}\right)^2 & if \quad \frac{t_{s,1}}{d} < 0.15 \end{cases}$$
(A.47)

where the subscripts 1 and 2 refer, respectively, to the inner and the outer shields, and S_{tot} refers to the sum of the spaces between the two shields and between the inner shield and the rear wall [cm].

De-Orbit Kits

The sizing process of the tether aims at verifying which length is more convenient to have a fast disposal of the debris and a low overall mass. Different lengths (from 10 to 20 km) have been considered. To determine the Lorentz force acting on the cable, the average current flowing through the wire is evaluated [46]:

$$\begin{cases}
I_{av} = \frac{3}{5} \eta_{tether} I_{ch} \\
I_{ch} = \frac{4w}{3\pi} N_e \sqrt{\frac{2E_r}{m_e} q_e^3 l^3}
\end{cases}$$
(A.48)

where w is the tether's width, N_e the electron density, E_r the projection of the local motional electric field along the tether's line, m_e the electron's mass, q_e the electron's

charge and l the tether's length; η_{tether} is the Ohmic efficiency of the tether, evaluated as in Equation A.49 [146]:

$$\begin{cases} \eta_{th} = \frac{1}{1+2\sqrt{\Gamma}} \\ \Gamma = \frac{\alpha\rho}{\beta\sigma E_m^2} \end{cases}$$
 (A.49)

where $\alpha = 2.25$, $\beta = 6$ kg/kW, $\sigma = 3.5 \cdot 10^7$ Ω m and $\rho = 2.7 \cdot 10^3$ kg/m³ are referred to an aluminium tether [146]. The value considered for E_r is estimated by developing the cross product in Equation A.50, considering the radial component of the electric field only (which develops along the tether's line, supposing a perfect Nadir deployment):

$$\begin{cases}
E_r = |\mathbf{E} \cdot \hat{e}_r| = |(\mathbf{B} \times \mathbf{v}) \cdot \hat{e}_r| = v_{\varphi} B_t = \sqrt{\frac{\mu}{r_E + h}} \cos(i) B_t \\
B_t = \frac{k_0}{(r_E + h)^3} \cos \Lambda
\end{cases}$$
(A.50)

where **B** is the magnetic field's vector, **v** the velocity vector of the debris, v_{φ} the speed component of **v** in the azimuthal direction, B_t the transversal (North-South) component of the Earth's magnetic field [287] (approximating it as a dipole, where $k_0 = 8 \cdot 10^{15} \text{ Tm}^3$ [287]), Λ the current latitude and \hat{e}_r the radial unit vector. For the evaluation of E_r , B_{φ} has been considered to be zero (according to [287]). The final Lorentz force acting on the tether is then:

$$|\mathbf{F}| = |I_{av}Bl(\hat{e}_r \times \hat{e}_B)| = I_{av}B_t l \tag{A.51}$$

since \hat{e}_B is the magnetic field's unit vector, and B_t is the only component of **B** perpendicular to the tether's direction line \hat{e}_r due to the dipole approximation [46, 287]. The Lorentz force is applied together with the aerodynamic drag, modelled from Equation A.52:

$$D = \frac{1}{2}C_D\rho(h)Av^2 \tag{A.52}$$

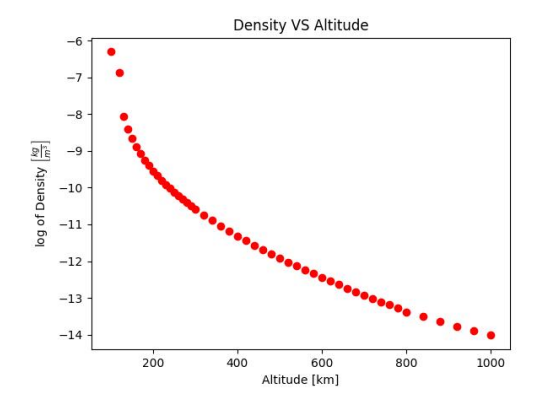
considering A as the sum of the exposed area of the (tumbling) debris and the tethers' surface [39]. $C_D = 2.2$ [288] has been considered. The time required to deorbit the satellite can be evaluated, solving the Ordinary Differential Equation (ODE) A.53 [289]:

$$\begin{cases}
\frac{\mathrm{d}v}{\mathrm{d}t} = -\frac{F+D}{m} \\
\frac{\mathrm{d}}{\mathrm{d}t} \left(-\frac{\mu m}{2(r_E+h)} \right) = \mathbf{D} \cdot \mathbf{v} + \mathbf{F} \cdot \mathbf{v}
\end{cases} \longrightarrow \begin{cases}
\frac{\mathrm{d}v}{\mathrm{d}t} = -\frac{F+D}{m} \\
\frac{\mathrm{d}r}{\mathrm{d}t} = \frac{\mathrm{d}h}{\mathrm{d}t} = -\frac{(D+F)v}{\mu m/[2(r_E+h)^2]}.
\end{cases} (A.53)$$

The models used for the simulations are:

- Atmospheric Model: the atmospheric density has been evaluated as a function of the altitude, considering an average value between the *Solar Maxima* and *Solar Minima* periods from [290] (see Figure A.4);
- Ionospheric Model: the electron density N_e for Equation A.48 has been evaluated using the International Reference Ionosphere (IRI), considering a day of medium solar activity (01/01/2026), during early morning, averaging the values for different latitudes [291] (see Figure A.5). Only the latitudes smaller than the orbit inclination have been used each time. N_e is then divided by 10, to better account for the interval of times where the electron density drastically drops (night-time and Solar Minima);

• Magnetic Field Model: a simple dipole model has been implemented [287], considering the mean integral value between the maximum and minimum latitudes that the debris covers during its orbit.



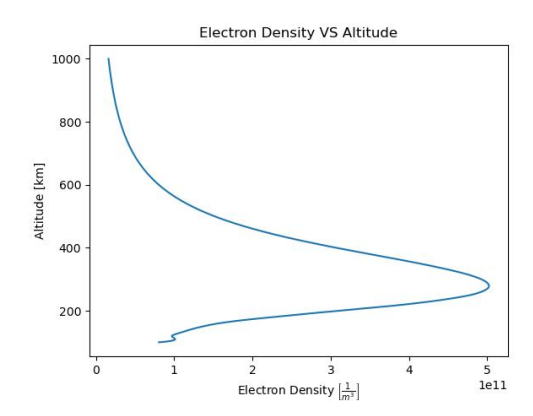


Figure A.4: Atmospheric Model

Figure A.5: Ionospheric Model

Once the current flowing through the tether has been evaluated, it is possible to determine whether or not an end-mass is needed for the deployment. A maximum allowable current before the Lorentz force is no longer balanced by the gravity gradient's effect can be obtained through Equation A.54 [292, 293]:

$$I_{max} = \frac{3\omega_0^2}{B_\perp} \left(m_{endmass} + \frac{1}{2} m_{tether} \right) = \frac{3\mu}{k_0 \cos(\Lambda)} \left(m_{endmass} + \frac{1}{2} m_{tether} \right)$$
 (A.54)

where $B_{\perp} = B_t$. The maximum current without an end-mass can be evaluated by considering $m_{endmass} = 0$; if $\max(I_{av}) > I_{max}$, a value for the end-mass is then obtained by substituting I_{max} with $\max(I_{av})$ and solving Equation A.54 for $m_{endmass}$.

Appendix B

1st Level Functions Sequence for the Selected ADR Architectures

In Figures B.1, B.2 and B.3 are contained the main phases of the missions (top), and the sequence of the identified 1st level functions for the whole mission duration (bottom).

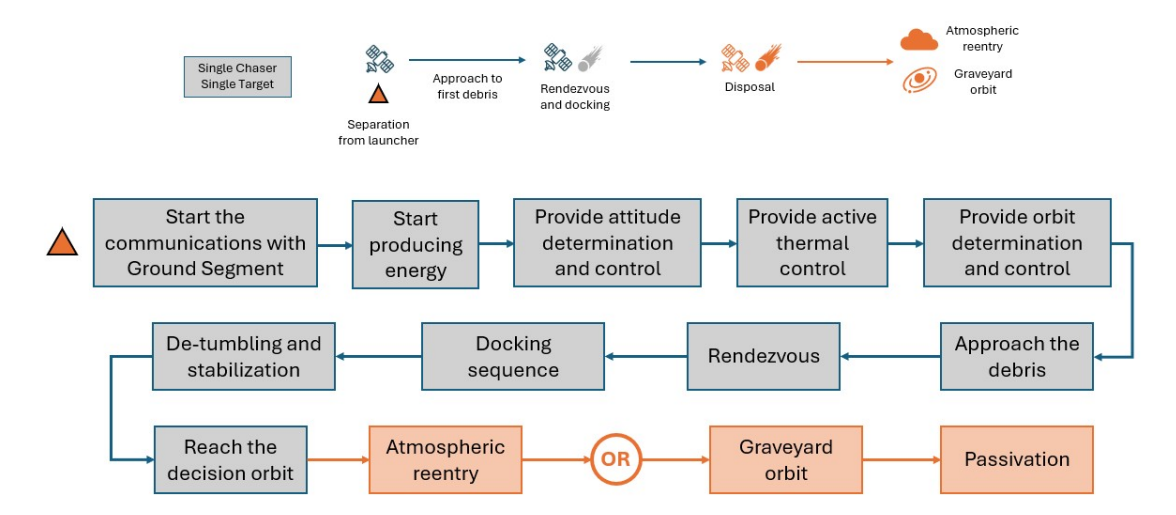


Figure B.1: Phases and 1st Level Functions for SCST

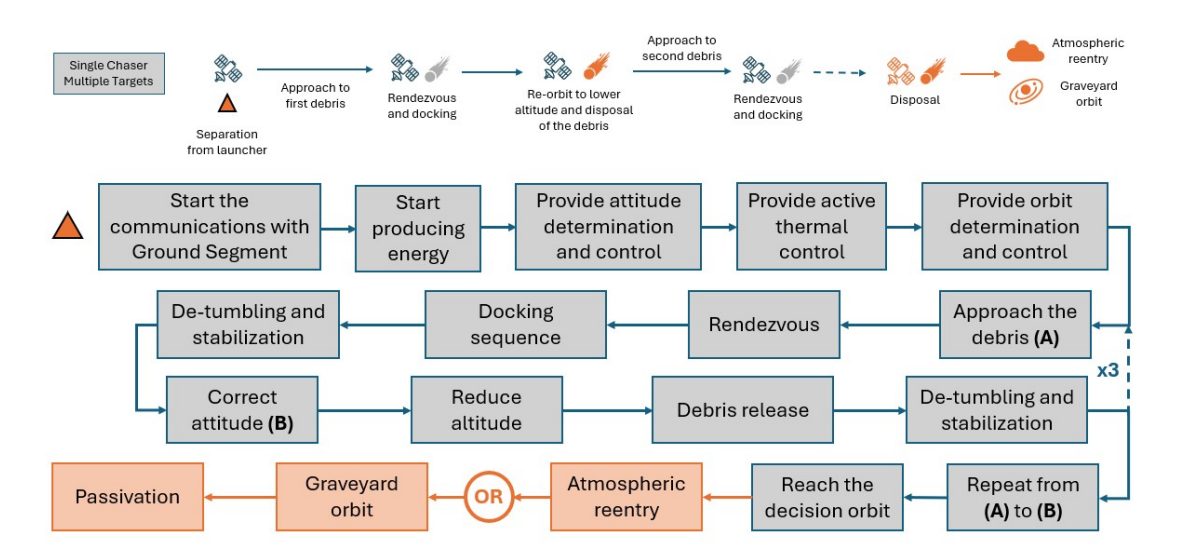


Figure B.2: Phases and 1st Level Functions for SCMT

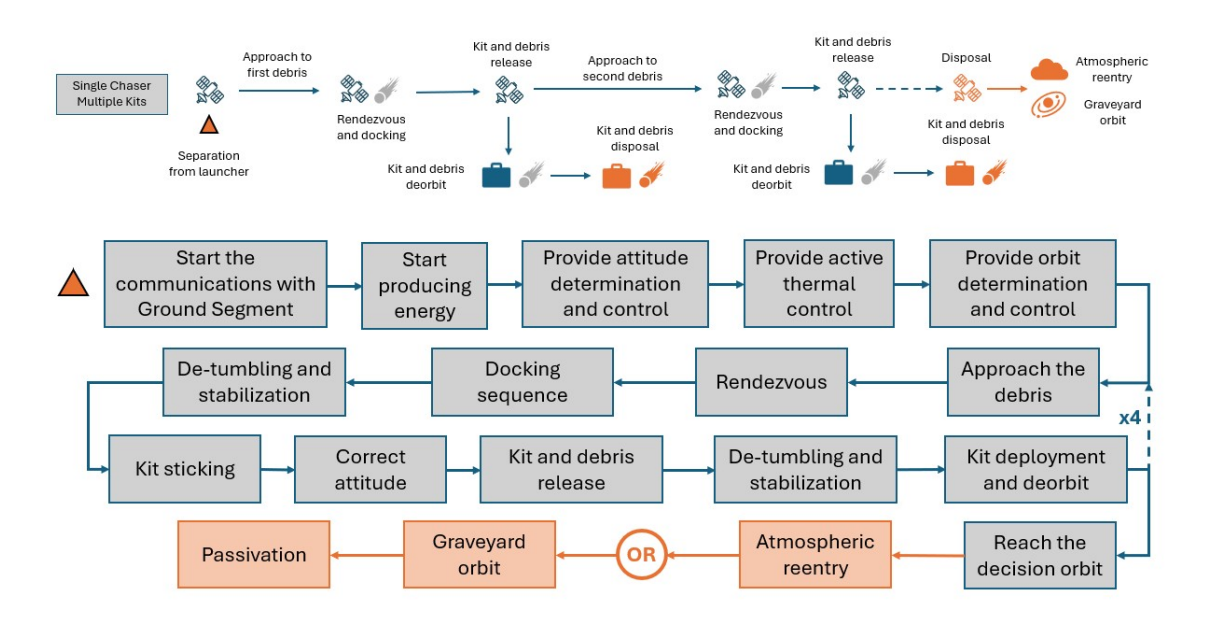


Figure B.3: Phases and 1st Level Functions for SCMK

Appendix C

Detailed N2 Diagrams

The next pages show the detailed N2 diagrams for each subsystem, highlighting the interfaces of each component with the others of the satellite: for each picture, red lines represent the items of the subsystem in analysis, while the others are kept in blue.

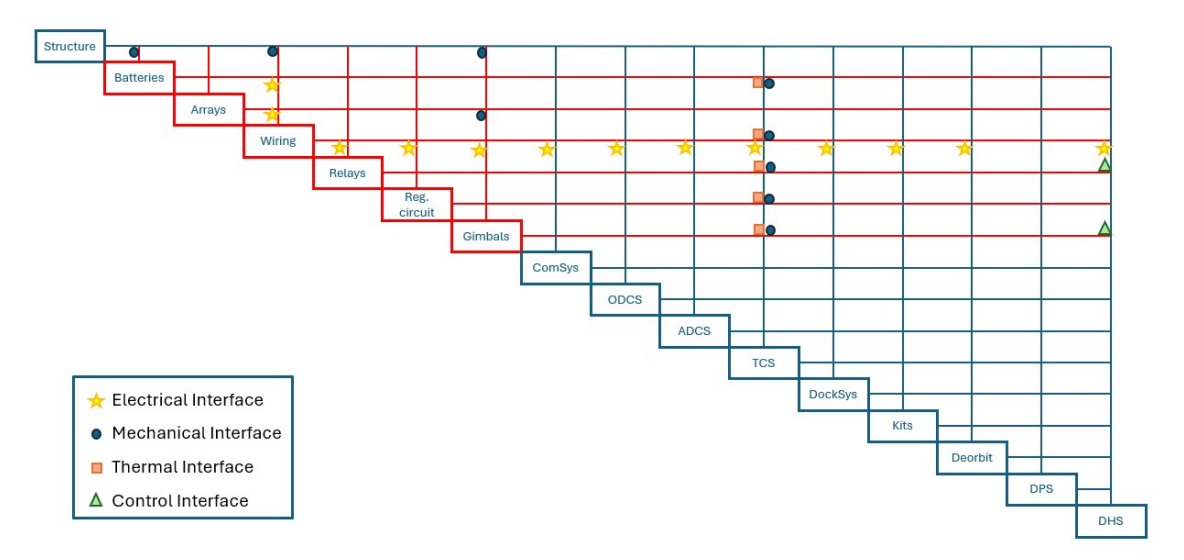


Figure C.1: N2 Diagram for the EPS

Figure C.1 shows the N2 diagram for the EPS: it becomes evident how the wiring is the medium for the electrical energy transfer, and the support function of the structure is again underlined. The solar arrays are not mechanically connected to the structure but to the gimbals, which are then linked to the satellite's frame. The control provided by the DHS is important for the relays (switches) management, and for the correct orientation of the solar panels as well. The TCS plays a crucial role, allowing for the correct temperature range to be applied to each component (without considering the solar arrays, whose temperature can be controlled by changing their orientation with respect to the Sun).

In Figure C.2 is represented the N2 diagram for the ComSys: all the components requiring electrical energy to exploit their functions (MODEM, transponder, etc.) are connected

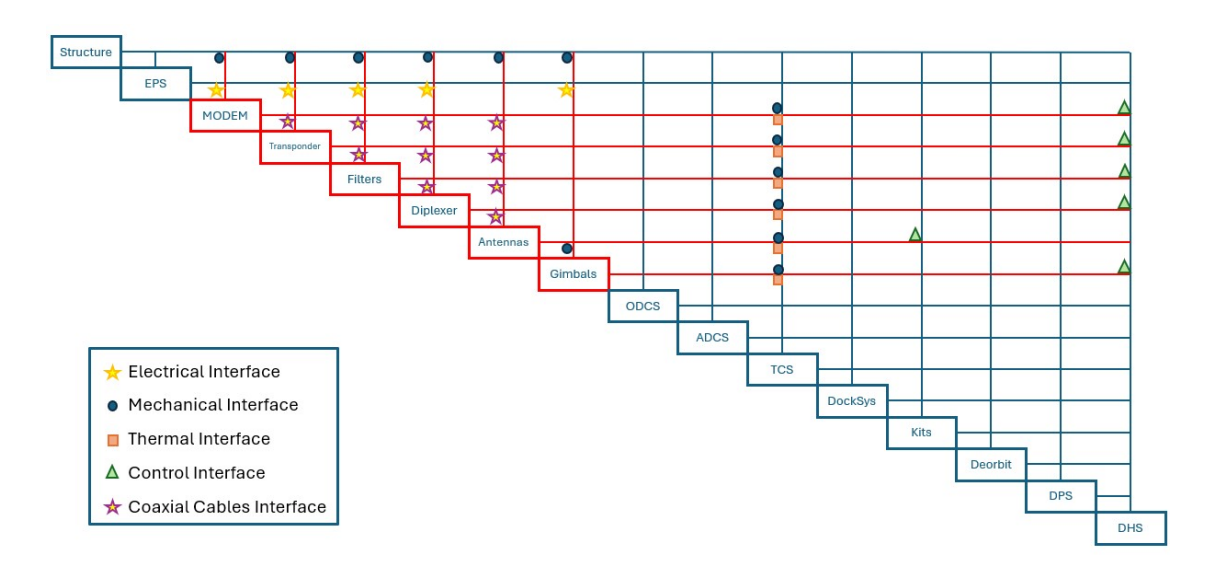


Figure C.2: N2 Diagram for the ComSys

to the EPS, and the structure acts as the support frame. The items requiring a cooling or heating system are interfaced to the TCS, and the DHS manages the data flux through the entire ComSys. Antennas are mechanically connected to the gimbals if necessary, and are responsible of the deployment of the deorbit kits on the debris (justifying the control interface with the "Kits" subsystem). Lastly, every component managing communication data is considered to be connected through coaxial cables, which represents an exclusive ComSys interface.

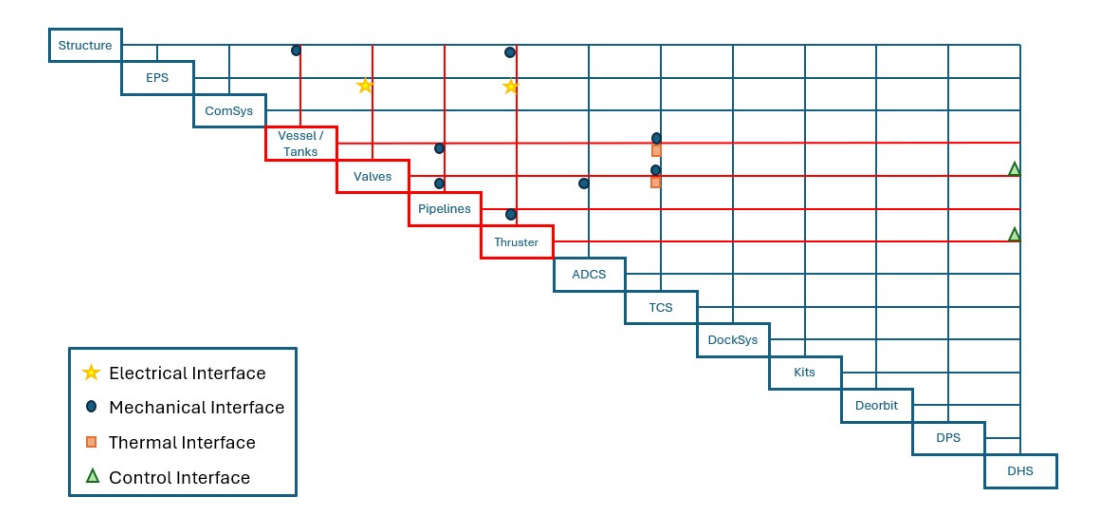


Figure C.3: N2 Diagram for the ODCS

The N2 diagram presented in Figure C.3 reports the interfaces of the ODCS. The connections are mainly mechanical, both between the components and the structure. Electrical

interfaces are present, mainly regarding valves (inside and outside the thruster), while thermal interfaces interest tanks and vessel (MLIs), and also other electrical components. DHS is connected to the thruster and the valves, allowing for propellant transfer when a maneuver is started.

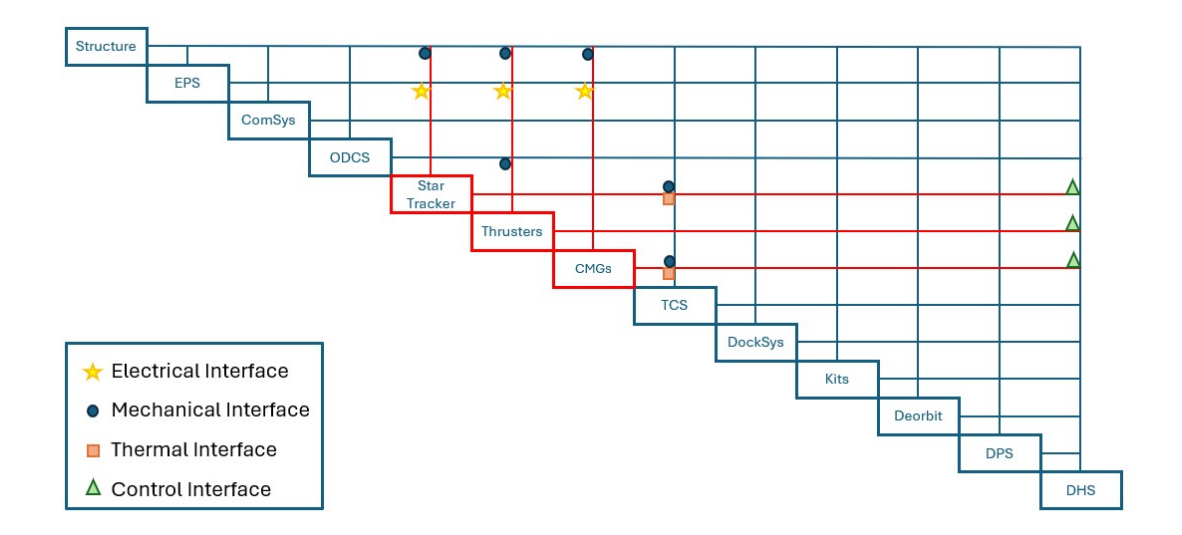


Figure C.4: N2 Diagram for the ADCS

Figure C.4 shows the interfaces of the ADCS. All the components are mechanically linked to the structure and get electrical power from the EPS, while the DHS receives signals from the sensors and orders corrective maneuvers to the actuators. Thrusters are mechanically interfaced to the ODCS, since the pipelines are responsible of delivering hydrazine, and the TCS is connected to the components having a restricted operative temperature range, such as CMGs and star trackers.

In Figure C.5 the interfaces of the TCS with the other subsystems are presented. As usual, the structure represents the frame that mechanically links the components together while the items requiring electrical energy to work are connected to the EPS (and to the DHS to collect data or command their switch on and off). All the subsystems whose components require a restricted operative temperature range are thermally (and, as a consequence, mechanically) connected to heaters and cold plates; the pump of the TCS itself is connected to heaters and cold plates as well. Another thermal interface is located between the pipes and the radiator, allowing for heat exchange with the exterior of the spacecraft. Lastly, the structure and the tanks of the ODCS are thermally connected to the passive TCS, consisting of coatings and MLIs.

The graph shown in Figure C.6 is the N2 diagram of the DockSys. The camera, the electrostatic pads and the electric motor require electrical power to work, and are connected to the EPS as a consequence; moreover, they are controlled by the DHS, which also receives data from the camera itself. The electrostatic pads are mechanically connected to the telescopic arm, which is linked to both the structure and the electric motor. The TCS is interfaced with the electrical components requiring active thermal control, such

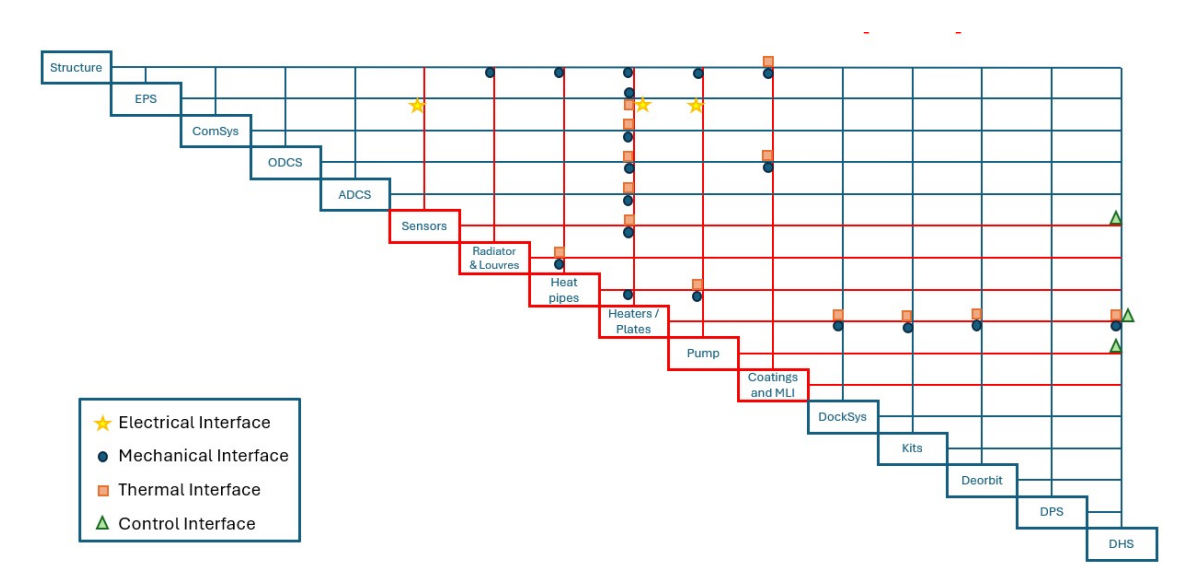


Figure C.5: N2 Diagram for the TCS

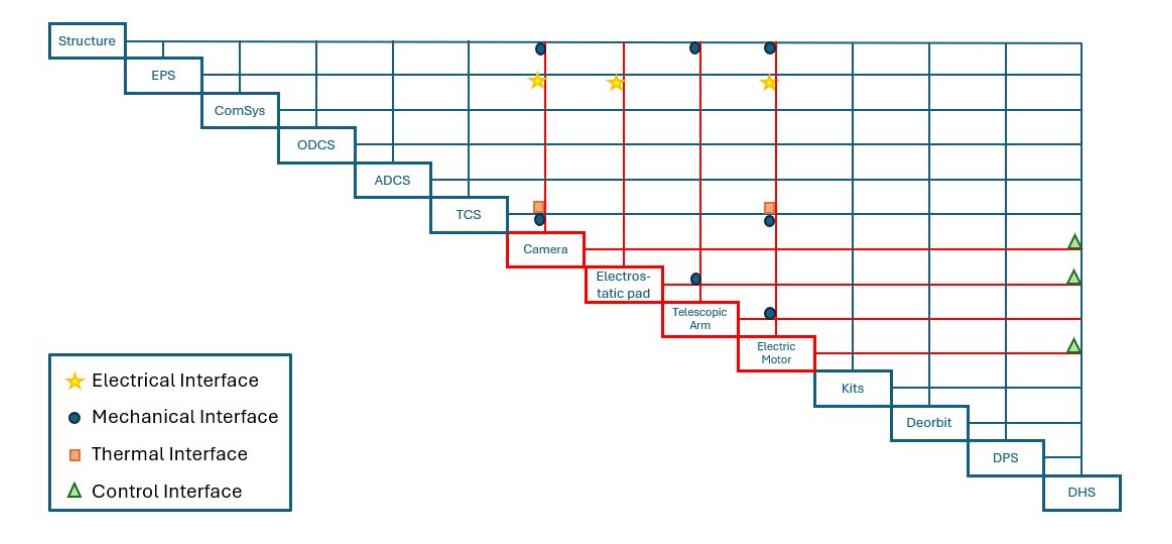


Figure C.6: N2 Diagram for the DockSys

as the camera and the arm's electric motor.

In Figure C.7 is shown the N2 diagram for the deorbit kits' subsystem (for SCMK architecture only). The only mechanical connection with the structure is the telescopic arm with its electric motor, while the other mechanical links are developed among the components of the subsystem itself. The electric motor, as well as the electrostatic pads and the control switches are interfaced with both EPS and DHS, to receive electrical power and control commands. Moreover, the electric motor and the switches are thermally and structurally connected to the TCS, allowing for active thermal control to be provided if necessary. Lastly, a control interface is developed between the kits and the ComSys, since

Structure

EPS

ODCS

ADCS

TCS

DockSys

Telescopic
Arm

Electric
Motor

Electrical Interface

Mechanical Interface

the kits' deployment can be directly commanded from the satellite itself.

Thermal Interface

▲ Control Interface

Figure C.7: N2 Diagram for the Deorbit Kits' Subsystem

DPS

DHS

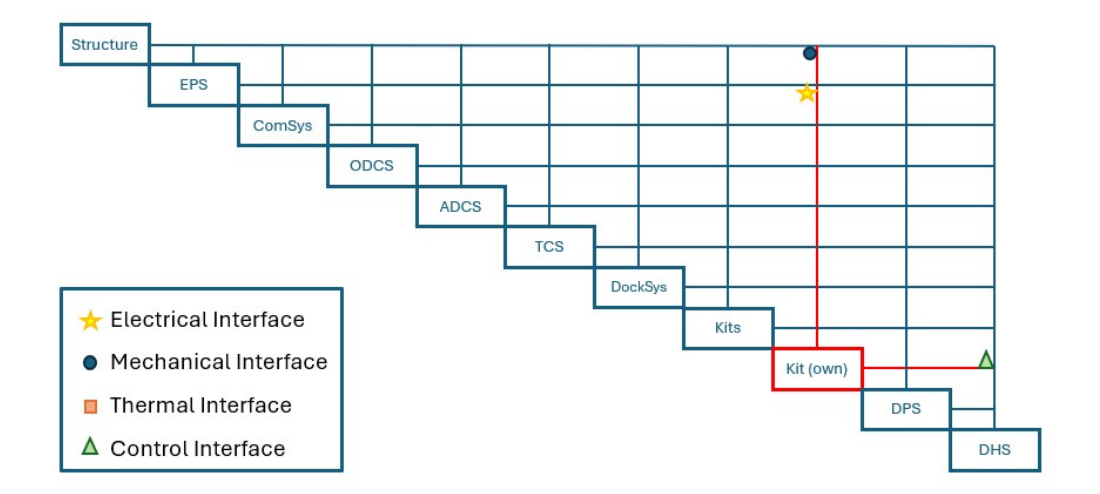


Figure C.8: N2 Diagram for the Own Deorbit Kit's Subsystem

Figure C.8 reports the N2 diagram for the own deorbit kit: this subsystem is not included in the final architectures, but it has been explored as a potential alternative to the burn to disposal maneuver, as presented in Section 5.2.2. The own deorbit kit is mechanically connected to the structure, while it is interfaced with both EPS and DHS to receive electric power and commands.

The least interfaced subsystem is the DPS: as represented in Figure C.9, it is only mechanically linked to the satellite's structure, without any electrical, thermal and control

connections with the other subsystems.

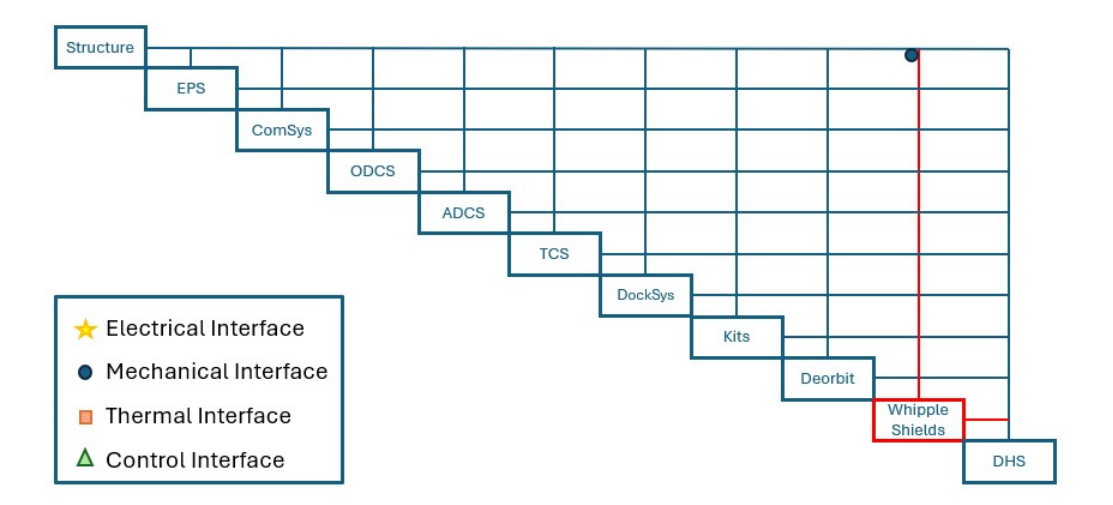


Figure C.9: N2 Diagram for the DPS

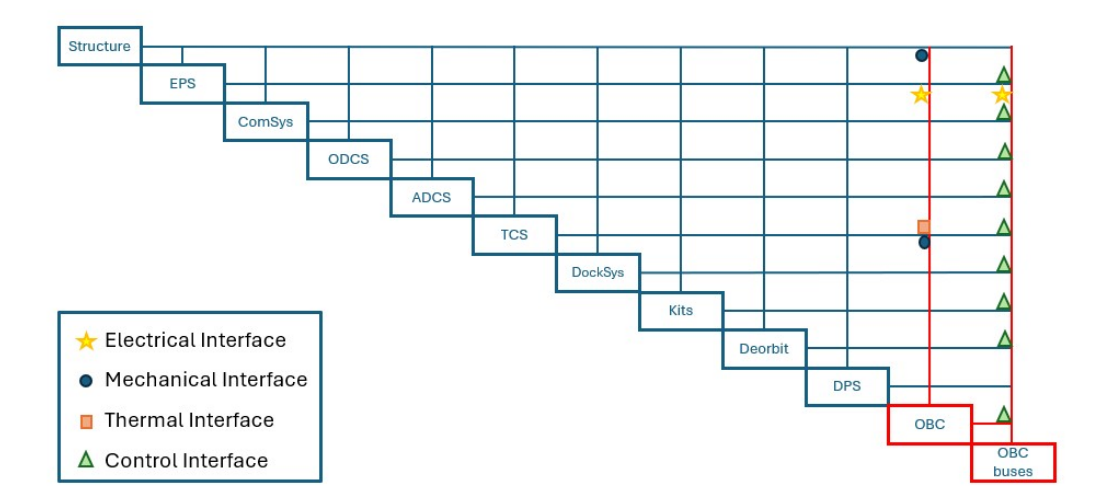


Figure C.10: N2 Diagram for the DHS

The last analysed subsystem is the DHS, which is shown in Figure C.10. The OBCs are mechanically linked to the structure, which acts as a support frame as usual; both the OBCs and their buses are connected to the EPS, while the OBCs are also linked to the TCS for active thermal control to be provided. The computers send the control signals through the buses, which are then connected to all the other subsystems, allowing for commands to be effectively delivered.